

# Continuous Processing of Multiphase Reactions for Pharmaceutical Applications

by

Yiming Mo

B.S. Chemical Engineering, Tsinghua University, China (2014)  
M.S. Chemical Engineering Practice, Massachusetts Institute of Technology (2016)

Submitted to the Department of Chemical Engineering  
in Partial Fulfillment of the Requirements for the Degree of

Doctor of Philosophy in Chemical Engineering  
at the  
MASSACHUSETTS INSTITUTE OF TECHNOLOGY

~~August 2019~~ [September 2019]  
© 2019 Massachusetts Institute of Technology. All rights reserved

**Signature redacted**

Signature of Author.....

Department of Chemical Engineering  
August 06, 2019

**Signature redacted**

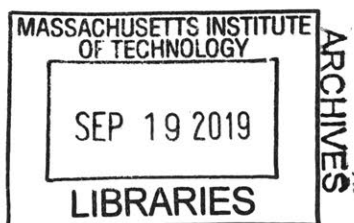
Certified by .....

Klavs F. Jensen  
Warren K. Lewis Professor of Chemical Engineering  
Professor of Materials Science and Engineering  
Thesis Supervisor

**Signature redacted**

Accepted by .....

Patrick S. Doyle  
Robert T. Haslam (1911) Professor of Chemical Engineering  
Graduate Officer Chairman, Committee for Graduate Students



# Continuous Processing of Multiphase Reactions for Pharmaceutical Applications

Yiming Mo

## Abstract

With current needs to expedite new drug development, reduce cost and increase availability of existing drugs, and improve stability and safety of pharmaceutical manufacturing, the continuous flow synthesis has appeared as an attractive alternative to the conventional batch processes. Numerous technologies have emerged to facilitate the development of continuous flow chemistry, and the benefits of flow chemistry have been successfully demonstrated for many chemistries that would otherwise be challenging in conventional batch process because of demanding process conditions, hazardous intermediates, and limitations in mass and heat transfer. However, in contrast to single-phase reaction, transformation of multiphase reactions from batch to continuous flow still remains cumbersome due to complicated multiphase hydrodynamics, mass transfer, interfacial reaction kinetics, and potential clogging issues of solids.

This thesis aims at developing enabling strategies and solutions to make challenging multiphase reaction systems amenable in continuous flow system. For solid-liquid reactions with reactor clogging problems, Chapter 2 presents a new modular miniature continuous stirred-tank reactor (CSTR) cascade to handle solid-forming reactions in flow, which serves as a robust strategy to study solid-containing reactions in small scale. For mass-transfer limited liquid-liquid systems, Chapter 3 describes a high-performance miniature CSTR unit with magnetic coupling rotation mechanism, which decouples mixing and residence time to accommodate different reaction kinetics. To alleviate tedious scale-up procedure and safety concerns of catalytic gas-liquid reactions, Chapter 4 provides a robust design of a thin-layer membrane reactor to safely and scalably perform catalytic heterogeneous hydrogenation and homogeneous aerobic oxidation, providing a superior alternative to conventional packed-bed reactors. For electrosynthesis involving electrode surface as a heterogeneous reaction surface, Chapter 5 demonstrates a cost-effective and scalable electrochemical flow cell engineered for the N-hydroxyphthalimide (NHPI) mediated electrochemical aerobic oxidation of benzylic C-H bonds, and Chapter 6 utilizes the microfluidic electrochemical flow cell to accurately control the lifetime of persistent and transient radicals in order to selectively generate cross-coupling products. The developed modular and plug-and-play reactors in this thesis offer additional tools to enable facile implementation of multiphase chemistries in flow.

Thesis Supervisor: Klavs F. Jensen  
Title: Warren K. Lewis Professor of Chemical Engineering  
Professor of Materials Science and Engineering



## Acknowledgement

It has been a long journey of my PhD research career, which started five years ago, and along with this “marathon”, many people gave me tremendous amount of support to help me come to the end today.

Undoubtedly, Prof. Klavs Jensen, my thesis advisor, is the person to acknowledge first and foremost. I felt very lucky I was able to join Prof. Jensen’s research when coming to MIT, and I still remember the moment that he wrote “Flow Chemistry” (only two words) as my PhD research project on my Advisor Selection Form, while all of my classmates got a very a long project name on their forms. To ease my shock of this short project name, he said a short project name means you can do a variety of different projects, and it turned out to be true. During my time in this lab, I got so many opportunities to work on different interesting projects, and at the same time, explore other research areas. With the weekly subgroup meeting and many individual meetings, Prof. Jensen is very accessible and gave a lot of valuable feedbacks and brilliant ideas, which greatly influenced and shaped my scientific thinking. Prof. Allan Myerson and Prof. Timothy Jamison, two of my thesis committee members, gave me very valuable suggestions and challenged me to look at problems in new ways and encouraged me to go beyond during all my thesis committee meetings.

I really learned a lot of new knowledge during the classes at MIT, which serves as the fuel for my research. Specifically, I would like to thank Prof. William Deen and Prof. Martin Bazant for Transport Phenomena, Prof. James W. Swan and Prof. Richard D. Braatz, for Numeric Methods, and Prof. Leslie Kaelbling for Machine Learning. Those three classes benefit me a lot to solve problems I encountered during my research.

I also have many wonderful mentors, colleagues, and collaborators, from whom I got many valuable advices and learned a lot of knowledge in the past five years. Prof. Gaurav Giri helped me get started in Jensen's research group. All of my flow chemistry experiment skills were initially taught by him, and his enthusiasm for research and life really gave me the passion to explore new ideas. Dr. Hongkun Lin, Dr. Guohua Liang and Prof. Yiming Wang gave me a lot of help on organic chemistry. Dr. Joseph Imbrogno and Prof. Haomiao Zhang worked together me on the membrane reactor project, and helped to get things planned and finished efficiently. Dr. Zhaohong Lu, a fantastic collaborator working together with me on the electrochemistry project, taught me a lot of chemistry knowledge. Dr. Girish Rughoobur helped me a lot with micro-fabrication, making many of my crazy ideas become possible. Thank you for the discussion with all the members from chemical synthesis subgroup, Prof. Milad Abolhasani, Prof. Andrew Teixeira, Prof. Ye-Jin Hwang, Prof. Jisong Zhang, Prof. Kai Wang, Dr. Stefano Lazzari, Prof. Connor Coley, Dr. Agnieszka Ladosz, Dr. Kosi Aroh, Dr. Ioannis Lignos, Anirudh Nambiar, and Alexander Pomberger. And I thank all my officemates, Dr. Lisi Xie, Francisco Navarro-Brull, Dr. Yi Shen, Dr. Eder Jose Guidelli, Prof. Haomao Zhang, Dr. Fang Zhao, Dr. Kakasaheb Nandiwale for all the help, chats, and time shared in the 66-503 office. Also I want to thank all other Jensen group members for all the help and discussions during the past five years.

MIT practice school provided me a great internship experience to explore the working style in two different companies, MedImmune and Woodside Energy. I would like to thank the station director Dr. George Huff for organizing projects and giving critical suggestions to improve our work. I would also like to thank all the practice school teammates for collaborating on different projects.

MIT community is also big part of my graduate student life. MIT hobby shop, a mechanical machine shop at MIT, gave me access to numerous machine tools, without which many of research and hobby ideas would not become reality. Specifically, I would like to thank the past and current directors of hobby shop, Ken Stone and Hayami Arakawa, for their great mechanic advices. I also spent one year in MIT Ventureships Club, where I got to know many MIT startups and got involved to help them build business plans. MIT-China Innovation and Entrepreneurship Forum (CHIEF), an inspiring entrepreneurship platform, helped me make friends with young entrepreneurs in the Boston area. I am very grateful it organized the China Entrepreneurship Trip, which helped me a lot to know about entrepreneurship and decide my future career path. MIT Chinese student community is very important for my time at MIT, and I had great time with them over the weekends and holidays. MIT Sailing, the most enjoyable sport during my time at MIT, gave me the opportunity to explore the Charles River in the sunny afternoons.

I really appreciate Fangyuan Qian that she supports me all the time during this long journey, and cheers me up whenever I came over some challenges. And most importantly, my mom and dad, even though they are 10,000 km away from me in China, gave me spiritual support through this five-year journey. Video calls every week with them always make me feel like at home no matter where I am in the world.



# Table of Contents

Abstract.....	1
Acknowledgement .....	3
Table of Contents.....	7
List of Figures.....	11
List of Tables .....	17
Chapter 1 Introduction .....	19
1.1 Background and motivation.....	19
1.2 Current approaches for multiphase reactions.....	20
1.2.1 Solid handling in flow chemistry.....	20
1.2.2 Reactors for liquid-liquid and gas-liquid reactions.....	23
1.2.3 Electrochemical reactors.....	27
1.3 Thesis overview and goals .....	29
Chapter 2 Solid handling in continuous flow .....	31
2.1 Introduction .....	31
2.2 Experimental methods.....	33
2.2.1 Miniature CSTR cascade design.....	33
2.2.2 Residence time distribution (RTD) characterization .....	35
2.2.3 Procedure for heat transfer efficiency validation of the CSTR cascade .....	36
2.2.4 Procedure for continuous handling of reactions containing solids .....	37
2.3 Results and discussion.....	40
2.3.1 Assessment of mixing properties.....	40
2.3.2 Predicting reaction conversions in the CSTR cascade.....	42
2.3.3 Continuous handling of reactions forming solids .....	43
2.4 Conclusion.....	47
Chapter 3 CSTR for enhancing liquid-liquid mixing .....	48
3.1 Introduction .....	48
3.2 Experimental methods.....	50
3.2.1 Reactor design.....	50
3.2.2 Residence time distribution (RTD) characterization .....	52
3.2.3 High-speed imaging characterization of biphasic hydrodynamics .....	52



3.2.4	Procedure for asymmetric phase-transfer reaction .....	52
3.2.5	General procedure for biphasic Suzuki-Mayaura C-C coupling reaction.....	54
3.3	Results and discussion.....	54
3.3.1	Assessment of single-phase mixing performance.....	54
3.3.2	Characterization of biphasic hydrodynamics.....	56
3.3.3	Estimation of mass transfer coefficients in the CSTR unit.....	57
3.3.4	Asymmetric phase-transfer catalyzed reaction and modeling of interfacial mechanism .....	61
3.3.5	Biphasic Suzuki-Miyaura C-C coupling reactions .....	66
3.4	Conclusion.....	68
Chapter 4 Membrane reactor for gas-liquid reaction.....		69
4.1	Introduction .....	69
4.2	Experimental methods.....	71
4.2.1	Materials and reagents .....	71
4.2.2	Thin-layer membrane reactor design .....	72
4.2.3	General membrane reactor operating procedures .....	73
4.3	Results and discussion.....	74
4.3.1	Heterogeneous catalytic hydrogenations .....	74
4.3.2	Homogeneous Cu/TEMPO catalyzed aerobic alcohol oxidations.....	77
4.3.3	Gas purge for oxygenation reactions .....	78
4.3.4	Membrane reactor design optimization .....	82
4.3.5	Scale-up of thin-layer membrane reactor.....	87
4.4	Conclusion.....	93
Chapter 5 Electrochemical aerobic oxidation in flow.....		94
5.1	Introduction .....	94
5.2	Experimental methods.....	96
5.2.1	Procedure for batch electrolysis.....	96
5.2.2	Procedure for operating electrochemical flow cell with recycle .....	97
5.2.3	Cyclic voltammetry procedure.....	97
5.3	Results and discussion.....	98
5.3.1	Batch condition optimization.....	98
5.3.2	Reaction mechanism .....	100
5.3.3	Reaction kinetics.....	101
5.3.4	Implementation in continuous flow .....	105
5.4	Conclusion.....	109

Chapter 6 Microfluidics-enabled redox-neutral electrochemistry .....	110
6.1 Introduction .....	110
6.2 Experimental methods.....	112
6.2.1 Electrochemical flow cell design .....	112
6.2.2 Setup for reaction condition optimization.....	113
6.2.3 Cyclic voltammetry study .....	113
6.3 Results and discussion.....	114
6.3.1 Electrochemical redox-neutral radical-radical cross-coupling concept.....	114
6.3.2 Decarboxylative aryl nitrile coupling .....	115
6.3.3 Cross-coupling of $\alpha$ -aminoalkyl radical and aryl nitrile .....	121
6.3.4 Cross-coupling of organoboron and aryl nitrile.....	122
6.3.5 Cross-coupling of $\alpha$ -aminoalkyl radical and aryl ketone.....	123
6.3.6 Organocatalyzed allylic C-H arylation .....	124
6.3.7 A fully electrochemical synthesis of liquid crystal material.....	125
6.4 Conclusion.....	128
Chapter 7 Summary and future research.....	129
References.....	134
Appendix A Chapter 3 Supporting Information .....	148
A.1 Reactor design details and driving motor design .....	148
A.2 Single-phase residence time distribution (RTD) measurement.....	151
A.3 Droplet Size Distribution Captured Using High-Speed Imagination.....	152
A.4 Asymmetric phase-transfer catalyzed reaction .....	154
A.5 Kinetic model for makosza interfacial mechanism .....	155
A.6 General Purification and Characterization Methods .....	156
A.7 Characterization of synthesized compounds .....	157
A.8 Nomenclature .....	160
Appendix B Chapter 4 Supporting Information.....	162
B.1 Membrane reactor design and dimensions.....	162
B.2 3-Dimensional COMSOL simulation of membrane reactor .....	164
B.3 Experimental reaction details .....	167
Appendix C Chapter 5 Supporting Information.....	171
C.1 Cyclic voltammetry kinetic study .....	171
C.2 Design and detailed dimensions of the electrochemical flow cell .....	174
Appendix D Chapter 6 Supporting Information .....	178

D.1	Electrode cleaning procedure .....	178
D.2	General procedure A for decarboxylative cross-coupling with aromatic nitriles .....	178
D.3	Procedure B for cross-coupling of $\alpha$ -aminoalkyl radical and aryl nitrile.....	179
D.4	Procedure C for cross-coupling of organoboron and aryl nitrile .....	179
D.5	Procedure D for cross-coupling $\alpha$ -aminoalkyl radical and aryl ketone.....	180
D.6	Procedure E for organocatalyzed allylic C-H arylation .....	180

## List of Figures

Figure 1.1. (a) Teflon reactor integrated with piezo actuators to provide ultrasonic agitation. <sup>33</sup> (b) The Coflore ACR unit. <sup>38</sup> (c) Multi-jet oscillating disk reactor. <sup>39</sup> .....	22
Figure 1.2. (a) Reaction droplets capsuled in the inert carrier phase to confine solids inside solids. <sup>41</sup> (b) Gas-liquid segmented flow with inert gas phase cleaning the tube to prevent clogging. <sup>43</sup> (c) Consumable packed-bed reactor. <sup>42</sup> .....	23
Figure 1.3. (a) Different flow regimes for liquid-liquid flow in a microchannel. <sup>54</sup> (b) Mixing by recirculation in droplets moving through a winding microfluidic channels. <sup>55</sup> (c) Packed-bed with glass beads or stainless steel for enhancing mass transfer between two phases. (d) Static mixing structures in a Corning Advanced Flow Reactor creates small droplets enhancing mass transfer. <sup>51</sup> .....	25
Figure 1.4. (a) Gas-liquid flow regime diagram for microreactors with schematics of bubbly, slug and annular flow regimes. <sup>54</sup> (b) Tube-in-tube reactor using Teflon AF as the gas-permeable membrane. <sup>65</sup> .....	26
Figure 1.5. The design of electrochemical reactors: (a) a two-compartment flow cell divided by a PTFE diaphragm, and carbon felt works as anode and Pt wire works as cathode. <sup>78</sup> (b) An electrochemical reactor design that utilizes short-lived intermediates in situ generated at the electrodes. <sup>79</sup> (c) Exploded-view of a modular divided-wall flow cell. <sup>80</sup> (d) Asia Flux electrochemical module from Syrris with several electrodes options, including carbon filled PVDF, SS 316L, SS 316L platinum coated, magnesium and copper. (syrris.com).....	28
Figure 2.1. Sketch of the miniature CSTR cascade design. (a) The single-stage CSTR shown in CAD drawing, and three main components of the actual product. (b) Multiple CSTRs in series on an aluminum holder. (The white scale bars in the pictures above are 10 mm).....	34
Figure 2.2. Scheme of the residence time distribution measurement using in-line UV-Vis to record concentration profiles for inlet and outlet.....	35
Figure 2.3. The Diels-Alder reaction of isoprene and maleic acid anhydride. ....	36
Figure 2.4. The scheme of the heat transfer efficiency validation using Diels-Alder reaction. ...	37
Figure 2.5. Imine formation reaction of glyoxal and cyclohexylamine.....	39
Figure 2.6 Sulfonylation of 2-octanol with methanesulfonyl chloride. ....	39
Figure 2.7. RTD profiles for n=1, 3, 5, 7 CSTRs in series. Solid lines are regressed experimental RTD profiles based on the EMG model and dashed lines are ideal CSTRs in series model.....	40
Figure 2.8. The inlet and outlet concentration profiles, and the outlet concentration profiles given by the EMG model regression. The CSTR cascade with different numbers of reactors are tested: (a) n=1; (b) n=3; (c) n=5; (d) n=7. ....	41
Figure 2.9. Comparison of measured and predicted reaction conversions for different numbers of CSTRs. Cross-hatched area: predicted conversions. Predicted conversions based on ideal CSTR cascade model. ....	43
Figure 2.10. Photograph of the CSTR cascade during the operation showing the solid fraction increasing along the flow direction. (The white arrow marked g shows the direction of gravity)44	

Figure 2.11. (a) Pressure profile during the continuous operation of the imine formation reaction. (b) Microscope image of the imine crystal. (c) The particle size distribution of the product. ....	45
Figure 2.12. (a) The microscope image of the triethylamine hydrochloride salt. (b) Relative pressure profile during the continuous operation of the sulfonylation reaction. ....	46
Figure 3.1. (a) Exploded-view CAD drawing of a CSTR unit. From top to bottom, it sequentially consists of aluminum cover, borosilicate glass cover, PTFE impeller, ZrO <sub>2</sub> ceramic bearing, polyethylene magnets holder, high-pull magnets, PTFE inner wall, and aluminum jacket. (b) Three main components of the actual CSTR unit. (The black scale bar in each picture represents 5 mm.) .....	51
Figure 3.2. Modularized cooling strategy for the CSTR unit. ....	53
Figure 3.3. (a) The inlet and outlet concentration profiles, and the outlet concentration profile given by the EMG model regression. (b) Normalized residence time distribution of the CSTR unit for various impeller rotation speed at the flowrate of 2 ml/min. The ideal CSTR line represents the theoretical RTD.....	55
Figure 3.4. Normalized residence time distribution of the CSTR unit for various impeller rotation speed at the flowrate of 6 ml/min. The ideal CSTR line represents the theoretical RTD .....	56
Figure 3.5. The hydrodynamics of hexane and water (1:1 ratio) in the CSTR unit at various rotation speeds: (a) 500 RPM, (b) 800 RPM, (c) 1000 RPM, and (d) 1300 RPM.....	57
Figure 3.6. Average hexane droplet size in water for various rotation speeds of the impeller with different two-phase volume ratios in the CSTR unit. ....	58
Figure 3.7. The schematic of the model for estimating the slip velocity.....	59
Figure 3.8. Overall mass transfer coefficients for various rotation speeds of the impeller and different two-phase volume ratios in the CSTR unit. ....	61
Figure 3.9. Asymmetric benzylation of 1 catalyzed by cinchonidine-derived catalyst.....	62
Figure 3.10. (a) The yield (HPLC yield) of asymmetric catalyzed reaction at different residence times and rotation speeds. The dashed lines are drawn based on the proposed interfacial mechanism model. Organic stream (toluene : DCM = 3:1): 0.025 M 1, 0.035 M 2, and 5 mol% 3. Aqueous stream: 50 % (wt.) KOH in water. (b) Proposed interfacial mechanism model to extract mass transfer coefficient. (A: 1, R: 2, PhCH <sub>2</sub> -, Q: cation of 3, X: Cl <sup>-</sup> or Br <sup>-</sup> ) .....	63
Figure 4.1. (a) Gas-liquid membrane reactor schematics: Teflon AF membrane sandwiched between two sheets of carbon cloth layers to offer separation of gas and liquid while allowing the gas phase to diffuse through the membrane to react in the liquid phase. (b) Exploded-view CAD drawing of the gas-liquid membrane reactor. Two thin black layers are carbon cloth, and the thin blue layer is a Teflon AF membrane. (c) Photograph of assembled single-layer membrane reactor. ....	73
Figure 4.2. Pictures of equipment used for controlling the gas-liquid membrane reactor: (a) gas flow controller for H <sub>2</sub> and O <sub>2</sub> (back) and pressure controller for N <sub>2</sub> used to pressurize the BPR (front), (b) in-line degasser (top) and HPLC pump (bottom), (c) variable BPR, and (d) 2 position 6-way valve for controlling the gas and liquid halves of the reactor. Position 1 is the venting position (used during startup and shutdown) and position 2 is used during operation of the reactor. ....	74
Figure 4.3. Schematics of the membrane reactor for estimating the required purge stream .....	80

Figure 4.4. Required purge stream flowrates for various reaction temperature and solvents. The inserted tables shows the LELs in pure oxygen, boiling points (BP), and diffusion coefficients at 25 °C of the studied solvents. ....	82
Figure 4.5. The mass transfer coefficient $kLa$ values under various carbon cloth thicknesses. Insert figure: the hydrogen concentration profile in the membrane and carbon cloth. (Membrane thickness is 40 $\mu\text{m}$ , and carbon cloth thickness is 0.6 mm).....	83
Figure 4.6. Flow velocity profile in membrane reactor. (a) Membrane reactor without porous carbon cloth. (b) Membrane reactor with porous carbon cloth.....	84
Figure 4.7. The schematics of the 1-D model.....	84
Figure 4.8. The reaction conversion dependence on $Da_I$ and $Da_{II}$ .....	86
Figure 4.9. COMSOL simulation of hydrogenation of nitrobenzene with ethanol as solvent in the membrane reactor. The residence time, carbon cloth thickness, and reaction kinetic constant are varied to obtain different values of $Da_I$ and $Da_{II}$ . Hydrogenation pressure: 2.8 MPa. Carbon cloth layer dimension: length (30 mm) $\times$ width (12 mm) $\times$ thickness (0.05 mm – 3 mm). Membrane thickness: 40 $\mu\text{m}$ . The reaction kinetics are available from reported literature, and changing the kinetic constant corresponds to the change of catalyst loading or reaction temperature. <sup>168</sup> .....	87
Figure 4.10. (a) Cross-section of the inlet channels in a 3-layer stacked membrane reactor with blue arrows indicating the liquid flow and purple arrows indicating the gas flow. The outlet channels collect flow from each layer with reversed arrow directions. (b) Photo of a 3-layer stacked membrane reactor.....	88
Figure 4.11. The multi-layer membrane reactor with periodic cooling plates (green). Each cooling plate uses copper tubing for coolant. Gas distribution plates are shown in blue and liquid distribution plates are purple.....	89
Figure 4.12. (a) Temperature profile of a simulated packed-bed reactor. (b) The maximum temperature dependence on coolant flowrate in stacked membrane reactor and packed-bed reactor under the same reaction conditions.....	90
Figure 4.13. The internal structure of stacked membrane reactor used for liquid hydrodynamics simulation in COMSOL. (a) The 3-layer stacked membrane reactor and (b) the 10-layer stacked membrane reactor.....	91
Figure 4.14. The flowrate at the outlet of each layer for (a) 3-layer and (b) 10-layer stacked membrane reactor. Non-porous: the carbon cloth is absent from the liquid channel. Porous: carbon cloth is present in the liquid channel.....	92
Figure 5.1. The batch setup and the RVC electrode. ....	97
Figure 5.2. The cell used for cyclic voltammetry studies. ....	98
Figure 5.3. (a) Cyclic voltammograms of 20 mM NHPI (red curve), and 50 mM pyridinium perchlorate at RVC electrode (blue curve) and Pt electrode (purple curve) scanned at 100 mV/s in 0.1 M solution of TBAP in 1:1 acetone and MeCN mixture. (b) Reaction mechanism for NHPI-mediated electrochemical aerobic oxidation of benzylic C-H bonds. ....	101
Figure 5.4. (a) Cyclic voltammograms recorded for various reagent concentrations of pyridine, corresponding to 2 mM NHPI, 0.2 M 4-ethylanisole, and 0.1 M TBAP in MeCN. Scan rate: 150 mV/s. (b) The catalytic current dependence on the pyridine concentration. ....	102

Figure 5.5. (a) Cyclic voltammograms of a MeCN solution containing 2 mM NHPI, 0.15 M pyridine, and 0.1 M TBAP at different scan rates. (b) linear dependence of peak currents versus (scan rate) <sup>0.5</sup> . .....	103
Figure 5.6. (a) Cyclic voltammograms for various reagent concentrations 1d, corresponding to 2 mM NHPI, 0.15 M pyridine, and 0.1 M TBAP in MeCN. Scan rate: 150 mV/s. (b) Linear regression of catalytic current versus half-order of reagent concentration. (c) Hammett plots of kinetic constants for para-substituted ethylbenzenes. ....	104
Figure 5.7. (a) Exploded-view CAD drawing of the electrochemical flow cell engineered for NHPI-mediated aerobic oxidation of benzylic C-H bonds. From top to bottom, it sequentially contains aluminum holder (with cartridge heaters and thermal insulation layer), polyether ether ketone (PEEK) electrical insulator, copper current collector, polytetrafluoroethylene (PTFE) electrolysis chamber, RVC electrode, and Nafion 117 membrane. The electrochemical flow cell is symmetric to incorporate the divided-wall configuration. (b) Schematics of the operation. Two streams are driven by peristaltic pumps to cycle through the RVC electrodes. Anolyte gets saturated with O <sub>2</sub> in a Teflon AF tube-in-tube device before entering anodic chamber. FlowIR device monitors the species concentration in the anolyte. ....	106
Figure 5.8. (a) FlowIR monitoring of product concentration in the anolyte during the recycle, and the corresponding electrolysis current. (b) Gas chromatograph analysis of two samples from each side during the electrolysis. Anolyte recycles at 1 ml/min: 0.1 M 1a, 0.02 M NHPI, 0.04 M pyridine, 0.1 M TBAP, 0.05 M pyridinium perchlorate, and 4 mM dodecane as internal standard in 16 mL of 1:1 acetone and MeCN. Catholyte recycles at 1 ml/min: 0.1 M 1a, 0.04 M pyridine, 0.1 M TBAP, 0.1 M pyridinium perchlorate, and 4 mM dodecane as internal standard in 8 mL of 1:1 acetone and MeCN. Reaction temperature: 50 °C. ....	107
Figure 6.1. (a) Conventional electrochemistry setup. (b) Photochemistry inspired redox-neutral electrochemistry design. ....	111
Figure 6.2. Exploded-view CAD drawing of the electrochemical flow cell engineered for MRN-Echem. ....	112
Figure 6.3. Scheme of the electrosynthesis condition optimization setup. ....	113
Figure 6.4. Microfluidic electrochemical redox-neutral radical-radical cross-coupling concept. ....	115
Figure 6.5. Electrochemical decarboxylative coupling. ....	116
Figure 6.6. Cyclic voltammogram recorded for 0.02 M 1,4-dicyanobenzene in 0.1 M Bu <sub>4</sub> NBF <sub>4</sub> MeCN solution. ....	117
Figure 6.7. Cyclic voltammogram recorded for 0.02 M butyric acid tetrabutylammonium salt in 0.1 M Bu <sub>4</sub> NBF <sub>4</sub> in DMSO (blue line) and MeCN (red line). ....	117
Figure 6.8. (a) UV-Vis spectroelectrochemical measurement of DCB <sup>•-</sup> lifetime. (b) Kinetic simulation for radical-radical simulation. ....	118
Figure 6.9. Decarboxylative radical-radical cross-coupling reactions. ....	120
Figure 6.10. Cyclic voltammogram recorded for 0.02 M N,N-dimethylaniline in 0.1 M Bu <sub>4</sub> NBF <sub>4</sub> DMSO solution. ....	121
Figure 6.11. Cross-coupling of $\alpha$ -aminoalkyl radical and aryl nitrile. ....	122
Figure 6.12 Cyclic voltammogram recorded for 0.02 M benzyl trifluoroborate tetrabutylammonium salt in 0.1 M Bu <sub>4</sub> NBF <sub>4</sub> in MeCN. ....	123

Figure 6.13. Cross-coupling of organoboron and aryl nitrile. ....	123
Figure 6.14. Cyclic voltammogram recorded for 0.02 M benzophenone in 0.1 M Bu <sub>4</sub> NBF <sub>4</sub> in MeCN. ....	124
Figure 6.15. Cross-coupling of $\alpha$ -aminoalkyl radical and aryl ketone .....	124
Figure 6.16. Cyclic voltammogram recorded for 0.01 M triisopropylsilanethiol and 0.01 M DBU in 0.1 M Bu <sub>4</sub> NBF <sub>4</sub> in acetone. ....	125
Figure 6.17. Organocatalyzed allylic C-H arylation .....	125
Figure 6.18. Fully solar-electrochemical synthesis of 5CB. ....	126
Figure 6.19. (a) Photo of recycling electrochemical flow cell. (b) Photo of continuous electrochemical homocoupling reaction setup powered by sunlight. (c) Synthesized 2.67 g of BPCN. ....	127
Figure 6.20. The comparison between small- and large- scale MRN-Echem flow cell. ....	128
Figure A.1. The design dimensions for aluminum jacket and inner PTFE wall. (unit: inch)....	148
Figure A.2. The design dimensions for the magnet holder. (unit: inch).....	149
Figure A.3. The design dimensions for the impeller. (unit: inch).....	149
Figure A.4. The design dimensions for the glass cover. (unit: inch).....	150
Figure A.5. The design dimensions for the aluminum cover. (unit: inch).....	150
Figure A.6. The driving motor with four magnets on its shaft. ....	151
Figure A.7. Scheme of the RTD measurement using in-line UV-Vis to record concentration profiles for inlet and outlet.....	152
Figure A.8. The droplet size distribution for hexane : water = 1:1 under various RPMs.....	153
Figure A.9. The droplet size distribution for hexane : water = 1:2 under various RPMs.....	153
Figure A.10. The droplet size distribution for hexane : water = 2:1 under various RPMs.....	154
Figure A.11. The yield (HPLC yield) of asymmetric catalyzed reaction at different residence and rotation speed. ....	155
Figure A.12. The relationship between yield and mass transfer coefficient calculated from the kinetic model. (Identical reaction conditions and the residence time is 43 min).....	155
Figure A.13. High-speed imaging of asymmetric phase transfer reaction system: (a) RPM=500, (b) RPM=800, and (c) RPM=1200. ....	156
Figure B.1. (a) Photo of aluminum cover for single-layer membrane reactor. (b) Detailed dimensions of the aluminum cover for single-layer membrane reactor. ....	162
Figure B.2. (a) Photo of liquid distribution plate assembled with O-ring, Teflon AF membrane and carbon cloth for single-layer membrane reactor. (b) Detailed dimensions of the liquid distribution plate for single-layer membrane reactor. ....	162
Figure B.3. (a) Photo of gas distribution plate assembled with O-ring and carbon cloth for single-layer membrane reactor. (b) Detailed dimensions of the gas distribution plate for single-layer membrane reactor.....	163



Figure B.4. (a) Photo of liquid distribution plate assembled with O-ring for multi-layer membrane reactor. (b) Detailed dimensions of the liquid distribution plate for multi-layer membrane reactor. ....	163
Figure B.5. (a) Photo of gas distribution plate assembled with O-ring for multi-layer membrane reactor. (b) Detailed dimensions of the gas distribution plate for multi-layer membrane reactor. ....	164
Figure B.6. The hydrogen concentration profile in membrane reactor. Carbon cloth thickness: 0.3mm. ....	165
Figure B.7. The schematics of the membrane reactor showing the positions indicated in Table B.1. ....	166
Figure C.1. The reaction scheme for anodic side.....	171
Figure C.2. (a) Cyclic voltammograms recorded for various reagent concentrations of ethylbenzene, corresponding to 2 mM NHPI, 0.15 M pyridine, and 0.1 M TBAP in MeCN. Scan rate: 150 mV/s. (b) Linear regression of catalytic current $i_{cat}$ versus $C_R^{0.5}$ .....	172
Figure C.3. (a) Cyclic voltammograms recorded for various reagent concentrations of 4-bromoethylbenzene, corresponding to 2 mM NHPI, 0.15 M pyridine, and 0.1 M TBAP in MeCN. Scan rate: 150 mV/s. (b) Linear regression of catalytic current $i_{cat}$ versus $C_R^{0.5}$ .....	172
Figure C.4. (a) Cyclic voltammograms recorded for various reagent concentrations of 4-ethylbenzotrifluoride, corresponding to 2 mM NHPI, 0.15 M pyridine, and 0.1 M TBAP in MeCN. Scan rate: 150 mV/s. (b) Linear regression of catalytic current $i_{cat}$ versus $C_R^{0.5}$ .....	173
Figure C.5. (a) Cyclic voltammograms recorded for various reagent concentrations of 4-ethylnitrobenzene, corresponding to 2 mM NHPI, 0.15 M pyridine, and 0.1 M TBAP in MeCN. Scan rate: 150 mV/s. (b) Linear regression of catalytic current $i_{cat}$ versus $C_R^{0.5}$ .....	173
Figure C.6. (a) Detailed dimensions for the aluminum holder; (b) Photo of the aluminum holder. ....	175
Figure C.7. (a) Detailed dimensions for the PEEK electrical insulator; (b) Photo of the PEEK electrical insulator. ....	175
Figure C.8. (a) Detailed dimensions for the copper current collector; (b) Photo of the copper current collector.....	176
Figure C.9. (a) Detailed dimensions for the anodic and cathodic chamber; (b) Photo of the chamber with RVC installed.....	176
Figure C.10. (a) Photo of the electrochemical flow cell during assembling. The Nafion membrane is sandwiched between two chambers. (b) Photo of the electrochemical cell during operation. ....	177

## List of Tables

Table 3.1. Mass transfer coefficients for the phase-transfer reaction estimated by: (i) Makosza interfacial mechanism kinetic model, and (ii) high-speed imaging.....	66
Table 3.2. Biphasic Suzuki-Miyaura C-C coupling reactions <sup>a</sup> .....	67
Table 4.1. Optimization of heterogeneous hydrogenation of nitrobenzene to aniline. <sup>a</sup> .....	76
Table 4.2. Heterogeneous hydrogenation substrate scope. <sup>a</sup> .....	76
Table 4.3. Homogeneous Cu/TEMPO catalyzed aerobic alcohol oxidation substrate scope. <sup>a</sup> .....	77
Table 4.4. Data used for estimating flowrate of oxygen purge stream. ....	79
Table 4.5. The coefficient of variation <sup>a</sup> for flow distribution with and without carbon cloth in a 3-layer and 10-layer membrane reactor. <sup>b</sup> .....	92
Table 5.1. Influence of batch reaction conditions on NHPI-mediated electrochemical aerobic oxidation of benzylic C-H bonds. <sup>a</sup> .....	99
Table 5.2. Substrate scope of NHPI-mediated electrochemical aerobic oxidation of benzylic C-H bonds in the electrochemical flow cell with recycle <sup>a</sup> .....	108
Table 6.1. Electrochemical reaction condition optimization .....	119
Table B.1. Domain controlling equations and boundaries conditions used in the COMSOL simulation.....	165
Table C.1. The comparison of kinetic constants between this study and literature values.....	174



# Chapter 1 Introduction

## 1.1 Background and motivation

Continuous-flow production is the basis of the petrochemical and bulk chemicals industry, where environmental and safety regulations, competition, and long development time drive high-performing, cost-effective, safe, and atom-efficient continuous chemical processes.<sup>1</sup> However, the diversity and complexity of fine chemical molecules combined with relatively small annual production leave continuous-flow process relatively less developed in the pharmaceutical industry.<sup>2</sup>

Currently, the production of fine chemicals, such as active pharmaceutical ingredients (APIs), typically relies on batch or semi-batch processes. The flexibility and versatility of the batch vessel reduce the investment and time cost of new equipment development for accommodation to different reaction kinetics.<sup>3</sup> However, a survey conducted at Lonza analyzed 86 different reactions in the pharmaceutical industry, and concluded that 50% of the reactions would benefit from transferring to continuous production.<sup>3</sup> Compared to the batch or semi-batch production, the continuous production has the advantages of steady state operation, improved heat and mass transfer rates, reproducibility, and improved safety and process reliability.<sup>4</sup>

In the past two decades, continuous flow chemistry has emerged as a complementary tool for organic synthesis.<sup>1,5-12</sup> Increasing interest in process intensification<sup>13-15</sup> and emergence of new materials along with microfabrication<sup>16,17</sup> and 3D printing technologies<sup>18</sup> have enabled the adoption of flow chemistry by the organic chemistry community with a corresponding rapid

implementation of reactions performed in flow.<sup>19–26</sup> The benefits of flow chemistry are most apparent when used to realize chemistries that would otherwise be challenging in conventional batch process because of demanding process conditions, hazardous intermediates, and limitations in mass and heat transfer.<sup>27</sup> Operating flow-reactors at elevated pressure allows heating of fluid streams above their normal atmospheric boiling points to accelerate slow reaction rates.<sup>28</sup> Careful design of channel geometry and flow rates also enables precise timing control over reagent addition and quenching. The high surface area to volume ratio resulting from the small channel dimensions increases heat transfer, giving better thermal profile for highly exothermic reactions, and enhances mass transfer characteristics for improved mixing of reagents, especially in multiphase systems.<sup>27</sup>

Transformation from batch to continuous process involves the understanding and control of the complex interactions among flow, mass and heat transfer rates, and reaction kinetics, a proper reactor design. Unlike batch glass vials or vessels, a universal flow reactor design is not feasible because of numerous different reaction conditions, especially when involving multiple phases. Different phase combinations have their own challenges when implemented in continuous flow. In order to make flow chemistry more accessible for a wider range of chemistries, the design of modular reactors would be the desired strategy to accommodate various multiphase chemistries.

## **1.2 Current approaches for multiphase reactions**

### **1.2.1 Solid handling in flow chemistry**

Numerous important reactions in the pharmaceutical industry involve stoichiometric amounts of solids, which can be present as reagents, intermediates, by-products or products.<sup>29</sup> However, handling solids in a flow reactor is challenging, especially at small scales, because of

flow-induced deposition, bridging, and aggregation of solid particles inside the reactor. These clogging issues might eventually lead to the failure of the process, and minimizing them will make flow chemistry more applicable for chemical and pharmaceutical synthesis.

A number of innovative strategies, passive and active, have been proposed to address handling of solids in flow. Passive approaches involve flows without mechanical agitation or any external forces applied beyond pumping. Active techniques are those requiring the implementation of external forces. Due to the limited particle-fluid interaction provided by the laminar flow inside the small-scale flow reactors, exerting external forces, such as acoustic<sup>30-33</sup>, magnetic<sup>34-36</sup>, and mechanical forces<sup>37-40</sup>, will excite the movement of solid particles to prevent aggregation, constriction, and bridging of particles from happening.

The easiest strategy to use in a research laboratory is applying ultrasound through the reactor by simply submerging the reactor into a sonication bath. Hartman et al.<sup>33</sup> developed an integrated ultrasonic reactor (Figure 1.1a) to perform Pd-catalyzed C-N cross-coupling reactions. They showed that a particular frequency was optimal in breaking up aggregates of solid particles and maintaining a sufficiently small particle size to avoid clogging. Ultrasound can be a convenient approach to minimizing for clogging issues on the small scale, but the energy input required and potential side effects inhibit use of ultrasound for large-scale synthesis. Increasing the local flow speed and creating vortices by mechanical agitation increases particle-fluid interaction without interfering with residence time. Moreover, active mixing provided by the addition of external stirring significantly enhances the heat and mass transfer inside the reactor. Ley et al. evaluated the commercially available Coflore ACR by delivering 208 g of N-iodomorpholinium hydroiodide salt over a 9-h period (equating to 3.88 kg/week) under optimized conditions.<sup>38</sup> The Coflore ACR uses a moveable agitator inside each reactor chamber (Figure 1.1b), while an external reactor

holder vibrates the whole reactor to create relative movement between the agitator and reactor chamber, which prevents solid particles from depositing in the reactor. Solid-producing reactions have also been run successfully with the multi-jet oscillating disc (MJOD) milli-reactor that oscillates a multi-jet disk assembly forward and backward in the longitudinal direction inside a tubular reactor as shown in Figure 1.1c.<sup>39,40</sup> The mechanical agitation strategy is typically easy to scale up in terms of handling solids continuously.

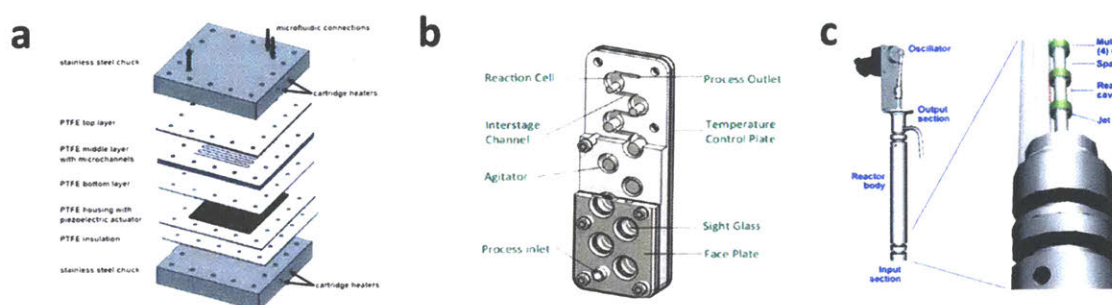


**Figure 1.1. (a) Teflon reactor integrated with piezo actuators to provide ultrasonic agitation.<sup>33</sup> (b) The Coflore ACR unit.<sup>38</sup> (c) Multi-jet oscillating disk reactor.<sup>39</sup>**

Passive strategies are typically suitable for specific reaction categories. For example, confining the reaction inside a droplet when the droplet is travelling through the tubular reactor was demonstrated by Poe et al. (Figure 1.2a).<sup>41</sup> The carrier phase, typically mineral oil or perfluorinated solvents, needs to be inert and immiscible with the reaction solvent. Since the solid products or by-products are confined inside the reaction droplet, the possibility of particles settling on the wall is reduced along with particle interactions between two droplets. Formation of large aggregates and large amount of solids will eventually disrupt the droplet flow and solids may settle out and clog the tube. The challenges of selecting a proper inert carrier phase and finding the optimal flowrate to maintain stable droplets inside the carrier phase limit the utility of the droplet approach. Similarly, the inert liquid phase can be replaced by inert gas slugs (Figure 1.2b), which will improve the solid handling capability of a tubular reactor compared to single-phase scenario.<sup>41</sup>

For reactions that involve solid reagents, such as reductive amination using  $\text{NaBH}_4$ , Gilmore et al.<sup>42</sup> designed a consumable packed bed reactor, in contrast to a packed-bed reactor with reusable catalyst (Figure 1.2c). This consumable packed-bed reactor needs to be replaced after the consumption of the solid reagents. Specific reaction types benefit from such passive strategies, but they are often difficult to generalize.

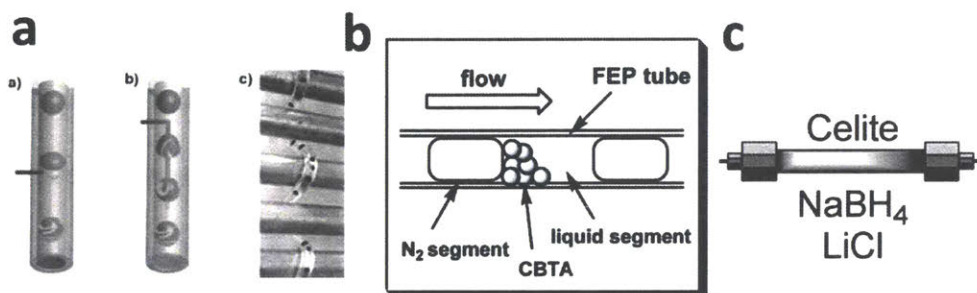


**Figure 1.2. (a) Reaction droplets capsuled in the inert carrier phase to confine solids inside solids.<sup>41</sup> (b) Gas-liquid segmented flow with inert gas phase cleaning the tube to prevent clogging.<sup>43</sup> (c) Consumable packed-bed reactor.<sup>42</sup>**

## 1.2.2 Reactors for liquid-liquid and gas-liquid reactions

Liquid-liquid system involves two immiscible fluids, typically aqueous and organic phases. Surface tension at the interface plays an important role in controlling the biphasic hydrodynamics in the reactor.<sup>44,45</sup> Aqueous solutions will wet hydrophilic surfaces (e.g., glass) while organic fluids tend to wet hydrophobic surfaces (e.g., PFA). Thus, a flow of organic and aqueous solutions in a glass tube will form a two-phase flow with the aqueous phase being the continuous wetting phase and the organic phase being the isolated dispersed phase (Figure 1.3a) – a so-called segmented flow. For similar volumetric flow rates of the two phases, a regular flow of isolated droplets is to be observed. At high flow rates, the influence of surface tension is reduced relative to the convective flow and a stratified flow results.



The segmented flow regime is the most often encountered regime in flow chemistry applications. The well-defined two-phase interface facilitates characterization of the mass-transfer performance in the system.<sup>46</sup> The slug length can be controlled by tuning flowrates, junction structure, and surface wettability.<sup>44</sup> Recirculation inside the dispersed droplet (Figure 1.3b) promotes material transport from one phase to the other phase. Using a meandering tube further enhances mixing in the droplets by periodically alternating the relative sizes of the recirculation cells.<sup>47</sup> The rate of the mixing in droplets, and hence the effectiveness of the segmented flows, depends on the relative differences in wetting characteristics of the fluids.<sup>48</sup> Faster mixing than that created by the natural recirculation patterns in segmented flow can be achieved by introducing static mixers. These can be realized by packing the tube with inert spheres (Figure 1.3c) to increase the interfacial area and mixing as demonstrated by Naber et al.<sup>49</sup> and Noël et al.<sup>50</sup> for Pd-catalyzed cross-coupling reactions. The yield of the C-N cross-coupling reaction was nearly 100% with stainless steel beads in 6 min as compared to a yield of only 94% obtained in batch with fast stirring (~ 900 RPM). In contrast, the open tube reactor with the same size yielded only 20% under the same conditions. Incorporating static mixing elements increases mass transfer by creating fine droplets, i.e., large interfacial areas (Figure 1.3d), but necessitates using sufficiently large flow rates.<sup>51,52</sup> The large flow rates in turn necessitate a large reactor volume for a biphasic reactions requiring long residence times.

Gas-liquid systems share similarities with liquid-liquid systems, but there are substantial physical property differences between liquids and gases, such as the density, viscosity, compressibility, and surface tension. As a result, the flow diagram (Figure 1.4a) shows different regimes compared to that for liquid-liquid systems (Figure 1.3a). For a given liquid flow rate, adding gas leads first to a bubbly flow that becomes slug flow (aka Taylor flow) at higher gas flow

rates.<sup>53</sup> Slug flow is equivalent to segmented flow for liquid-liquid flows and is the gas-liquid contact pattern typically used in flow chemistry applications. Further increases in gas flow leads to annular flow in which a thin liquid flow wets the wall and the central core is solely gas, analogous to the stratified flow for liquid-liquid systems. Mass transport rates and flow characteristics vary significantly among the different regimes.<sup>54</sup>

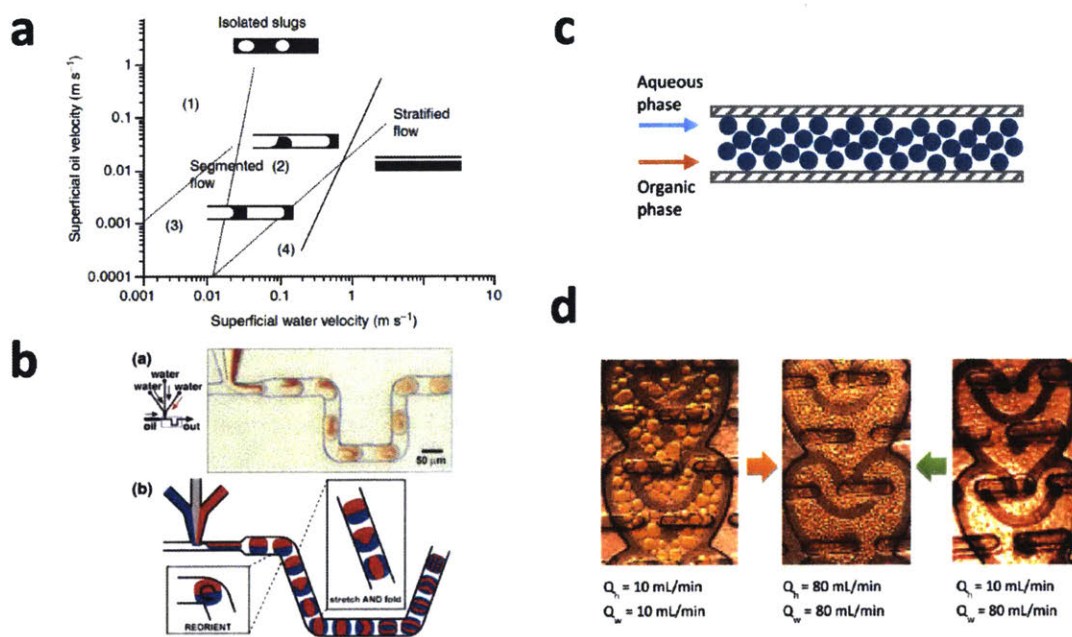


**Figure 1.3. (a) Different flow regimes for liquid-liquid flow in a microchannel.<sup>54</sup> (b) Mixing by recirculation in droplets moving through a winding microfluidic channels.<sup>55</sup> (c) Packed-bed with glass beads or stainless steel for enhancing mass transfer between two phases. (d) Static mixing structures in a Corning Advanced Flow Reactor creates small droplets enhancing mass transfer.<sup>51</sup>**

Slug flow for gas-liquid flows have stronger internal recirculation than in typical liquid-liquid segmented flows because of larger differences in surface tension. The rate of mass transfer depends on a number of variables including the length of the slugs/bubbles, channel diameter, and flow rates of the respective phases.<sup>56</sup> As in the liquid-liquid phase systems, mass transfer rates can be increased by introducing static mixers,<sup>57</sup> posts,<sup>58</sup> or a package of solid spheres.<sup>59</sup> These

structures act to disperse the flow and create larger interfacial areas. Many gas-liquid reactions have been converted to flow including carboxylation,<sup>60</sup> chlorination,<sup>61</sup> hydrogenation,<sup>62</sup> fluorination,<sup>63</sup> and ozonolysis<sup>64</sup> reactions. The use of high pressures provides for higher concentrations of gas phase species in the liquid phase leading to faster reaction rates. Moreover, given the comparatively small amounts of gas used in flow systems, many of the special precautions normally required for handling dangerous gases are significantly reduced.

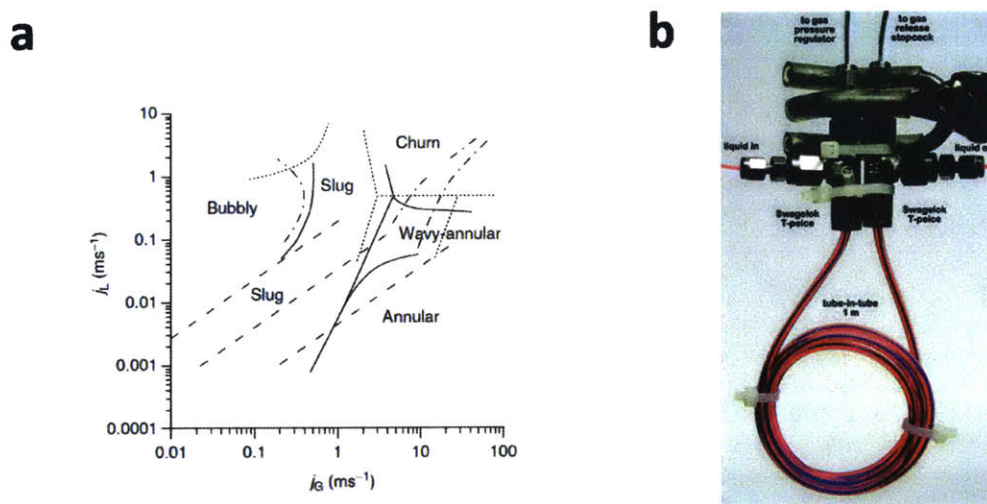


**Figure 1.4. (a) Gas-liquid flow regime diagram for microreactors with schematics of bubbly, slug and annular flow regimes.<sup>54</sup> (b) Tube-in-tube reactor using Teflon AF as the gas-permeable membrane.<sup>65</sup>**

Gas liquid contact can also be achieved by using selective membranes, such as Teflon AF permeable to gas but not liquid. Ley et al. thoroughly investigated the tube-in-tube reactor design for gas-liquid reactions as shown in Figure 1.4b.<sup>65–67</sup> This reactor has a smaller Teflon AF tubular membrane inside of outer tubing which is standard PFA or PFP tubing. They demonstrated this reactor using a series of reactions, which include ozonolysis<sup>66</sup>, Paal–Knorr reaction using ammonia<sup>65</sup>, and synthesis of carboxylic acid using CO<sub>2</sub><sup>67</sup>. This technology avoids direct contact of gas and liquid, which enables safe operation of highly flammable oxidant and organic solvent

systems, such as ozonolysis reactions. The mass transfer characteristics of these systems have been characterized, and associated challenges for scale-up were evaluated.<sup>68</sup>

### 1.2.3 Electrochemical reactors

Organic electrochemistry started with the development of Kolbe electrolysis in 1848.<sup>69</sup> However, electrochemistry is often not practiced due to the perceived complexity of reaction setup (e.g., potentiostat, divided/undivided cell, electrode composition, and reactor design), and the seemingly endless number of reaction variables (e.g., electrolyte, electrode composition, cell type, etc.).<sup>70</sup> Additionally, researchers often utilize homemade electrochemical devices, which makes it challenging for other researchers to replicate published work. Despite these obstacles, there is a growing trend towards developing new electrochemical methods to synthesize complex molecules due to advantages of environmental friendliness, ability to operate at reduced temperatures, scalability, and sustainability.<sup>71-76</sup> Flow chemistry appears as a promising alternative to batch with its intrinsic advantages, including existence of steady state, small sample volume required for screening, and ease of scale up.<sup>77</sup>

Because electrochemical reactors necessarily contain electrodes in contact with the reaction mixtures, their design is significantly more complicated than other flow reactor designs. Additional considerations beyond reactor geometry, mass transfer performance, and heat transformer performance include material selection, sealing choice, and electrode connection and insulation; the electron transfer process adds a new dimension of complexity. Despite this, researchers have successfully fabricated customized electrochemical reactors and demonstrated them with synthetically useful reactions.<sup>77</sup>

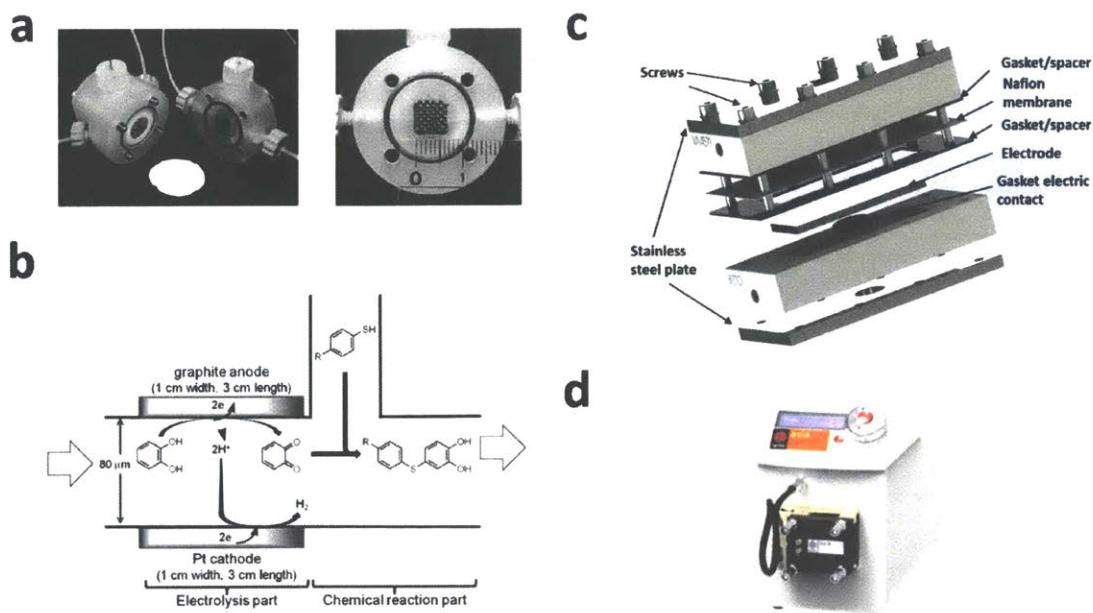


**Figure 1.5.** The design of electrochemical reactors: (a) a two-compartment flow cell divided by a PTFE diaphragm, and carbon felt works as anode and Pt wire works as cathode.<sup>78</sup> (b) An electrochemical reactor design that utilizes short-lived intermediates in situ generated at the electrodes.<sup>79</sup> (c) Exploded-view of a modular divided-wall flow cell.<sup>80</sup> (d) Asia Flux electrochemical module from Syrris with several electrodes options, including carbon filled PVDF, SS 316L, SS 316L platinum coated, magnesium and copper. (syrris.com)

Yoshida et al.<sup>81</sup> developed the cation pool method, in which highly reactive carbocations are generated in the absence of nucleophiles by low-temperature (-78 °C) electrolysis and are allowed to react with carbon nucleophiles to achieve direct electrooxidative C-C bond formation (Figure 1.5a). The flow cell can generate the unstable carbocations *in situ* and use them immediately after coming out of the reactor.<sup>78</sup> Atobe et al. engineered a micro electrolysis cell shown in Figure 1.5b which has an 80 μm electrode separation distance to greatly enhance the species electron transfer with the electrode surface.<sup>79</sup> Rapid generation and usage of short-lived intermediates were realized using this reactor. Gütz et al. designed and demonstrated a highly modular electrochemical flow cell (Figure 1.5c) with domino-oxidation-reduction reaction.<sup>80</sup>

Green et al. demonstrated a laboratory-scale flow electrolysis cell.<sup>82</sup> Using the methoxylation of N-formylpyrrolidine as a model reaction, they were able to obtain around 100% conversion in a single pass with a product formation rate of  $>20 \text{ g h}^{-1}$ . They also evaluated a commercially available electrochemical reactor (Asia Flux) as shown in Figure 1.5d with the same reaction.<sup>83</sup>

With the current status of flow electrolysis reactors, there is much work to be done to fully explore the benefits that flow chemistry can contribute to enabling electroorganic synthesis. One immediate benefit is that the operation of flow reactors at steady state enables straightforward constant-potential operation. For batch electrolysis, it is often operated at constant current instead of constant potential, which leads the potential to increase during the course of the electrolysis. The uncontrolled potential might cause side reactions because functional groups on complex organic molecules have different oxidation and reduction potentials. However, the potential in a flow electrolysis reactor will stay unchanged during steady state operation, which could help the optimization of the electrolysis conditions. Developments of flow batteries over the last two decades could potentially be useful in further advancing the development of electroorganic synthesis in flow.<sup>84</sup>

### **1.3 Thesis overview and goals**

Even though many strategies haven't already been developed to handle multiphase reactions in pharmaceutical applications, it would still be desired to explore more robust solutions to alleviate challenges associated with multiphase systems. This thesis aims at developing enabling strategies and solutions to make challenging multiphase reaction systems amenable in continuous flow system.

Chapter 2 presents a new modular miniature continuous stirred-tank reactor (CSTR) cascade to handle solid-forming reactions in flow, which serves as a robust strategy to study solid-containing reactions in small scale. Chapter 3 describes a high-performance miniature CSTR unit for biphasic systems, decoupling mixing and residence time to accommodate different reaction kinetics. Non-contact magnetic coupling, the key design concept, provides intensive agitation inside the sealed miniaturized chamber. Chapter 4 provides a robust design of a thin-layer membrane reactor to safely and scalably perform catalytic homogeneous and heterogeneous gas-liquid reactions, providing a superior alternative to conventional packed-bed or trickle-bed reactors. Additionally, the simulations and models provide fundamental understanding and design principles for optimizing the membrane reactor structure for different reaction systems. Chapter 5 demonstrates a cost-effective and scalable electrochemical flow cell engineered for the N-hydroxyphthalimide (NHPI) mediated electrochemical aerobic oxidation of benzylic C-H bonds, in order to provide a general strategy for realizing continuous electrochemical organic synthesis with inherently slow reaction kinetics. Chapter 6 utilizes the microfluidic electrochemical flow cell to accurately control the lifetime of persistent and transient radicals in order to selectively generate cross-coupling products. A series of new chemistries are developed and demonstrated on this new platform.

# Chapter 2 Solid handling in continuous flow

## 2.1 Introduction

Handling of solid compounds in flow systems without clogging is always challenging. Numerous important reactions in the pharmaceutical industry involve stoichiometric amount of solids, which can be present as reagents, intermediates, byproducts or as products. Large-scale continuous transport of solid particles, such as flow of suspensions in pipelines, is a well-studied area.<sup>85-87</sup> In centimeter- or meter- scale tubes, the particle-fluid interactions generated by turbulent flow balance the effect of gravity to prevent settling of particles in the pipe. Below a critical deposit velocity of the fluid, a stationary bed of particles will form on the bottom of the pipe. Due to the complexity of the slurry system, researchers have extensively studied numerous empirical equations for predicting the critical deposit velocity.<sup>88</sup>

With the laminar flow characteristic of micro- and milli-reactors, particle-wall and particle-particle interaction become important in controlling the behavior of particles in flow. The constriction of particles on the wall caused by particle-wall interaction and agglomeration and bridging of particles caused by particle-particle interaction make the small-scale transport of slurry more difficult than on larger scales.<sup>89,90</sup>

Researchers have proposed innovative methods to avoid solid clogging in the flow reactors. For example, Poe et al. used “droplet reactors,” travelling in the carrier phase, to confine solid particles in the liquid droplets, thus keeping them away from the tube wall and preventing clogging of the tube reactor.<sup>91</sup> Exerting non-contact external forces on particles, such as acoustic<sup>92-95</sup>,



magnetic<sup>96-98</sup>, and electrophoretic forces<sup>99,100</sup>, has been used to keep solid particles suspended in the flowing fluid. Application of ultrasonic irradiation to a tube reactor breaks apart agglomerates, which reduces particle sizes and minimizes the chance of forming channel spanning agglomerates plugging the flow tube.<sup>92</sup> Sonication effectively extends the operation time of the tube reactor compared to the scenario without sonication, but scaling of ultrasound has challenges.

Agitated millireactors have been developed for handling solids. Ley et al. used the Coflore ACR agitated cell reactor to demonstrate the continuous formation of the hydroiodide salt of N-iodomorpholine through the reaction of morpholine with iodine<sup>101</sup> and built a back pressure regulator to accommodate superheated conditions for slurry-forming reactions<sup>102</sup>. Recently, Baxendale et al. realized kg-quantity continuous production of triacetic acid lactone solid, a building block as part of a synthesis program preparing bromodomain containing proteins modulators.<sup>103</sup> Solid producing reactions have also been run successfully with the multijet oscillating disc (MJOD) millireactor that oscillates a multijet disk assembly forward and backward in the longitudinal direction inside a tubular reactor.<sup>104,105</sup> Cascades of continuous stirred tank reactors (CSTRs) are used in the pharmaceutical industry for continuous crystallization in so-called continuous mixed suspension, mixed product removal (MSMPR) crystallizers<sup>106-109</sup>, but the liquid hold up in these systems is often too large (liters) for small scale organic synthesis.

Despite the current solutions to enable handling solids in a small-scale continuous flow reactor, it would still be desired to have a lab-scale CSTR that can be versatile and robust to serve as a tool for investigating solid-containing reaction conditions that can be easily translated into large-scale CSTRs. In this chapter, a new cascade of miniature continuous stirred-tank reactors (CSTRs) will be described for reactions containing solids in lab scale. The single-phase mixing properties of the miniature CSTR cascade is characterized and compared to the ideal CSTR

performance. In addition, two examples that generate solids as product and by byproduct during the reaction serve to assess the ability of the reactor to handle solids continuously.

## 2.2 Experimental methods

### 2.2.1 Miniature CSTR cascade design

A single CSTR unit consists of three main components, including polytetrafluoroethylene (PTFE) reactor block, heat-resistance glass cover and stainless steel cover. (Figure 2.1) The PTFE reactor is a 30 mm × 30 mm square block with a thickness of 19 mm. The cylinder-shape inner chamber has a diameter of 18 mm and a depth of 10 mm. An O-ring gap surrounds the chamber for the 1/16" FEP O-ring with silicone core. The glass cover is heat-resistant borosilicate glass (Pyrex) with the dimensions of 30 mm × 30 mm × 4.8 mm. The stainless steel cover is super-corrosion-resistant 316 stainless steel with the dimensions of 30 mm × 30 mm × 3.2 mm. All extruded 2D shapes were fabricated using water jet machining (OMAX MicroMAX JetMachining Center). In addition to 2D shapes, the reactor chamber and the O-ring gap were machined using CNC milling (ProtoTRAK SMX). Multiple CSTR units are mounted on an aluminum holder. (Figure 2.1b) The aluminum holder (150 mm × 70 mm × 3.2 mm) can hold up to 8 CSTRs. All the connection ports have 1/4-28 threads, which can be directly connected using common IDEX fittings (IDEX Health & Science LLC.) without additional adapters. Two CSTRs are connected using a tube with 1/4-28 thread outside.

In the constructed miniature CSTR cascade system, each of the polytetrafluoroethylene (PTFE) reactor chambers has an inner diameter of 18 mm and holds a cross-shape magnetic stir bar (Φ9.5 mm × H4.7 mm). For simplicity, a single magnetic stirrer plate provides the driving force for all stir bars. Based on the magnetic coupling force available from the stirrer plate,

spinning the stir bar at maximum speed of 600 rotations per minute (RPM) increases the local flow speed to keep particles suspended against gravity, particle-wall interaction, and particle-particle interaction. At the same time, the agitation enhances the mixing and heat transfer in each CSTR chamber. PTFE has good chemical compatibility suitable for common organic reactions, and the non-stick nature of PTFE contributes to reducing the particle-wall interactions to avoid build-up of particles on the reactor walls. The chamber is covered by heat-resistant borosilicate glass (Pyrex), allowing viewing particle flow in the chamber. In order to minimize the chance of clogging the 3.2 mm diameter flow channel between two adjacent CSTR chambers, the units are placed in close contact to avoid interconnections becoming the threshold of the cascade. The system is simple to assemble for reactor cleaning and rearrangement.

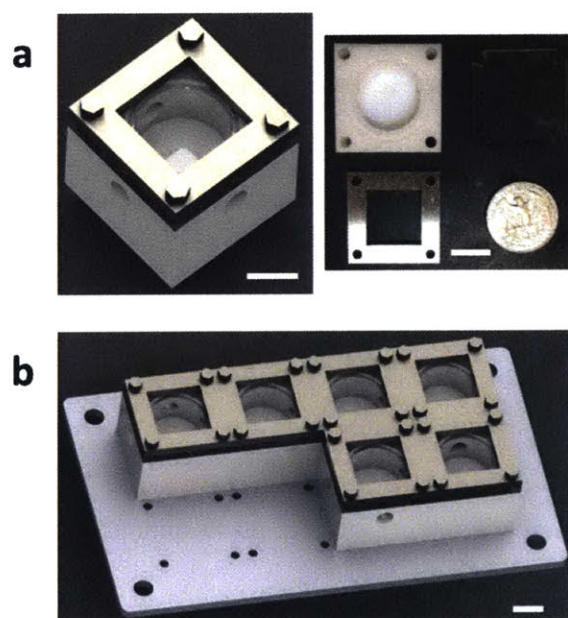


**Figure 2.1. Sketch of the miniature CSTR cascade design. (a) The single-stage CSTR shown in CAD drawing, and three main components of the actual product. (b) Multiple CSTRs in series on an aluminum holder. (The white scale bars in the pictures above are 10 mm)**

The residence time distribution (RTD) profile for the single-stage CSTR is an exponential decay<sup>110</sup>, which is usually undesired when side reactions exist in the system. A narrow RTD profile

is favored for increasing yield and selectivity. Connecting CSTRs in series (Figure 2.1) narrows the RTD and approaches plug flow reactor (PFR) behavior for a large number of CSTRs.<sup>110</sup> Thus, the RTD profile can be tuned from CSTR to PFR characteristics by choosing the number of CSTRs

### 2.2.2 Residence time distribution (RTD) characterization

The residence time distribution (RTD) measurement was carried out using the pulse injection method. The carrier phase was water and the tracer was methylene blue, which is UV-Vis sensitive. A 6-way valve (IDEX Health & Science LLC., MXP7900-000) was used to inject the tracer into the reactor. The UV-Vis light source (Ocean Optics, Inc., DH-2000-BAL) and spectrometer (Ocean Optics, Inc., HR2000+) were used to measure the concentration profiles at the inlet and outlet of the reactor. LabVIEW was used to control the system to realize automatic tracer injection and UV-Vis signal recording.

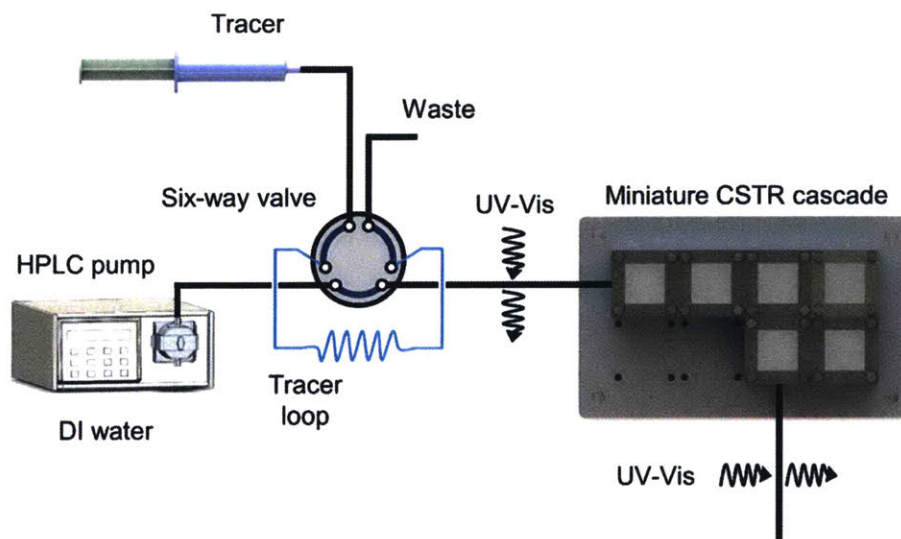


**Figure 2.2. Scheme of the residence time distribution measurement using in-line UV-Vis to record concentration profiles for inlet and outlet.**

The amount of tracer used was determined by the number CSTR chambers that were tested. A certain level of tracer concentration is required to get strong enough UV-Vis signal response. In

this RTD measurement, the amount of the tracer was proportional to the number of CSTRs in series.

Measurement was stopped while there was negligible amount of tracer in the outlet stream. The concentration profiles of the inlet stream and outlet stream were normalized by the total amount of the tracer in each stream, which was obtained by integration over the whole measurement time.

### 2.2.3 Procedure for heat transfer efficiency validation of the CSTR cascade

Isoprene and maleic acid anhydride were prepared in the DMF solvent. The concentration of isoprene solution is 1 mol/L and the concentration of maleic acid anhydride solution is 1.5 mol/L. The solutions were all used immediately after preparing in order to avoid degradation of the reagents due to the air or light.

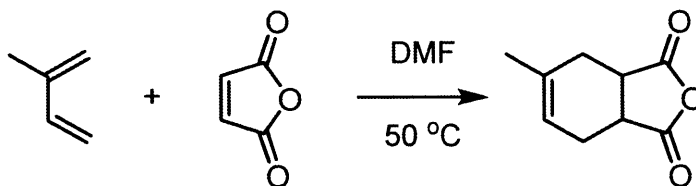


**Figure 2.3. The Diels-Alder reaction of isoprene and maleic acid anhydride.**

The scheme of the setup for evaluating the heat transfer efficiency is shown in Figure 2.4. Two HPLC pumps (AZURA P 4.1S) were used to deliver two solutions into the reactor. The flow rates for both streams were equal to 200  $\mu\text{L}/\text{min}$ . 1-, 3-, 5-, 7- unit CSTR cascades were tested using the same flow rate. The reactor was placed on a magnetic stirrer (VWR, VMS-C7 Advanced magnetic hotplate stirrer), which is integrated with the heating system. The magnetic stirrer operated at the 600 revolutions per min (rpm). In order to prevent the heat loss due to the free convection of air, mineral wool was used to insulate the reactor. The temperature was set at 50 °C.

The CSTR cascade was preheated to the setting temperature before pumping two reagents into the reactor. As the reaction continuously proceeded in the reactor, the samples were collected after five reactor volumes, which was considered to be at steady state. Three samples were taken at fifth, sixth, and seventh reactor volumes. As soon as the samples were collected, the mixture was diluted using ethyl acetate (1:20) and cooled down to 0 °C in the ice bath in order to quench the reaction. The gas chromatography (Agilent 6890 Gas Chromatograph) was used to obtain the conversion of the samples.

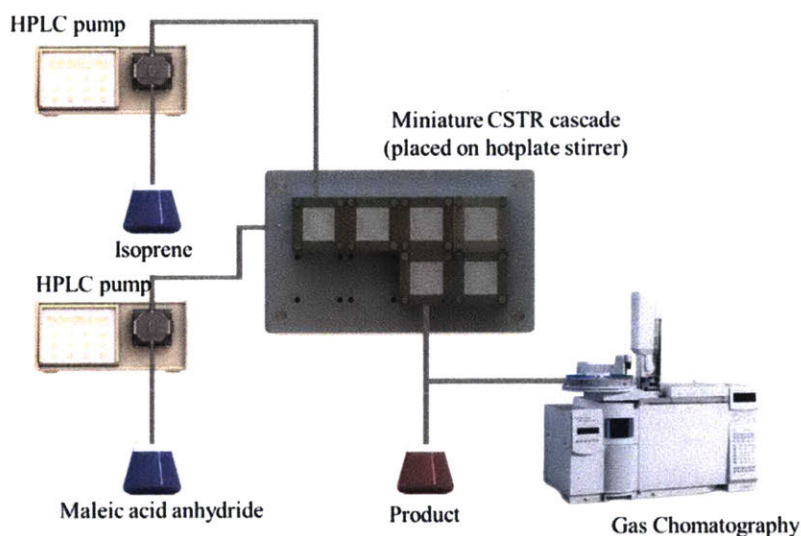


**Figure 2.4. The scheme of the heat transfer efficiency validation using Diels-Alder reaction.**

#### 2.2.4 Procedure for continuous handling of reactions containing solids

The scheme of the setup is similar to Figure 2.4. The reagents for the reactions were separated into two streams and they were pumped into the CSTR cascade by HPLC pump. There was an in-line pressure sensor connected at the inlet of the reactor in order to measure the pressure profile in the system. The CSTR cascade was placed on the magnetic stirrer for providing driven force to spin the magnetic stir bars in the CSTR chambers. The rotation speed of stir bar in each

chamber was set to be the same, which was 600 RPM. 600 RPM was the upper limit of rotation speed that can keep the magnetic stir bars spinning on a single magnetic stirrer for a long period. Beyond this rotation speed limit, the magnetic stirrer (Corning® 11 x 11 Inch Top PC-611 Stirrer) could not provide enough magnetic coupling force to spin the stir bars (VWR® Spinplus® Magnetic Stir Bars, 58947-820), which would lead to shaking of stir bars instead of rotation. Operation under the maximum RPM of the system improved mixing, and at the same time, provided high local flow speed to keep particles suspended against gravity, particle-wall interaction, and particle-particle interaction.

Since the two reaction examples that were used in this section could proceed under the ambient temperature, heating was not required in this setup. The magnetic stirrer was placed vertically in order to operate the CSTR cascade in the vertical mode, which helped to minimize clogging at the outlet tube of the reactor. Products were collected at the outlet of the reactor using a flask.

The optical characterization of the solid particles formed in the CSTR cascade were carried out by using the optical microscope (ZEISS Axiovert 200). 100  $\mu$ L of well-mixed slurry was loaded onto the glass slide, and another glass slide was used to cover the sample in order to prevent evaporation of the solvent. In this case, the crystals would remain unchanged under the microscope.

The particle size distribution was measured by the Malvern particle sizer (Malvern Mastersizer 2000). Original solvent was used to make sure that the particle size and morphology did not change when injecting the samples into the particle sizer. With the solid concentration coming out of the reactor, 0.5 mL sample was enough to fulfill the low limit of detectable particle concentration that was needed for the machine to measure the size distribution. Only the product from the first reaction example, imine formation reaction, was measured. The crystals generated

in the second reaction were needle-shape, and the results given by the Malvern particle sizer would not represent the meaningful sizes of the crystals because the Malvern particle sizer assumes that the shape of particles is close to sphere.

Continuous processing of the imine formation reaction (Figure 2.5): Glyoxal and cyclohexylamine were dissolved into the ethanol. The concentration of the glyoxal solution was 0.4 mol/L and the concentration of the cyclohexylamine solution was 0.8 mol/L. Full conversion can be achieved in 15 min. The conversion was measured using gas chromatography.

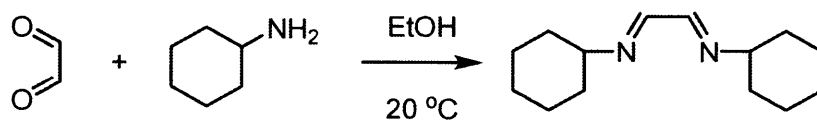


**Figure 2.5. Imine formation reaction of glyoxal and cyclohexylamine**

Continuous processing of the sulfonylation of alcohol reaction (Figure 2.6): All reagents were separated into two streams. One stream contained 2-octanol, triethylamine and DMAP, and they were prepared in the DCM solvent. The concentrations of 2-octanol, triethylamine and DMAP were 0.6 mol/L, 0.72 mol/L, 0.08 mol/L. Methanesulfonyl chloride was prepared in the other stream, and the concentration was 0.5 mol/L. The conversion was measured using gas chromatography.

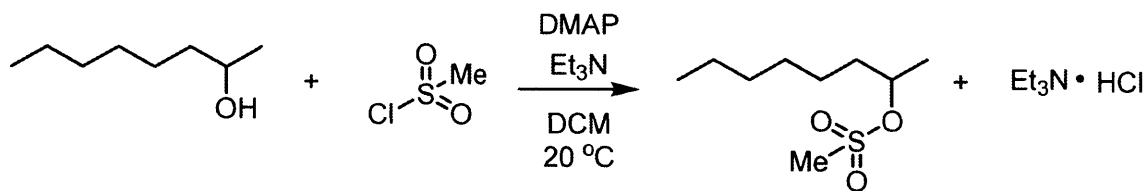


**Figure 2.6 Sulfonylation of 2-octanol with methanesulfonyl chloride.**



## 2.3 Results and discussion

### 2.3.1 Assessment of mixing properties

Dead volume and bypass are two key factors that introduce non-ideality in CSTRs making it difficult to predict the performance of a given reaction. RTD measurements for different numbers of CSTRs in series yielded the expected trend of RTD profiles with increasing the reactor number. (Figure 2.7) RTD profiles of for a single CSTR and 3, 5, and 7 CSTRs in series were determined for constant mean residence time (reactor volume divided by the flow rate).

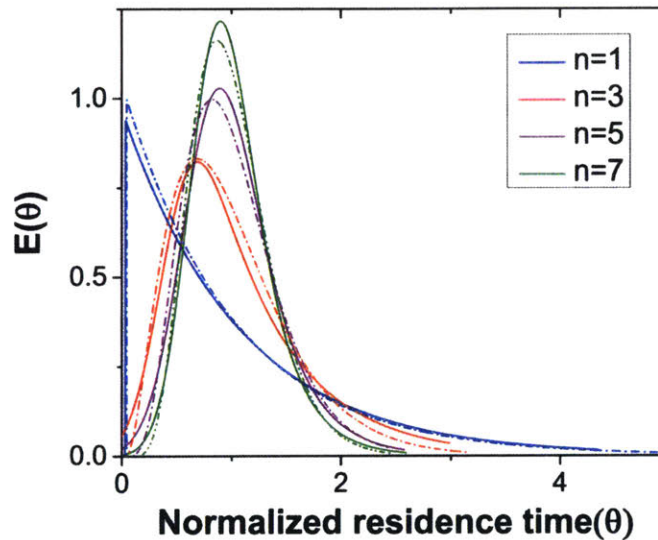


**Figure 2.7. RTD profiles for  $n=1, 3, 5, 7$  CSTRs in series. Solid lines are regressed experimental RTD profiles based on the EMG model and dashed lines are ideal CSTRs in series model.**

Since the pulse injection was not a perfect pulse, the outlet concentration profile was a convolution of the inlet concentration profile and RTD. Discrete Fourier transform methods would be preferred for deconvolution of the signals due to its simplicity, but noise in the data and the large number of data points introduced numerical errors. Therefore, the RTD was extracted from the inlet and outlet concentration profiles by model regression with the exponentially modified

Gaussian (EMG) distribution model. (Equation 2.1) This model combines exponential decay and Gaussian distribution, which is generally suitable for RTD profiles that contain only one peak.<sup>111</sup>

$$E(t) = \frac{\lambda}{2} \exp\left(\frac{\lambda}{2}(2\mu + \lambda\delta^2 - 2t)\right) \operatorname{erfc}\left(\frac{\mu + \lambda\delta^2 - t}{\sqrt{2}\sigma}\right) \quad \text{Equation 2.1}$$

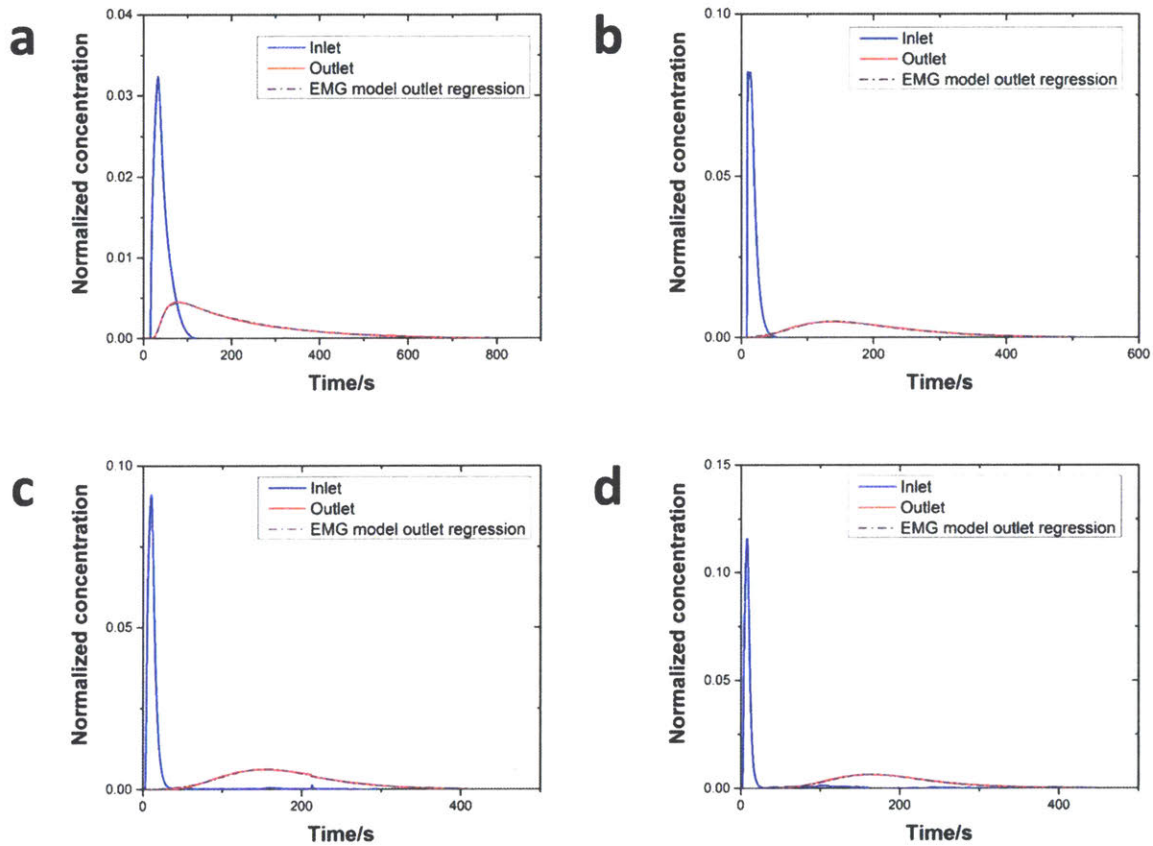


**Figure 2.8.** The inlet and outlet concentration profiles, and the outlet concentration profiles given by the EMG model regression. The CSTR cascade with different numbers of reactors are tested: (a) n=1; (b) n=3; (c) n=5; (d) n=7.

The outlet concentration profiles given by the convolution of inlet concentration and regressed EMG model show excellent agreement with the experimentally measured outlet concentration profiles (Figure 2.8) showing that the EMG model is efficient in extracting the RTD profiles of the CSTR cascade. The tail of outlet concentration profile becomes shorter when the

number of CSTRs increases as expected since the cascade will approach plug flow reactor (PFR) behavior as the number of units become large.<sup>110</sup>

The mixing performance of the CSTRs was assessed by comparing the regressed EMG model to the RTD of the ideal CSTRs in series model (Equation 2.2).<sup>110</sup>

$$E(t) = \frac{\lambda}{2} \exp\left(\frac{\lambda}{2}(2\mu + \lambda\delta^2 - 2t)\right) \operatorname{erfc}\left(\frac{\mu + \lambda\delta^2 - t}{\sqrt{2}\sigma}\right) \quad \text{Equation 2.2}$$

For the same number of CSTRs in series, the ideal and measured RTD profiles show high consistency (Figure 2.7), which suggests that the agitation provided by the magnetic stir bar in each chamber is sufficient to achieve rapid mixing and reproduce the CSTR characteristics. In addition, the dead volume in the reactor is nearly negligible. The RTD profile becomes sharper with increasing number of CSTRs as expected. The nearly ideal CSTR cascade performance is essential for predicting the performance of an existing reaction system and rationally designing new processes.

### 2.3.2 Predicting reaction conversions in the CSTR cascade

Considering the nearly ideal CSTR mixing characteristics in each chamber of the miniature CSTR cascade, the system was further characterized by predicting reaction conversions based on reaction kinetics and RTD information. The Diels-Alder reaction between maleic acid anhydride and isoprene (Figure 2.3) served as a model based on reported kinetic data.<sup>112-114</sup>

The reaction temperature was set to 50 °C to have a moderate rate of reaction and significant differences in conversions for different residence times. 1-, 3-, 5-, and 7- unit CSTR cascades were tested at a constant flow rate of 400 µl/min. Reaction conversions were computed based on reputed kinetic data ( $k = A \times \exp(-E_a/RT)$ ),  $A = (4.02 \pm 2.5) \times 10^6 \text{ L} \cdot \text{mol}^{-1} \cdot \text{s}^{-1}$ ,  $E_a = 58.5 \pm$

$2.0 \text{ kJ} \cdot \text{mol}^{-1}$ )<sup>113</sup> along with ideal CSTR cascade model. The experimental values fall at the lower side of the envelope of predicted conversions based on the reported uncertainty in rate constants. The close agreement between predicted and measured conversions is consistent with the RTD results in Figure 2.7. The lower than predicted conversions is attributed to the reaction temperature measured at the reactor outer wall, which would be slightly higher than the temperature of reactants inside the reactor given the external heating. Constructing the CSTR in stainless steel would reduce temperature gradients. PTFE is chosen for its chemical compatibility and higher barrier for nucleation of solids on the walls.

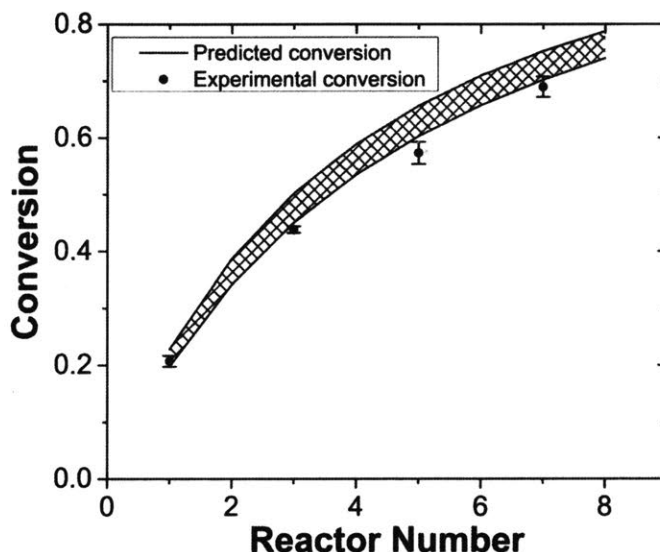


**Figure 2.9. Comparison of measured and predicted reaction conversions for different numbers of CSTRs. Cross-hatched area: predicted conversions. Predicted conversions based on ideal CSTR cascade model.**

### 2.3.3 Continuous handling of reactions forming solids

Two reactions were selected to assess the ability of CSTR cascade to handle the formation of solids (1) glyoxal reacting with cyclohexylamine to form N,N'-dicyclohexylethylenediimine that is insoluble in the reaction solvent, ethanol (Figure 2.5),<sup>91</sup> and (2) sulfonylation of 2-octanol

(Figure 2.6),<sup>115</sup> for which the side product, triethylamine hydrochloride, has limited solubility in the solvent, dichloromethane (DCM).<sup>115</sup>

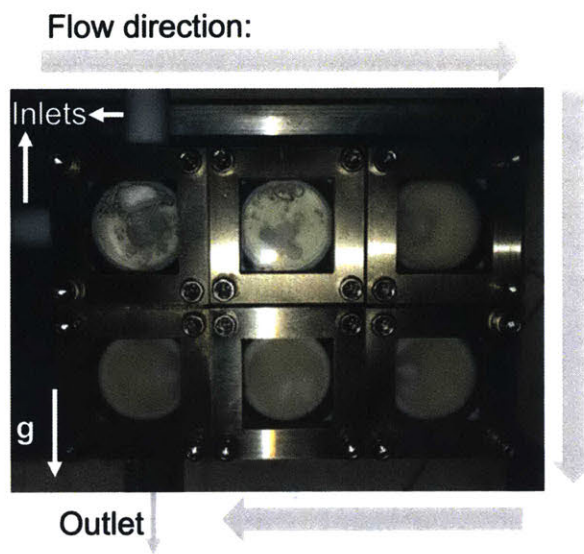


**Figure 2.10. Photograph of the CSTR cascade during the operation showing the solid fraction increasing along the flow direction. (The white arrow marked g shows the direction of gravity)**

The first reaction (Figure 2.5) tested the ability of the CSTR cascade to handle formation of a solid product at relatively high solid loadings, 4.4% (wt.), corresponding to stoichiometric amounts of the reagents and a glyoxal concentration of 0.4 M. The reaction reached nearly 100 % conversion in 15 min with a 6-unit CSTR cascade. Adding more CSTRs after the 6-unit cascade would not lead to the growth of particles since reaction was complete and, instead, help rebalance the particle size distribution. A total flow rate of 1 ml/min, rapid stirring (~600 RPMs), and short connections between adjacent chambers allowed transport of solid particles inside the CSTR cascade without clogging (Figure 2.10). However, gravity caused particles to accumulate in the outlet tube. To avoid this problem and enable facile flow of particles through the entire system, the CSTR cascade was positioned vertically to align the gravity force and the outlet flow direction.

As the reaction proceeded, the particle concentration in each chamber increased along the flow direction (Figure 2.10).

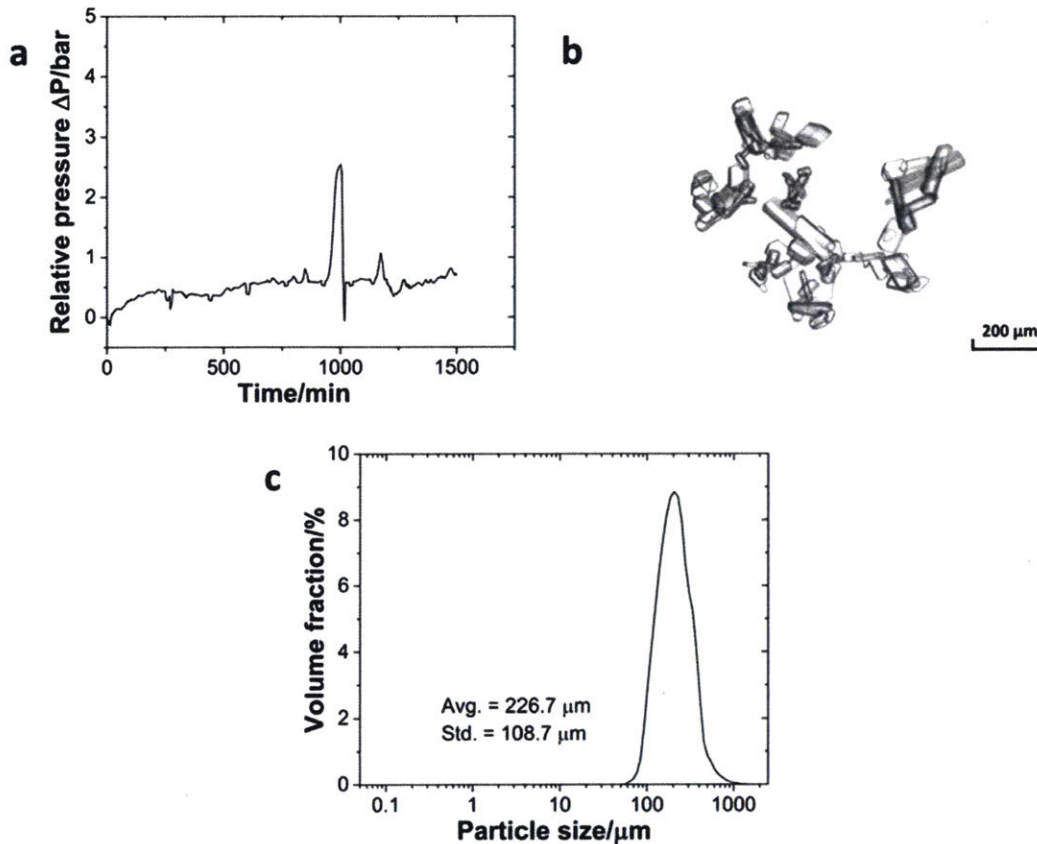


**Figure 2.11. (a) Pressure profile during the continuous operation of the imine formation reaction. (b) Microscope image of the imine crystal. (c) The particle size distribution of the product.**

Pressure measurements at the reactor inlet was a sensitive indicator of potential clogging problems. If particles built up at in the reactor and clogged the flow path, the relative pressure would rise dramatically without going back. The system automatically would stop the pump to avoid damages to pump or reactor when the pressure exceeded 10 bar. The pressure profile (Figure 2.11a) demonstrates that the system could run continuously for 24 h without significant signs of clogging. Besides small pressure fluctuations in the reactor, a pressure spike occurred around 1000 min reflecting minor particle accumulations at the outlet and the solid clusters being pushed

through by the elevated pressure. Once the particle clusters had left the system, the pressure returned to the base line. The solid product was an organic crystal, which had a slice-shaped morphology (Figure 2.11b) and an average size of 226.7  $\mu\text{m}$  with a standard deviation of 108.7  $\mu\text{m}$ . (Figure 2.11c). Although particles with sizes over 500  $\mu\text{m}$  existed in the outlet stream, due to the fact that interconnections had a diameter of 3.2 mm and only a limited amount of particles had relatively large sizes, those particles would flow through the interconnections without problems.

In the previous case, the solid particles were the main product of the reaction. In the next example sulfonylation of 2-octanol (Figure 2.6), the side product, triethylamine hydrochloride, has limited solubility in the solvent, dichloromethane (DCM).<sup>115</sup> Moreover, the crystals are needle-shaped (Figure 2.12a) and thus agglomerate easily. When feasible, needle-shaped crystals are avoided in the pharmaceutical industry due to poor flow properties. A 3-unit CSTR cascade sufficed to obtain full conversion at a flow rate of 1.00 ml/min of 0.6 M 2-octanol and 0.72 M methanesulfonyl chloride. Even with a solid loading of 4.1% (wt.), the CSTR cascade ran continuously for 8 h without clogging, as reflected by the pressure profile (Figure 2.12b).

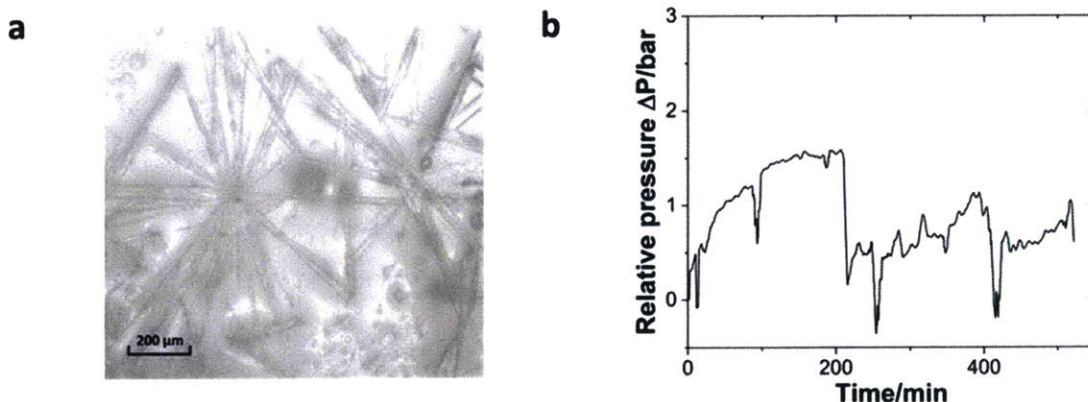


**Figure 2.12. (a) The microscope image of the triethylamine hydrochloride salt. (b) Relative pressure profile during the continuous operation of the sulfonylation reaction.**

## 2.4 Conclusion

The case studies demonstrate the ability of the CSTR cascade to process continuously reactions containing solids. The reactor assembly, consisting of PTFE reactor chambers, glass and stainless steel covers, has excellent chemical resistance for most chemical reactions and is easy to clean after usage. The chambers mount is easy to vary the number of units in the reaction cascade. The homogeneous concentration and temperature profiles realized by the high agitation in each chamber result in nearly ideal CSTR in series RTD profile and accurate predictability of reaction conversions. Moreover, the high rate of stirring keeps the particles suspended in each reactor chamber, preventing them from sticking to the reactor wall or agglomerating. The short distance between adjacent reactor chambers minimizes the possibility of clogging at connections. Running the CSTR cascade in a vertical mode so that gravity aids particle transport out of the reactor eliminates clogging of outlet tube. These rational design aspects contribute to the capability of long-time continuous handling of solids in the reactor. For different types of solid forming reactions, such as rapid solid formation with fast growth kinetics, a careful investigation on suitable reaction conditions (e.g. reagent concentrations, reaction temperature, flow rates and etc.) need to be performed in order to proceed those reaction in the CSTR cascade.

The capability to handle solids also enables its application for continuous crystallization, where tuning different operation parameters (e.g. rotation speed of stir bar and flow rates) can control the morphology of crystals in the CSTR cascade. The scope of the miniature CSTR cascade could be expanded by giving each unit a set of functions, such as independent temperature control and multi-injection points. Such modular units would enable telescoped multistep reactions in a single miniature CSTR cascade. Furthermore, the high agitation in each chamber would also be beneficial in creating large contacting areas and resulting mass transfer for liquid-liquid reactions.



# Chapter 3 CSTR for enhancing liquid-liquid mixing

## 3.1 Introduction

Many reaction systems involves multiple liquid phases. For example, phase-transfer alkylation<sup>116-118</sup> and biphasic Suzuki-Miyaura cross-coupling<sup>119-121</sup>, as the widely used C-C bond-forming reactions in the pharmaceutical industry, both employ two immiscible solvents, benefiting from inexpensive and environmentally benign water-soluble inorganic bases. However, the presence of two immiscible phases introduces the barrier of material exchange at the interface, leading to reduced apparent reaction kinetics, which creates challenges to optimize reactor design and operation parameters to meet desired productivity in continuous flow chemistry.

One common strategy to enhance biphasic mixing performance is implementing static mixing components inside the fluidic channels. (Since no external agitation is present, it is called “passive mixing” in the following context.) The Corning Advanced-Flow Reactor (AFR)<sup>122</sup>, Lonza FlowPlate from Ehrfeld Mikrotechnik BST<sup>123</sup>, and Chemtrix KILOFLOW glass reactor, representing the state of the art of commercial continuous flow reactors, all employ this strategy to improve the performance. Nonetheless, the passive mixing effect, relying on pressure drop introduced by the internal structures to enhance mixing, has a dependence on the flowrate. Low flowrate will lead to decreased heat and mass transfer rates, implying more reactor volume required for a specific residence time to keep a certain mixing performance<sup>124,125</sup>. Besides, the pressure drop induced by increased flowrates raises the requirement for the reactor sealing and reactant-

delivering pump. Together with more reactor volume required, all these factors contribute to elevated investment to continuous manufacturing equipment.

An alternative strategy is active mixing by introducing external agitation inside the fluidic channel. Several agitated milli-reactors have been developed specifically for handling solids.<sup>101,105,126,127</sup> Ley et al. used the Coflore ACR agitated cell reactor to demonstrate the continuous formation of the hydroiodide salt of N-iodomorpholine through the reaction of morpholine with iodine<sup>101</sup>. A modular miniature CSTR cascade was also designed and demonstrated to handle solids continuously for a long time without significant sign of clogging.<sup>127</sup> Vortex fluidics device also appears as a promising mixing enhancement tool enabled by high shear rate under rotation.<sup>128,129</sup> However, an agitated miniature reactor with comparable performance to passive mixing flow reactors has not been developed and demonstrated for liquid-liquid reaction systems due to the challenges of creating intense agitation in a small confined space without losing sealing and ability to tolerate aggressive chemicals. Thus, a universal active-mixing reactor design with flowrate-independent and tunable mass transfer performance would have advantages in realizing important biphasic reactions

In this chapter, a new CSTR unit will be described to decouple the mixing performance and flowrate to accommodate various reaction kinetics from seconds to hours using non-contact magnetic coupling. The whole unit is built with materials designed for chemical compatibility. Residence time distribution (RTD) measurements of the CSTR unit show nearly ideal CSTR single-phase mixing performance. Mass transfer coefficients are estimated based on high-speed images of the biphasic hydrodynamics. Two important C-C bond-forming reactions are demonstrated in the CSTR unit, (1) asymmetric alkylation catalyzed by cinchonidine-derived phase transfer catalyst, and (2) biphasic Suzuki-Miyaura C-C coupling reactions. Moreover, a

kinetic model was developed for phase-transfer catalyzed reaction with Makosza interfacial mechanism to provide insights into how mass transfer performance affects the outcome of the reaction.

## **3.2 Experimental methods**

### **3.2.1 Reactor design**

An aluminum jacket encloses the polytetrafluoroethylene (PTFE) reactor chamber to provide uniform cooling and heating (Figure 3.1). The baffles in the reactor chamber interrupt the centrifugal separation of a rotating liquid-liquid system with non-identical densities, and increase the shear rates to break the dispersed droplets. Four high-pull rare earth magnets (follower) coupled with driving magnets on the motor (Figure A.6) outside provide magnetic-coupling force to rotate the impeller. A full ceramic bearing (VXB Balling Bearing Company) with grease-free and chemically resistant features is implemented to keep the rotation components (i.e. impeller, magnet holder, magnets) concentric on the shaft minimizing friction during the rotation, such that this design can achieve a rotation speed up to 3000 revolutions per minute (RPM), even for viscous fluids. A polyethylene film (thickness: 0.01", McMaster-Carr) covers the high-pull rare earth magnets inside the polyethylene magnet holder using thermal infusing method to prevent magnets from corrosion. The impeller design, modified from the Rushton impeller design, has a large Power number ( $N_p$ ), which greatly enhances multiphase mixing. The reactor is sealed with Kalrez O-ring and heat-resistant borosilicate glass (Pyrex). The inlet and outlet have standard 1/4-28 threads, which can be easily connected with IDEX-HS fittings. The Pyrex glass cover and aluminum top cover were fabricated using water jet machining (OMAX MicroMAX Jet Machining Center). All

the other components were machined using Proto Labs' CNC service. The detailed dimensions of the CSTR unit are described in Supporting Information. (Figure A.1 – Figure A.5)

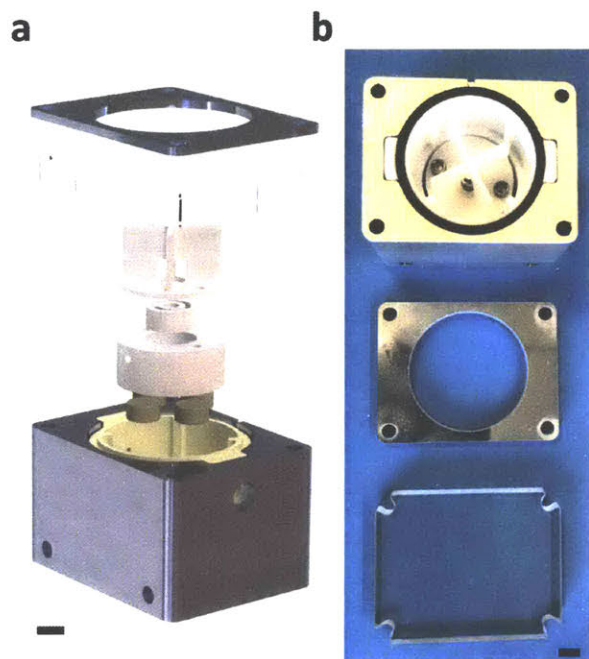


**Figure 3.1. (a) Exploded-view CAD drawing of a CSTR unit. From top to bottom, it sequentially consists of aluminum cover, borosilicate glass cover, PTFE impeller, ZrO<sub>2</sub> ceramic bearing, polyethylene magnets holder, high-pull magnets, PTFE inner wall, and aluminum jacket. (b) Three main components of the actual CSTR unit. (The black scale bar in each picture represents 5 mm.)**

The whole unit has the capability to withstand harsh chemical environment, and the magnetic coupling design avoids requirement for the seal of motor shaft, which is typically challenging for small-scale reactors. The reactor design relies on cost-effective CNC machining, which significantly reduces the cost of fabricating such a CSTR unit. Similar design strategy utilizing magnetic coupling is also applicable for CSTRs with larger scales without significantly compromising the performance, since the larger shear resistance imposed on the impeller can be compensated by easier implementation of stronger and larger magnets in the larger reactor space.

### 3.2.2 Residence time distribution (RTD) characterization

The previously described pulse injection method (Section 2.2.2) was used to measure RTD for the CSTR (setup scheme in Figure A.7). The carrier phase was deionized (DI) water, and the tracer was methylene blue. In-line UV-Vis spectroscopy (light source: Ocean Optics, Inc., DH-2000-BAL; spectrometer: Ocean Optics, Inc., HR2000+) was used to determine the concentration profiles of the tracer at the inlet and outlet. A six-way valve (IDEX Health & Science, MXP7900-000) combined with LabVIEW control enabled automatic pulse injection and data collection. RTDs under various flowrates and impeller rotation speeds were measured for the CSTR unit.

### 3.2.3 High-speed imaging characterization of biphasic hydrodynamics

The Pyrex glass cover allowed observations of biphasic hydrodynamics inside the reactor. A high speed camera (Photron FASTCAM Mini AX200) with 6400 frames per second (FPS) and 1/8000 s exposure time captured the movement of dispersed droplets under high rotation speed. A classical two-phase system<sup>124</sup>, hexane (with Sudan red as the dye) dispersed in water, was examined in the CSTR unit. Impeller rotated in the CSTR unit, pre-filled with a predetermined percentage of hexane and water, for 10 s to reach stable hydrodynamics before high-speed image recording for 0.5 s. The images were processed using Matlab to increase contrast and visibility of the dispersed droplets, and the droplet size distributions were collected by manual measurement of the droplet dimensions.

### 3.2.4 Procedure for asymmetric phase-transfer reaction

N-(diphenylmethylene)glycine tert-butyl ester, benzyl bromide, N-(9-anthracenylmethyl)cinchonidinium chloride, toluene, dichloromethane (DCM), and potassium hydroxide were purchased from Sigma Aldrich and used without further purification. Purification

of the reaction mixture by flash column chromatography on SiO<sub>2</sub> (hexane – ethyl acetate = 20:1) afforded the desired product as a colorless oil. The enantiomeric excess (ee) was determined by chiral HPLC analysis (DAICEL Chiralcel OD, hexane – i-PrOH (98:2), flow rate = 0.4 mL/min).

The reaction was carried out at 0 °C in the CSTR unit. In order to realize accurate temperature control, thermoelectric cooling is used instead of conventional coolant, which was enabled by incorporating thermoelectric modules and CPU liquid cooling modules. (Figure 3.2). Two CPU liquid cooling modules attached to the hot side of the thermoelectric units served as heat sinks. A thermocouple was directly placed inside the chamber to measure the temperature of the fluid. Good mixing (see below) ensured uniform temperature distribution in the fluid, allowing control of the temperature with a thermocouple and a PID control loop built in LabVIEW.

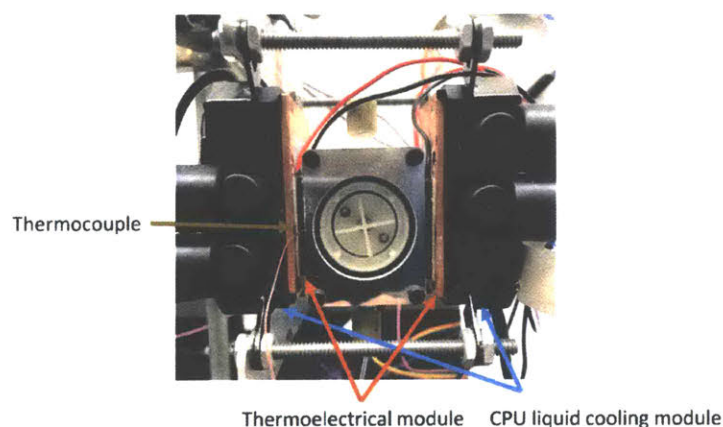


**Figure 3.2. Modularized cooling strategy for the CSTR unit.**

For the asymmetric phase transfer reaction in flow, the organic phase stream (toluene : DCM = 3:1) contained 0.025 M N-(diphenylmethylene) glycine tert-butyl ester, 0.035 M benzyl bromide, and 5 mol% catalyst and the aqueous stream had 50% (wt.) KOH. Two HPLC pumps delivered the streams with the same flowrates. Wait 3 reactor volumes for steady state before collecting samples. An Agilent ZORBAX Eclipse XDB 80Å C18 1.8 μm column was used to detect the yield of the reaction with acetonitrile and water as the mobile phase.

### 3.2.5 General procedure for biphasic Suzuki-Mayaura C-C coupling reaction

2-Bromoquinoline, 4-bromoanisole, 2-chloroquinoline, 5-chloro-1,3-benzodioxol, phenylboronic acid, 2-chloro-5-(trifluoromethyl)-pyridine, N-Boc-2-pyrroleboronic acid, and XPhos Pd G3 precatalyst were purchased from Sigma Aldrich and used without further purification. Gas chromatograph (GC) was used to determine the yield of the reaction with dodecane as the internal standard.

The reaction was carried out at 65 °C, enabled by two cartridge heaters inserted in the aluminum jacket with a PID temperature controller to keep the desired reaction temperature. All the reagents were prepared under argon atmosphere and the CSTR unit was purged with argon to eliminate oxygen. Two HPLC pumps delivered the reagent streams into the CSTR unit. Wait 3 reactor volumes for the steady state before sample collection. An aliquot of the organic phase was filtered through a short plug of silica gel, and washed with DI water before GC analysis.

## 3.3 Results and discussion

### 3.3.1 Assessment of single-phase mixing performance

Dead volume and bypass are two key factors that introduce non-ideality in CSTR performance making it difficult to predict the outcome of a given reaction. Therefore, the RTD for single-phase mixing is measured and compared to the one predicted for an ideal CSTR.

Since the pulse injection was not a perfect tracer spike, the outlet concentration profile was a convolution of the inlet concentration profile and RTD. Two inline UV-Vis spectrometer, positioned at the inlet and outlet of reactor, recorded the relative concentration of the tracer. The concentration was normalized based on the total amount of tracer injected. Discrete Fourier transform methods are often preferred for deconvolution of the signals, but noise in the data and

the large number of data points introduced numerical errors. Therefore, the RTD is extracted from the inlet and outlet concentration profiles by model regression with the exponentially modified Gaussian (EMG) distribution model, shown in Equation 2.2. ( $\lambda, \mu, \sigma$  are model parameters) This model combining exponential decay with a Gaussian distribution is generally suitable for RTD profiles that contain only one peak<sup>11</sup>.

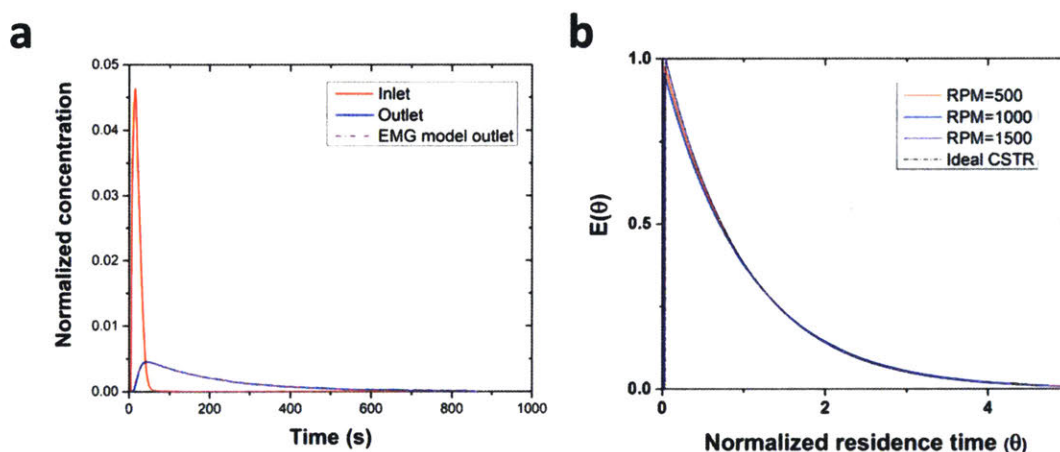


**Figure 3.3. (a) The inlet and outlet concentration profiles, and the outlet concentration profile given by the EMG model regression. (b) Normalized residence time distribution of the CSTR unit for various impeller rotation speed at the flowrate of 2 ml/min. The ideal CSTR line represents the theoretical RTD.**

The outlet concentration profiles given by the convolution of inlet concentration and regressed EMG model show excellent agreement with the experimentally measured outlet concentration profiles (Figure 3.3a) demonstrating that the EMG model is efficient in extracting the RTD profiles of the CSTR. The RTD profiles under various impeller rotation speeds using a 2 ml/min flowrate (Figure 3.3b) are nearly identical, and all of them show good agreement with ideal CSTR RTD<sup>10</sup>. The results demonstrate that even under low agitation speeds (500 RPM), the rotation of the impeller provides rapid mixing for single phase. Further increasing the flowrate to 6 ml/min did not compromise the single-phase mixing (Figure 3.4).



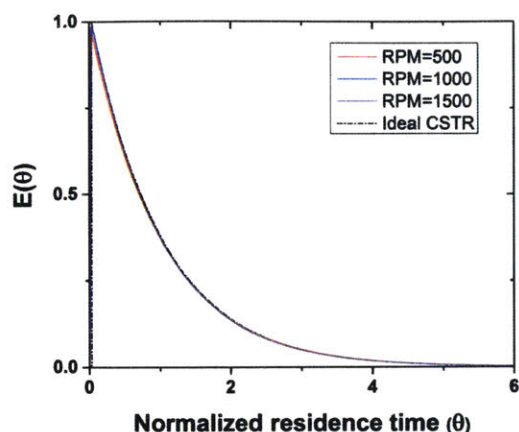


**Figure 3.4. Normalized residence time distribution of the CSTR unit for various impeller rotation speed at the flowrate of 6 ml/min. The ideal CSTR line represents the theoretical RTD**

### 3.3.2 Characterization of biphasic hydrodynamics

The unique design of the miniature CSTR with the transparent top plate made it feasible to capture the biphasic hydrodynamics. Unlike traditional CSTR, the headspace gas is absent allowing observation of the liquid-liquid system to record flow fields needed to estimate mass transfer coefficients. With 6400 frames per second (FPS) and 1/8000 s exposure time, the high-speed camera was able to record the behavior of the dispersed hexane droplets in water under various rotation speeds and hexane/water volume ratios. (Figure 3.5) Large droplets experience high shear rate at the edges of impeller and baffles, and break down into smaller droplets. Due to density difference between hexane and water, hexane droplets experience centrifugal force pointing to the center of the reactor, and they bounce back and recirculate to the reactor sidewall after colliding the impeller. Collision of droplets transfers momentum among droplets increasing the slip velocity (the velocity of droplets traveling through the continuous phase).

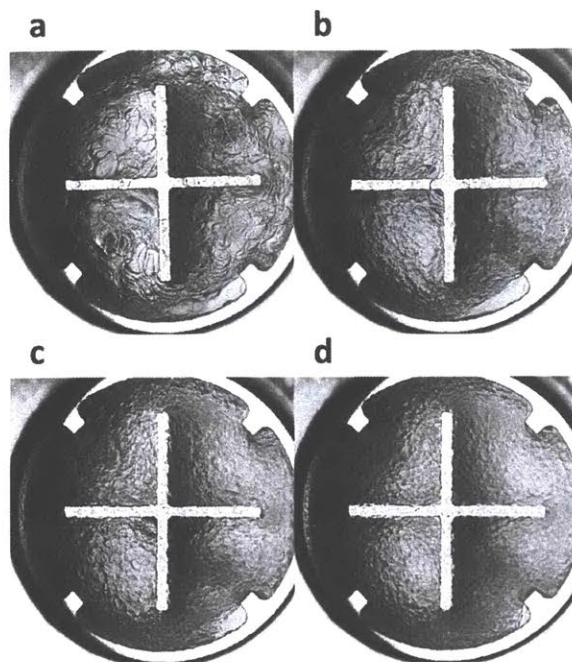


**Figure 3.5. The hydrodynamics of hexane and water (1:1 ratio) in the CSTR unit at various rotation speeds: (a) 500 RPM, (b) 800 RPM, (c) 1000 RPM, and (d) 1300 RPM.**

Counting the hexane droplet sizes under different conditions reveals that droplet size has a negative dependence on rotation speed of the impeller (Figure 3.6 and droplet size distributions available in Figure A.8 – Figure A.10) since increasing the rotation speed creates a higher shear rate leading to smaller droplets. At the same rotation speed, the hexane/water ratio of 1:1 has the smallest droplet size compared to the other two ratios. The dispersed droplets have a smaller chance to interact with edges of baffles and impeller to split into smaller droplets when the ratio equals 1:2. For the ratio of 2:1, the droplets have a larger total volume resulting in faster coalescence rate of droplets.

### 3.3.3 Estimation of mass transfer coefficients in the CSTR unit

The high-speed imaging provides enough information to evaluate the overall mass transfer rate, consisting of mass transfer resistance in both the continuous phase and dispersed phase. The

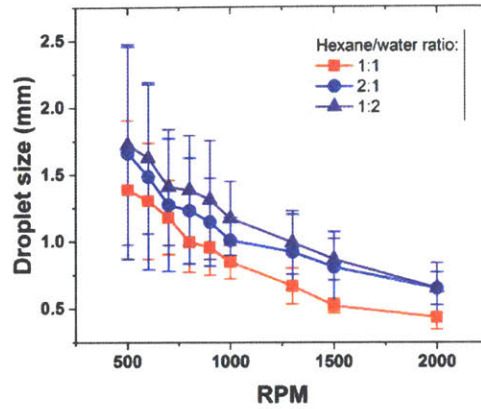


**Figure 3.6. Average hexane droplet size in water for various rotation speeds of the impeller with different two-phase volume ratios in the CSTR unit.**

slip velocity is an important contribution to the mass transfer coefficient. However, the complexity of the biphasic system makes it impossible to calculate the slip velocity of the individual droplets inside the rotating fluid. Here, the system is simplified to the scenario in which a single droplet moves through the rotating fluid. (Figure 3.7) The droplet experiences two major forces, a centrifugal force resulting from the density difference between the dispersed and continuous phases, and a drag force exerted by the surrounding fluid. Gravity can be ignored since the gravitational force is much smaller than the centrifugal force in this case. Although this model ignores the collision of droplets with other droplets and wall, which typically increases the slip velocity, it provides a useful order-of-magnitude estimate of the slip velocity under various rotation speeds of the impeller.

A force balance of the droplet gives the path moving through the fluid and the average slip velocity. The ordinary differential equations (ODEs) describing the movement of the droplet are:

$$\frac{d\theta}{dt} = \frac{u_{\theta}}{r} \quad \text{Equation 3.1}$$

$$\frac{dr}{dt} = u_r \quad \text{Equation 3.2}$$

$$\frac{du}{dt} = -\omega^2 \frac{\rho_w - \rho_h}{\rho_h} - F_{drag} \cos(\varphi) \quad \text{Equation 3.3}$$

$$\frac{d\theta}{dt} = -F_{drag} \sin(\varphi) \quad \text{Equation 3.4}$$

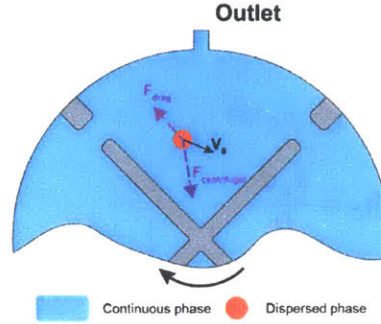


**Figure 3.7. The schematic of the model for estimating the slip velocity.**

Those ODEs describe the droplet in a polar coordinate system, where  $r$  is the distance from the center,  $\theta$  is the angular coordinate.  $u_r$  and  $u_\theta$  are radical velocity and angular velocity, respectively.  $\rho_h$  is hexane density, and  $\rho_w$  is water density.  $\omega$  is the angular velocity of the rotating impeller.  $F_{drag}$  is the drag force exerted by the surrounding fluid. The parameters are given by the following equations:

$$\omega = 2\pi \frac{RPM}{60} \quad \text{Equation 3.5}$$

$$\sin(\varphi) = \frac{u_\theta - u_c}{u_{relative}} \quad \text{Equation 3.6}$$

$$\cos(\varphi) = \frac{u_r}{u_{relative}} \quad \text{Equation 3.7}$$

$$F_{drag} = C_D \cdot \frac{1}{2} \rho u_{relative}^2 A \quad \text{Equation 3.8}$$

$$C_D = 0.28 + \frac{6}{Re^{1/2}} + \frac{21}{Re} \quad \text{Equation 3.9}^{130}$$

where  $u_{relative}$  is the relative velocity between droplet and continuous phase.  $u_c$  is the velocity of continuous phase.  $A$  is the cross-section area of the droplet.  $Re$  is the Reynolds number based on the droplet.

With the estimated slip velocity available, considering the continuous phase side, the Péclet number (Pe) inside the rotating fluid of the CSTR unit is on the order of  $10^6$ , which is much larger than 1. Accordingly, the mass transfer boundary layer is much larger than the momentum boundary layer so the Sherwood number (Sh) has the following scaling with respect to  $Pe^{131}$ .

$$Sh_c = C \cdot Pe^{1/2} \quad \text{Equation 3.10}$$

$$Sh_c = \frac{k_c d}{D} \quad \text{Equation 3.11}$$

It is assume that the droplet contact time with continuous phase can be calculated by<sup>132</sup>:

$$t = \frac{d}{u_{slip}} \quad \text{Equation 3.12}$$

where  $d$  is the droplet diameter, and  $u_{slip}$  is the slip velocity. The constant in Equation 3.10 can be obtained as shown in Equation 3.13, consistent with the Higbie's penetration theory<sup>133</sup>.

$$Sh_c = \frac{2}{\sqrt{\pi}} \cdot Pe^{1/2} \quad \text{Equation 3.13}$$

For the mass transfer in the dispersed phase, the Reynolds number is on the order of  $10^3$  resulting in the turbulent droplets<sup>134</sup>. Assuming that the droplet has long contact time with the continuous phase (consistent with operation of the CSTR unit), the mass transfer coefficient in the dispersed phase can be estimated by:

$$k_d = \frac{0.00375 u_{slip}}{1 + \mu_d / \mu_c} \quad \text{Equation 3.14}$$

where  $\mu_d$  is the viscosity of the dispersed phase, and  $\mu_c$  is the viscosity of the continuous phase.

In order to have a fair comparison with commercial flow reactors, the overall mass transfer coefficient is estimated based on the extraction of phenol from hexane into water, which is the same system reported in the literature<sup>124</sup>. The overall mass transfer rate ( $k_{LA}$ ) calculated based on

Equation 3.15 and Equation 3.16 increases with rotation speed (Figure 3.8). The mass transfer rates are similar for hexane/water ratios of 1:1 and 2:1 since the effect of larger droplet sizes for the 2:1 case is offset by the larger volume of dispersed phase. The hexane/water ratio 1:2 has the lowest mass transfer because of the smaller dispersed phase volume and larger droplet size. In general, the mass transfer coefficients are of order 10, implying that the CSTR unit has a comparable mass-transfer performance to its commercial counterparts.

$$\frac{1}{k_L} = \frac{m}{k_c} + \frac{1}{k_d} \quad \text{Equation 3.15}$$

$$a = \frac{6\varepsilon_d}{d_{32}} \quad \text{Equation 3.16}$$

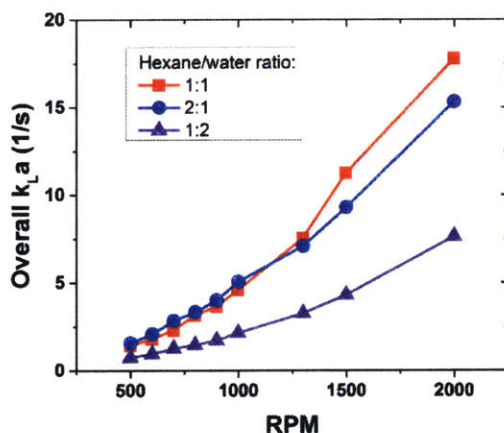


**Figure 3.8. Overall mass transfer coefficients for various rotation speeds of the impeller and different two-phase volume ratios in the CSTR unit.**

### 3.3.4 Asymmetric phase-transfer catalyzed reaction and modeling of interfacial mechanism

The asymmetric benzylation of N-(diphenylmethylene) glycine tert-butyl ester **1** catalyzed by cinchonidine-derived compound **3** (Figure 3.9) is one of the benchmark reactions for examining the performance of new asymmetric phase-transfer catalysts<sup>116-118</sup>. Since this phase-transfer reaction obeys the Makosza interfacial mechanism<sup>118,135</sup>, the apparent reaction rate depends on the

agitation intensity. Consequently, it is a reasonable test reaction for evaluating the two-phase mixing performance of our miniature CSTR unit. The organic stream (**1** (0.025 M), **2** (0.035 M), and **3** (5 mol %) in toluene and DCM mixture (3:1)) and the aqueous stream (50 wt% KOH) were delivered into the CSTR unit by two HPLC pumps as described in the Experimental Methods (Section 3.2.4).

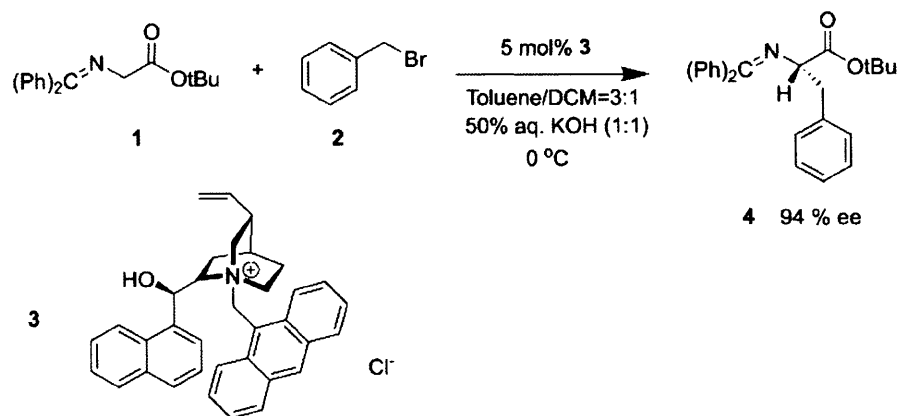


**Figure 3.9. Asymmetric benzylation of 1 catalyzed by cinchonidine-derived catalyst.**

The phase-transfer reaction was examined under various residence times and agitation intensities. The increased yield with agitation (Figure 3.10a) implies that the apparent kinetics depends on the mass transfer rate between phases, consistent with the Makosza interfacial mechanism. Further increasing the rotation speed did not show an improvement for the reaction yield (Figure A.11), indicating the intensive agitation (above 1200 RPM) eliminates the mass transfer limitation, such that the reaction rate is controlled by the intrinsic kinetics. Although the Makosza interfacial mechanism is well-known, few kinetic studies have been performed<sup>135</sup>. Here, the kinetics of interfacial mechanism was systematically investigated, and a model was proposed to extract the intrinsic kinetic parameters and estimate the mass transfer coefficient of the CSTR unit.

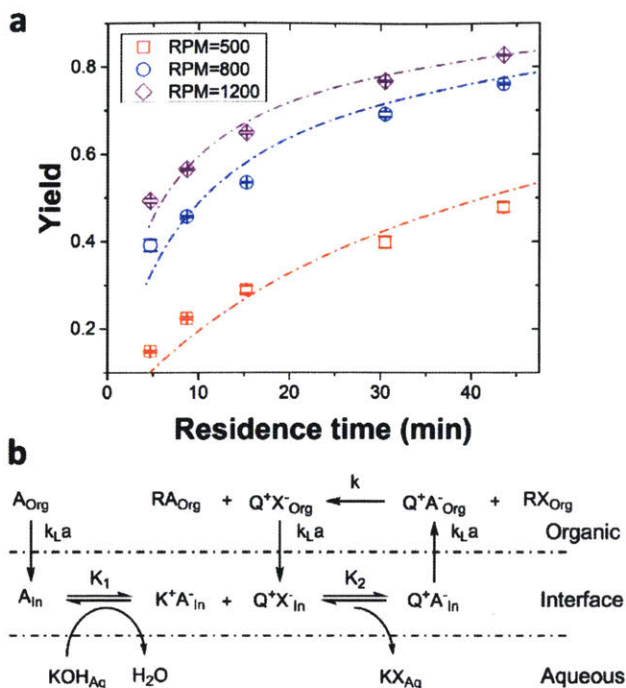


**Figure 3.10. (a) The yield (HPLC yield) of asymmetric catalyzed reaction at different residence times and rotation speeds. The dashed lines are drawn based on the proposed interfacial mechanism model. Organic stream (toluene : DCM = 3:1): 0.025 M 1, 0.035 M 2, and 5 mol% 3. Aqueous stream: 50 % (wt.) KOH in water. (b) Proposed interfacial mechanism model to extract mass transfer coefficient. (A: 1, R: 2, PhCH<sub>2</sub>-, Q: cation of 3, X: Cl<sup>-</sup> or Br<sup>-</sup>)**

According to the Makosza interfacial mechanism, ion exchange reactions only occur at the interface, so a phase-transfer description must include three domains, organic phase, aqueous phase, and interface (Figure 3.10b). The fast ion-exchange steps happening in the interface are assumed to be at pseudo-equilibrium. Increasing the interfacial areas by more rigorous agitation can afford more reagent-catalyst complex  $Q^+A^-$ , which leads to faster reaction rate. The aqueous phase has KOH in large excess, and hence the material exchange between interface and aqueous phase will not be limiting. The key step that determines the chirality of the product is the formation of complex  $Q^+A^-$  at the interface, and the following benzylation of  $Q^+A^-$  occurs in the organic



phase. The reaction system is at steady state, such that consumption and generation of reaction species are equal. The system can be described using the following material mass balances:

$$\begin{aligned}
 F([A]_{inlet} - [A]_{org}) &= V_t k_L a ([A]_{org} - M_1 [A]_{in}) \\
 &= V_t k_L a ([QX]_{org} - M_2 [QX]_{in}) \\
 &= V_t k_L a (M_3 [QA]_{in} - [QA]_{org}) \\
 &= V_{org} k [QA]_{org} [RX]_{org}
 \end{aligned}
 \tag{Equation 3.17}$$

where  $F$  is the flowrate of the organic phase,  $[A]_{inlet}$  is the inlet concentration of A in the organic phase,  $V_t$  is the total volume of organic phase and aqueous phase,  $V_{org}$  is the volume of the organic phase,  $k_L a$  is the overall mass transfer coefficient,  $M_1$ ,  $M_2$ , and  $M_3$  are the partition coefficients for A, QX, and QA, respectively.

Since the total amount of catalyst in all phases is constant, the mass balance for the catalyst is:

$$[QX]_{org} + [QX]_{in} + [QA]_{in} + [QA]_{org} = [Q]_t \tag{Equation 3.18}$$

The two fast ion-exchange steps in the mechanism are assumed to be at pseudo-equilibrium with equilibrium constant,  $K_1$  and  $K_2$ , respectively.

$$\frac{[KA]_{in}}{[A]_{in}} = K_1 \tag{Equation 3.19}$$

$$\frac{[QA]_{in}}{[QX]_{in}[KA]_{in}} = K_2 \tag{Equation 3.20}$$

Combining Equation 3.19 and Equation 3.20 yields:

$$[A]_{in} = \frac{1}{K_1 K_2} \frac{[QA]_{in}}{[QX]_{in}} \tag{Equation 3.21}$$

Using Equation 3.17 and Equation 3.18 can obtain:

$$(M_2 + 1)[QX]_{in} + (M_3 + 1)[QA]_{in} = [Q]_t \tag{Equation 3.22}$$

Combining Equation 3.17, Equation 3.21, and Equation 3.22 yields the following result:

$$\frac{F}{V_t k_L \alpha} x = (1 - x) - \frac{\alpha}{[A]_{inlet}} \frac{[QA]_{in}}{[Q]_t - (M_3 + 1)[QA]_{in}} \quad \text{Equation 3.23}$$

where  $x$  is the reaction conversion, and  $\alpha$  is defined as:

$$\alpha = \frac{M_1(M_2 + 1)}{K_1 K_2} \quad \text{Equation 3.24}$$

Using Equation 3.17 and the concentration ratio of RX and A is 1.4 at the inlet stream (0.025 M A and 0.035 M RX) to obtain the expression for  $[QA]_{org}$  and  $[QA]_{in}$  as shown in Equation 3.25 and Equation 3.26, respectively.

$$[QA]_{org} = \frac{Fx}{V_{org} k (1.4 - x)} \quad \text{Equation 3.25}$$

$$[QA]_{in} = \frac{1 + (1.4 - x)\beta}{M_3} [QA]_{org} \quad \text{Equation 3.26}$$

where  $\beta$  is defined as:

$$\beta = \frac{V_{org} k [A]_{inlet}}{V_t k_L \alpha} \quad \text{Equation 3.27}$$

Inserting Equation 3.25 and Equation 3.26 in Equation 3.23 gives an expression that describes the reaction conversion with four unknown constants only,  $\alpha$ ,  $k$ ,  $M_3$ , and  $k_L \alpha$ :

$$\frac{F}{V_t k_L \alpha} x = (1 - x) - \frac{\alpha}{[A]_{inlet}} \left\{ \frac{[Q]_t V_{org} k M_3}{F} \frac{1.4 - x}{(1 + (1.4 - x)\beta)x} - (M_3 + 1) \right\}^{-1} \quad \text{Equation 3.28}$$

A genetic algorithm was used to find the global optimal solution for those four unknown parameters with experimental reaction yields above. The proposed kinetic model accurately predicts the experimental data (Figure 3.10a), and provides key process and reaction parameters

including the mass transfer coefficient  $k_{L,a}$  and rate constant  $k$ . In order to understand the relationship between mass transfer coefficient ( $k_{L,a}$ ) and reaction yield, the corresponding plot obtained from the kinetic model is illustrated in Figure A.12, which explicitly shows that the mass transfer limitation is nearly eliminated for RPM over 1200.

In order to further validate the kinetic model and mass transfer coefficient estimation method, the asymmetric phase-transfer catalyzed reaction system was also studied with high-speed imaging (Figure A.13). The mass transfer coefficient estimation produced mass transfer coefficients consistent with those determined from the Makosza interfacial kinetic model proposed above. (Table 3.1) There is less agreement between mass transfer coefficients estimated from two methods when the RPM is 500 since the highly viscous 50 % KOH aqueous solution leads to non-spherical droplets under low rotation speed (see Figure A.13), which makes it challenging to calculate the average droplet diameter.

**Table 3.1. Mass transfer coefficients for the phase-transfer reaction estimated by: (i) Makosza interfacial mechanism kinetic model, and (ii) high-speed imaging.**

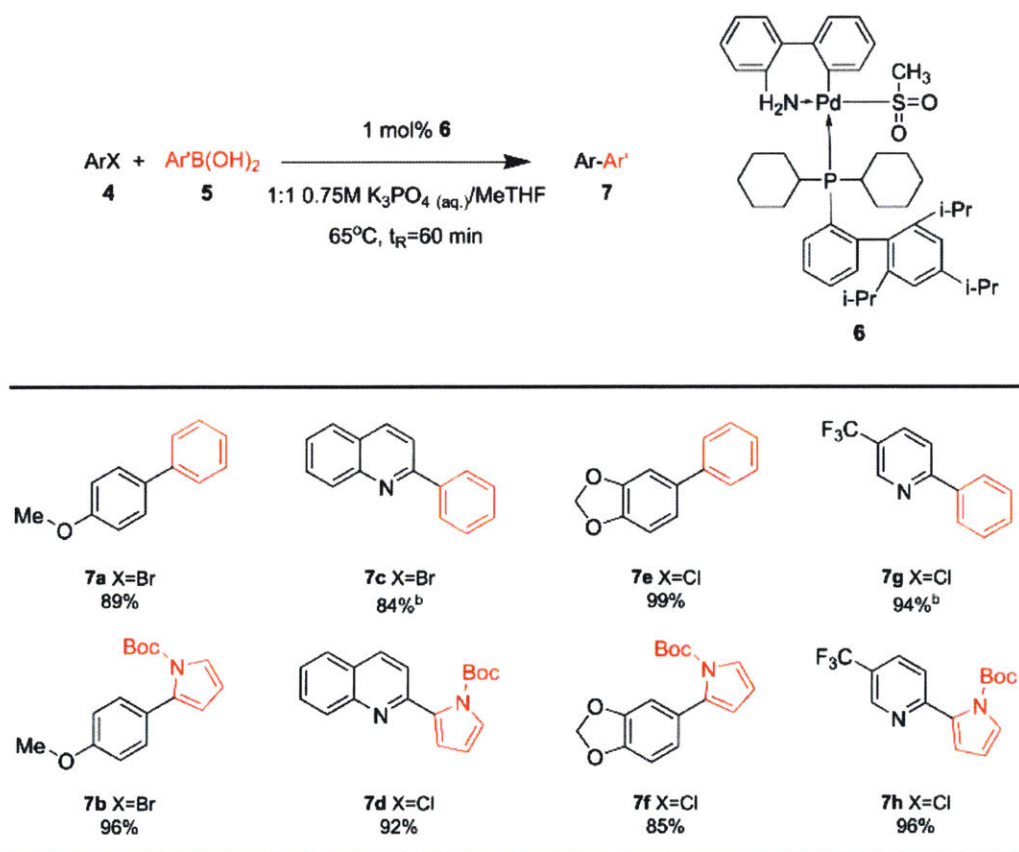
RPM	Kinetic model ( $s^{-1}$ )	High-speed imaging ( $s^{-1}$ )
500	0.19±0.06	0.58
800	1.39±0.42	1.38
1200	10.75±2.15	11.52

### 3.3.5 Biphasic Suzuki-Miyaura C-C coupling reactions

Biphasic Suzuki-Miyaura palladium-catalyzed C-C coupling reactions, a widely used bond-forming synthetic route in pharmaceutical industry, were chosen to expand the scope of the biphasic reactions. This reaction generally requires oxygen-free environment to avoid

decomposition of the palladium catalyst. The utilization of aqueous phase dissolves inorganic base and salt byproduct, making the reactions feasible for continuous flow processes. Various aryl halides and arylboronic acids were demonstrated to perform a series of Suzuki-Miyaura cross-coupling reactions with pre-catalyst **6**<sup>121</sup> in the CSTR unit to demonstrate its capability of sustaining oxygen-free environment and agitating viscous aqueous base solution. (Table 3.2) After

**Table 3.2. Biphasic Suzuki-Miyaura C-C coupling reactions<sup>a</sup>**



<sup>a</sup> 0.05 mL/min of **4** (0.25 M), **5** (0.3 M), and precatalyst **6** (1 mol %) in 2-methyltetrahydrofuran (MeTHF), 0.05 mL/min of K<sub>3</sub>PO<sub>4</sub> (0.75 M) aqueous phase. Agitation rate: RPM=1200. Yields were determined by GC analysis. <sup>b</sup> 2 mol % of precatalyst **6** and  $t_{\text{R}}$ =90 min was used.

reaction condition optimization, since Suzuki-Miyaura reaction was not mass transfer limited within the rotation speed window (500 RPM – 3000 RPM) of the CSTR, the CSTR unit was stirred with a moderate RPM=1200. Under optimized conditions, most reactions finished with good yields. (**7a-b**, **7d-f**, **7h**) For substrates **7c** and **7g**, 2 mol% of pre-catalyst **6** and 90 min of residence time were required to achieve reasonable yields.

### **3.4 Conclusion**

In summary, this chapter designed and demonstrated an active-mixing miniature CSTR unit that is capable of overcoming the mass transfer limitations for biphasic reactions. Our reactor design concept is a step forward in the development of continuous manufacturing of fine chemicals by allowing intensive agitation, reactor sealing, and chemical compatibility to withstand harsh chemical environments (i.e., cooling, heating, strong aqueous base, and aggressive organic solvents). The active mixing, decoupling the mixing and flowrate, makes the reactor versatile for reaction kinetics of different time scales. The highly efficient liquid-liquid mass transfer enables mass-transfer-limited reactions. In addition, the modular CSTR unit with individual cooling and heating capabilities, featured as plug-and-play, affords the opportunity for combination into a CSTR cascade and integration into current small scale continuous processes.

# Chapter 4 Membrane reactor for gas-liquid reaction

## 4.1 Introduction

Among numerous pharmaceutical transformations, gas-liquid reactions, such as hydrogenation<sup>136</sup>, aerobic oxidation<sup>137,138</sup>, and ozonolysis<sup>139</sup>, show attractive atom economy in comparison to other chemical transformations. For example, direct hydrogenation of pharmaceutical precursors with hydrogen gas outpaces other costly sacrificial reducing reagents, such as hydrides ( $\text{LiAlH}_4$  and  $\text{NaBH}_4$ ) or borane reagents. In addition to atom economy, the general availability of gaseous reagents and facile downstream separation make gas-liquid reactions potential green chemistry processes.<sup>140</sup> However, concerns of process efficiency, scalability, and safety of gas-liquid systems create barriers for pharmaceutical applications and this becomes even more challenging when heterogeneous catalysts are present in gas-liquid systems.<sup>136,141</sup>

The advantages of continuous technology over conventional batch or semi-batch processes include steady state operation, enhanced heat and mass transfer rates, reproducibility, and improved safety and process reliability.<sup>5,6,127,142-144</sup> And these benefits are especially true for gas-liquid reaction systems, where the absence of high-pressure headspace gas and reduced reactor volume of continuous flow reactors significantly improve the safety profiles compared to high-pressure reaction vessels. In addition, the increased interfacial area per volume in flow reactors accelerates multiphase mass transfer rates.

Packed-bed reactors, a common type of gas-liquid reactor, despite their mature development in the petrochemical industry, have been adopted in pharmaceutical manufacturing.<sup>145</sup> Zaborenko et al. studied packed-bed reactors of small scale (20 g catalyst), medium scale (120 g catalyst), and pilot scale (1.5 kg catalyst) for successful development of continuous hydrogenation of a pharmaceutical intermediate.<sup>145</sup> Yang et al. provided in-depth characterization of the micro-packed-bed reactor to establish a fundamental understanding of the multiphase hydrodynamics and mass transfer properties.<sup>136</sup>

The complex multiphase hydrodynamics in packed-bed reactors requires extensive understanding of the system behavior across different scales. Additionally, direct contact of gas and liquid is unfavorable for aerobic oxidations due to the formation of flammable oxidant and organic solvent mixtures.<sup>141</sup> The low cross-tube heat transfer of packed-bed reactors can also lead to a non-uniform temperature profile for highly exothermic reactions, leaving APIs with temperature-sensitive functional groups at risk for degradation.

Recently, Gavriilidis et al. demonstrated heterogeneously catalyzed benzyl alcohol oxidation in a ceramic membrane packed-bed reactor.<sup>146</sup> However, the pressure-driven mechanism of the ceramic membrane has no selectivity over gas and liquid permeation, leading to difficulty in operating under desired two-phase pressure profile. Ley et al. proposed and demonstrated the concept of a tube-in-tube reactor using gas-permeable Teflon amorphous fluoroplastic (AF) membranes for various gas-liquid reactions, including heterogeneous and homogeneous hydrogenation<sup>147</sup>, ozonolysis<sup>139</sup>, and carboxylation<sup>148</sup>. The implementation of Teflon AF membrane (highly permeable to gas phase and impermeable to liquid phase) greatly simplifies the reactor operation compared to ceramic membrane. The capabilities and physical properties of the Teflon AF membrane have been described elsewhere.<sup>149–152</sup> Yang et al. used both analytical and

numerical methods to understand the behavior of the tube-in-tube reactor, and indicated challenges in scale-up due to radial-diffusion-limited mass transfer.<sup>153</sup> The challenge of incorporating heterogeneous catalysts in a tube-in-tube reactor makes it less attractive for a broad category of heterogeneous catalytic gas-liquid reactions.

Thus, an efficient, safe, scalable, and widely applicable continuous flow reactor design for gas-liquid reactions is still desirable for low-volume applications. This chapter presents a scalable, sustainable, and safe thin-layer membrane reactor for heterogeneous and homogenous catalytic gas-liquid reactions.<sup>154</sup> The reactor uses a Teflon AF membrane sandwiched between two sheets of thin-layer carbon cloth, which enables superior gas-liquid mass transfer performance. The carbon cloth layer works as a heterogeneous catalyst support, making this reactor design applicable for heterogeneous catalytic gas-liquid reactions. Additionally, nearly all of the gas is consumed by the reaction, removing the need for recycle and increasing the safety of operation by minimizing the amount of gas required. The membrane reactor is demonstrated using popular heterogeneous Pd-catalyzed hydrogenations and homogeneous Cu(I)/TEMPO aerobic alcohol oxidations. The membrane reactor is also stackable allowing for scale-up. In-depth modeling of the membrane reactor affords fundamental understanding and design principles for application to various gas-liquid reactions with different kinetics.

## **4.2 Experimental methods**

### **4.2.1 Materials and reagents**

Woven carbon cloth with palladium and platinum catalyst was purchased from Fuel Cell Store. Teflon AF membrane (40  $\mu\text{m}$  thick) was purchased from Biogeneral. Nitrobenzene, 2-ethyl cinnamate, 10-undecyn-1-ol, benzyl alcohol, 3-phenyl-1-propanol, furfuryl alcohol,



tetrakisacetonitrile copper(I) triflate  $\text{Cu}(\text{MeCN})_4(\text{OTf})$ , 2,2'-bipyridine, 1-methylimidazole (NMI), and (2,2,6,6-tetramethylpiperidin-1-yl)oxyl (TEMPO) were purchased from Sigma-Aldrich and used without further purification. Hydrogen (99.999%), oxygen (99.99%), and nitrogen (99.999%) were purchased from Airgas.

#### 4.2.2 Thin-layer membrane reactor design

A Teflon AF membrane was sandwiched between two sheets of woven carbon cloth (Figure 4.1a) with the gas and liquid phases flowing separately through the two porous carbon cloth layers. The unique property of Teflon AF membranes (highly permeable to gas phase and impermeable to liquid phase) offers the capability of separating the two phases while allowing gas to diffuse through the membrane into the liquid phase. The design was engineered to minimize the thickness of the combined assembly (carbon cloth: 300  $\mu\text{m}$  and Teflon AF membrane: 40  $\mu\text{m}$ ) in order to reduce the gas molecule diffusion length and improve the mass transfer performance. The reactor volume of liquid side is 0.05 ml. (Carbon cloth dimensions: 30 mm  $\times$  13 mm  $\times$  0.3 mm, porosity: 43%)

For demonstration purposes, the membrane reactor (Figure 4.1b and c) was fabricated out of aluminum, due to its excellent thermal conductivity. The membrane reactor can also be coated with perfluoroalkoxy alkane (PFA) or fabricated out of 316 stainless steel for better chemical compatibility. The cartridge heaters inside the reactor combined with a proportional–integral–derivative (PID) temperature controller kept the membrane reactor at the desired reaction temperature.

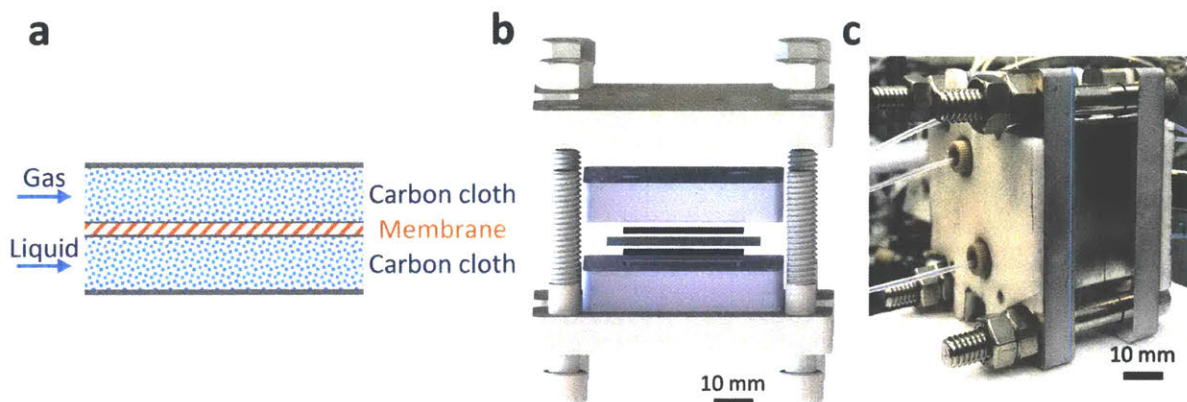


**Figure 4.1. (a) Gas-liquid membrane reactor schematics: Teflon AF membrane sandwiched between two sheets of carbon cloth layers to offer separation of gas and liquid while allowing the gas phase to diffuse through the membrane to react in the liquid phase. (b) Exploded-view CAD drawing of the gas-liquid membrane reactor. Two thin black layers are carbon cloth, and the thin blue layer is a Teflon AF membrane. (c) Photograph of assembled single-layer membrane reactor.**

### 4.2.3 General membrane reactor operating procedures

**General start-up procedure.** Prior to each experiment, the system was rinsed with appropriate liquid solvent on the liquid side and nitrogen on the gas side. The liquid side was then filled with the liquid reagent stream, and the gas side was adequately purged by the gas reagent. The gas side was pressurized while maintaining a small (~150 kPa) transmembrane pressure with the back-pressure regulator (BPR) on the liquid side, which is necessary to prevent gas from passing through the BPR and avoid rupturing the membrane. The reaction gas flow was controlled using a mass flow controller (MFC, Brooks Instrument 5850i) and the BPR was pressurized using nitrogen gas controlled by a pressure controller (Alicat Scientific).

**General reaction procedure.** Once the gas side pressure had reached the appropriate pressure set-point, the temperature controller was turned on and the liquid flow was started. The reagent stream was degassed before entering the reactor. The system was purged with three reactor volumes in order to reach steady state before sample collection. Reaction parameters, such as

temperature and flow rate, were varied to collect samples under different reaction conditions. Samples were analyzed with gas chromatography (GC, Agilent 6890).

**General shut-down procedure.** The liquid and gas flow rates were stopped. Then, simultaneously, the BPR pressure was reduced to atmospheric pressure and the gas and liquid outlets were switched to venting positions, allowing for safe de-pressurization of the system and avoiding membrane rupture. After every experiment, the system was flushed with the same solvent used during the experiment on the liquid side and nitrogen on the gas side.

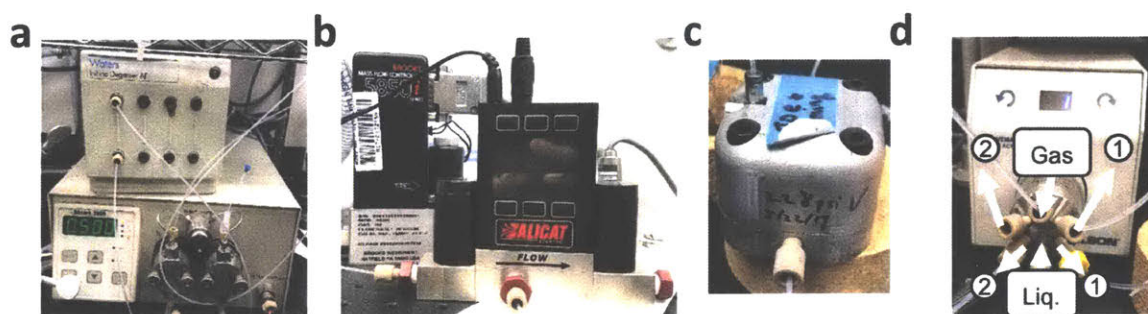


**Figure 4.2.** Pictures of equipment used for controlling the gas-liquid membrane reactor: (a) gas flow controller for  $H_2$  and  $O_2$  (back) and pressure controller for  $N_2$  used to pressurize the BPR (front), (b) in-line degasser (top) and HPLC pump (bottom), (c) variable BPR, and (d) 2 position 6-way valve for controlling the gas and liquid halves of the reactor. Position 1 is the venting position (used during startup and shutdown) and position 2 is used during operation of the reactor.

## 4.3 Results and discussion

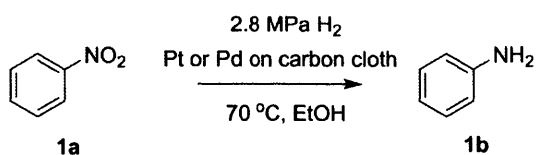
### 4.3.1 Heterogeneous catalytic hydrogenations

Direct  $H_2$  hydrogenation reactions with heterogeneous catalysts are attractive chemical transformations for synthesis because of their atom economy and easy-to-reuse heterogeneous catalysts.<sup>140</sup> However, the major challenge for  $H_2$  heterogeneous hydrogenations is the poor solubility of  $H_2$  in the organic solvent coupled with the slow mass transfer rate from the gas phase

to the liquid phase and the catalyst surface. The thin-layer membrane reactor design minimizes the diffusion distance for H<sub>2</sub> molecules to the reactive catalyst surface in order to maximize the mass transfer performance. In addition, the membrane reactor was engineered for high pressure operation (tested up to 3.1 MPa), which improves the solubility of H<sub>2</sub> in the organic solvent, intensifying the hydrogenation process.

To investigate the potential of the membrane reactor in heterogeneous catalysis, our investigation started with hydrogenation of nitrobenzene **1a** to aniline **1b** with cost-effective carbon cloth embedded with platinum (Pt) or palladium (Pd) as the heterogeneous catalyst (commercially available from Fuel Cell Store, ~\$1/cm<sup>2</sup>) (Table 4.1). The loading of the catalyst on the carbon cloth for both Pt and Pd catalysts was 4 mg/cm<sup>2</sup> (based on carbon cloth surface area: width × length). The Pt catalyst was too aggressive, leading to extensive formation of the over-reduction product, while Pd showed a better selectivity towards the desired product **1b** compared to Pt. (Table 4.1, entry 1 and 2) Increasing the residence time from 0.5 min to 1 min did not show significant improvement of yield of **1b**. (Table 4.1, entry 2 and 3)

With the optimal catalyst (Pd), the heterogeneous catalytic hydrogenation scope was expanded to other substrates. (Table 4.2) The reduction of C-C double and triple bonds is facile under these optimized reaction conditions (full conversion of the starting material). In order to keep the theoretical hydrogen consumption per reagent volume the same, the concentration of the reagent was determined based on the number of hydrogen molecules needed per reagent molecule. All substrates achieved excellent yields with the optimized hydrogenation conditions. (Table 4.2, entries 1-3)

**Table 4.1. Optimization of heterogeneous hydrogenation of nitrobenzene to aniline.<sup>a</sup>**

No.	Catalyst	RT <sup>b</sup> (min)	1a	Intermediates	Over-reduction	1b
1	Pt	0.5	19%	20%	11%	50%
2	Pd	0.5	3%	7%	5%	85%
3	Pd	1	2%	5%	7%	86%

<sup>a</sup> 0.2 M **1a** in ethanol (EtOH). <sup>b</sup> RT: residence time.

**Table 4.2. Heterogeneous hydrogenation substrate scope.<sup>a</sup>**

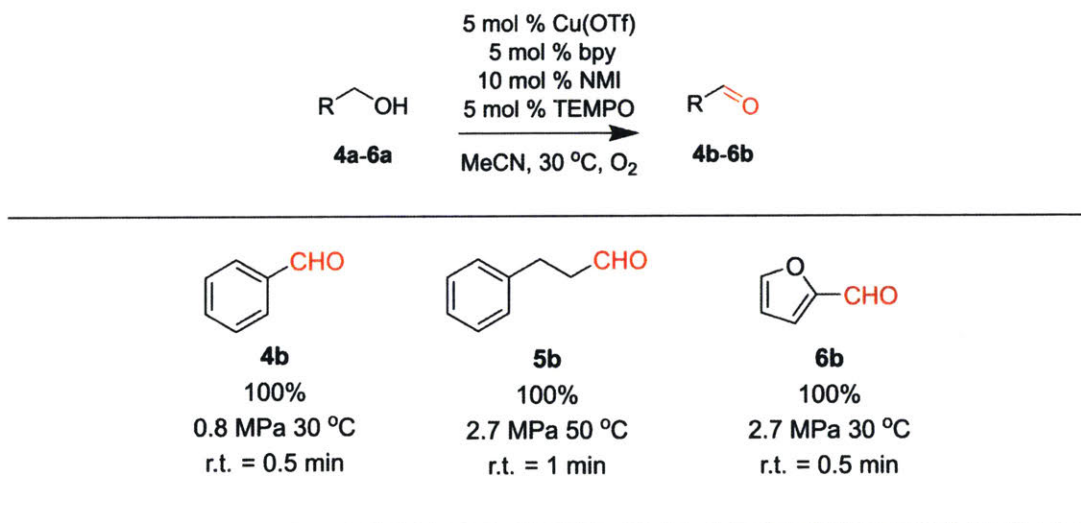
No.	Substrate	Product	RT (min)	T (°C)	Yield
1 <sup>b</sup>			0.5	70	85%
2 <sup>c</sup>			0.5	50	94%
3 <sup>d</sup>			0.5	50	95%

<sup>a</sup> Hydrogen pressure: 2.8 MPa. <sup>b</sup> 0.2 M **1a** in EtOH. <sup>c</sup> 0.6 M **2a** in ethyl acetate. <sup>d</sup> 0.3 M **3a** in ethyl acetate.

### 4.3.2 Homogeneous Cu/TEMPO catalyzed aerobic alcohol oxidations

Recent developments of aerobic oxidation reactions provide attractive alternatives to conventional approaches employing stoichiometric oxidants.<sup>155–157</sup> However, the practical usage of aerobic oxidation in large-scale synthesis raises safety concerns, namely the formation of explosive mixtures (flammable organic solvents in oxygen). A number of microreactor-based biphasic flow implementations of aerobic oxidation improve the safety profile by accurately controlling oxygen flow in the microchannels.<sup>158,159</sup> However, the explosive mixtures are still present in the microreactor system. Tube-in-tube membrane reactors show great potential to avoid the formation of explosive mixtures, but still have inherent scalability issues for large-scale synthesis.<sup>153,160</sup> Implementing the thin-layer membrane reactor designed in this work offers the opportunity to make the aerobic oxidation reactions both safe and scalable for industrial applications.

**Table 4.3. Homogeneous Cu/TEMPO catalyzed aerobic alcohol oxidation substrate scope.<sup>a</sup>**



<sup>a</sup> 0.2 M alcohol substrate with 0.05 equiv. Cu(OTf), 0.05 equiv. 2,2'-bipyridyl (bpy), 0.1 equiv. 1-methylimidazole (NMI), and 0.05 equiv. TEMPO dissolved in MeCN.

Instead of using a catalyst-embedded carbon cloth layer, pristine carbon cloth was installed in the membrane reactor, along with the same Teflon AF membrane to accommodate the homogeneous catalytic aerobic oxidation. Cu/TEMPO catalyzed oxidation of alcohols is an efficient approach to selective aldehyde synthesis.<sup>155</sup> This reaction was demonstrated to have first-order kinetics on oxygen concentration in the solvent, which directly corresponds to the oxygen pressure in the gas phase. The ability to handle high pressures in the membrane reactor would intensify this reaction by orders of magnitude compared to batch processing. Meanwhile, the Teflon AF membrane separates the oxygen and organic solvent to circumvent the formation of explosive mixtures.

Three substrates (**4a-6a**) were examined in the membrane reactor with optimized conditions, and all products were achieved in excellent yields (Table 4.3). The residence times required to reach full conversion were around 1 min, significantly shorter than the several-hour reaction time required under batch conditions.<sup>155</sup>

### 4.3.3 Gas purge for oxygenation reactions

Even though the explosive mixture of liquid organic solvents and oxygen is avoided in the membrane reactor for oxygenation reactions, the organic solvent vapors could potentially penetrate through the Teflon AF membrane to the gas side, which raises safety concerns for large-scale applications. Unlike hydrogenation reactions in the membrane reactor, where the gas side outlet is plugged to reduce the unnecessary hydrogen consumption, an additional oxygen purge stream is required to avoid the accumulation of organic solvent vapors in the gas side, which could exceed lower explosive limits under certain reaction conditions.

In order to ensure safe operation of the membrane reactor for reactions involving oxygen, the required oxygen purge stream flowrate needed to keep the solvent vapor concentration under the lower explosive limit (LEL) was calculated for various reaction temperatures and organic solvents. Since the LEL data of organic solvents in pure oxygen are rarely available, the approach developed by Chen<sup>161</sup> for estimating the LEL in pure oxygen with the LEL in air was used. (Equation 4.1)

$$LEL_{O_2} = \frac{LEL_{air} \hat{C}_{PO_2}}{LEL_{air} \hat{C}_{PO_2} + (1 - LEL_{air})(0.21 \hat{C}_{PO_2} + 0.79 \hat{C}_{PN_2})} \quad \text{Equation 4.1}$$

where  $LEL_{O_2}$  is lower explosive limit in pure oxygen, and  $LEL_{air}$  is the lower explosive limit in air.  $\hat{C}_{PO_2}$  is the average heat capacity of oxygen, and  $\hat{C}_{PN_2}$  is the average heat capacity of nitrogen.

The diffusion data of organic solvent molecules in the Teflon AF membrane is available from several previous publications.<sup>162-166</sup> The data for several common organic solvents is shown in Table 4.4.

**Table 4.4. Data used for estimating flowrate of oxygen purge stream.**

	LEL	LEL in O <sub>2</sub>	MW (g/mol)	Boiling point (°C)	Sorption parameter S <sub>0</sub> @25 °C (g/100 g)	D <sub>0</sub> @25 °C (m <sup>2</sup> /s)	ΔH <sub>s</sub> (kJ/mol)	E <sub>D</sub> (kJ/mol)
Acetone	0.026	0.0245	58.08	56.0	2.43	7.67E-11	-35.8	18.8
Methanol	0.06	0.0566	32.04	64.7	1.84	1.60E-11	-44.6	33.9
Ethanol	0.033	0.0311	46.07	78.4	2.81	7.09E-12	-48.4	23.2
Cyclohexane	0.013	0.0122	84.16	80.75	6.75	1.61E-12	-35.2	15.8



The sorption parameter determines the concentration of organic solvent in the Teflon AF membrane, which has a temperature dependence as described in Equation 4.2. The diffusion coefficient organic molecule in the membrane also depends on the temperature (Equation 4.3).

$$S = S_0 \exp(-\Delta H_S / RT) \quad \text{Equation 4.2}$$

$$D = D_0 \exp(-E_D / RT) \quad \text{Equation 4.3}$$

The model used to estimate the purge stream is shown in Figure 4.3. The diffusion of organic solvent vapor in the gas phase is orders of magnitudes larger than that in the membrane. Thus, it can be assumed the gas side is a homogenous mixture of organic solvent vapor and oxygen. Even though other substrates in the reaction mixture can also potentially penetrate through the membrane, those substrates were neglected considering their much lower volume concentration, slower diffusion rate, and higher boiling points compared to the organic solvent.

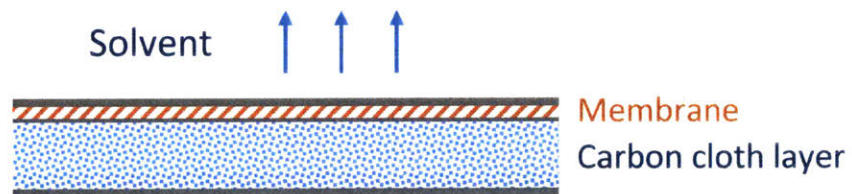


**Figure 4.3. Schematics of the membrane reactor for estimating the required purge stream**

The flowrate of the purge stream can be estimated with Equation 4.4:

$$\text{Flowrate} = DA_{mem.} \frac{C_{sat.}}{d_{mem.}} \left(1 - \frac{LEL_{O_2} * p}{p_{sat.}}\right) / C_{sol} \quad \text{Equation 4.4}$$

$$C_{sol} = r_{safety} * LEL_{O_2} * \frac{p}{RT} \quad \text{Equation 4.5}$$

$$\log(p_{sat.}) = A - \frac{B}{C + T} \quad \text{Equation 4.6}$$

where  $D$  is the diffusion coefficient of the organic solvent molecule in the Teflon AF membrane.  $A_{mem.}$  is the surface area of the membrane,  $C_{sat.}$  is the saturated organic solvent concentration in the gas phase,  $d_{mem.}$  is the thickness of the membrane,  $p$  is the absolute pressure on the gas side, and  $p_{sat.}$  is the saturated organic solvent partial pressure, which can be calculated by Antoine equation (Equation 4.6).  $C_{sol}$  is the upper limit of organic solvent concentration in the gas phase, which can be determined with Equation 4.5.  $r_{safety}$  is the safety ratio (ranging from 0 to 1). Safety ratio of 0 corresponds to no tolerance to any solvent vapor in the gas phase, while the value of 1 corresponds to the largest tolerance operating at the lower explosive limit.

Figure 4.4 shows the required gas purge stream flowrates for four solvents under various reaction temperatures with a safety ratio of 0.5 (0.5 is selected as a medium value between 0 and 1, and the actual value can be determined based on desired safety level). Reaction temperature plays an important role in determining the required purge stream, since temperature has an impact on the diffusion coefficient, saturated solvent vapor pressure, and solvent solubility in membrane. For all solvents studied, a purge stream is not required if the reaction is carried out under 40 °C. Acetone requires a very large purge stream to keep the solvent vapor concentration under  $C_{sol}$ . due to its low LEL, low boiling point and high diffusion coefficient. Cyclohexane, even with the lowest LEL, requires a small purge stream because of its high boiling point and low diffusion coefficient. Methanol and ethanol, with relatively high LEL values, high boiling points, and low diffusion coefficients, require no purge stream up to 75 °C, appearing to be the two safest solvents among the solvents studied.

For oxygenation reactions, implementing a safe solvent (e.g. methanol and ethanol) and operating under a low reaction temperature are essential to improve the safety profile of the

membrane reactor, otherwise a purge stream is required to avoid the accumulation of the penetrated organic solvent vapor in the gas side.

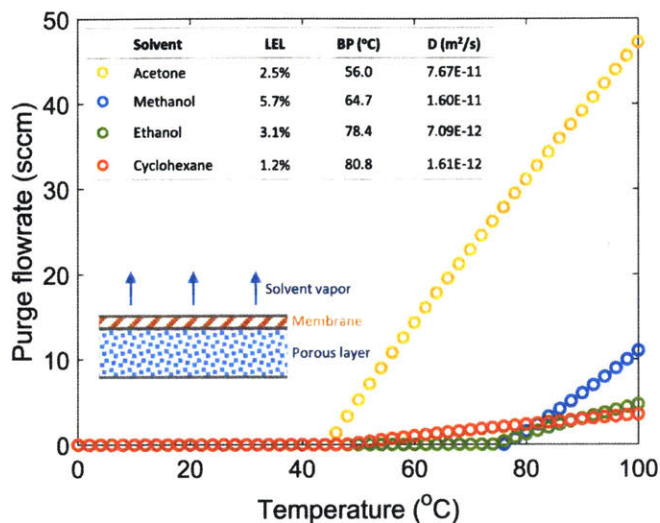


**Figure 4.4. Required purge stream flowrates for various reaction temperature and solvents. The inserted tables shows the LELs in pure oxygen, boiling points (BP), and diffusion coefficients at 25 °C of the studied solvents.**

#### 4.3.4 Membrane reactor design optimization

Gas molecules have such a high permeability through the thin Teflon AF membrane that the dominant gas mass transfer resistance is in the liquid layer.<sup>153</sup> Hence, the mass transfer performance of the membrane reactor mainly depends on the thickness of the carbon cloth layer, which also determines the reactor volume if the same membrane area is used. A thin carbon cloth layer is favorable when the reaction is mass transfer limited, while kinetically limited reactions would require a thicker carbon cloth layer (large reactor volume) to increase the residence time. In order to maximize the productivity of the membrane reactor with the same membrane area, the optimal thickness of the carbon cloth layer needs to be determined according to relative ratio of mass transfer rate and reaction rate.

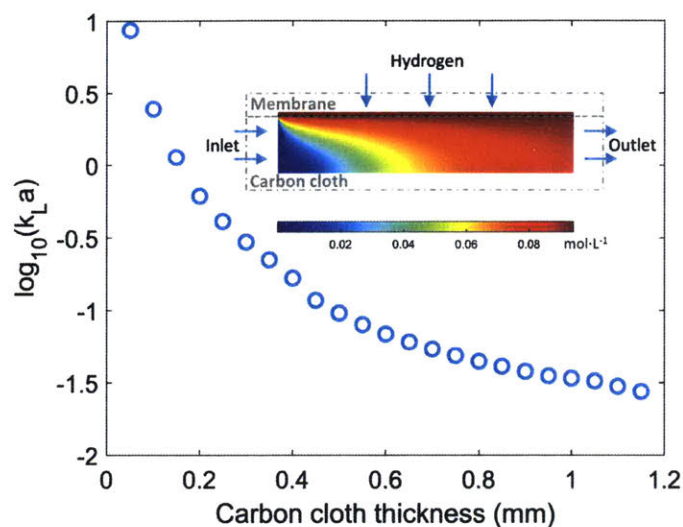


**Figure 4.5. The mass transfer coefficient  $k_L a$  values under various carbon cloth thicknesses. Insert figure: the hydrogen concentration profile in the membrane and carbon cloth. (Membrane thickness is 40  $\mu\text{m}$ , and carbon cloth thickness is 0.6 mm)**

Understanding and calculating the mass transfer coefficient  $k_L a$  in the membrane reactor provides the basis for comparison with other typical gas-liquid-solid reactor configurations (e.g. trickle-bed or packed-bed reactors). COMSOL simulation of hydrogen mass transfer into ethanol under various carbon cloth thicknesses was conducted. As shown in Figure 4.5, the mass transfer performance strongly depends on the thickness of the carbon cloth layer ranging across two orders of magnitude. The hydrogen concentration profile in the membrane is nearly homogeneous indicating negligible mass transfer resistance in the membrane, which is consistent with reported results<sup>153</sup>. The thin-layer membrane reactor with a carbon cloth thickness of 0.3 mm used in the previous experiments has a  $k_L a$  value of  $0.3 \text{ s}^{-1}$ . Even a relatively thick carbon cloth ( $>1 \text{ mm}$ ) has a  $k_L a$  value on the order  $10^{-2} - 10^{-1} \text{ s}^{-1}$ , which is comparable to the  $k_L a$  values ( $0.01 - 0.08 \text{ s}^{-1}$ ) reported for conventional laboratory-scale trickle-bed reactors.<sup>167</sup> In addition to the superior mass transfer performance, it is also tunable by changing the carbon cloth thickness according to the kinetics of the reaction system.

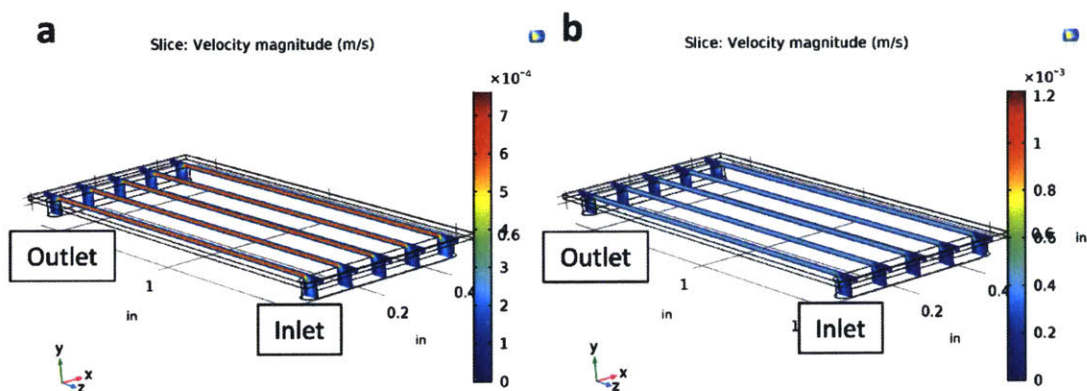


**Figure 4.6. Flow velocity profile in membrane reactor. (a) Membrane reactor without porous carbon cloth. (b) Membrane reactor with porous carbon cloth.**

COMSOL 3-D simulation shows a uniform liquid phase flow distribution across the carbon cloth, and a “plug-flow” velocity profile in the cross section of the carbon cloth (Figure 4.6a). Compared to the scenario without porous carbon cloth (Figure 4.6b), the porous structure simplifies the hydrodynamics making it possible to understand the system with a one-dimensional (1-D) model.

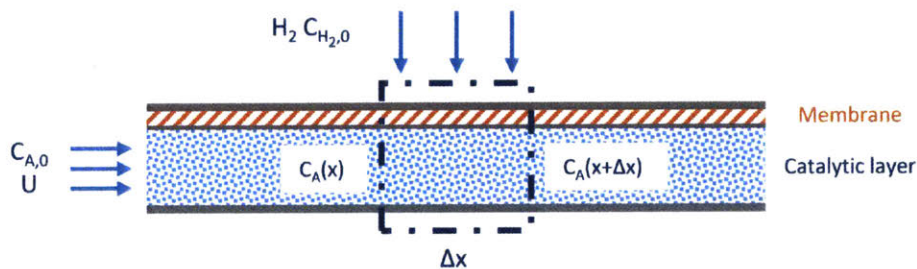


**Figure 4.7. The schematics of the 1-D model.**

1-D model is illustrated in Figure 4.7. Hydrogenation of nitrobenzene with ethanol as solvent is simulated in the 1-D model. Nitrobenzene (A) is fed into the membrane with a concentration of  $C_{A,0}$ , and a velocity of  $U$ . Hydrogen diffuses through the membrane to the catalytic region to react with nitrobenzene to form the hydrolysis product.

With finite element analysis, the mass balance equations can be formulated as:

$$UC_A(x) = UC_A(x + \Delta x) + \Delta x k R(C_A, C_{H_2}) \quad \text{Equation 4.7}$$

$$UC_{H_2}(x) + \Delta x k_L a (C_{H_2,0} - C_{H_2}) = UC_{H_2}(x + \Delta x) + \Delta x k R(C_A, C_{H_2}) \quad \text{Equation 4.8}$$

where  $x$  indicates the location in the membrane reactor with range from 0 to  $L$ , ( $L$  is the length of the membrane reactor),  $k$  is the kinetic constant of the hydrogenation with the unit of  $s^{-1}$ ,  $R(C_A, C_{H_2})$  is the rate dependence on concentrations of nitrobenzene and hydrogen,<sup>168</sup> and  $k_L a$  is the mass transfer coefficient, which determines the rate of hydrogen diffusion into the catalytic regime.  $k_L a$  is defined in the 1-D model, and it can be calculated with a 3-D simulation shown in a later section.

Simplifying Equation 4.7 and Equation 4.8 can get the following equations:

$$-\frac{1}{Da_I} \frac{dC_A}{d\xi} = R(C_A, C_{H_2}) \quad \text{Equation 4.9}$$

$$-\frac{1}{Da_I} \frac{dC_{H_2}}{d\xi} = R(C_A, C_{H_2}) - \frac{1}{Da_{II}} (C_{H_2,0} - C_{H_2}) \quad \text{Equation 4.10}$$

$$\xi = \frac{x}{L} \quad \text{Equation 4.11}$$

$$Da_I = k \frac{L}{U} = k\tau \quad \text{Equation 4.12}$$

$$Da_{II} = \frac{k}{k_L a} \quad \text{Equation 4.13}$$

$\tau$  is the residence time in the membrane reactor calculated with Equation 4.12.  $Da_I$  denotes the residence time versus the reaction time scale, which can roughly indicate the reaction conversion for homogeneous single-phase reaction.  $Da_{II}$  is introduced due to the diffusion of gas through membrane and liquid phase, which represents the ratio between diffusion time scale and time scale.

As shown in Equation 4.9 and Equation 4.10, the system behavior is controlled by two dimensionless numbers,  $Da_I$  (Equation 4.12) and  $Da_{II}$  (Equation 4.13). The dependence of the

reaction conversion at the outlet of the membrane can be calculated by varying the values of two dimensionless numbers. (Figure 4.8) When  $Da_{II} \ll 1$ , indicating the reaction rate is much slower than the diffusion rate, the reaction conversion in the membrane reactor is insensitive to the value of  $Da_{II}$ , corresponding to the “reaction limited” regime. In contrast, the dependence of the reaction conversion on  $Da_{II}$  becomes much stronger when  $Da_{II} > 1$ , corresponding to the “mass transfer limited” regime. Thus, identifying the ratio between the mass transfer time scale and reaction time scale is essential for choosing the optimal membrane reactor design (i.e. carbon cloth layer thickness) in order to balance the trade-off between productivity and reactor fabrication cost.

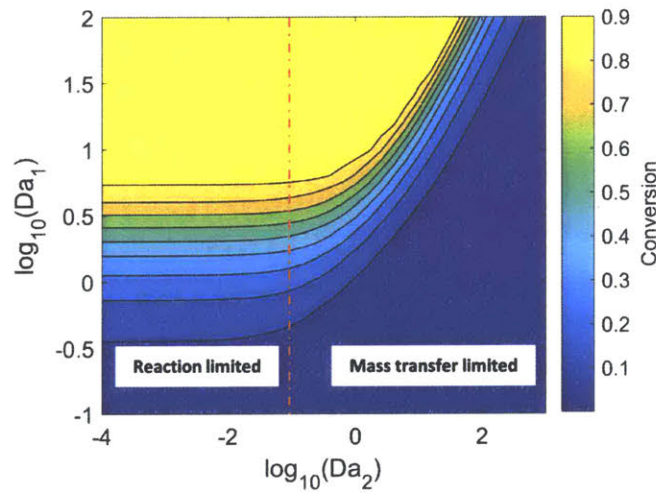


**Figure 4.8. The reaction conversion dependence on  $Da_I$  and  $Da_{II}$ .**

COMSOL 3D simulation illustrates the dependence of reaction outcome on different values of  $Da_I$  and  $Da_{II}$ . (Figure 4.9) When  $Da_{II} \ll 1$ , indicating the reaction rate is much slower than the diffusion rate, the reaction conversion in the membrane reactor is insensitive to the value of  $Da_{II}$ , corresponding to the “reaction limited” regime in Figure 4.9. In contrast, the dependence of the reaction conversion on  $Da_{II}$  becomes much stronger when  $Da_{II} > 1$ , corresponding to the “mass transfer limited” regime, where an efficient mass transfer configuration is beneficial for reaction conversion. Thus, identifying the ratio between mass transfer time scale and reaction time scale is

essential for choosing the optimal membrane reactor design (i.e. carbon cloth layer thickness) in order to balance the trade-off of productivity and reactor fabrication cost.

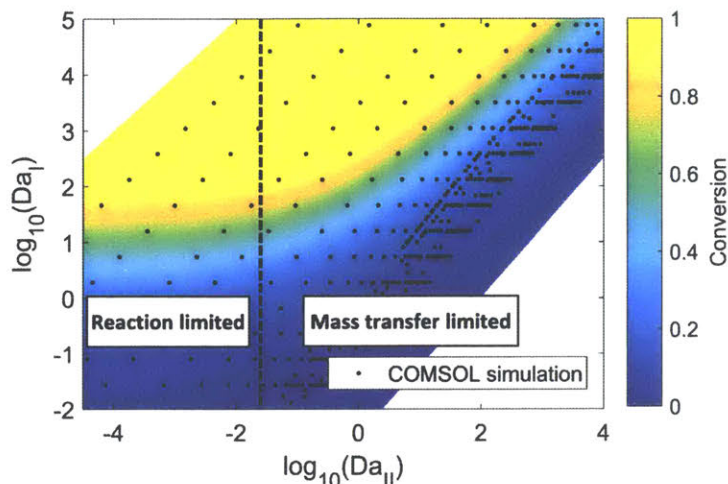


**Figure 4.9. COMSOL simulation of hydrogenation of nitrobenzene with ethanol as solvent in the membrane reactor. The residence time, carbon cloth thickness, and reaction kinetic constant are varied to obtain different values of  $Da_I$  and  $Da_{II}$ . Hydrogenation pressure: 2.8 MPa. Carbon cloth layer dimension: length (30 mm)  $\times$  width (12 mm)  $\times$  thickness (0.05 mm – 3 mm). Membrane thickness: 40  $\mu$ m. The reaction kinetics are available from reported literature, and changing the kinetic constant corresponds to the change of catalyst loading or reaction temperature.<sup>168</sup>**

#### 4.3.5 Scale-up of thin-layer membrane reactor

The complex process needed to scale up conventional trickle-bed or packed-bed reactors is mainly attributed to the change in multiphase hydrodynamics, mass, and heat transfer properties across different scales.<sup>145</sup> The simplified fluid hydrodynamics in the thin-layer membrane reactor offers the opportunity for straightforward scale-up with a stackable design. The stackable design maintains a fixed heat and mass transfer distance (carbon cloth thickness) while increasing the reactor size laterally and in parallel, resulting in preserved heat and mass transfer advantages of the single-layer membrane reactor while meeting the required productivity. As shown in Figure



4.10a, the main channels of a 3-layer stacked membrane reactor distribute or collect gas streams and liquid streams into or from each layer. The design of distribution channels follows barrier-based uniform flow distribution criteria.<sup>169,170</sup> Figure 4.10b shows an assembled 3-layer membrane reactor, and each layer has identical inner dimensions as the single-layer membrane reactor.

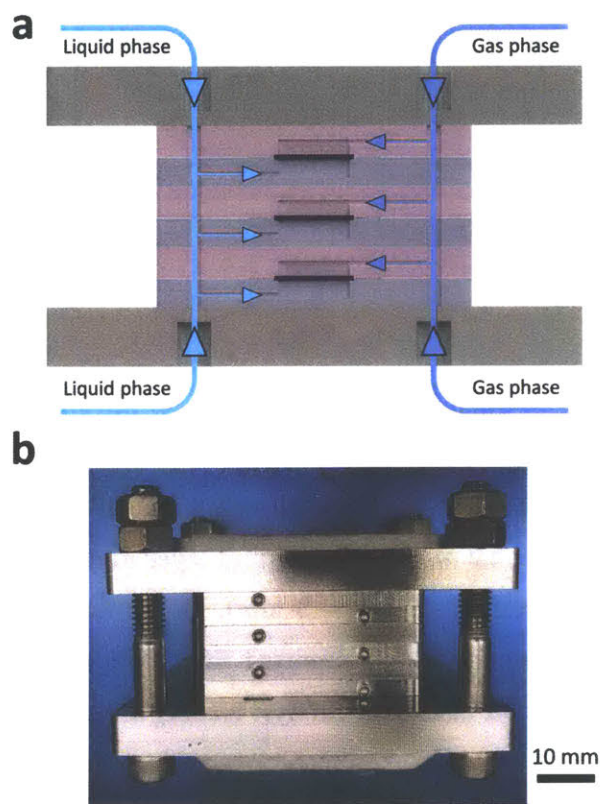


**Figure 4.10. (a) Cross-section of the inlet channels in a 3-layer stacked membrane reactor with blue arrows indicating the liquid flow and purple arrows indicating the gas flow. The outlet channels collect flow from each layer with reversed arrow directions. (b) Photo of a 3-layer stacked membrane reactor.**

For highly exothermic reactions, a large-scale trickle-bed or packed-bed will suffer from insufficient heat transfer problems. The high temperature in the center of the reactor might lead to the decomposition of heat sensitive substrates. The membrane reactor designed in this work can efficiently solve the insufficient heat transfer problems for catalytic hydrogenation reactions. In

order to preserve the heat transfer property of the single-layer reactor when stacking multiple layers together, cooling layers can be inserted between two layers as shown in Figure 4.11.

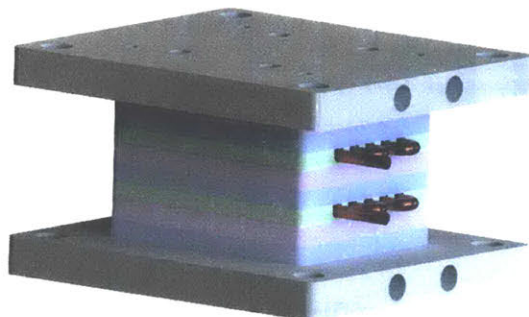


**Figure 4.11. The multi-layer membrane reactor with periodic cooling plates (green). Each cooling plate uses copper tubing for coolant. Gas distribution plates are shown in blue and liquid distribution plates are purple.**

Since it is impractical to evaluate the heat transfer difference between a packed-bed reactor and a membrane reactor at the lab-scale, COMSOL simulation is employed to qualitatively compare the heat transfer rate between packed-bed reactor and membrane reactor in this work. An exothermic reaction was simulated in both reactors with the same reaction enthalpy and coolant capacity. As shown in Figure 4.12a, the packed-bed reactor has a comparatively long distance for heat dissipation, while membrane reactor has a very short heat dissipation distance when using periodic cooling plates. The centerline in the packed-bed reactor has the highest temperature, and the temperature difference between the reactor wall and centerline is much larger the temperature difference for the membrane reactor. Figure 4.12b shows the maximum temperature in two reactors under different coolant flowrate. Increasing the coolant flowrate shows negligible reduction in maximum temperature since the heat dissipation of the packed-bed is insufficient to remove heat generated, while membrane reactor benefits significantly from the increased coolant flowrate due to better heat transfer capacity. The results demonstrate the advantages of the membrane reactor designed in this work for highly exothermic reactions at the large scale.

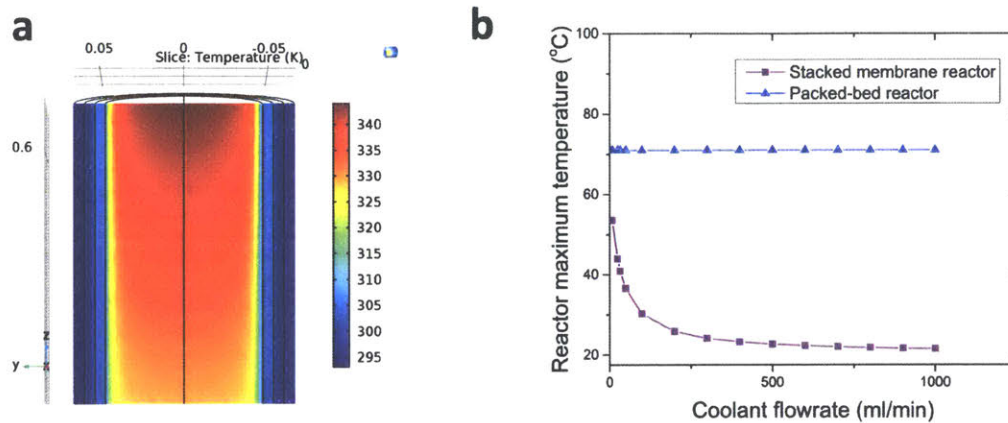


**Figure 4.12. (a) Temperature profile of a simulated packed-bed reactor. (b) The maximum temperature dependence on coolant flowrate in stacked membrane reactor and packed-bed reactor under the same reaction conditions.**

In order to enable direct scale-up from a single-layer to multiple-layers, it is essential to have identical flow distribution across each layer in the stacked membrane reactor. Poor distribution will lead to different residence times in each layer, which might result in unconverted starting substrate. In addition, the results obtained from single-layer membrane reactor cannot be directly translated into multi-layer configuration, which causes the same issue of a tedious scale-up process as for a trickle-bed or packed-bed reactor. Besides the optimized distribution channel design shown in Figure 4.10a, the porous carbon cloth in each layer also plays an important role in unifying flow distribution. COMSOL hydrodynamics simulations illustrate the difference of flow distribution with and without carbon cloth for a 3-layer and 10-layer membrane reactor. (Figure 4.13)

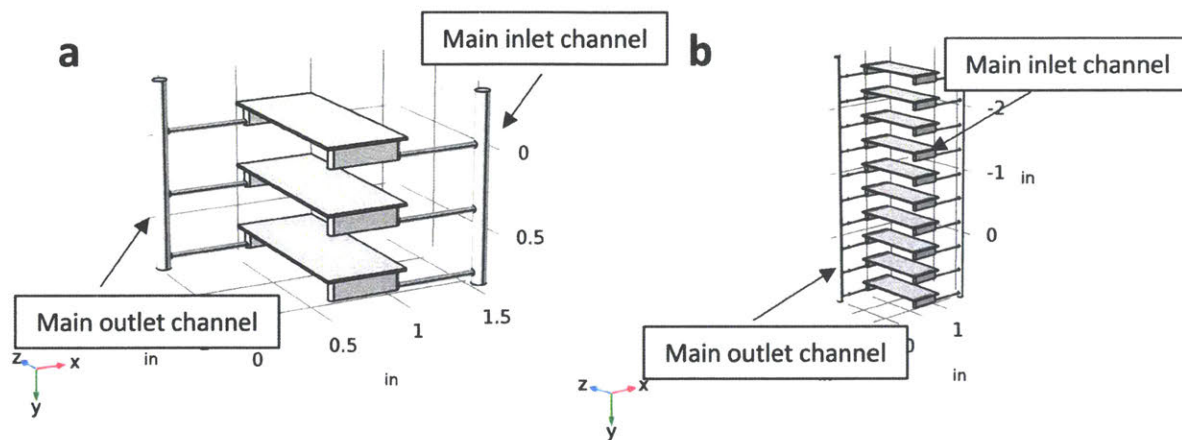


**Figure 4.13. The internal structure of stacked membrane reactor used for liquid hydrodynamics simulation in COMSOL. (a) The 3-layer stacked membrane reactor and (b) the 10-layer stacked membrane reactor.**

COMSOL hydrodynamics simulations illustrate the difference of flow distribution with and without carbon cloth for 3-layer and 10-layer membrane reactors. (Table 4.5) The flowrate at the outlet of each layer is shown in Figure 4.14. For the 3-layer stacked membrane reactor, the existence of the carbon cloth does not have a strong effect on the flow distribution; however, for the 10-layer stacked membrane reactor, the carbon cloth helps induce a uniform flow distribution. Compared to the case without carbon cloth, the porous structure of the carbon cloth adjusts the flow pressure drop profile, which helps to maintain an even distribution of flow from the main channel. This effect becomes more important as an increasing number of layers are stacked together.

The 3-layer membrane reactor (Figure 4.10b) was demonstrated using the hydrogenation of ethyl cinnamate (**2a**). Using identical reaction conditions as the single-layer membrane reactor, (Table 4.2, entry 2) except for 0.3 ml/min liquid flowrate (0.1 ml/min in the single-layer membrane reactor), the 3-layer membrane reactor was able to produce 1.9 g/h of the hydrolyzed product in

91% yield continuously, tripling the hydrogenation productivity of the single-layer membrane reactor without any reaction condition optimization.

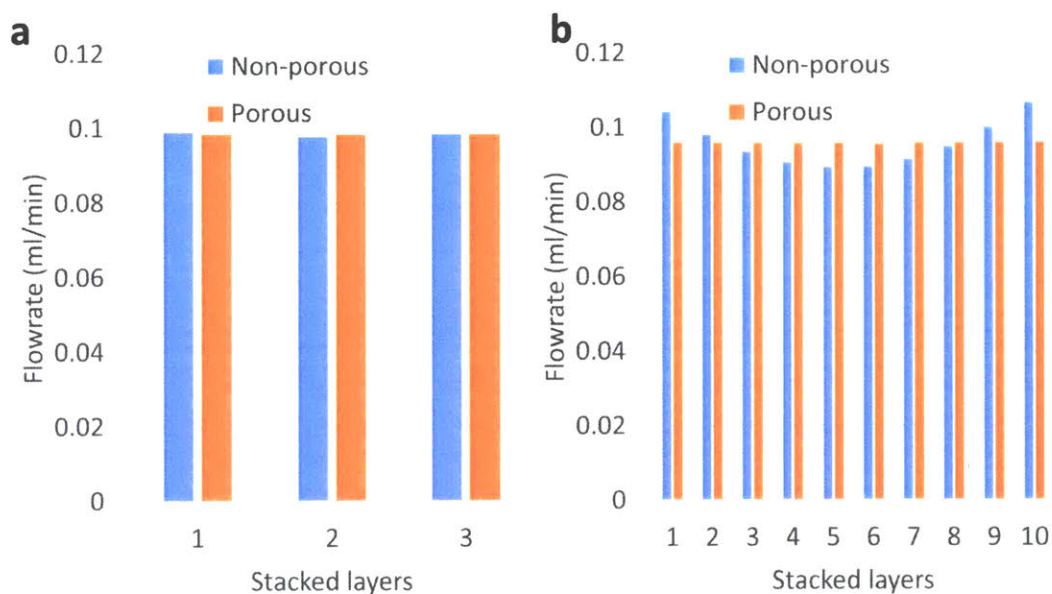


**Figure 4.14. The flowrate at the outlet of each layer for (a) 3-layer and (b) 10-layer stacked membrane reactor. Non-porous: the carbon cloth is absent from the liquid channel. Porous: carbon cloth is present in the liquid channel.**

**Table 4.5. The coefficient of variation<sup>a</sup> for flow distribution with and without carbon cloth in a 3-layer and 10-layer membrane reactor.<sup>b</sup>**

	3-Layer	10-Layer
With carbon cloth	0.05%	0.14%
Without carbon cloth	0.61%	6.45%

<sup>a</sup>Coefficient of variation is the ratio between standard deviation and average. <sup>b</sup>Only the flow distribution of liquid is considered. Gas flow distribution is typically uniform due to the low viscosity of gas.

## 4.4 Conclusion

This chapter presents the development and experimental validation of a thin-layer membrane reactor with commonly used heterogeneous Pd-catalyzed hydrogenations and homogeneous Cu(I)/TEMPO aerobic alcohol oxidations. The unique structure implemented a Teflon AF membrane and porous carbon cloth in the membrane reactor to separate the gas from the liquid, simplifying the multiphase hydrodynamics for predictable reactor performance and straightforward scale-up. The thin-layer design minimized mass transfer resistance in gas-liquid systems. Optimizing the carbon cloth thickness according to the reaction kinetics balanced the trade-off between reactor manufacturing cost and productivity. Both the membrane design and the detailed guidelines for safe operation of oxygenation reactions provided in this work could potentially accelerate the adoption of oxygen and hydrogen as cheap, green reagents in industrial applications. In addition, a stackable membrane design demonstrated a possible scale-up strategy.

# Chapter 5 Electrochemical aerobic oxidation in flow

## 5.1 Introduction

Organic electrochemistry has emerged as an environmentally friendly, atom-economic, and sustainable alternative to traditional synthetic methods because of the use of the redox power from clean electrons in place of stoichiometric amount of oxidants or reductants.<sup>171–173</sup> In addition, electrochemical methods are able to make certain complex molecular moieties easily accessible under mild conditions. The advantages above drive synthetic chemists to start embracing this technology, and many innovative electrochemical transformations for fine chemical synthesis have been developed recently. Moeller's group extensively studied the anodic cyclization reactions of electron-rich olefins.<sup>174–176</sup> Baran's group discovered various synthetic strategies to utilize electrochemical reactions to generate reactive radical species to accomplish challenging C-H functionalization, such as allylic C-H oxidation<sup>177</sup>, trifluoromethylation<sup>178</sup>, and functionalization of methylene and methine moieties<sup>179</sup>.

Advantages of continuous manufacturing over the conventional batch or semi-batch process, such as efficient heat and mass transfer rates, reproducibility, and improved safety and process reliability, drive the transformation of manufacturing process from batch to continuous.<sup>5,9,127</sup> Incorporating newly developed organic electrochemical synthetic methods into continuous manufacturing will have additional benefits, such as low cell resistance due to the reduced electrode distance, improved throughput, and easy flow cell setup. Considering the

complexity of the organic electrochemical systems, the design of a continuous electrochemical cell needs to accommodate the coupled electrochemical reaction and chemical reaction, various electrode materials, utilization of the gaseous reagents, and allow for cost-effective scale-up.

Researchers have already devoted efforts to developing efficient continuous electroorganic synthesis.<sup>180</sup> Yoshida's group used a divided-wall microfluidic cell under -72 °C to generate cationic intermediates *in situ*, and subsequently mixed with nucleophiles to obtain corresponding C-C formation products.<sup>181</sup> Wirth's group demonstrated an easy-to-machine electrochemical microreactor for facile synthesis of amidyl radicals used in intramolecular hydroaminations to produce isoindolinones.<sup>182</sup> Noël's group employed the commercially available electrochemical flow cell, Asia Flux, to evaluate the effect of applied electrolysis potential on the selectivity of thioethers and thiols oxidation reactions, and also elucidate the mass-transfer limitations under low-flowrate regimes.<sup>183</sup> In addition, over the past two decades, research on flow batteries for large-scale energy storage applications has advanced the knowledge of how to design scalable and mass-transfer efficient flow cells. This progress could translate to improvement in electroorganic flow cells.<sup>184,185</sup> However, it is particularly challenging to realize scalable flow systems for electrochemical reactions with inherently slow chemical reaction kinetics, possible side reactions of mediators and intermediate radical species, and the usage of gaseous reagents.

Liquid-phase radical-chain autoxidation reactions are among the large-scale oxidation reactions performed in industry.<sup>186</sup> The oxidation of the side chain of alkyl aromatics is an important method for the preparation of aromatic carbonyl compounds.<sup>187-190</sup> Electrochemistry offers a pathway to conduct those oxidations under mild conditions. This chapter demonstrates an electrochemical flow system specifically engineered for NHPI-mediated electrochemical aerobic oxidations of benzylic C-H bonds.<sup>191</sup> This transformation is a metal-free and sustainable synthetic



pathway, and compatible with heterocycles, suggesting the suitability for pharmaceutical applications.<sup>137,177</sup> With detailed electrochemical analysis of the reaction system, two NHPI decomposition mechanisms are identified that may lead to decreased product yield. To avoid the reductive decomposition of NHPI at the cathode and enable the usage of the cost-effective RVC electrode, a Nafion membrane serves to circumvent the crossover of NHPI from anolyte to catholyte. To limit PINO radical self-decomposition at the anode, the recycle operation mode of the flow cell provides sufficiently small driving force for the electron transfer step to accommodate the inherently slow chemical reaction step, and thus limit the buildup of PINO radical. Moreover, the recycle allowed the efficient usage of the gaseous molecular oxygen as a green co-oxidant instead of other oxidation reagents.

## **5.2 Experimental methods**

### **5.2.1 Procedure for batch electrolysis**

The RVC electrode (ERG Aerospace Corp) were cut into a semi-cylindrical shape, and soldered on a 316 stainless steel wire for electrical contact. Similarly, the platinum foil (Alfa Aesar) was soldered on the stainless steel wire. (Figure 5.1) With no precautions to exclude air or moisture, a glass tube was charged with a stir bar, 0.4 mmol 2-ethylpyridine, 0.2 equiv. NHPI, 0.2 equiv. pyridine 0.04 mmol tetrabutylammonium perchlorate (TBAP), and 4 mL of 1:1 acetone and acetonitrile (MeCN) mixture. Insert the electrodes into the glass tube and start constant current electrolysis. The electrolysis was stopped when there was a sharp increase in potential. After the reaction, an aliquot of the reaction mixture was washed with 0.1 M Na<sub>2</sub>CO<sub>3</sub> solution, extracted with ethyl acetate, and dried over Na<sub>2</sub>SO<sub>4</sub> before GC analysis.

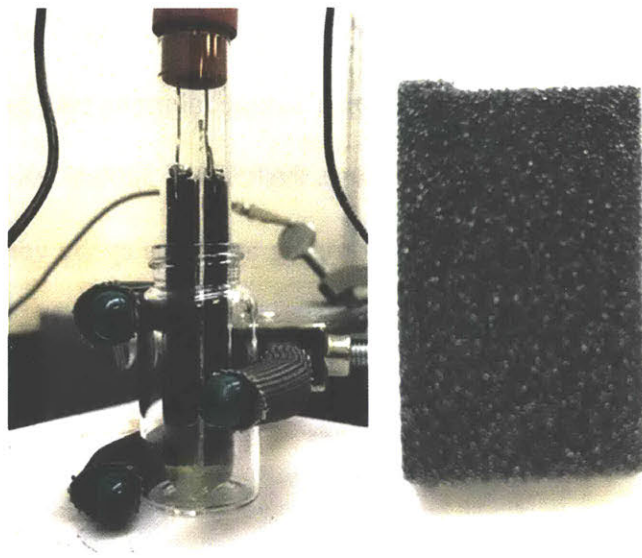


**Figure 5.1. The batch setup and the RVC electrode.**

### 5.2.2 Procedure for operating electrochemical flow cell with recycle

The anolyte and catholyte were prepared as described in Figure 5.8. Peristaltic pumps (Masterflex L/S) with chemically resistant GORE Style 500 tubing were used to recycle both streams at 1 mL/min. Anolyte was saturated with 15 psi oxygen using Teflon AF tube-in-tube device. The electrochemical flow cell temperature was controlled by cartridge heaters and thermocouple. In-line FlowIR recorded the infrared spectrum of anodic stream every 1.5 min. The electrolysis was carried out under constant potential condition. The electrolysis process without continuous feed and withdraw was stopped when current dropped to a negligible value. When there were continuous feed and withdraw, their flowrates were controlled by LabVIEW determined by the electrolysis current and theoretical electron needed.

### 5.2.3 Cyclic voltammetry procedure

Working electrode: glassy carbon or platinum (BASi). Counter electrode: platinum wire (Pine Instrument). Reference electrode: silver wire in the solution of 0.01 M  $\text{AgNO}_3$  and 0.1 M TBAP in MeCN (Pine Instrument). The setup is shown in Figure 5.2. The potential measured vs.

$\text{Ag}/\text{Ag}^+$  was transformed into potential vs.  $\text{Fc}/\text{Fc}^+$  for reproducibility. The glassy carbon working electrode was polished with  $0.03\ \mu\text{m}$  alumina on a Texmet/alumina pad, and rinsed and sonicated with deionized (DI) water (Millipore) prior to use. PARSTAT 3000A-DX potentiostat (Princeton Applied Research) was used to record the voltammograms. The cyclic voltammetry is performed at the scan rate of  $150\ \text{mV/s}$ .



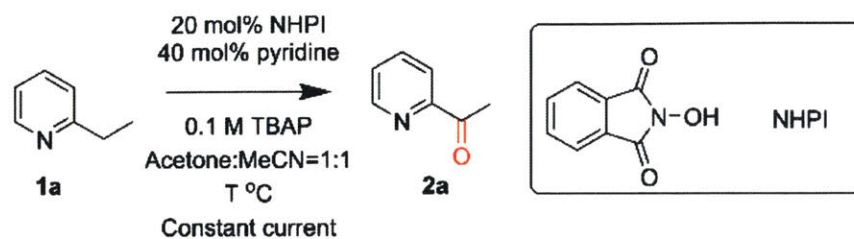
**Figure 5.2.** The cell used for cyclic voltammetry studies.

## 5.3 Results and discussion

### 5.3.1 Batch condition optimization

Investigation of the optimal reaction conditions in batch is shown Table 5.1. Considering the scalability and mass transfer performance for future flow cell designs, RVC was selected as electrode material, which offers large interfacial areas (100 pores per inch) and is cost-effective ( $\$1.50$  per cubic inch). Initial trial only offered 43% yield (Table 5.1, entry 1). The variations of

**Table 5.1. Influence of batch reaction conditions on NHPI-mediated electrochemical aerobic oxidation of benzylic C-H bonds.<sup>a</sup>**



Entry	Anode/Cathode	T (°C)	Current (mA)	Yield <sup>b</sup>	Other conditions
1	RVC/RVC	40	5	43%	
2	RVC/RVC	40	2	41%	
3	RVC/RVC	40	5	35%	1.5 equiv. t-BuOOH
4	RVC/RVC	40	5	44%	Bubble O <sub>2</sub>
5	RVC/RVC	40	5	43%	40% NHPI
6	RVC/RVC	50	5	54%	
7	RVC/RVC	70	5	50%	Pure MeCN as solvent
8	RVC/Pt <sup>c</sup>	50	2	89%	

<sup>a</sup>Reaction conditions: 0.4 mmol of **1a** was electrolyzed under constant current in presence of 0.2 equiv. NHPI and 0.2 equiv. pyridine in 4 mL of 0.1 M solution of tetrabutylammonium perchlorate (TBAP) in 1:1 acetone and acetonitrile (MeCN) mixture.

<sup>b</sup>Yield was determined using gas chromatograph (GC) with dodecane as the internal standard. <sup>c</sup>Platinum foil electrode.

galvanostatic current, co-oxidants (air, t-BuOOH, and 1 atm O<sub>2</sub>), and NHPI loading (Table 5.1, entries 2-5) did not have an impact on the reaction yield. Increasing the temperature from 40 °C to 50 °C led to an improved yield (Table 5.1, entry 6), and further increasing the reaction temperature to 70 °C with pure MeCN as solvent (acetone has a boiling point of 56 °C) did not show further

improvement (Table 5.1, entry 7). On the other hand, changing the cathode to platinum foil gave an excellent yield (Table 5.1, entry 8), which can be rationalized in terms of the cyclic voltammetry (CV) characteristics of the chemical species in the system.

### 5.3.2 Reaction mechanism

Based on the reaction mechanism (Figure 5.3b)<sup>137,177</sup>, deprotonation of NHPI by pyridine, followed by anodic electron transfer, leads to PINO radical, and this reversible conversion has a half-wave redox potential  $E_{1/2} = 0.47$  V (vs. Fc/Fc<sup>+</sup>). PINO radical subsequently mediates selective abstraction of benzylic hydrogen atom to generate a benzyl radical. This radical can be trapped by O<sub>2</sub> to form peroxy radical, which then decomposes to yield the oxygenated carbonyl products.<sup>177,188</sup> The corresponding cathode reaction is supposed to be the reduction of pyridinium cation to evolve gaseous hydrogen and regenerate pyridine. The potential of cathode reaction displays a dependence on the cathode materials, where it is irreversible with a half-peak potential -1.79 V (vs. Fc/Fc<sup>+</sup>) at RVC electrode, and reversible with a half-wave potential -0.92 V (vs. Fc/Fc<sup>+</sup>) at Pt electrode. Interestingly, the reduction potential of pyridinium at the RVC electrode overlaps with the irreversible cathodic decomposition of NHPI, which corresponds to the reduction of the amide group in NHPI<sup>192</sup>. Nevertheless, the cathodic pyridinium reduction on Pt electrode avoids the NHPI decomposition potential range, leading to the significantly improved reaction yield (Table 5.1, entry 6 vs. entry 8).

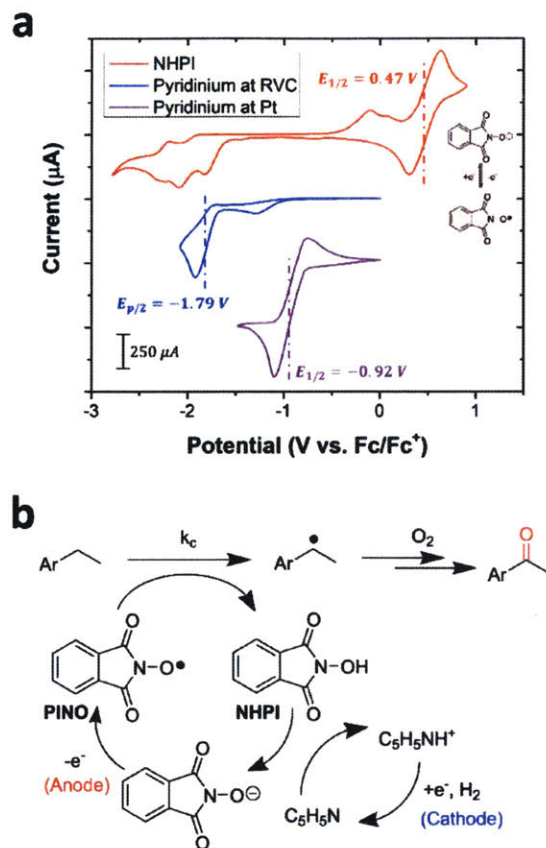


**Figure 5.3. (a) Cyclic voltammograms of 20 mM NHPI (red curve), and 50 mM pyridinium perchlorate at RVC electrode (blue curve) and Pt electrode (purple curve) scanned at 100 mV/s in 0.1 M solution of TBAP in 1:1 acetone and MeCN mixture. (b) Reaction mechanism for NHPI-mediated electrochemical aerobic oxidation of benzylic C-H bonds.**

### 5.3.3 Reaction kinetics

The PINO radical, generated at the anode, is known to undergo a bimolecular self-decomposition with a kinetic constant on the order  $1 \text{ L mol}^{-1} \text{ s}^{-1}$ .<sup>193</sup> The benzylic hydrogen abstraction rate ( $k_c$ ) from the substrate must match with the PINO radical electrochemical generation rate at the anode. Otherwise, if the PINO radical generation rate is faster than its consumption rate, the accumulation of PINO radical will lead to its bimolecular self-decomposition. Thus, insights of the chemical reaction kinetics ( $k_c$ ) will provide in-depth

understanding of how to precisely control the overpotential that governs the generation of the PINO radical.

CV was used to measure the reaction kinetics of the para-substituted ethylbenzenes.<sup>194,195</sup> The catalytic current exhibits a saturation dependence on the concentration of pyridine (Figure 5.4). Hence, the pyridine concentration is chosen in the concentration-independent regime (0.15 M) in order to eliminate the kinetic effect of the NHPI and pyridine reaction on the overall reaction rate.

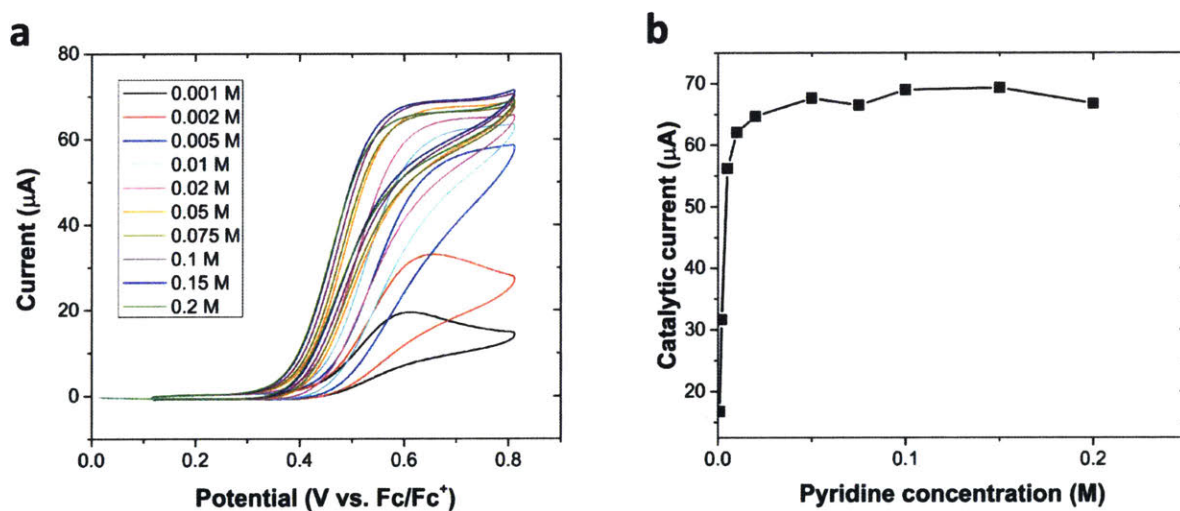


**Figure 5.4. (a) Cyclic voltammograms recorded for various reagent concentrations of pyridine, corresponding to 2 mM NHPI, 0.2 M 4-ethylanisole, and 0.1 M TBAP in MeCN. Scan rate: 150 mV/s. (b) The catalytic current dependence on the pyridine concentration.**

The S-shaped voltammograms (Figure 5.6a) indicate that the electrocatalytic rate is independent on the diffusion of base, substrate or NHPI to the electrode, and catalytic current is limited only by first-order chemical step as shown in the reaction mechanism (Figure 5.3b). The catalytic current can be described as following<sup>195</sup>:

$$i_{cat} = FAC_{NHPI}\sqrt{D_{NHPI}k_c C_R} \quad \text{Equation 5.1}$$

where  $F$  is the Faraday constant,  $A$  is the working electrode area,  $C_{NHPI}$  is the NHPI concentration,  $D_{NHPI}$  is the diffusion coefficient of NHPI, and  $C_R$  is the concentration of reagent with benzylic C-H bond.

In order to know the diffusion coefficient of NHPI,  $D_{NHPI}$  was measured based on Randles-Sevcik equation (Equation 5.2).

$$i_p = 0.446FAC_{NHPI} \sqrt{\frac{F}{RT} v D_{NHPI}} \quad \text{Equation 5.2}$$

where  $v$  is the scan rate,  $R$  is the gas constant, and  $T$  is the temperature. Varying the scan rate can give NHPI diffusion constant of  $6.9 \times 10^{-10} \text{ m}^2/\text{s}$  (Figure 5.5).

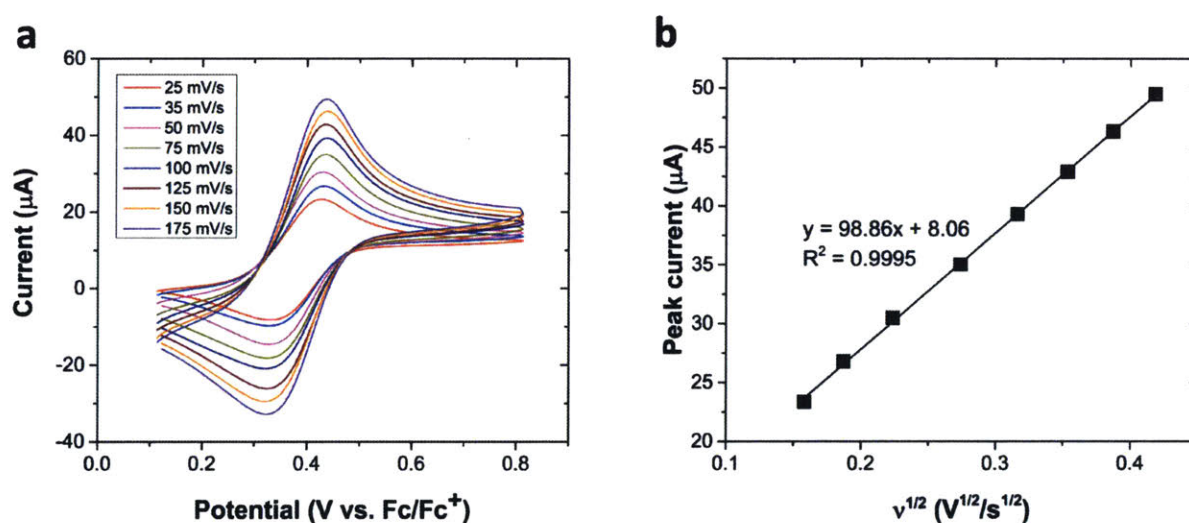


**Figure 5.5.** (a) Cyclic voltammograms of a MeCN solution containing 2 mM NHPI, 0.15 M pyridine, and 0.1 M TBAP at different scan rates. (b) linear dependence of peak currents versus (scan rate)<sup>0.5</sup>.

The cyclic voltammograms of NHPI with 4-ethylanisole **1d** of various concentrations were measured (Figure 5.6a). The catalytic current corresponds to the current plateau after the anodic peak, and is averaged between 0.7 V – 0.8 V to minimize minor effects of side-phenomena (e.g. consumption of the substrate and deactivation of the catalyst)<sup>195</sup>. Increasing the reagent



concentration increases the catalytic current, which is linearly dependent on the half-order of reagent concentration (**1d**), giving the  $k_c$  value of  $9.2 \pm 1.70 \text{ L mol}^{-1} \text{ s}^{-1}$  (Figure 5.6b).

A Hammett study was carried out for five different para-substituted ethylbenzenes by measuring the kinetic constants individually by cyclic voltammetry, providing additional insights into the electronic effects on the reactivity. The Hammett plot (Figure 5.6c) reveals a strong electronic trend with a slope  $\rho$  of -1.09. The benzylic hydrogen abstraction of electron-donating ethylbenzenes will proceed more rapidly with the PINO radical, which may be rationalized as the stabilization of the partially positive charged reaction center on the C-H abstraction transition state.<sup>193,196</sup>

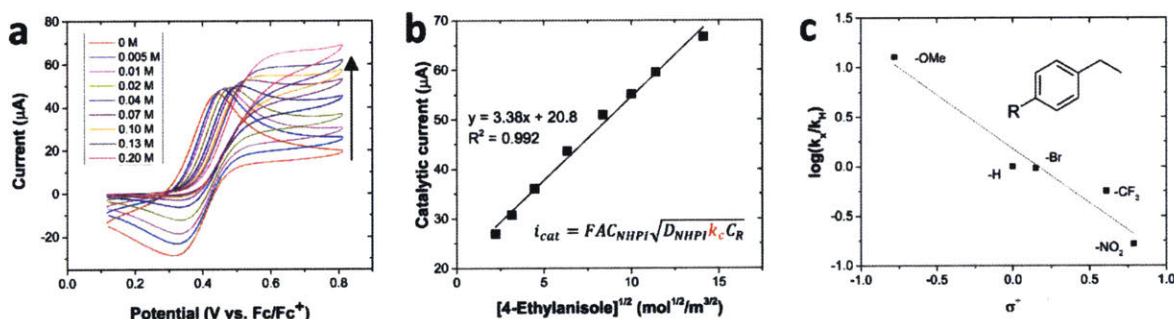


**Figure 5.6. (a) Cyclic voltammograms for various reagent concentrations **1d**, corresponding to 2 mM NHPI, 0.15 M pyridine, and 0.1 M TBAP in MeCN. Scan rate: 150 mV/s. (b) Linear regression of catalytic current versus half-order of reagent concentration. (c) Hammett plots of kinetic constants for para-substituted ethylbenzenes.**

The kinetic study shows the  $k_c$  value is comparable to PINO radical self-decomposition rate constant. Thus, controlling the overpotential applied on the electrodes, which determines the generation rate of PINO radical, is essential to limit the PINO radical to a low concentration avoiding its self-decomposition. However, the slow overall reaction rate associated with the small overpotential applied will result in a prolonged residence time in a continuous flow reactor, implying a large reactor volume, which is unfavorable considering the electrode material cost

associated with large-volume electrochemical flow cell. To realize NHPI aerobic electrochemical oxidation in flow, implementing recycle stream offers the feasibility of controlling the PINO radical concentration at a low level without a large-volume electrochemical flow cell.

#### 5.3.4 Implementation in continuous flow

Two NHPI decomposition mechanisms were identified as discussed above: (1) NHPI irreversible reductive decomposition at the cathode, and (2) PINO radical bimolecular self-decomposition at the anode, competing with benzylic hydrogen abstraction. To facilitate the transformation of NHPI aerobic electrochemical oxidation from batch to flow, an electrochemical flow cell (Figure 5.7a) was engineered and fabricated to incorporate the cation-exchange membrane and operated the reactor in recycle mode (Figure 5.7b) in order to circumvent two NHPI decomposition pathways. The anodic and cathodic chambers are filled with porous RVC electrodes providing uniform flow distribution and enhanced interfacial areas for electron transfer<sup>185</sup>. A Nafion 117 membrane is sandwiched between two RVC electrodes to selectively block the crossover of NHPI anion from anolyte to catholyte. Considering the reaction requires molecular oxygen as the co-oxidant and the oxygen solubility is limited in organic solvent, the anolyte is saturated with oxygen (15 psi) using a Teflon AF tube-in-tube device<sup>147</sup> to supply the required co-oxidant. During the recycle, the pyridinium cation is continuously generated at the anode, is transported across the Nafion membrane driven by the electric field, and gets reduced at the cathode to form gaseous hydrogen and regenerate pyridine. The hydrogen generated at the cathode can be released from the catholyte in catholyte holding tank instead of accumulating in the reactor and occupying the effective electrode surface area. Since the cathodic side only involves the counter electrode reaction, the catholyte will have a stable composition at steady state, allowing

continuous usage throughout the operation. And the process can be transformed into fully continuous mode with continuous feed and withdraw at the anolyte holding tank.

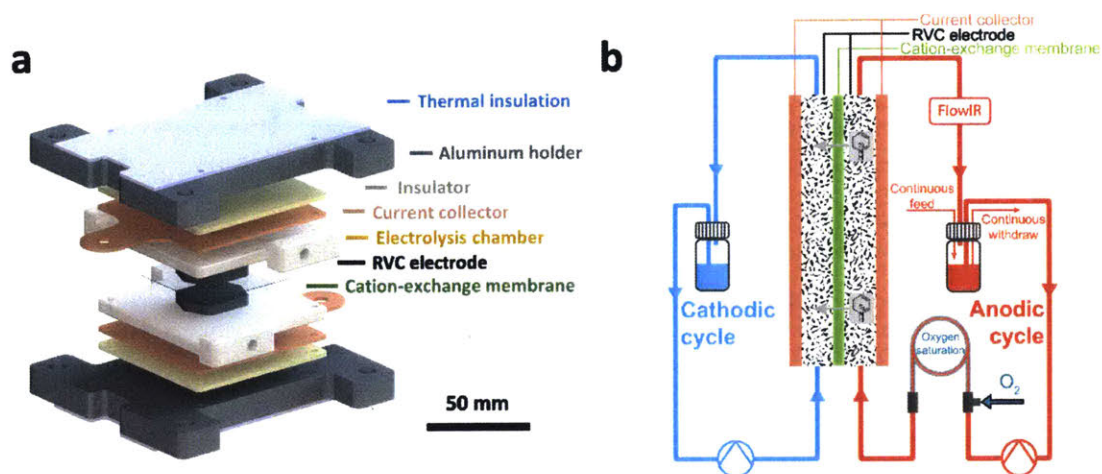


**Figure 5.7.** (a) Exploded-view CAD drawing of the electrochemical flow cell engineered for NHPI-mediated aerobic oxidation of benzylic C-H bonds. From top to bottom, it sequentially contains aluminum holder (with cartridge heaters and thermal insulation layer), polyether ether ketone (PEEK) electrical insulator, copper current collector, polytetrafluoroethylene (PTFE) electrolysis chamber, RVC electrode, and Nafion 117 membrane. The electrochemical flow cell is symmetric to incorporate the divided-wall configuration. (b) Schematics of the operation. Two streams are driven by peristaltic pumps to cycle through the RVC electrodes. Anolyte gets saturated with  $O_2$  in a Teflon AF tube-in-tube device before entering anodic chamber. FlowIR device monitors the species concentration in the anolyte.

The evolution of oxygenated product concentration in the anolyte during the recycle as an overall batch can provide further insights into the behavior of the reaction in the electrochemical flow cell. Thus, an in-line flow infrared spectroscopy apparatus<sup>197</sup> (FlowIR), installed at the outlet of the anodic chamber, continuously monitors 2-acetylpyridine **2a** concentration during the electrochemical oxygenation of 2-ethylpyridine **1a**. Figure 5.8a shows the evolutions of product **2a** concentration and electrolysis current under potentiostatic conditions. The product concentration keeps increasing with a steady current, and after around 8 h, the current sharply decreases to a low value, with the product concentration reaching the maximum value, indicating completion of the

reaction. The product concentration in the anolyte slowly decreases over time afterwards, due to the crossover of product from anolyte to catholyte. GC analysis of two samples from each side collected during the recycle (Figure 5.8b) shows negligible crossover of NHPI from anolyte to catholyte, which validates the function of the cation-exchange membrane. The overall yield was 94% (based on anodic side), significantly higher than the yield (54%, Table 5.1, entry 6) in batch with the same electrode material.

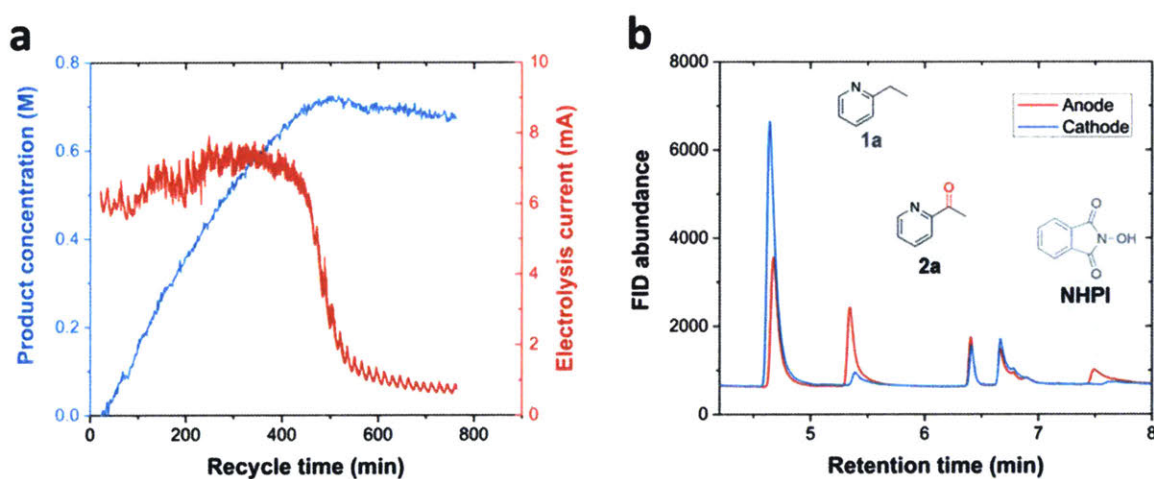


**Figure 5.8.** (a) FlowIR monitoring of product concentration in the anolyte during the recycle, and the corresponding electrolysis current. (b) Gas chromatograph analysis of two samples from each side during the electrolysis. Anolyte recycles at 1 ml/min: 0.1 M 1a, 0.02 M NHPI, 0.04 M pyridine, 0.1 M TBAP, 0.05 M pyridinium perchlorate, and 4 mM dodecane as internal standard in 16 mL of 1:1 acetone and MeCN. Catholyte recycles at 1 ml/min: 0.1 M 1a, 0.04 M pyridine, 0.1 M TBAP, 0.1 M pyridinium perchlorate, and 4 mM dodecane as internal standard in 8 mL of 1:1 acetone and MeCN. Reaction temperature: 50 °C.

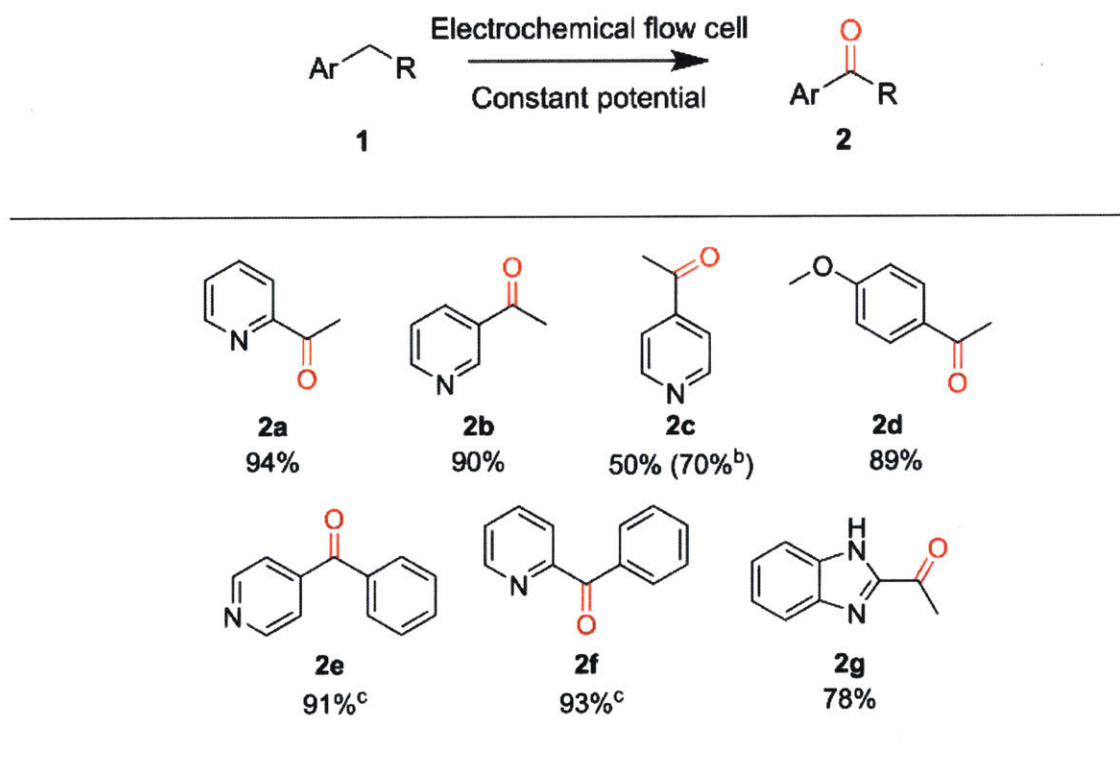
To demonstrate the capability of producing the oxygenated compounds continuously, the standard condition was implemented with 1a, and added the continuous feed and withdraw streams as shown in Figure 5.7b. The flowrates of continuous feed and withdraw are identical, determined by the current and theoretical electrons needed (2 F/mol):

$$\text{Flowrate} = i/(2FC_R)$$

Equation 5.3

where the  $i$  is the electrolysis current and  $C_R$  is the concentration of **1a** in the feed stream. The crossover of product from anolyte to catholyte is not a concern since the product concentration in catholyte will be the same as anolyte during steady state. The system is able to give 0.35 g of **2a** in 74% yield continuously for 24 h. The reduction in yield is primarily attributed to the reduction in reagent concentration compensation from the catholyte during the steady state as compared to the case without continuous feed and withdraw.

**Table 5.2. Substrate scope of NHPI-mediated electrochemical aerobic oxidation of benzylic C-H bonds in the electrochemical flow cell with recycle<sup>a</sup>**



<sup>a</sup>Standard conditions are the same as described in Figure 5.8. The optimized reaction potentials are available in Supporting Information. Yield (based on the anodic side) was determined using GC with dodecane as the internal standard. <sup>b</sup>Spike 0.2 equiv. more NHPI after current significantly reduces. <sup>c</sup>0.6 equiv. NHPI.

The electrochemical flow cell was examined for oxygenation of various substrates, giving good-to-excellent yields (Table 5.2, **1a-1g**). 2- and 3- substituted ethylpyridines (**1a** and **1b**) give similar yields, while 4-ethylpyridine **1c** is comparatively ineffective with standard conditions, and requires adding more NHPI during the recycle to obtain higher yield. The difference of yields for various substituted ethylpyridines are consistent with results from chemical oxidation methods<sup>137</sup>. Benzylpyridines **1e** and **1f** requires 0.6 equiv. NHPI in order to reach good yields. Substituted ethylbenzene **1d** and benzimidazole **1g** have good yields with the standard conditions.

## 5.4 Conclusion

This chapter demonstrates an electrochemical flow system for NHPI-mediated electrochemical aerobic oxidation of benzylic C-H bonds. The use of a cation-exchange membrane avoided the reductive decomposition NHPI at the cathode, which in turn allowed the usage of the RVC as the electrodes instead of Pt to achieve a high yield. The use of porous RVC significantly reduced the cost of the electrochemical flow cell and increased the interfacial areas to enhance mass transfer, enabling process for further scaling-up. Operating the electrochemical flow cell with recycle avoided the PINO radical self-decomposition, and enabled use of green molecular oxygen as the co-oxidant. The electrochemical analysis of the NHPI-mediated electrochemical oxidation in this work offers a strategy to identify the essential mediator decomposition mechanisms rationalizing reaction conditions, and the flow system design provides insights enabling electroorganic synthesis with inherently slow reaction kinetics and gaseous reagents in flow.

# Chapter 6 Microfluidics-enabled redox-neutral electrochemistry

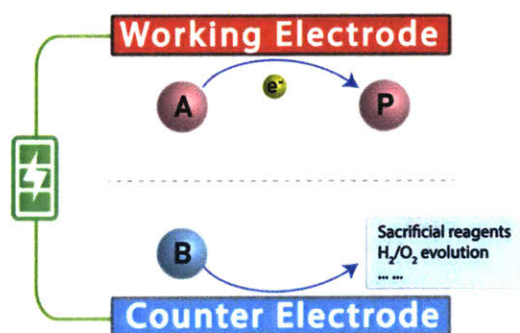
## 6.1 Introduction

Electroorganic synthesis is a fast-growing synthetic methodology for organic chemists to explore environmentally benign, cost-effective, efficient and unprecedented transformations.<sup>198</sup> The majority of electro-synthetic methods reported primarily relies on reactions on a single electrode, anode or cathode; as such, the nature of the electrochemical transformations is either oxidative or reductive. (Figure 6.1) To maintain electron neutrality of the overall electrochemical system, a compatible counter electrode reaction, often sacrificial, is necessary, such as the sacrificial magnesium or aluminum anode during electrocarboxylation<sup>199,200</sup> or Birch electroreduction<sup>201</sup>, and hydrogen evolution for various electrooxidative cross-coupling reactions<sup>202</sup>. However, identifying a suitable counter reaction is often challenging, and sometimes a complicated setup (i.e. divided electrochemical cell) is required due to chemical or electrochemical incompatibility. In contrast, coupled electrode reaction system, where both electrodes are utilized to generate desired products, is attractive for its improved energy efficiency and reduced waste.<sup>203</sup> However, only limited coupled electrode reaction systems have been reported to date because of challenges in chemistry mechanism and engineering system design.

Single-electron transfer (SET) visible-light photoredox chemistry, a redox-neutral system, has been extensively explored and developed in the last decade, appearing to be mechanistically similar to the coupled electrode system.<sup>204</sup> It is questioned whether this mechanistic similarity of

redox-neutral photochemistry can shine a light on the development of coupled electrode system, while at the same time, the attractive features of electrochemistry, such as photocatalyst-free, low-cost, green, and easily scalable, can be embraced to foster the practical implementation of these redox-neutral reactions. Thus, this chapter presents an electrochemical methodology that can synergistically employ both anode and cathode to generate various reactive species for redox-neutral cross-coupling reactions.

**a) Electrochemistry on single electrode**



**b) Redox-neutral photochemistry inspired electrochemistry design strategy**

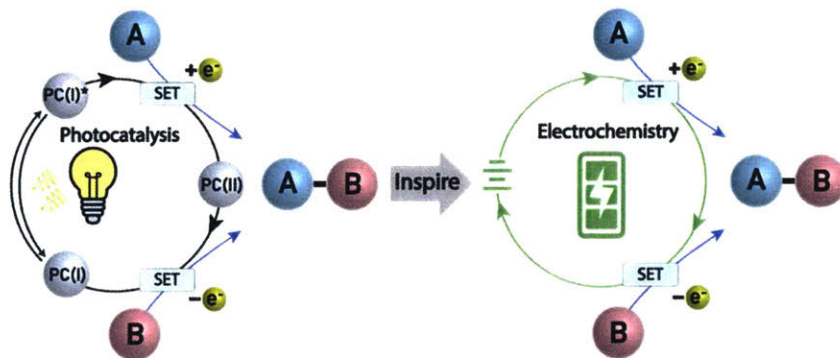


**Figure 6.1. (a) Conventional electrochemistry setup. (b) Photochemistry inspired redox-neutral electrochemistry design.**



## 6.2 Experimental methods

### 6.2.1 Electrochemical flow cell design

The microfluidic redox-neutral electrochemical (MRN-Echem) flow cell is composed of two parallel glassy carbon electrodes separated by an extremely thin fluorinated ethylene propylene (FEP) film with a known thickness. (Figure 6.2) Glassy carbon electrodes (50 mm \* 50 mm \* 3 mm) were purchased from Alfa Aesar (P.N. 42820-FI) without further treatment. Fluorinated ethylene propylene (FEP) films with various thickness (0.0005 inch – 0.005 inch) for spacers were obtained from CS Hyde Company. PTFE and PFA films were also tested for flow cell sealability. However, FEP film proved to be the best for sealing the thin gap between glassy carbon electrodes (no leakage tested up to 40 psig of nitrogen gas).

All the individual components of the electrochemical reactor were machined using Proto Labs' CNC milling service (Proto Labs, Inc.). A laser machine (A-series Laser Micromachining System, Oxford Lasers) created holes on glassy carbon plate for reagent inlet and outlet. The exploded view of the electrochemical flow cell is shown in Figure 6.2.

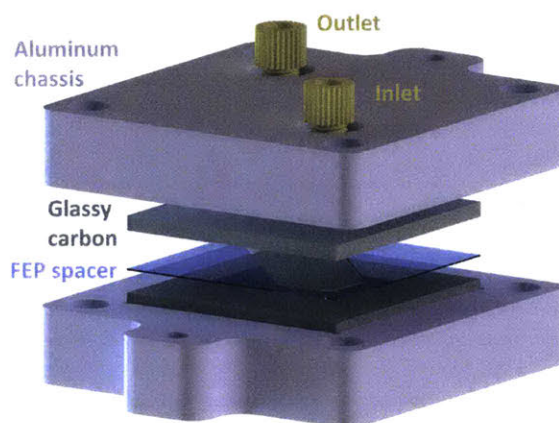


**Figure 6.2. Exploded-view CAD drawing of the electrochemical flow cell engineered for MRN-Echem.**

## 6.2.2 Setup for reaction condition optimization

Due to the vast parameter space of electrosynthesis (potential, electrode polarity switching frequency, temperature, and flowrate), a high-throughput optimization technique was developed to quickly identify the optimal condition for a specific substrate with minimal reagent consumption. As shown in Figure 6.3, an in-line High Performance Liquid Chromatography (HPLC, Agilent 1260 Infinity II LC System) is directly attached at the outlet of the MRN-Echem flow cell to analyze a 2  $\mu\text{l}$  sample of the outlet reagent mixture. It only requires  $\sim 20$  min and  $\sim 100$   $\mu\text{l}$  of reagent to examine the reaction outcome under one reaction condition. A LabVIEW computer program automates all the equipment, including syringe pump, temperature controller, potentiostat, and HPLC analysis, which allows users to accomplish condition optimization remotely without physically being in the lab.

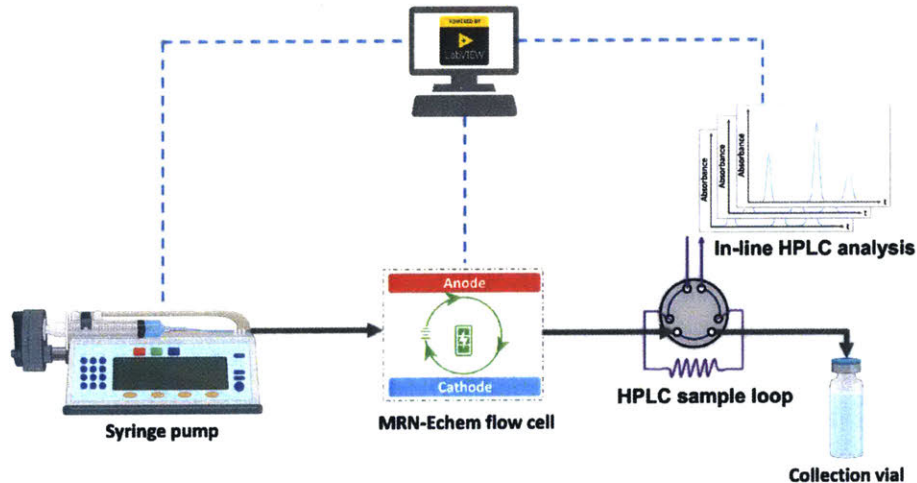


**Figure 6.3. Scheme of the electrosynthesis condition optimization setup.**

## 6.2.3 Cyclic voltammetry study

Cyclic voltammetry study was carried out to understand the required the oxidation/reduction potentials for various radical precursors thermodynamics. The cyclic

voltammetry study was carried in a three-electrode cell (BASi Inc.). The working electrode was glassy carbon. Reference electrode was pure silver wire with 0.01 M AgNO<sub>3</sub> and 0.1 M Bu<sub>4</sub>NBF<sub>4</sub> in acetonitrile. The counter electrode was platinum wire. The solution was well stirred and degassed with nitrogen before running cyclic voltammetry with 150 mV/s scan rate. The potential reported was converted to ferrocene/ferrocenium for reproducibility.

## 6.3 Results and discussion

### 6.3.1 Electrochemical redox-neutral radical-radical cross-coupling concept

Utilizing reactive radical species generated at different electrodes for cross-coupling reactions in a conventional electrochemical reactor (electrode distance typically is on the order of millimeter - centimeter), is hindered by the decomposition rate of radicals often outpacing the mixing rate of two radicals, yielding nonselective side products. Here, it is proposed that combining persistent radical effect<sup>205</sup> and short inter-electrode distance in microfluidic devices<sup>206</sup> could enable selective cross-coupling reactions via precise control of radical lifetime in a microfluidic electrochemical flow cell. As depicted in Figure 6.4, a persistent radical precursor (P) undergoes a reductive SET process giving a persistent radical (P•). Within the lifetime of P•, transporting it to the surface of anode to trap an oxidatively generated transient radical (T•) giving the desired cross-coupling product P-T. To effectively suppress the decomposition of P• and T• requires rapid transport rate of P• from cathode to anode, and microfluidics offers the opportunity to accelerate transport process achieving an instantaneous mixing of P• and T• through engineering a  $\mu$ -meter electrode distance electrochemical flow cell. The inter-electrode radical transport in a parallel flow channel is primarily controlled by molecular diffusion, the characteristic time of which can be estimated by  $t=d^2/D$ . (d is inter-electrode distance, and D is molecular diffusivity)<sup>207</sup>

If it is significantly shorter than the lifetime of persistent radical, it is supposed to expect an efficient suppression of side reactions caused by radical decomposition and enable MRN-Echem.

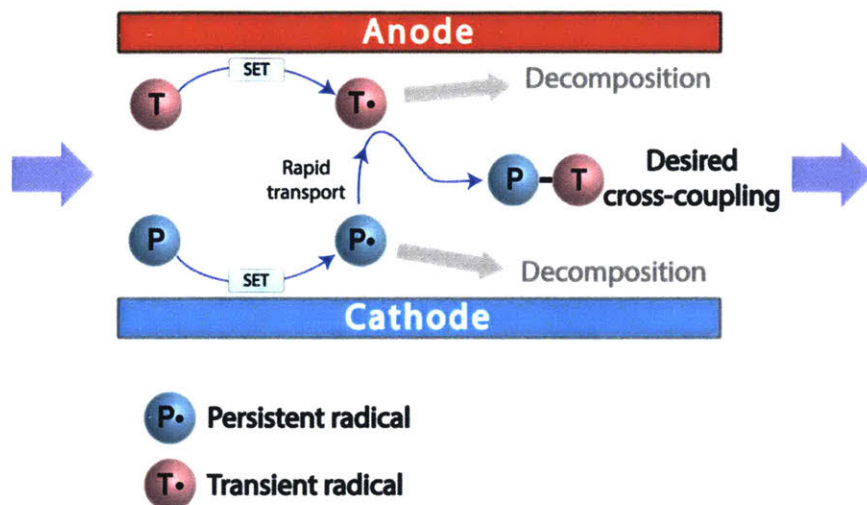


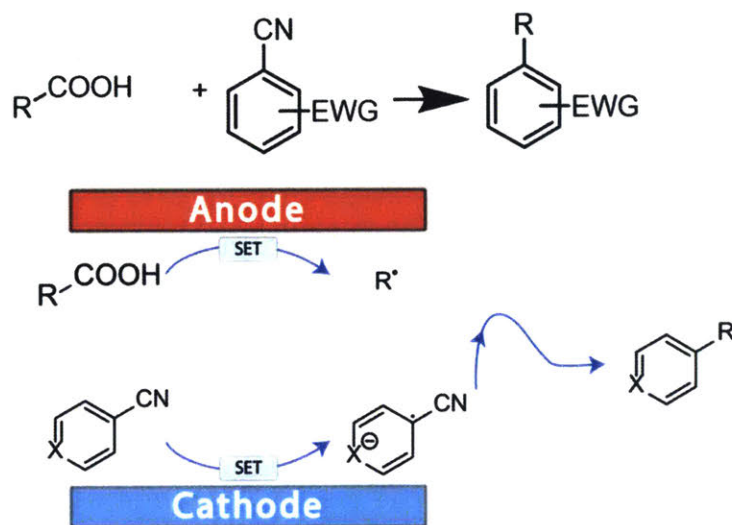
**Figure 6.4. Microfluidic electrochemical redox-neutral radical-radical cross-coupling concept.**

### 6.3.2 Decarboxylative aryl nitrile coupling

Kolbe dimerization, the oldest synthetic organic electrochemical reaction discovered in 1847, is an anodic decarboxylative radical generation and combination process to convert alkyl carboxylic acids to their dimers.<sup>208</sup> Despite extensive exploration of this electrochemical radical chemistry beyond dimerization, such as cross-coupling of two carboxylic acids<sup>209</sup> and decarboxylative radical addition<sup>210</sup>, its implementation is still limited because of the challenge of designing a selective cross-coupling pathway on a single electrode that involves generation of multiple reactive species with similar oxidation potentials. However, MRN-Echem offers the capability to isolate the generation of coupling partner, a persistent radical obtained from cathode, from anodic decarboxylation process.

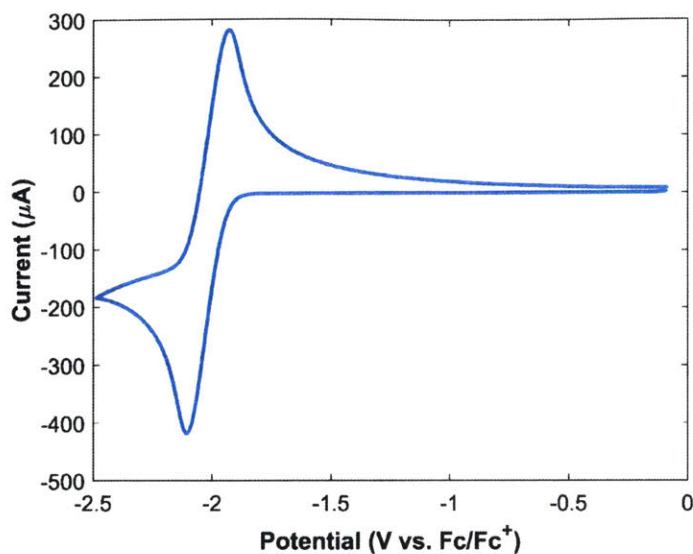
Here, the electron-deficient aryl nitrile compound was selected as the persistent radical precursor to cross couple with transient alkyl radical generated by anodic decarboxylation.<sup>211</sup>

(Figure 6.5)

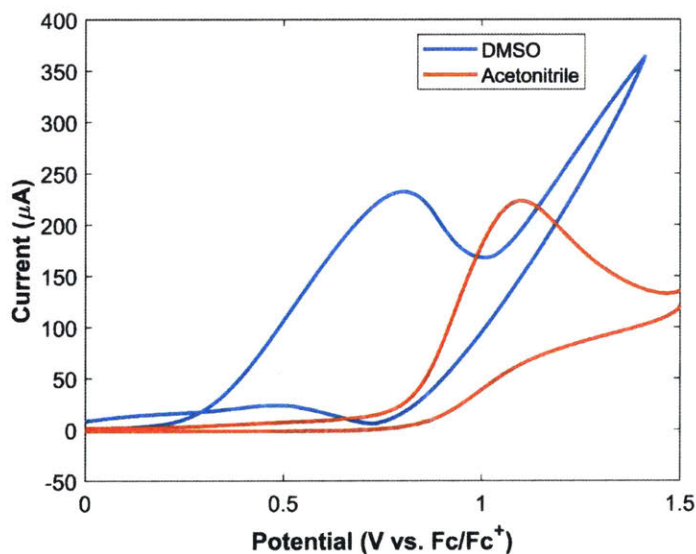


**Figure 6.5. Electrochemical decarboxylative coupling**

1,4-Dicyanobenzene (DCB), a representative electron-deficient aryl nitrile, can undergo a SET event on cathode to form a persistent radical anion (DCB<sup>•-</sup>) under  $E_{1/2} = -2.01$  V vs. Fc/Fc<sup>+</sup> on glassy carbon (GC) electrode in acetonitrile (MeCN). (Figure 6.6) Deprotonation of alkyl carboxylic acid with Brønsted base gives alkyl carboxylate, which can undergo SET oxidation with subsequent instantaneous loss of CO<sub>2</sub> to yield a transient alkyl radical at  $E_{p/2} = +0.93$  V vs. Fc/Fc<sup>+</sup> on GC electrode in MeCN. (Figure 6.7) Solvent choice will have an impact on the overpotential of the decarboxylation process. Such a broad electrochemical window would typically require extensive screening and tuning of photocatalysts to achieve thermodynamically favorable conversion<sup>212</sup>, while electrochemistry can easily initiate the redox reactions by setting a proper potential.



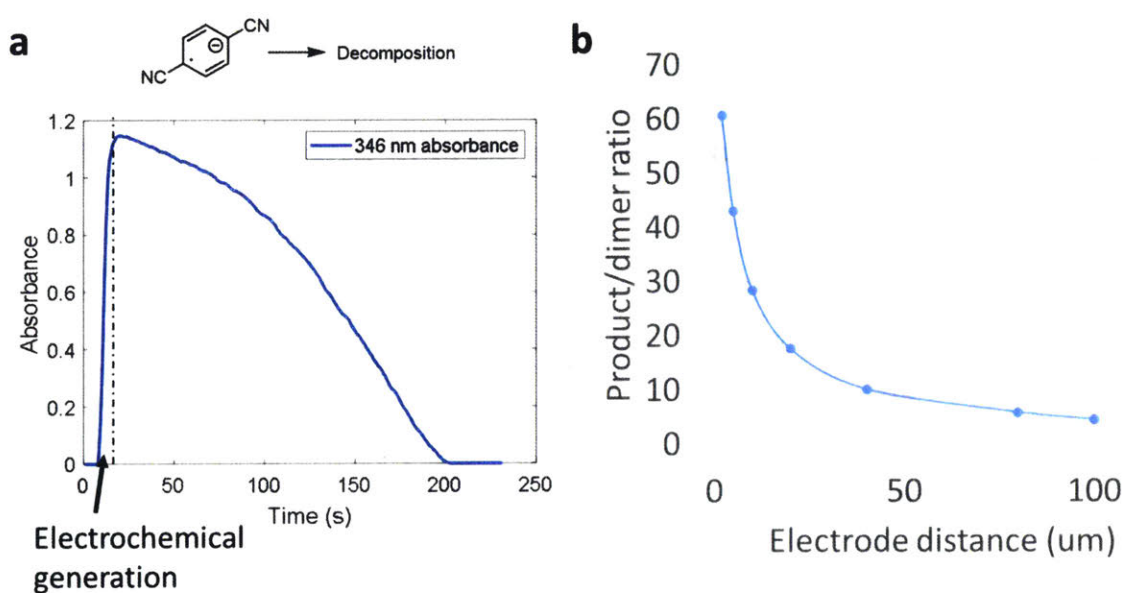
**Figure 6.6.** Cyclic voltammogram recorded for 0.02 M 1,4-dicyanobenzene in 0.1 M  $\text{Bu}_4\text{NBF}_4$  MeCN solution.



**Figure 6.7.** Cyclic voltammogram recorded for 0.02 M butyric acid tetrabutylammonium salt in 0.1 M  $\text{Bu}_4\text{NBF}_4$  in DMSO (blue line) and MeCN (red line).

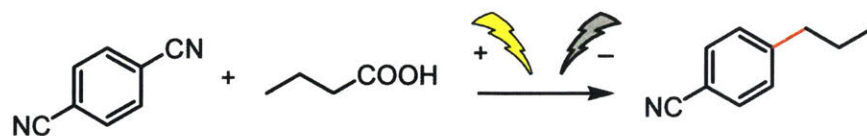
Next, a MRN-Echem flow cell should offer a rapid diffusion transport of  $\text{DCB}^{\cdot-}$  from cathode to anode to selectively form cross-coupling product with alkyl radical. UV-Vis spectroelectrochemical measurement of  $\text{DCB}^{\cdot-}$  yielded a half-life of  $\sim 100$  s in MeCN (Figure 6.8a). Based on this decomposition and diffusion-controlled reaction of radical chemistry<sup>205</sup>, simulations

validate the hypothesis that a shorter inter-electrode distance can significantly improve the selectivity of the desired cross-coupling product. (Figure 6.8b) Thus, a MRN-Echem flow cell was engineered correspondingly, composed of two parallel glassy carbon electrodes separated by an extremely thin fluorinated ethylene propylene (FEP) film with a known thickness. By decreasing the distance between two glassy carbon electrodes, indeed, a more selective cross-coupling reaction is obtained due to the suppression of radical decompositions.



**Figure 6.8. (a) UV-Vis spectroelectrochemical measurement of DCB•<sup>-</sup> lifetime. (b) Kinetic simulation for radical-radical simulation.**

A series of electrochemical reaction condition optimization experiments were performed to identify a suitable condition for efficient decarboxylative aryl nitrile cross-coupling. Experiments in Table 6.1 were conducted in small-scale electrochemical flow cell with 0.001” FEP as the spacer. After some reaction condition optimization, a reasonable yield was achieved.

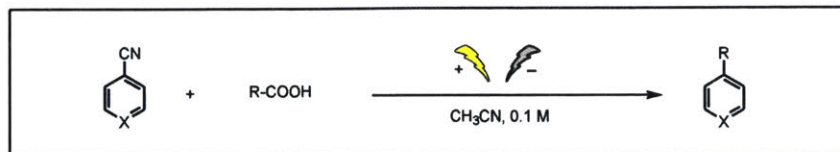
**Table 6.1. Electrochemical reaction condition optimization**

No.	Base <sup>1</sup>	Acid/ DCB ratio	Solvent	Supporting electrolyte	Potential (V)	T (°C)	t (min)	Polarity switch time <sup>2</sup> (s)	Yield <sup>3</sup>
1	/	3	DMSO	Bu <sub>4</sub> NBF <sub>4</sub>	2.9	20	4	20	N.R.
2	CsF	3	DMSO	Bu <sub>4</sub> NBF <sub>4</sub>	2.9	20	4	20	35%
3	CsF	3	DMSO	Bu <sub>4</sub> NBF <sub>4</sub>	2.9	20	12	20	44%
4	CsF	3	DMSO	/	2.9	20	12	20	43%
5	CsF	3	DMSO	/	2.9	20	12	1	15%
6	CsF	3	DMSO	/	2.9	20	12	60	48%
7	CsF	3	HFIP <sup>4</sup>	/	2.9	20	12	20	N.R.
8	Bu <sub>4</sub> NOH	3	DMSO	/	2.9	20	12	60	48%
9	Bu <sub>4</sub> NOH	3	DMSO	/	2.9	50	4	60	53%
10	Bu <sub>4</sub> NOH	3	DMF	/	2.9	50	4	60	52%
11	Bu <sub>4</sub> NOH	3	MeCN	/	3.3	50	4	60	56%
12	Bu <sub>4</sub> NOH	6	MeCN	/	3.3	50	4	60	64%

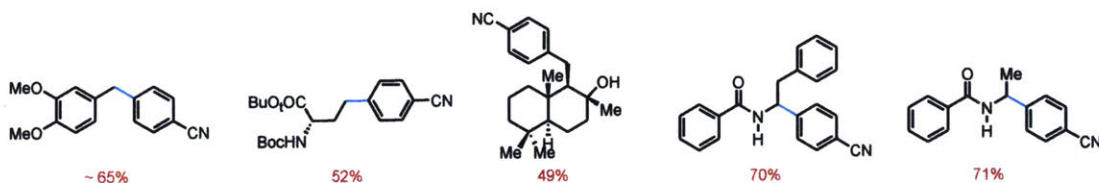
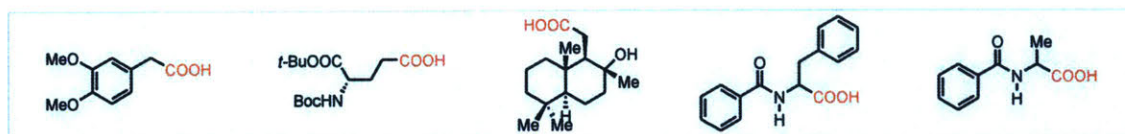
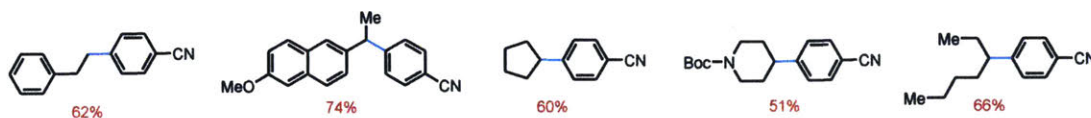
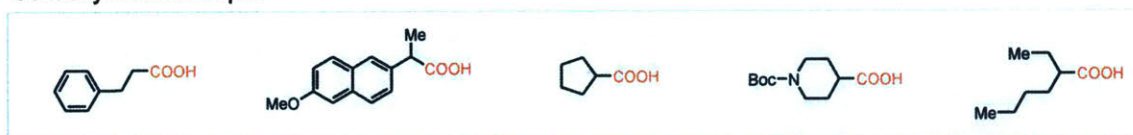
<sup>1</sup>Base was added as the same equivalence as the butyric acid. <sup>2</sup>Switching the electrode polarity after certain time. <sup>3</sup>0.05 mmol of DCB was continuously collected for yield analysis. Yield was determined by <sup>1</sup>H-NMR with mesitylene as the internal standard. <sup>4</sup>HFIP: hexafluoroisopropanol.

Switching the polarity of electrode is a means to avoid fouling of the electrode surface, since constantly using single electrode for oxidation or reduction will result in a gradual passivation of the electrode. Carboxylic acid is not redox active in its acid form, requiring neutralization to form carboxylate for facile oxidation at the anode. (Table 6.1, entry 1 vs. entry 2) A supporting electrolyte is not necessary with the MRN-Echem flow cell design because extremely small inter-electrode distance offers minimal electrolyte resistance. (Table 6.1, entry 3 vs. entry 4) Despite HFIP is a solvent known for its capability of stabilizing radicals<sup>213</sup>, the DCB radical anion is not a persistent radical in HFIP solvent (Table 6.1, entry 7). Cesium fluoride (CsF) is soluble up

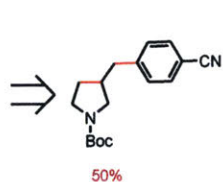
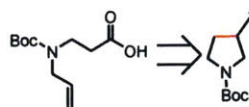




Carboxylic acid scope:



Cascade reaction:



Aryl nitrile scope:

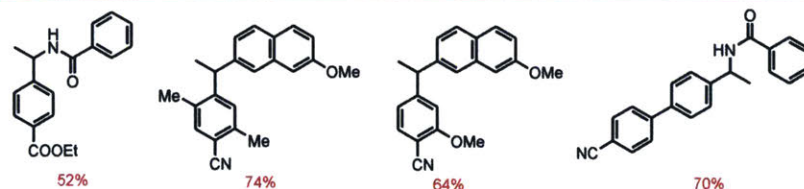
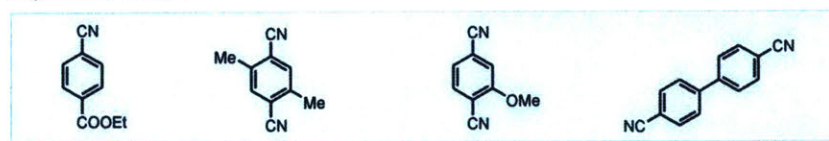


Figure 6.9. Decarboxylative radical-radical cross-coupling reactions

to 0.15 M in DMSO. However, some small precipitates were observed on the glassy carbon electrode after disassembling the flow cell. (The precipitates were presumably cesium cyanide, where the cyanide anion came from the aryl nitrile.) Switching the base from CsF to Bu<sub>4</sub>NOH greatly improved the reagent concentration. Switching the solvent from DMSO/DMF to

acetonitrile (MeCN) resulted in a cleaner reaction because the oxidation potential of DMSO/DMF is close to that of carboxylate, while acetonitrile has much broader electrochemical window.<sup>214</sup>

Having identified the optimal microfluidic electrochemical flow cell design and reaction conditions for cross-coupling of DCB and butyric acid, various carboxylic acids and various aryl nitriles were demonstrated to have good-to-excellent yields with this MRN-Echem design diagram. (Figure 6.9)

### 6.3.3 Cross-coupling of $\alpha$ -aminoalkyl radical and aryl nitrile

Based on the successful demonstration of MRN-Echem with decarboxylative arylation reactions, we hypothesized that other transient and persistent radical precursors would enjoy similar applicability under this chemistry design paradigm. Functionalization at  $\alpha$ -position of amine is an important transformation.<sup>215</sup> Tertiary amine can undergo anodic oxidation at  $E_{p/2} = 0.5$  V vs. Fc/Fc<sup>+</sup> to generate a radical cation. (Figure 6.10). The C–H bond adjacent to the nitrogen atom in amine radical cation is weakened by about 40 kcal/mol and so could undergo deprotonation

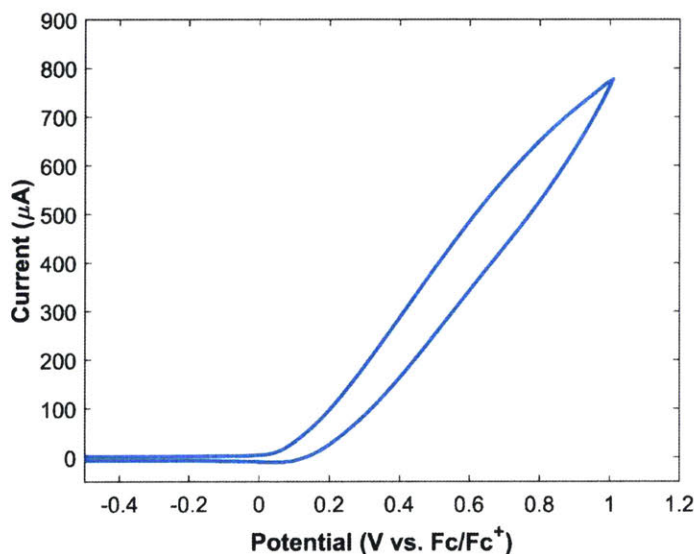


**Figure 6.10. Cyclic voltammogram recorded for 0.02 M N,N-dimethylaniline in 0.1 M Bu<sub>4</sub>NBF<sub>4</sub> DMSO solution**

by weak base to give  $\alpha$ -amino radical<sup>216</sup>, which can subsequently react with a persistent radical generated from the cathodic reduction (Figure 6.11). This MRN-Echem mechanism was demonstrated with cross-coupling of DCB and N,N-dimethylaniline with the yield of 69%.

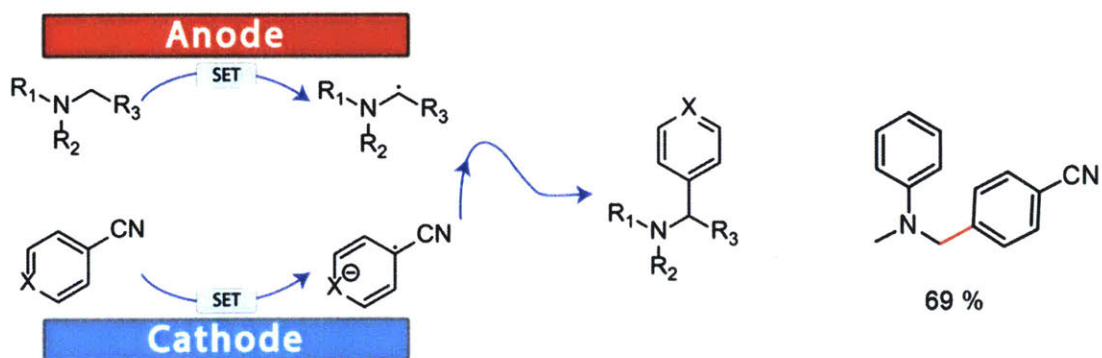


**Figure 6.11. Cross-coupling of  $\alpha$ -aminoalkyl radical and aryl nitrile.**

#### 6.3.4 Cross-coupling of organoboron and aryl nitrile

Organotrifluoroborates are also promising transient radical precursors, as previous reports have documented their ability to function as carbon radical sources upon SET oxidation.<sup>217</sup> With GC electrode, benzyl trifluoroborate can undergo anodic oxidation at  $E_{p/2} = +0.55$  V vs. Fc/Fc<sup>+</sup> to fragment boron trifluoride generating a benzyl radical. This benzyl radical can be subsequently trapped by the persistent radical generated from cathode to yield the cross-coupling product with 70% yield. (Figure 6.13)

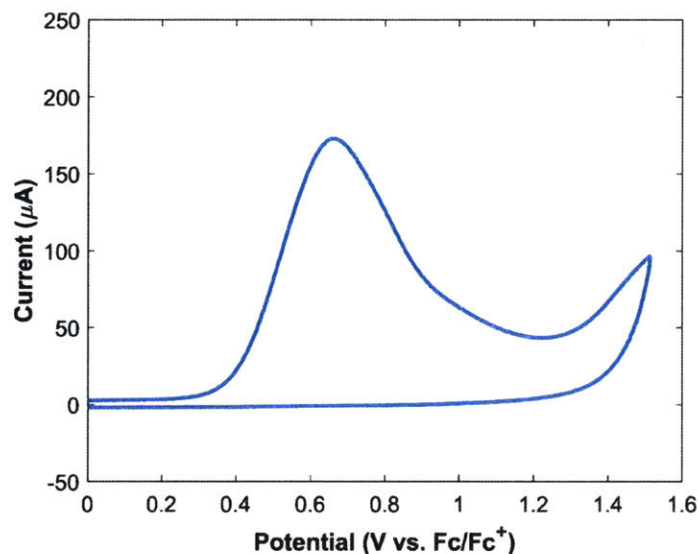


Figure 6.12 Cyclic voltammogram recorded for 0.02 M benzyl trifluoroborate tetrabutylammonium salt in 0.1 M  $\text{Bu}_4\text{NBF}_4$  in MeCN.

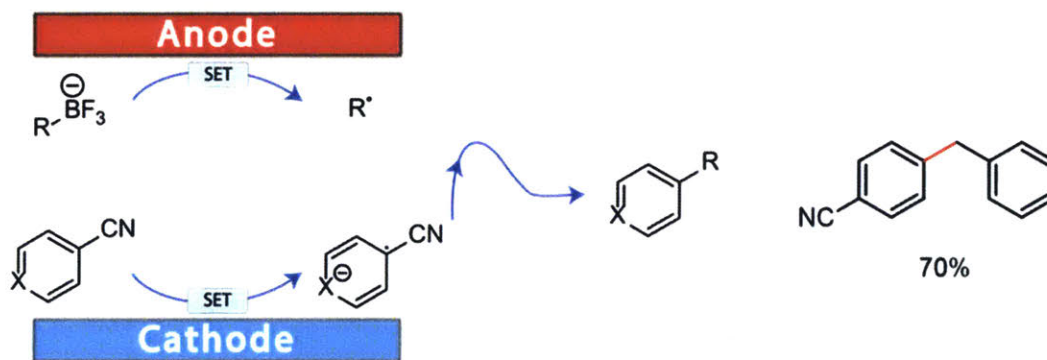


Figure 6.13. Cross-coupling of organoboron and aryl nitrile.

### 6.3.5 Cross-coupling of $\alpha$ -aminoalkyl radical and aryl ketone

Electron-deficient aryl nitriles are not the only persistent radicals that can work under MRN-Echem design. Diaryl ketone is also a viable persistent radical precursor. As shown in Figure 6.14, benzophenone can be reversibly reduced at  $E_{1/2} = -2.15$  V vs.  $\text{Fc}/\text{Fc}^+$ . This persistent radical anion generated from benzophenone can diffuse to anode and be trapped by a transient  $\alpha$ -aminoalkyl radical with the yield of 30%. (Figure 6.15)

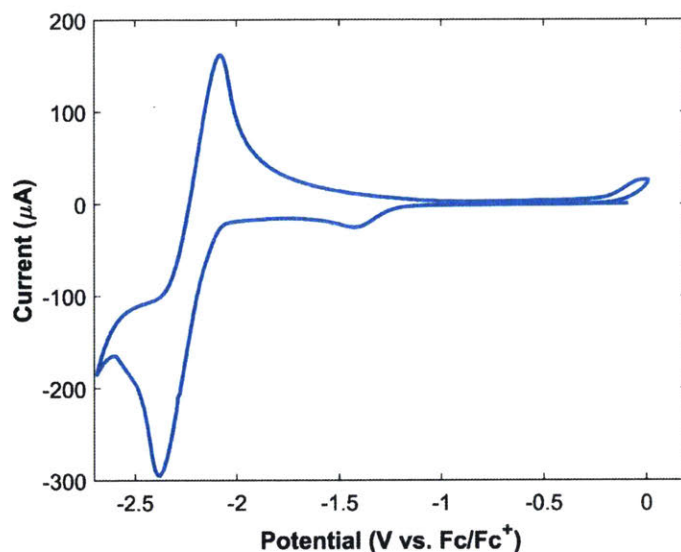


Figure 6.14. Cyclic voltammogram recorded for 0.02 M benzophenone in 0.1 M  $\text{Bu}_4\text{NBF}_4$  in MeCN.

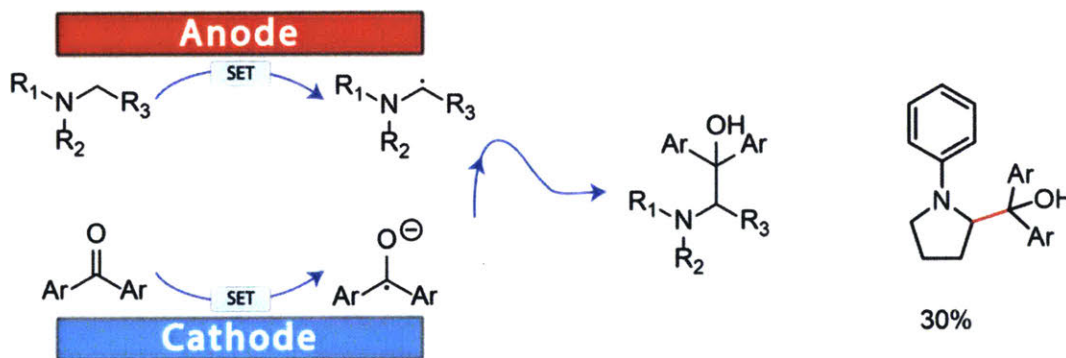
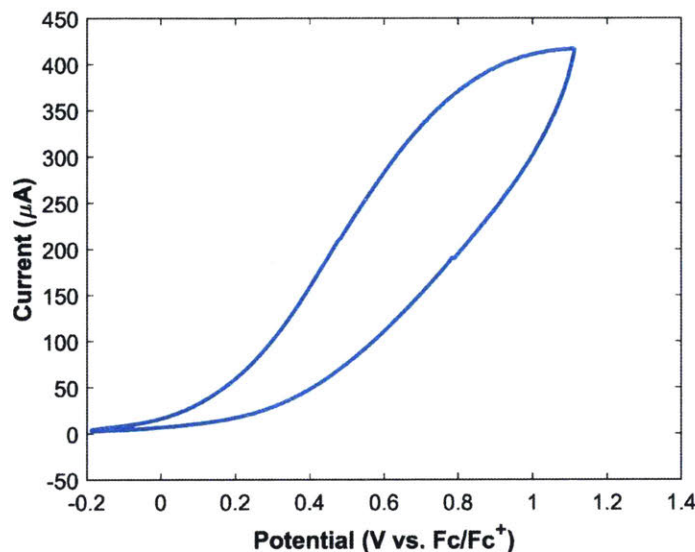


Figure 6.15. Cross-coupling of  $\alpha$ -aminoalkyl radical and aryl ketone

### 6.3.6 Organocatalyzed allylic C-H arylation

The MRN-Echem design can also be coupled organocatalysts to generate the required transient radicals. A thiol radical (triisopropylsilanethiol radical) can be generated by anodic oxidation at  $E_{p/2} = +0.4$  V vs.  $\text{Fc}/\text{Fc}^+$  (Figure 6.16), which then abstracts a hydrogen from a weak C-H bond of a molecule in the reaction system to form a radical. Here,  $\alpha$ -pinene has an allylic C-H bond that has a bond dissociation energy (BDE) of around 83 kcal/mol. This weak allylic C-H can be thermodynamically fragmented by thiol radical to give allylic radical, which can be trapped

the persistent radical diffused from cathode to generate the desired cross-coupling product. (Figure 6.17)



**Figure 6.16.** Cyclic voltammogram recorded for 0.01 M triisopropylsilanethiol and 0.01 M DBU in 0.1 M  $\text{Bu}_4\text{NBF}_4$  in acetone.

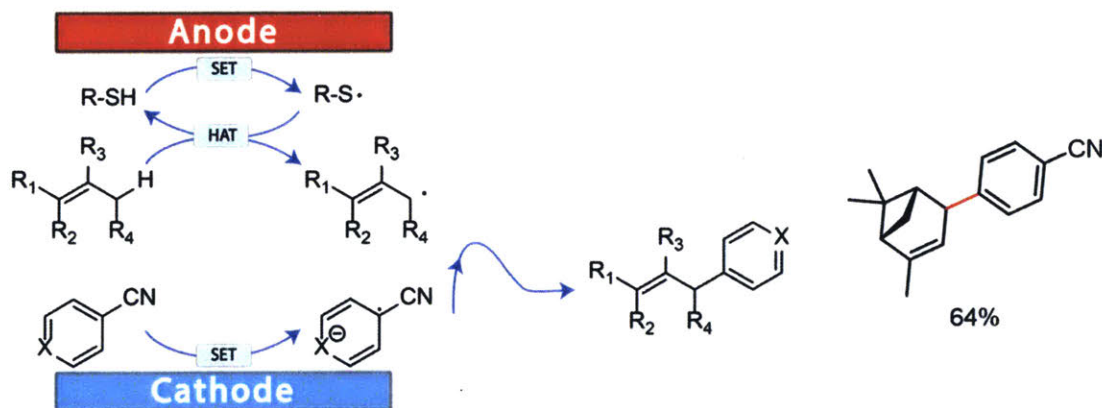


**Figure 6.17.** Organocatalyzed allylic C-H arylation

### 6.3.7 A fully electrochemical synthesis of liquid crystal material

Compared to redox-neutral visible-light photochemistry, the catalyst-free and low-cost characteristics of MRN-Echem makes it more economically applicable to synthesizing medium-value chemicals in addition to high-value fine chemicals (e.g. pharmaceuticals). 4-Cyano-4'-

pentylbiphenyl (5CB), a commonly used nematic liquid crystal material, is currently produced from biphenyl in a linear synthesis, which suffers from low yields and low efficiency.<sup>218</sup> Following current vision of electrifying chemical synthesis from renewable energy<sup>219</sup>, a fully electrochemical two-step synthesis was proposed utilizing sunlight as the renewable energy source to upgrade readily available 4-chlorobenzonitrile (4-CIBN) (<\$1/g) to 5CB (~\$100/g) with inexpensive reagents (Figure 6.18). The two-step electrochemical synthesis was powered by a 50 W solar panel on the roof, with a solar-charged battery allowing reactions to continue when cloudy or at night.

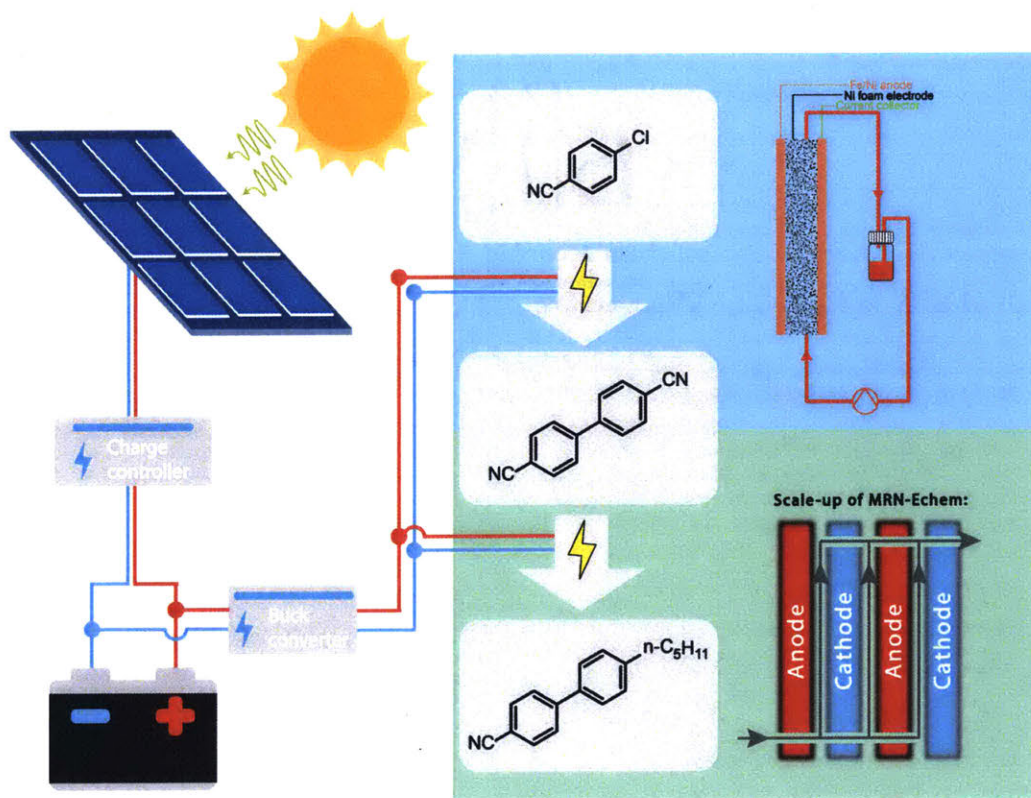


**Figure 6.18. Fully solar-electrochemical synthesis of 5CB.**

First step involves synthesis of 4,4'-biphenyldicarbonitrile (BPCN) via an electrochemical reductive homocoupling reaction of 4-CIBN utilizing inexpensive  $\text{NiCl}_2$  and bipyridine ligand as the catalyst.<sup>220</sup> Operating this reaction in a recycled electrochemical flow cell (Figure 6.19a-b) can greatly simplify the handling of synthetic organic electrochemistry. Use nitrogen gas to purge the

electrochemical flow cell, and then, recycle reagent mixture through the flow cell with 2.5 ml/min flowrate using a peristaltic pump (GORE Style 500 tubing and Masterflex L/S peristaltic pump, Cole-Parmer). The reagent mixture was kept under stirring with 800 RPM to ensure catalyst particles homogeneously suspended. Start heating the flow cell to 80 °C and the inlet tubing to 60 °C. (The heated inlet tubing is for pre-heating the reagent mixture stream to minimize the nonuniform temperature distribution inside the flow cell.) Then, apply 40 mA constant current (powered by solar energy) to start the electrochemical homocoupling reaction. After 24 h (~ 1.2 F/mol), the reagent mixture went from green to dark red, and to black, and stop the reaction. Rinse the flow cell with pure DMF to collect product residue inside the flow cell. Gram-scale synthesis of BPCN (2.67 g, 87% yield) was achieved (Figure 6.19c).

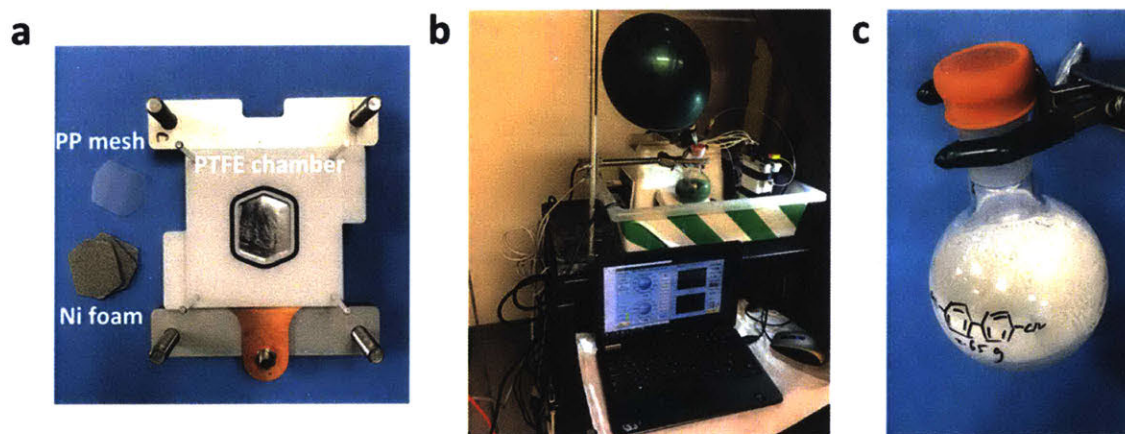


**Figure 6.19. (a) Photo of recycling electrochemical flow cell. (b) Photo of continuous electrochemical homocoupling reaction setup powered by sunlight. (c) Synthesized 2.67 g of BPCN.**

The obtained BPCN can undergo SET reduction to generate a persistent radical anion, which can take the advantage of our MRN-Echem to cross couple with n-pentyl radical generated by anodic decarboxylation of hexanoic acid to form 5CB. To demonstrate the scalability of MRN-Echem, a stacked electrode design was implemented to increase effective electrode surface area laterally and in parallel, leading to a 12-fold increase in productivity (Figure 6.20). With identify



electrochemical conditions as in the small electrochemical flow cell, 50% yield was achieved with a long-term stable operation.

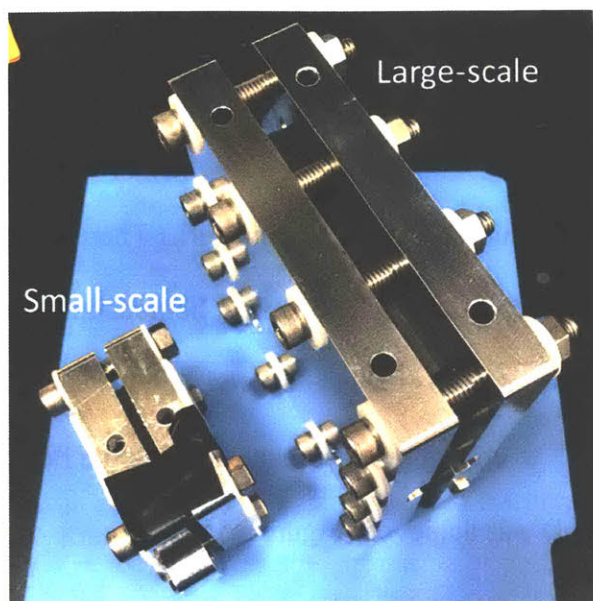


**Figure 6.20.** The comparison between small- and large- scale MRN-Echem flow cell.

## 6.4 Conclusion

This chapter developed the concept of MRN-Echem which enabled conventionally challenging redox-neutral radical chemistry under electrochemical conditions. MRN-Echem proves to be a platform technique, applicable for various types of transient and persistent radical precursors. The concept has the potential to not only demonstrated catalyst-free, low-cost, and sustainable characteristics of electrosynthesis, but could also inspire more interesting electrochemical redox-neutral reactions that fully explore the translational potential of dual-electrode systems.

## Chapter 7 Summary and future research

As continuous manufacturing of pharmaceuticals gradually gains popularity, a fully integrated flow process would be the desired diagram to have continuous material input and output without human intervention in between two unit operations. Unlike bulk chemical production, the complexity and large variety of pharmaceutical synthesis increase the cost and time for continuous process development of a specific compound. Thus, new strategies to streamline the continuous process development should be proposed with the consideration of unique characteristics of pharmaceuticals manufacturing, including relatively small scale, general applicability of various multiphase chemistry, safety concern of hazardous chemicals, environmentally friendliness, and low cost. This thesis focuses on the unsolved challenges of multiphase chemistry in flow, and correspondingly gives a modular and plug-and-play solution to each of those challenges.

- (1) Flowing of solids is always a challenge especially in small scale, which hinders many solid-containing reactions to be translated and studied in flow. Chapter 2 gives a modular CSTR cascade design as a general strategy to handle solid particles with various properties in flow. The CSTR cascade is demonstrated to have close-to-ideal residence time distribution profiles and homogeneous heating capabilities. Thus, the CSTR cascade can also serve as a lab-scale tool to study solid-containing reactions in order to help directly understand kinetics and hydrodynamics in large-scale CSTRs
- (2) Chemical transformations used in fine chemical manufacturing often involve two-phase interaction for which mass transfer limitations can lead to prolonged reaction time and reduced productivity. Following the CSTR concept proposed in Chapter 2,

Chapter 3 modifies the CSTR design with non-contact magnetic coupling stirring providing intensive agitation inside the sealed miniaturized chamber to overcome mass transfer limitations in liquid-liquid systems. High-speed imaging of the biphasic hydrodynamics gives an estimated mass transfer coefficient ( $k_{LA}$ ) on the order of  $10 \text{ s}^{-1}$ , comparable to commercial passive mixing flow reactors. Case studies with two important biphasic C-C bond-forming reactions: (1) asymmetric alkylation catalyzed by cinchonidine-derived phase-transfer catalyst, and (2) biphasic Suzuki-Miyaura C-C coupling reactions, demonstrate the versatility of the CSTR unit. Moreover, a detailed kinetic model proposed for phase-transfer reaction systems controlled by the Makosza interfacial mechanism further cross-validates the mass transfer coefficient estimates.

(3) Catalytic gas-liquid reactions have potential as environmentally benign methods for organic synthesis, particularly hydrogenation and oxidation reactions. However, safety and scalability are concerns in the large-scale application of gas-liquid reactions. Chapter 4 presents a scalable, sustainable, and safe thin-layer membrane reactor for heterogeneous Pd-catalyzed hydrogenations and homogeneous Cu(I)/TEMPO alcohol oxidations. The implementation of a Teflon AF membrane and porous carbon cloth in the membrane reactor provides sufficient gas-liquid mass transfer to afford superior performance compared to conventional packed-bed or trickle-bed reactors. The membrane separates the gas from the liquid, which avoids the formation of explosive mixtures for oxygenation reactions and simplifies the two-phase hydrodynamics to facilitate scale-up by stacking modules, while significantly reducing gas consumption. In addition, 3-dimensional simulations deliver insights into the mass transfer and hydrodynamic behavior to inform optimal membrane reactor design and operation.

- (4) Electroorganic chemistry has emerged as an environmentally benign tool for synthetic chemists to achieve efficient transformations that are challenging with traditional reagent-based methods. Continuous flow chemistry brings pharmaceutical industry numerous advantages, but implementing electroorganic synthesis in flow is challenging, especially for electroorganic reactions with coupled electrode reactions and slow chemical reactions. Chapter 5 presents a continuous electrolysis system engineered for the N-hydroxyphthalimide (NHPI) mediated electrochemical aerobic oxidation of benzylic C-H bonds. First, a cation-exchange membrane prevents the crossover of the NHPI anion from anolyte to catholyte avoiding reductive decomposition of NHPI at the cathode, and enables the usage of a cost-effective reticulated vitreous carbon (RVC) cathode instead of a platinum electrode. Second, running the electrochemical flow cell with recycle streams accommodates the inherently slow kinetics of the chemical reaction without phthalimide-N-oxyl (PINO) radical self-decomposition at the anode, and allows the usage of gaseous oxygen as co-oxidant.
- (5) The oxidative or reductive nature of electro-synthesis inevitably requires sacrificial counter electrode reactions for electron neutrality, which causes potential issues, such as waste of sacrificial material and chemical incompatibility. Chapter 6 introduces a microfluidic redox-neutral electrochemistry (MRN-Echem) strategy, synergistically utilizing both electrodes, to enable redox-neutral radical-radical cross-coupling reactions. Central to this chemistry and engineering design, persistent radical and transient radical are generated simultaneously at cathode and anode, respectively, giving the selective radical-radical cross-coupling product facilitated by the rapid diffusion of persistent radical across the  $\mu$ -meter inter-electrode gap. Various radical

precursors, including unactivated carboxylic acids, undergo facile catalyst-free cross-coupling reactions with MRN-Echem, demonstrating the translational potential of this technique.

The effort in this thesis is to make continuous flow synthesis of pharmaceuticals more amenable to a broader range of multiphase chemistry. In terms of the continuation of this effort, several directions can be pursued in the future to expand the scope and depth of solutions developed in this thesis.

- (1) A direct extension of this thesis work is looking into strategies to scale up the modular reactor designs proposed. CSTR cascade design in the small scale has close-to-ideal RTD and extremely high biphasic mass transfer performance, but those characteristics will inevitably deviate from ideal situation when increasing the dimensions. Thus, a strategy (scale-out instead of scale-up) that can scale up the productivity without losing the ideal performance will be desired. The scale-up concept of membrane reactor and electrochemical synthesis has already been discussed in this thesis, but the detailed mathematical models and kinetics simulations are still necessary when further increasing the scale.
- (2) Currently, end-to-end continuous flow synthesis primarily relies on simple existing reactors (i.e. tubular reactor, large-scale CSTR, and packed bed reactor).<sup>142,221</sup> Integration of the new reactor designs with conventional multi-step synthesis process designs can further intensify the process. In addition, the membrane reactor design can enable gaseous oxygen as a safe and green oxidant, which is previously avoided due to the safety concerns. Electrosynthesis, even though relatively new to organic chemists

and even newer to process chemists and engineers, can be gradually to be implemented for certain processes that are challenging with conventional synthetic methodologies.

- (3) Those new reactor modules are small enough to be used as an analytical tool to be integrated into current reaction screening and condition optimization platforms to enable challenging multiphase chemistry screening.<sup>222-224</sup> For example, screening solid reagent still remains as a challenge in a microfluidic screening platform, however, utilizing a CSTR unit can improve the capability to hand solid reagent screening in a continuous mode, which can also help to obtain kinetic information of solid-containing reactions using ramping methods<sup>225</sup>.
- (4) Despite the strategies developed in this thesis are tailored for pharmaceutical applications, they can be generalized to other reaction systems, such as bulk chemical synthesis, polymer synthesis, and nanomaterial synthesis. As demonstrated in Chapter 6, a new synthesis pathway of 5CB, a commonly used liquid crystal material, has been enabled by the microfluidic redox-neutral electrochemistry, which greatly improves the efficiency and cost over the conventional synthetic pathway.

## References

- (1) Gutmann, B.; Cantillo, D.; Kappe, C. O. Continuous-Flow Technology—A Tool for the Safe Manufacturing of Active Pharmaceutical Ingredients. *Angew. Chem. Int. Ed.* **2015**, *54* (23), 6688–6728.
- (2) Wernet, G.; Conradt, S.; Isenring, H. P.; Jiménez-González, C.; Hungerbühler, K. Life Cycle Assessment of Fine Chemical Production: A Case Study of Pharmaceutical Synthesis. *Int. J. Life Cycle Assess.* **2010**, *15* (3), 294–303.
- (3) Roberge, D. M.; Ducry, L.; Bieler, N.; Cretton, P.; Zimmermann, B. Microreactor Technology: A Revolution for the Fine Chemical and Pharmaceutical Industries? *Chem. Eng. Technol.* **2005**, *28* (3), 318–323.
- (4) Wegner, J.; Ceylan, S.; Kirschning, A. Ten Key Issues in Modern Flow Chemistry. *Chem. Commun.* **2011**, *47* (16), 4583–4592.
- (5) Tsubogo, T.; Oyamada, H.; Kobayashi, S. Multistep Continuous-Flow Synthesis of (R)- and (S)-Risperidone Using Heterogeneous Catalysts. *Nature* **2015**, *520* (7547), 329–332.
- (6) Wiles, C.; Watts, P. Continuous Flow Reactors: A Perspective. *Green Chem.* **2012**, *14* (1), 38–54.
- (7) Ley, S. V.; Baxendale, I. R. New Tools and Concepts for Modern Organic Synthesis. *Nat. Rev. Drug Discov.* **2002**, *1* (8), 573–586.
- (8) Geyer, K.; Codée, J. D. C.; Seeberger, P. H. Microreactors as Tools for Synthetic Chemists—The Chemists’ Round-Bottomed Flask of the 21st Century? *Chem. – Eur. J.* **2006**, *12* (33), 8434–8442.
- (9) Hartman, R. L.; McMullen, J. P.; Jensen, K. F. Deciding Whether To Go with the Flow: Evaluating the Merits of Flow Reactors for Synthesis. *Angew. Chem. Int. Ed.* **2011**, *50* (33), 7502–7519.
- (10) Ley, S. V.; Fitzpatrick, D. E.; Ingham, Richard. J.; Myers, R. M. Organic Synthesis: March of the Machines. *Angew. Chem. Int. Ed.* **2015**, *54* (11), 3449–3464.
- (11) Ley, S. V.; Fitzpatrick, D. E.; Myers, R. M.; Battilocchio, C.; Ingham, Richard. J. Machine-Assisted Organic Synthesis. *Angew. Chem. Int. Ed.* **2015**, *54* (35), 10122–10136.
- (12) Hessel, V.; Kralisch, D.; Kockmann, N.; Noël, T.; Wang, Q. Novel Process Windows for Enabling, Accelerating, and Uplifting Flow Chemistry. *ChemSusChem* **2013**, *6* (5), 746–789.
- (13) A. I. Stankiewicz; J. A. Moulijn. Process Intensification: Transforming Chemical Engineering. *Chem. Eng. Prog.* **2000**, 22–34.
- (14) Górak, A.; Stankiewicz, A. Intensified Reaction and Separation Systems. *Annu. Rev. Chem. Biomol. Eng.* **2011**, *2*, 431–451.
- (15) Hessel, V. Novel Process Windows – Gate to Maximizing Process Intensification via Flow Chemistry. *Chem. Eng. Technol.* **2009**, *32*, 1655–1681.
- (16) V. Hessel; A. Renken; J. C. Schouten; J. I. Yoshida. *Handbook of Micro Process Technology (Volume 1 - 3)*; Handbook of Micro Process Technology; Wiley-VCH: Weinheim, Germany, 2009.
- (17) Jensen, K. F.; Reizman, B. J.; Newman, S. G. Tools for Chemical Synthesis in Microsystems. *Lab. Chip* **2014**, *14*, 3206–3212.

- (18) Kitson, P. J.; Glatzel, S.; Cronin, L. The Digital Code Driven Autonomous Synthesis of Ibuprofen Automated in a 3D-Printer-Based Robot. *Beilstein J. Org. Chem.* **2016**, *12* (1), 2776–2783.
- (19) Jensen, K. F. Flow Chemistry—Microreaction Technology Comes of Age. *AIChE J.* **2017**, *63* (3), 858–869.
- (20) Gutmann, B.; Cantillo, D.; Kappe, C. O. Continuous-Flow Technology A Tool for the Safe Manufacturing of Active Pharmaceutical Ingredients. *Angew. Chem. Int. Ed.* **2015**, *54*, 6688–6728.
- (21) Hessel, V.; Kralisch, D.; Kockmann, N.; Noel, T.; Wang, Q. Novel Process Windows for Enabling, Accelerating, and Uplifting Flow Chemistry. *Chemsuschem* **2013**, *6*, 746–789.
- (22) Ley, S. V.; Fitzpatrick, D. E.; Myers, R. M.; Battilocchio, C.; Ingham, R. J. Machine-Assisted Organic Synthesis. *Angew. Chem. Int. Ed.* **2015**, *54*, 10122–10136.
- (23) Ley, S. V.; Fitzpatrick, D. E.; Ingham, R. J.; Myers, R. M. Organic Synthesis: March of the Machines. *Angew. Chem. Int. Ed.* **2015**, *54*, 3449–3464.
- (24) Movsisyan, M.; Delbeke, E. I. P.; Berton, J. K. E. T.; Battilocchio, C.; Ley, S. V.; Stevens, C. V. Taming Hazardous Chemistry by Continuous Flow Technology. *Chem. Soc. Rev.* **2016**, *45*, 4892–4928.
- (25) Plutschack, M. B.; Pieber, B.; Gilmore, K.; Seeberger, P. H. The Hitchhiker’s Guide to Flow Chemistry. *Chem. Rev.* **2017**.
- (26) Yoshida, J.; Takahashi, Y.; Nagaki, A. Flash Chemistry: Flow Chemistry That Cannot Be Done in Batch. *Chem. Commun.* **2013**, *49*, 9896–9904.
- (27) Hartman, R. L.; McMullen, J. P.; Jensen, K. F. Deciding Whether To Go with the Flow: Evaluating the Merits of Flow Reactors for Synthesis. *Angew. Chem. Int. Ed.* **2011**, *50*, 7502–7519.
- (28) Bedore, M. W.; Zaborenko, N.; Jensen, K. F.; Jamison, T. F. Aminolysis of Epoxides in a Microreactor System: A Continuous Flow Approach to  $\beta$ -Amino Alcohols. *Org. Process Res. Dev.* **2010**, *14* (2), 432–440.
- (29) Hartman, R. L. Managing Solids in Microreactors for the Upstream Continuous Processing of Fine Chemicals. *Org. Process Res. Dev.* **2012**, *16*, 870–887.
- (30) Sedelmeier, J.; Ley, S. V.; Baxendale, I. R.; Baumann, M. KMnO<sub>4</sub>-Mediated Oxidation as a Continuous Flow Process. *Org. Lett.* **2010**, *12* (16), 3618–3621.
- (31) Naber, J. R.; Hartman, R. L.; McMullen, J. P.; Jensen, K. F.; Buchwald, S. L. Palladium-Catalyzed Amination Reactions in Flow: Overcoming the Challenges of Clogging via Acoustic Irradiation. *Chem. Sci.* **2011**, *2* (2), 287–290.
- (32) Hartman, R. L.; Naber, J. R.; Zaborenko, N.; Buchwald, S. L.; Jensen, K. F. Overcoming the Challenges of Solid Bridging and Constriction during Pd-Catalyzed C–N Bond Formation in Microreactors. *Org. Process Res. Dev.* **2010**, *14* (6), 1347–1357.
- (33) Kuhn, S.; Noël, T.; Gu, L.; Heider, P. L.; Jensen, K. F. A Teflon Microreactor with Integrated Piezoelectric Actuator to Handle Solid Forming Reactions. *Lab. Chip* **2011**, *11* (15), 2488–2492.
- (34) Pamme, N. Magnetism and Microfluidics. *Lab. Chip* **2006**, *6* (1), 24–38.
- (35) Rodríguez-Villarreal, A. I.; Tarn, M. D.; Madden, L. A.; Lutz, J. B.; Greenman, J.; Samitier, J.; Pamme, N. Flow Focussing of Particles and Cells Based on Their Intrinsic Properties Using a Simple Diamagnetic Repulsion Setup. *Lab. Chip* **2011**, *11* (7), 1240–1248.



- (36) Pamme, N.; Wilhelm, C. Continuous Sorting of Magnetic Cells via On-Chip Free-Flow Magnetophoresis. *Lab. Chip* **2006**, *6* (8), 974–980.
- (37) Mo, Y.; Jensen, K. F. A Miniature CSTR Cascade for Continuous Flow of Reactions Containing Solids. *React. Chem. Eng.* **2016**, *1* (5), 501–507.
- (38) Browne, D. L.; Deadman, B. J.; Ashe, R.; Baxendale, I. R.; Ley, S. V. Continuous Flow Processing of Slurries: Evaluation of an Agitated Cell Reactor. *Org. Process Res. Dev.* **2011**, *15* (3), 693–697.
- (39) Liguori, L.; Bjørsvik, H.-R. Multijet Oscillating Disc Millireactor: A Novel Approach for Continuous Flow Organic Synthesis. *Org. Process Res. Dev.* **2011**, *15* (5), 997–1009.
- (40) Spaccini, R.; Liguori, L.; Punta, C.; Bjørsvik, H.-R. Organocatalyzed Epoxidation of Alkenes in Continuous Flow Using a Multi-Jet Oscillating Disk Reactor. *ChemSusChem* **2012**, *5* (2), 261–265.
- (41) Poe, S. L.; Cummings, M. A.; Haaf, M. P.; McQuade, D. T. Solving the Clogging Problem: Precipitate-Forming Reactions in Flow. *Angew. Chem. Int. Ed.* **2006**, *45* (10), 1544–1548.
- (42) Gilmore, K.; Vukelić, S.; McQuade, D. T.; Kokschi, B.; Seeberger, P. H. Continuous Reductions and Reductive Aminations Using Solid NaBH<sub>4</sub>. *Org. Process Res. Dev.* **2014**, *18* (12), 1771–1776.
- (43) Horie, T.; Sumino, M.; Tanaka, T.; Matsushita, Y.; Ichimura, T.; Yoshida, J. Photodimerization of Maleic Anhydride in a Microreactor Without Clogging. *Org. Process Res. Dev.* **2010**, *14* (2), 405–410.
- (44) Günther, A.; F. Jensen, K. Multiphase Microfluidics: From Flow Characteristics to Chemical and Materials Synthesis. *Lab. Chip* **2006**, *6* (12), 1487–1503.
- (45) Dreyfus, R.; Tabeling, P.; Willaime, H. Ordered and Disordered Patterns in Two-Phase Flows in Microchannels. *Phys. Rev. Lett.* **2003**, *90* (14), 144505.
- (46) Yang, L.; Nieves-Remacha, M. J.; Jensen, K. F. Simulations and Analysis of Multiphase Transport and Reaction in Segmented Flow Microreactors. *Chem. Eng. Sci.* **2017**, *169*, 106–116.
- (47) Song, H.; Chen, D. L.; Ismagilov, R. F. Reactions in Droplets in Microfluidic Channels. *Angew. Chem. Int. Ed Engl.* **2006**, *45* (44), 7336–7356.
- (48) Sebastian Cabeza, V.; Kuhn, S.; Kulkarni, A. A.; Jensen, K. F. Size-Controlled Flow Synthesis of Gold Nanoparticles Using a Segmented Flow Microfluidic Platform. *Langmuir* **2012**, *28* (17), 7007–7013.
- (49) Naber, J. R.; Buchwald, S. L. Packed-Bed Reactors for Continuous-Flow C–N Cross-Coupling. *Angew. Chem. Int. Ed.* **2010**, *49* (49), 9469–9474.
- (50) Noël, T.; Kuhn, S.; Musacchio, A. J.; Jensen, K. F.; Buchwald, S. L. Suzuki–Miyaura Cross-Coupling Reactions in Flow: Multistep Synthesis Enabled by a Microfluidic Extraction. *Angew. Chem. Int. Ed.* **2011**, *50* (26), 5943–5946.
- (51) Nieves-Remacha, M. J.; Kulkarni, A. A.; Jensen, K. F. Hydrodynamics of Liquid–Liquid Dispersion in an Advanced-Flow Reactor. *Ind. Eng. Chem. Res.* **2012**, *51*, 16251–16262.
- (52) Nieves-Remacha, M. J.; Yang, L.; Jensen, K. F. OpenFOAM Computational Fluid Dynamic Simulations of Two-Phase Flow and Mass Transfer in an Advanced-Flow Reactor. *Ind. Eng. Chem. Res.* **2015**, *54*, 6649–6659.
- (53) Kreutzer, M. T.; Kapteijn, F.; Moulijn, J. A.; Heiszwolf, J. J. Multiphase Monolith Reactors: Chemical Reaction Engineering of Segmented Flow in Microchannels. *Chem. Eng. Sci.* **2005**, *60*, 5895–5916.

- (54) Gunther, A.; Jensen, K. F. Multiphase Microfluidics: From Flow Characteristics to Chemical and Materials Synthesis. *Lab. Chip* **2006**, *6*, 1487–1503.
- (55) Song, H.; Bringer, M. R.; Tice, J. D.; Gerdt, C. J.; Ismagilov, R. F. Experimental Test of Scaling of Mixing by Chaotic Advection in Droplets Moving through Microfluidic Channels. *Appl. Phys. Lett.* **2003**, *83* (22), 4664–4666.
- (56) van Baten, J. M.; Krishna, R. CFD Simulations of Wall Mass Transfer for Taylor Flow in Circular Capillaries. *Chem. Eng. Sci.* **2005**, *60*, 1117–1126.
- (57) Nieves-Remacha, M. J.; Kulkarni, A. A.; Jensen, K. F. Gas–Liquid Flow and Mass Transfer in an Advanced-Flow Reactor. *Ind. Eng. Chem. Res.* **2013**, *52*, 8996–9010.
- (58) Yang, L.; Shi, Y.; Abolhasani, M.; Jensen, K. F. Characterization and Modeling of Multiphase Flow in Structured Microreactors: A Post Microreactor Case Study. *Lab. Chip* **2015**, *15* (15), 3232–3241.
- (59) Zhang, J.; Teixeira, A. R.; Jensen, K. F. Automated Measurements of Gas-Liquid Mass Transfer in Micropacked Bed Reactors. *AIChE J.* **2018**, *64* (2), 564–570.
- (60) Murphy, E. R.; Martinelli, J. R.; Zaborenko, N.; Buchwald, S. L.; Jensen, K. F. Accelerating Reactions with Microreactors at Elevated Temperatures and Pressures: Profiling Aminocarbonylation Reactions. *Angew. Chem. Int. Ed.* **2007**, *46*, 1734–1737.
- (61) Cantillo, D.; Oliver Kappe, C. Halogenation of Organic Compounds Using Continuous Flow and Microreactor Technology. *React. Chem. Eng.* **2017**, *2* (1), 7–19.
- (62) Losey, M. W.; Schmidt, M. A.; Jensen, K. F. Microfabricated Multiphase Packed-Bed Reactors: Characterization of Mass Transfer and Reactions. *Ind. Eng. Chem. Res.* **2001**, *40* (12), 2555–2562.
- (63) Chambers, R. D.; Holling, D.; Spink, R. C. H.; Sandford, G. Elemental Fluorine Part 13. Gas-Liquid Thin Film Microreactors for Selective Direct Fluorination. *Lab. Chip* **2001**, *1*, 132–137.
- (64) Wada, Y.; Schmidt, M. A.; Jensen, K. F. Flow Distribution and Ozonolysis in Gas–Liquid Multichannel Microreactors. *Ind. Eng. Chem. Res.* **2006**, *45* (24), 8036–8042.
- (65) Cranwell, P. B.; O’Brien, M.; Browne, D. L.; Koos, P.; Polyzos, A.; Peña-López, M.; Ley, S. V. Flow Synthesis Using Gaseous Ammonia in a Teflon AF-2400 Tube-in-Tube Reactor: Paal–Knorr Pyrrole Formation and Gas Concentration Measurement by Inline Flow Titration. *Org. Biomol. Chem.* **2012**, *10* (30), 5774–5779.
- (66) O’Brien, M.; Baxendale, I. R.; Ley, S. V. Flow Ozonolysis Using a Semipermeable Teflon AF-2400 Membrane To Effect Gas–Liquid Contact. *Org. Lett.* **2010**, *12* (7), 1596–1598.
- (67) Polyzos, A.; O’Brien, M.; Petersen, T. P.; Baxendale, I. R.; Ley, S. V. The Continuous-Flow Synthesis of Carboxylic Acids Using CO<sub>2</sub> in a Tube-In-Tube Gas Permeable Membrane Reactor. *Angew. Chem. Int. Ed.* **2011**, *50* (5), 1190–1193.
- (68) Yang, L.; Jensen, K. F. Mass Transport and Reactions in the Tube-in-Tube Reactor. *Org. Process Res. Dev.* **2013**, *17* (6), 927–933.
- (69) Zersetzung Der Valeriansäure Durch Den Elektrischen Strom. *Justus Liebigs Ann. Chem.* **1848**, *64* (3), 339–341.
- (70) Horn, E. J.; Rosen, B. R.; Baran, P. S. Synthetic Organic Electrochemistry: An Enabling and Innately Sustainable Method. *ACS Cent. Sci.* **2016**, *2* (5), 302–308.
- (71) Badalyan, A.; Stahl, S. S. Cooperative Electrocatalytic Alcohol Oxidation with Electron-Proton-Transfer Mediators. *Nature* **2016**, *535* (7612), 406–410.
- (72) Xu, H.-C.; Moeller, K. D. Intramolecular Anodic Olefin Coupling Reactions: The Use of a Nitrogen Trapping Group. *J. Am. Chem. Soc.* **2008**, *130* (41), 13542–13543.

- (73) Ashikari, Y.; Nokami, T.; Yoshida, J. Integrated Electrochemical–Chemical Oxidation Mediated by Alkoxysulfonium Ions. *J. Am. Chem. Soc.* **2011**, *133* (31), 11840–11843.
- (74) O’Brien, A. G.; Maruyama, A.; Inokuma, Y.; Fujita, M.; Baran, P. S.; Blackmond, D. G. Radical C–H Functionalization of Heteroarenes under Electrochemical Control. *Angew. Chem. Int. Ed.* **2014**, *53* (44), 11868–11871.
- (75) Kawamata, Y.; Yan, M.; Liu, Z.; Bao, D.-H.; Chen, J.; Starr, J. T.; Baran, P. S. Scalable, Electrochemical Oxidation of Unactivated C–H Bonds. *J. Am. Chem. Soc.* **2017**, *139* (22), 7448–7451.
- (76) Horn, E. J.; Rosen, B. R.; Chen, Y.; Tang, J.; Chen, K.; Eastgate, M. D.; Baran, P. S. Scalable and Sustainable Electrochemical Allylic C–H Oxidation. *Nature* **2016**, *533* (7601), 77–81.
- (77) Atobe, M.; Tateno, H.; Matsumura, Y. Applications of Flow Microreactors in Electrosynthetic Processes. *Chem. Rev.* **2017**.
- (78) Suga, S.; Okajima, M.; Fujiwara, K.; Yoshida, J. Electrochemical Combinatorial Organic Syntheses Using Microflow Systems. *QSAR Comb. Sci.* **2005**, *24* (6), 728–741.
- (79) Kashiwagi, T.; Amemiya, F.; Fuchigami, T.; Atobe, M. In Situ Electrogeneration of O-Benzoquinone and High Yield Reaction with Benzenethiols in a Microflow System. *Chem. Commun.* **2012**, *48* (22), 2806–2808.
- (80) Gütz, C.; Stenglein, A.; Waldvogel, S. R. Highly Modular Flow Cell for Electroorganic Synthesis. *Org. Process Res. Dev.* **2017**, *21* (5), 771–778.
- (81) Suga, S.; Okajima, M.; Fujiwara, K.; Yoshida, J. “Cation Flow” Method: A New Approach to Conventional and Combinatorial Organic Syntheses Using Electrochemical Microflow Systems. *J. Am. Chem. Soc.* **2001**, *123* (32), 7941–7942.
- (82) Green, R. A.; Brown, R. C. D.; Pletcher, D.; Harji, B. A Microflow Electrolysis Cell for Laboratory Synthesis on the Multigram Scale. *Org. Process Res. Dev.* **2015**, *19* (10), 1424–1427.
- (83) Green, R. A.; Brown, R. C. D.; Pletcher, D. Understanding the Performance of a Microfluidic Electrolysis Cell for Routine Organic Electrosynthesis. *J. Flow Chem.* **2014**, *5* (1), 31–36.
- (84) Leung, P.; Shah, A. A.; Sanz, L.; Flox, C.; Morante, J. R.; Xu, Q.; Mohamed, M. R.; Ponce de León, C.; Walsh, F. C. Recent Developments in Organic Redox Flow Batteries: A Critical Review. *J. Power Sources* **2017**, *360*, 243–283.
- (85) Kaushal, D. R.; Tomita, Y. Solids Concentration Profiles and Pressure Drop in Pipeline Flow of Multisized Particulate Slurries. *Int. J. Multiph. Flow* **2002**, *28* (10), 1697–1717.
- (86) Cui, H.; Grace, J. R. Flow of Pulp Fibre Suspension and Slurries: A Review. *Int. J. Multiph. Flow* **2007**, *33* (9), 921–934.
- (87) H. A. Nasr-El-Din. Flow of Suspensions in Pipelines. In *Suspensions: Fundamentals and Applications in the Petroleum Industry*; Advances in Chemistry; American Chemical Society, 1996; Vol. 251, pp 177–225.
- (88) Oroskar, A. R.; Turian, R. M. The Critical Velocity in Pipeline Flow of Slurries. *AIChE J.* **1980**, *26* (4), 550–558.
- (89) Hartman, R. L. Managing Solids in Microreactors for the Upstream Continuous Processing of Fine Chemicals. *Org. Process Res. Dev.* **2012**, *16* (5), 870–887.
- (90) Pal, S.; Kulkarni, A. A. Interfacial Precipitation and Clogging in Straight Capillaries. *Chem. Eng. Sci.*

- (91) Poe, S. L.; Cummings, M. A.; Haaf, M. P.; McQuade, D. T. Solving the Clogging Problem: Precipitate-Forming Reactions in Flow. *Angew. Chem. Int. Ed.* **2006**, *45* (10), 1544–1548.
- (92) Hartman, R. L.; Naber, J. R.; Zaborenko, N.; Buchwald, S. L.; Jensen, K. F. Overcoming the Challenges of Solid Bridging and Constriction during Pd-Catalyzed C–N Bond Formation in Microreactors. *Org. Process Res. Dev.* **2010**, *14* (6), 1347–1357.
- (93) Naber, J. R.; Hartman, R. L.; McMullen, J. P.; Jensen, K. F.; Buchwald, S. L. Palladium-Catalyzed Amination Reactions in Flow: Overcoming the Challenges of Clogging via Acoustic Irradiation. *Chem. Sci.* **2011**, *2* (2), 287–290.
- (94) Sedelmeier, J.; Ley, S. V.; Baxendale, I. R.; Baumann, M. KMnO<sub>4</sub>-Mediated Oxidation as a Continuous Flow Process. *Org. Lett.* **2010**, *12* (16), 3618–3621.
- (95) Kuhn, S.; Noël, T.; Gu, L.; Heider, P. L.; Jensen, K. F. A Teflon Microreactor with Integrated Piezoelectric Actuator to Handle Solid Forming Reactions. *Lab. Chip* **2011**, *11* (15), 2488–2492.
- (96) Pamme, N.; Wilhelm, C. Continuous Sorting of Magnetic Cells via On-Chip Free-Flow Magnetophoresis. *Lab. Chip* **2006**, *6* (8), 974–980.
- (97) Rodríguez-Villarreal, A. I.; Tarn, M. D.; Madden, L. A.; Lutz, J. B.; Greenman, J.; Samitier, J.; Pamme, N. Flow Focussing of Particles and Cells Based on Their Intrinsic Properties Using a Simple Diamagnetic Repulsion Setup. *Lab. Chip* **2011**, *11* (7), 1240–1248.
- (98) Pamme, N. Magnetism and Microfluidics. *Lab. Chip* **2006**, *6* (1), 24–38.
- (99) Kralj, J. G.; Lis, M. T. W.; Schmidt, M. A.; Jensen, K. F. Continuous Dielectrophoretic Size-Based Particle Sorting. *Anal. Chem.* **2006**, *78* (14), 5019–5025.
- (100) Dürr, M.; Kentsch, J.; Müller, T.; Schnelle, T.; Stelzle, M. Microdevices for Manipulation and Accumulation of Micro- and Nanoparticles by Dielectrophoresis. *ELECTROPHORESIS* **2003**, *24* (4), 722–731.
- (101) Browne, D. L.; Deadman, B. J.; Ashe, R.; Baxendale, I. R.; Ley, S. V. Continuous Flow Processing of Slurries: Evaluation of an Agitated Cell Reactor. *Org. Process Res. Dev.* **2011**, *15* (3), 693–697.
- (102) Deadman, B. J.; Browne, D. L.; Baxendale, I. R.; Ley, S. V. Back Pressure Regulation of Slurry-Forming Reactions in Continuous Flow. *Chem. Eng. Technol.* **2015**, *38* (2), 259–264.
- (103) Filipponi, P.; Gioiello, A.; Baxendale, I. R. Controlled Flow Precipitation as a Valuable Tool for Synthesis. *Org. Process Res. Dev.* **2015**, *20* (2), 371–375.
- (104) Liguori, L.; Bjørsvik, H.-R. Multijet Oscillating Disc Millireactor: A Novel Approach for Continuous Flow Organic Synthesis. *Org. Process Res. Dev.* **2011**, *15* (5), 997–1009.
- (105) Spaccini, R.; Liguori, L.; Punta, C.; Bjørsvik, H.-R. Organocatalyzed Epoxidation of Alkenes in Continuous Flow Using a Multi-Jet Oscillating Disk Reactor. *ChemSusChem* **2012**, *5* (2), 261–265.
- (106) Morris, G.; Power, G.; Ferguson, S.; Barrett, M.; Hou, G.; Glennon, B. Estimation of Nucleation and Growth Kinetics of Benzoic Acid by Population Balance Modeling of a Continuous Cooling Mixed Suspension, Mixed Product Removal Crystallizer. *Org. Process Res. Dev.* **2015**, *19* (12), 1891–1902.
- (107) Yang, Y.; Nagy, Z. K. Advanced Control Approaches for Combined Cooling/Antisolvent Crystallization in Continuous Mixed Suspension Mixed Product Removal Cascade Crystallizers. *Chem. Eng. Sci.* **2015**, *127*, 362–373.

- (108) Yang, Y.; Nagy, Z. K. Combined Cooling and Antisolvent Crystallization in Continuous Mixed Suspension, Mixed Product Removal Cascade Crystallizers: Steady-State and Startup Optimization. *Ind. Eng. Chem. Res.* **2015**, *54* (21), 5673–5682.
- (109) Alvarez, A. J.; Singh, A.; Myerson, A. S. Crystallization of Cyclosporine in a Multistage Continuous MSMR Crystallizer. *Cryst. Growth Des.* **2011**, *11* (10), 4392–4400.
- (110) Levenspiel, O. *Chemical Reaction Engineering*, 3rd ed.; Wiley: New York, 1999.
- (111) Yang, Q.; Drak, A.; Hasson, D.; Semiat, R. RO Module RTD Analyses Based on Directly Processing Conductivity Signals. *J. Membr. Sci.* **2007**, *306* (1–2), 355–364.
- (112) McMullen, J. P.; Jensen, K. F. Rapid Determination of Reaction Kinetics with an Automated Microfluidic System. *Org. Process Res. Dev.* **2011**, *15* (2), 398–407.
- (113) Hoffmann, W.; Kang, Y.; Mitchell, J. C.; Snowden, M. J. Kinetic Data by Nonisothermal Reaction Calorimetry: A Model-Assisted Calorimetric Evaluation. *Org. Process Res. Dev.* **2007**, *11* (1), 25–29.
- (114) Silvestri, M. G.; Dills, C. E. A Kinetic Study of the Diels-Alder Reaction: An Experiment Illustrating Simple Second-Order Reaction Kinetics. *J. Chem. Educ.* **1989**, *66* (8), 690.
- (115) Yoshida, Y.; Sakakura, Y.; Aso, N.; Okada, S.; Tanabe, Y. Practical and Efficient Methods for Sulfonylation of Alcohols Using Ts(Ms)Cl/Et<sub>3</sub>N and Catalytic Me<sub>3</sub>H·HCl as Combined Base: Promising Alternative to Traditional Pyridine. *Tetrahedron* **1999**, *55* (8), 2183–2192.
- (116) Shirakawa, S.; Maruoka, K. Recent Developments in Asymmetric Phase-Transfer Reactions. *Angew. Chem. Int. Ed.* **2013**, *52* (16), 4312–4348.
- (117) E. Denmark, S. Deconstructing Quinine. Part 1. Toward an Understanding of the Remarkable Performance of Cinchona Alkaloids in Asymmetric Phase Transfer Catalysis. *HETEROCYCLES* **2010**, *82* (2), 1527.
- (118) Ooi, T.; Maruoka, K. Recent Advances in Asymmetric Phase-Transfer Catalysis. *Angew. Chem. Int. Ed.* **2007**, *46* (23), 4222–4266.
- (119) Kinzel, T.; Zhang, Y.; Buchwald, S. L. A New Palladium Precatalyst Allows for the Fast Suzuki–Miyaura Coupling Reactions of Unstable Polyfluorophenyl and 2-Heteroaryl Boronic Acids. *J. Am. Chem. Soc.* **2010**, *132* (40), 14073–14075.
- (120) Noël, T.; Kuhn, S.; Musacchio, A. J.; Jensen, K. F.; Buchwald, S. L. Suzuki–Miyaura Cross-Coupling Reactions in Flow: Multistep Synthesis Enabled by a Microfluidic Extraction. *Angew. Chem. Int. Ed.* **2011**, *50* (26), 5943–5946.
- (121) Bruno, N. C.; Tudge, M. T.; Buchwald, S. L. Design and Preparation of New Palladium Precatalysts for C–C and C–N Cross-Coupling Reactions. *Chem. Sci.* **2013**, *4* (3), 916–920.
- (122) Calabrese, G. S.; Pissavini, S. From Batch to Continuous Flow Processing in Chemicals Manufacturing. *AIChE J.* **2011**, *57* (4), 828–834.
- (123) Roberge, D. Lonza – Hazardous Flow Chemistry for Streamlined Large Scale Synthesis. *Green Process. Synth.* **2012**, *1* (1), 129–130.
- (124) Nieves-Remacha, M. J.; Kulkarni, A. A.; Jensen, K. F. Hydrodynamics of Liquid–Liquid Dispersion in an Advanced-Flow Reactor. *Ind. Eng. Chem. Res.* **2012**, *51* (50), 16251–16262.
- (125) Nieves-Remacha, M. J.; Kulkarni, A. A.; Jensen, K. F. Gas–Liquid Flow and Mass Transfer in an Advanced-Flow Reactor. *Ind. Eng. Chem. Res.* **2013**, *52* (26), 8996–9010.
- (126) Liguori, L.; Bjørsvik, H.-R. Multijet Oscillating Disc Millireactor: A Novel Approach for Continuous Flow Organic Synthesis. *Org. Process Res. Dev.* **2011**, *15* (5), 997–1009.

- (127) Mo, Y.; Jensen, K. F. A Miniature CSTR Cascade for Continuous Flow of Reactions Containing Solids. *React. Chem. Eng.* **2016**, *1* (5), 501–507.
- (128) Britton, J.; Meneghini, L. M.; Raston, C. L.; Weiss, G. A. Accelerating Enzymatic Catalysis Using Vortex Fluidics. *Angew. Chem. Int. Ed.* **2016**, *55* (38), 11387–11391.
- (129) Britton, J.; Dalziel, S. B.; Raston, C. L. The Synthesis of Di-Carboxylate Esters Using Continuous Flow Vortex Fluidics. *Green Chem.* **2016**, *18* (7), 2193–2200.
- (130) Clift, R.; Grace, J. R.; Weber, M. E. *Bubbles, Drops, and Particles*; Academic Press, 1978.
- (131) Deen, W. M. *Analysis of Transport Phenomena, Topics in Chemical Engineering*; Oxford University Press, New York, 1998.
- (132) Timson, W.; Dunn, C. Mechanism of Gas Absorption from Bubbles under Shear. *Ind. Eng. Chem.* **1960**, *52* (9), 799–802.
- (133) Higbie, R. *The Rate of Absorption of a Pure Gas into Still Liquid during Short Periods of Exposure*; 1935.
- (134) Handlos, A. E.; Baron, T. Mass and Heat Transfer from Drops in Liquid-Liquid Extraction. *AIChE J.* **1957**, *3* (1), 127–136.
- (135) Yang, H.-M.; Wu, H.-S. Interfacial Mechanism and Kinetics of Phase-Transfer Catalysis. *Catal. Rev.* **2003**, *45* (3–4), 463–540.
- (136) Yang, C.; Teixeira, A. R.; Shi, Y.; Born, S. C.; Lin, H.; Song, Y. L.; Martin, B.; Schenkel, B.; Lachegurabi, M. P.; Jensen, K. F. Catalytic Hydrogenation of N-4-Nitrophenyl Nicotinamide in a Micro-Packed Bed Reactor. *Green Chem.* **2018**, *20* (4), 886–893.
- (137) Hruszkewycz, D. P.; Miles, K. C.; Thiel, O. R.; Stahl, S. S. Co/NHPI-Mediated Aerobic Oxygenation of Benzylic C–H Bonds in Pharmaceutically Relevant Molecules. *Chem. Sci.* **2017**, *8* (2), 1282–1287.
- (138) Gemoets, H. P. L.; Su, Y.; Shang, M.; Hessel, V.; Luque, R.; Noël, T. Liquid Phase Oxidation Chemistry in Continuous-Flow Microreactors. *Chem. Soc. Rev.* **2015**, *45* (1), 83–117.
- (139) O'Brien, M.; Baxendale, I. R.; Ley, S. V. Flow Ozonolysis Using a Semipermeable Teflon AF-2400 Membrane To Effect Gas–Liquid Contact. *Org. Lett.* **2010**, *12* (7), 1596–1598.
- (140) Carey, J. S.; Laffan, D.; Thomson, C.; Williams, M. T. Analysis of the Reactions Used for the Preparation of Drug Candidate Molecules. *Org. Biomol. Chem.* **2006**, *4* (12), 2337–2347.
- (141) Osterberg, P. M.; Niemeier, J. K.; Welch, C. J.; Hawkins, J. M.; Martinelli, J. R.; Johnson, T. E.; Root, T. W.; Stahl, S. S. Experimental Limiting Oxygen Concentrations for Nine Organic Solvents at Temperatures and Pressures Relevant to Aerobic Oxidations in the Pharmaceutical Industry. *Org. Process Res. Dev.* **2015**, *19* (11), 1537–1543.
- (142) Adamo, A.; Beingessner, R. L.; Behnam, M.; Chen, J.; Jamison, T. F.; Jensen, K. F.; Monbaliu, J.-C. M.; Myerson, A. S.; Revalor, E. M.; Snead, D. R.; et al. On-Demand Continuous-Flow Production of Pharmaceuticals in a Compact, Reconfigurable System. *Science* **2016**, *352* (6281), 61–67.
- (143) Imbrogno, J.; Rogers, L.; Thomas, D. A.; Jensen, K. F. Continuous Purification of Active Pharmaceutical Ingredients Utilizing Polymer Membrane Surface Wettability. *Chem. Commun.* **2017**, *54* (1), 70–73.
- (144) Mo, Y.; Lin, H.; Jensen, K. F. High-Performance Miniature CSTR for Biphasic C–C Bond-Forming Reactions. *Chem. Eng. J.* **2018**, *335*, 936–944.

- (145) Zaborenko, N.; Linder, R. J.; Braden, T. M.; Campbell, B. M.; Hansen, M. M.; Johnson, M. D. Development of Pilot-Scale Continuous Production of an LY2886721 Starting Material by Packed-Bed Hydrogenolysis. *Org. Process Res. Dev.* **2015**, *19* (9), 1231–1243.
- (146) Constantinou, A.; Wu, G.; Corredera, A.; Ellis, P.; Bethell, D.; Hutchings, G. J.; Kuhn, S.; Gavriilidis, A. Continuous Heterogeneously Catalyzed Oxidation of Benzyl Alcohol in a Ceramic Membrane Packed-Bed Reactor. *Org. Process Res. Dev.* **2015**, *19* (12), 1973–1979.
- (147) O'Brien, M.; Taylor, N.; Polyzos, A.; Baxendale, I. R.; Ley, S. V. Hydrogenation in Flow: Homogeneous and Heterogeneous Catalysis Using Teflon AF-2400 to Effect Gas–Liquid Contact at Elevated Pressure. *Chem. Sci.* **2011**, *2* (7), 1250–1257.
- (148) Polyzos, A.; O'Brien, M.; Petersen, T. P.; Baxendale, I. R.; Ley, S. V. The Continuous-Flow Synthesis of Carboxylic Acids Using CO<sub>2</sub> in a Tube-In-Tube Gas Permeable Membrane Reactor. *Angew. Chem. Int. Ed.* **2011**, *50* (5), 1190–1193.
- (149) Pinnau, I.; Toy, L. G. Gas and Vapor Transport Properties of Amorphous Perfluorinated Copolymer Membranes Based on 2,2-Bistrifluoromethyl-4,5-Difluoro-1,3-Dioxole/Tetrafluoroethylene. *J. Membr. Sci.* **1996**, *109* (1), 125–133.
- (150) Bernardo, P.; Drioli, E.; Golemme, G. Membrane Gas Separation: A Review/State of the Art. *Ind. Eng. Chem. Res.* **2009**, *48* (10), 4638–4663.
- (151) Lowry, J. H.; Mendlowitz, J. S.; Subramanian, N. S. (Mani). Optical Characteristics of Teflon AF<sup>®</sup> Fluoroplastic Materials. *Opt. Eng.* **1992**, *31* (9), 1982–1986.
- (152) Resnick, P. R.; Buck, W. H. Teflon<sup>®</sup> AF: A Family of Amorphous Fluoropolymers with Extraordinary Properties. In *Fluoropolymers 2; Topics in Applied Chemistry*; Springer, Boston, MA, 2002; pp 25–33.
- (153) Yang, L.; Jensen, K. F. Mass Transport and Reactions in the Tube-in-Tube Reactor. *Org. Process Res. Dev.* **2013**, *17* (6), 927–933.
- (154) Mo, Y.; Imbrogno, J.; Zhang, H.; Jensen, K. F. Scalable Thin-Layer Membrane Reactor for Heterogeneous and Homogeneous Catalytic Gas–Liquid Reactions. *Green Chem.* **2018**, *20* (16), 3867–3874.
- (155) Hoover, J. M.; Stahl, S. S. Highly Practical Copper(I)/TEMPO Catalyst System for Chemoselective Aerobic Oxidation of Primary Alcohols. *J. Am. Chem. Soc.* **2011**, *133* (42), 16901–16910.
- (156) Hoover, J. M.; Ryland, B. L.; Stahl, S. S. Copper/TEMPO-Catalyzed Aerobic Alcohol Oxidation: Mechanistic Assessment of Different Catalyst Systems. *ACS Catal.* **2013**, *3* (11), 2599–2605.
- (157) Hoover, J. M.; Ryland, B. L.; Stahl, S. S. Mechanism of Copper(I)/TEMPO-Catalyzed Aerobic Alcohol Oxidation. *J. Am. Chem. Soc.* **2013**, *135* (6), 2357–2367.
- (158) Ye, X.; Johnson, M. D.; Diao, T.; Yates, M. H.; Stahl, S. S. Development of Safe and Scalable Continuous-Flow Methods for Palladium-Catalyzed Aerobic Oxidation Reactions. *Green Chem.* **2010**, *12* (7), 1180–1186.
- (159) Steves, J. E.; Preger, Y.; Martinelli, J. R.; Welch, C. J.; Root, T. W.; Hawkins, J. M.; Stahl, S. S. Process Development of CuI/ABNO/NMI-Catalyzed Aerobic Alcohol Oxidation. *Org. Process Res. Dev.* **2015**, *19* (11), 1548–1553.
- (160) Greene, J. F.; Preger, Y.; Stahl, S. S.; Root, T. W. PTFE-Membrane Flow Reactor for Aerobic Oxidation Reactions and Its Application to Alcohol Oxidation. *Org. Process Res. Dev.* **2015**, *19* (7), 858–864.

- (161) Chen, C.-C. A Study on Estimating Flammability Limits in Oxygen. *Ind. Eng. Chem. Res.* **2011**, *50* (17), 10283–10291.
- (162) Bondar, V. I.; Freeman, B. D.; Yampolskii, Yu. P. Sorption of Gases and Vapors in an Amorphous Glassy Perfluorodioxole Copolymer. *Macromolecules* **1999**, *32* (19), 6163–6171.
- (163) Polyakov, A. M.; Starannikova, L. E.; Yampolskii, Yu. P. Amorphous Teflons AF as Organophilic Pervaporation Materials: Transport of Individual Components. *J. Membr. Sci.* **2003**, *216* (1), 241–256.
- (164) Polyakov, A. M.; Starannikova, L. E.; Yampolskii, Yu. P. Amorphous Teflons AF as Organophilic Pervaporation Materials: Separation of Mixtures of Chloromethanes. *J. Membr. Sci.* **2004**, *238* (1), 21–32.
- (165) Polyakov, A.; Bondarenko, G.; Tokarev, A.; Yampolskii, Yu. Intermolecular Interactions in Target Organophilic Pervaporation through the Films of Amorphous Teflon AF2400. *J. Membr. Sci.* **2006**, *277* (1), 108–119.
- (166) Tokarev, A.; Friess, K.; Machkova, J.; Šipek, M.; Yampolskii, Yu. Sorption and Diffusion of Organic Vapors in Amorphous Teflon AF2400. *J. Polym. Sci. Part B Polym. Phys.* **2006**, *44* (5), 832–844.
- (167) Al-Dahhan, M. H.; Larachi, F.; Dudukovic, M. P.; Laurent, A. High-Pressure Trickle-Bed Reactors: A Review. *Ind. Eng. Chem. Res.* **1997**, *36* (8), 3292–3314.
- (168) Holler, V.; Wegricht, D.; Yuranov, I.; Kiwi-Minsker, L.; Renken, A. Three-Phase Nitrobenzene Hydrogenation over Supported Glass Fiber Catalysts: Reaction Kinetics Study. *Chem. Eng. Amp Technol.* **2000**, *23* (3), 251–255.
- (169) de Mas, N.; Günther, A.; Kraus, T.; Schmidt, M. A.; Jensen, K. F. Scaled-Out Multilayer Gas–Liquid Microreactor with Integrated Velocimetry Sensors. *Ind. Eng. Chem. Res.* **2005**, *44* (24), 8997–9013.
- (170) Al-Rawashdeh, M.; Yue, F.; Patil, N. G.; Nijhuis, T. A.; Hessel, V.; Schouten, J. C.; Rebrov, E. V. Designing Flow and Temperature Uniformities in Parallel Microchannels Reactor. *AIChE J.* **2014**, *60* (5), 1941–1952.
- (171) Horn, E. J.; Rosen, B. R.; Baran, P. S. Synthetic Organic Electrochemistry: An Enabling and Innately Sustainable Method. *ACS Cent. Sci.* **2016**, *2* (5), 302–308.
- (172) Francke, R.; Little, R. D. Redox Catalysis in Organic Electrosynthesis: Basic Principles and Recent Developments. *Chem. Soc. Rev.* **2014**, *43* (8), 2492–2521.
- (173) Frontana-Urbe, B. A.; Little, R. D.; Ibanez, J. G.; Palma, A.; Vasquez-Medrano, R. Organic Electrosynthesis: A Promising Green Methodology in Organic Chemistry. *Green Chem.* **2010**, *12* (12), 2099–2119.
- (174) Feng, R.; Smith, J. A.; Moeller, K. D. Anodic Cyclization Reactions and the Mechanistic Strategies That Enable Optimization. *Acc. Chem. Res.* **2017**, *50* (9), 2346–2352.
- (175) Xu, H.-C.; Campbell, J. M.; Moeller, K. D. Cyclization Reactions of Anode-Generated Amidyl Radicals. *J. Org. Chem.* **2014**, *79* (1), 379–391.
- (176) Xu, H.-C.; Moeller, K. D. Intramolecular Anodic Olefin Coupling Reactions: The Use of a Nitrogen Trapping Group. *J. Am. Chem. Soc.* **2008**, *130* (41), 13542–13543.
- (177) Horn, E. J.; Rosen, B. R.; Chen, Y.; Tang, J.; Chen, K.; Eastgate, M. D.; Baran, P. S. Scalable and Sustainable Electrochemical Allylic C–H Oxidation. *Nature* **2016**, *533* (7601), 77–81.



- (178) O'Brien, A. G.; Maruyama, A.; Inokuma, Y.; Fujita, M.; Baran, P. S.; Blackmond, D. G. Radical C–H Functionalization of Heteroarenes under Electrochemical Control. *Angew. Chem. Int. Ed.* **2014**, *53* (44), 11868–11871.
- (179) Kawamata, Y.; Yan, M.; Liu, Z.; Bao, D.-H.; Chen, J.; Starr, J. T.; Baran, P. S. Scalable, Electrochemical Oxidation of Unactivated C–H Bonds. *J. Am. Chem. Soc.* **2017**, *139* (22), 7448–7451.
- (180) Atobe, M.; Tateno, H.; Matsumura, Y. Applications of Flow Microreactors in Electrosynthetic Processes. *Chem. Rev.* **2018**, *118* (9), 4541–4572.
- (181) Suga, S.; Okajima, M.; Fujiwara, K.; Yoshida, J. “Cation Flow” Method: A New Approach to Conventional and Combinatorial Organic Syntheses Using Electrochemical Microflow Systems. *J. Am. Chem. Soc.* **2001**, *123* (32), 7941–7942.
- (182) Folgueiras-Amador, A. A.; Philipps, K.; Guilbaud, Sébastien; Poelakker, J.; Wirth, T. An Easy-to-Machine Electrochemical Flow Microreactor: Efficient Synthesis of Isoindolinone and Flow Functionalization. *Angew. Chem. Int. Ed.* **2017**, *56* (48), 15446–15450.
- (183) Laudadio, G.; Straathof, N. J. W.; Lanting, M. D.; Knoops, B.; Hessel, V.; Noël, T. An Environmentally Benign and Selective Electrochemical Oxidation of Sulfides and Thiols in a Continuous-Flow Microreactor. *Green Chem.* **2017**, *19* (17), 4061–4066.
- (184) Soloveichik, G. L. Flow Batteries: Current Status and Trends. *Chem. Rev.* **2015**, *115* (20), 11533–11558.
- (185) Kjeang, E.; Michel, R.; Harrington, D. A.; Djilali, N.; Sinton, D. A Microfluidic Fuel Cell with Flow-Through Porous Electrodes. *J. Am. Chem. Soc.* **2008**, *130* (12), 4000–4006.
- (186) Teles, J. H.; Hermans, I.; Franz, G.; Sheldon, R. A. Oxidation. In *Ullmann's Encyclopedia of Industrial Chemistry*; American Cancer Society, 2015; pp 1–103.
- (187) Recupero, F.; Punta, C. Free Radical Functionalization of Organic Compounds Catalyzed by N-Hydroxyphthalimide. *Chem. Rev.* **2007**, *107* (9), 3800–3842.
- (188) Zhang, C.; Huang, Z.; Lu, J.; Luo, N.; Wang, F. Generation and Confinement of Long-Lived N-Oxyl Radical and Its Photocatalysis. *J. Am. Chem. Soc.* **2018**, *140* (6), 2032–2035.
- (189) Cooper, J. C.; Luo, C.; Kameyama, R.; Van Humbeck, J. F. Combined Iron/Hydroxytriazole Dual Catalytic System for Site Selective Oxidation Adjacent to Azaheterocycles. *J. Am. Chem. Soc.* **2018**, *140* (4), 1243–1246.
- (190) Chen, K.; Zhang, P.; Wang, Y.; Li, H. Metal-Free Allylic/Benzylic Oxidation Strategies with Molecular Oxygen: Recent Advances and Future Prospects. *Green Chem.* **2014**, *16* (5), 2344–2374.
- (191) Mo, Y.; Jensen, K. F. Continuous N-Hydroxyphthalimide (NHPI)-Mediated Electrochemical Aerobic Oxidation of Benzylic C–H Bonds. *Chem. – Eur. J.* **2018**, *24* (40), 10260–10265.
- (192) *Organic Electrochemistry*; Hammerich, O., Speiser, B., Eds.; CRC Press, 2015.
- (193) Koshino, N.; Saha, B.; Espenson, J. H. Kinetic Study of the Phthalimide N-Oxyl Radical in Acetic Acid. Hydrogen Abstraction from Substituted Toluenes, Benzaldehydes, and Benzyl Alcohols. *J. Org. Chem.* **2003**, *68* (24), 9364–9370.
- (194) Badalyan, A.; Stahl, S. S. Cooperative Electrocatalytic Alcohol Oxidation with Electron-Proton-Transfer Mediators. *Nature* **2016**, *535* (7612), 406–410.
- (195) Costentin, C.; Savéant, J.-M. Multielectron, Multistep Molecular Catalysis of Electrochemical Reactions: Benchmarking of Homogeneous Catalysts. *ChemElectroChem* **2014**, *1* (7), 1226–1236.

- (196) Wentzel, B. B.; Donners, M. P. J.; Alsters, P. L.; Feiters, M. C.; Nolte, R. J. M. N-Hydroxyphthalimide/Cobalt(II) Catalyzed Low Temperature Benzylic Oxidation Using Molecular Oxygen. *Tetrahedron* **2000**, *56* (39), 7797–7803.
- (197) ReactIR For Continuous Flow Chemistry [www.mt.com](http://www.mt.com) (accessed Mar 25, 2018).
- (198) Yan, M.; Kawamata, Y.; Baran, P. S. Synthetic Organic Electrochemical Methods Since 2000: On the Verge of a Renaissance. *Chem. Rev.* **2017**, *117* (21), 13230–13319.
- (199) Liu, R.; Yuan, G.; Joe, C. L.; Lightburn, T. E.; Tan, K. L.; Wang, D. Silicon Nanowires as Photoelectrodes for Carbon Dioxide Fixation. *Angew. Chem. Int. Ed.* **2012**, *51* (27), 6709–6712.
- (200) Matthessen, R.; Fransær, J.; Binnemans, K.; Vos, D. E. D. Electrocarboxylation: Towards Sustainable and Efficient Synthesis of Valuable Carboxylic Acids. *Beilstein J. Org. Chem.* **2014**, *10* (1), 2484–2500.
- (201) Peters, B. K.; Rodriguez, K. X.; Reisberg, S. H.; Beil, S. B.; Hickey, D. P.; Kawamata, Y.; Collins, M.; Starr, J.; Chen, L.; Udyavara, S.; et al. Scalable and Safe Synthetic Organic Electroreduction Inspired by Li-Ion Battery Chemistry. *Science* **2019**, *363* (6429), 838–845.
- (202) Tang, S.; Liu, Y.; Lei, A. Electrochemical Oxidative Cross-Coupling with Hydrogen Evolution: A Green and Sustainable Way for Bond Formation. *Chem* **2018**, *4* (1), 27–45.
- (203) Paddon, C. A.; Atobe, M.; Fuchigami, T.; He, P.; Watts, P.; Haswell, S. J.; Pritchard, G. J.; Bull, S. D.; Marken, F. Towards Paired and Coupled Electrode Reactions for Clean Organic Microreactor Electrosyntheses. *J. Appl. Electrochem.* **2006**, *36* (6), 617–634.
- (204) Shaw, M. H.; Twilton, J.; MacMillan, D. W. C. Photoredox Catalysis in Organic Chemistry. *J. Org. Chem.* **2016**, *81* (16), 6898–6926.
- (205) Fischer, H. The Persistent Radical Effect: A Principle for Selective Radical Reactions and Living Radical Polymerizations. *Chem. Rev.* **2001**, *101* (12), 3581–3610.
- (206) Kim, H.; Min, K.-I.; Inoue, K.; Im, D. J.; Kim, D.-P.; Yoshida, J. Submillisecond Organic Synthesis: Outpacing Fries Rearrangement through Microfluidic Rapid Mixing. *Science* **2016**, *352* (6286), 691–694.
- (207) Hartman, R. L.; McMullen, J. P.; Jensen, K. F. Deciding Whether To Go with the Flow: Evaluating the Merits of Flow Reactors for Synthesis. *Angew. Chem. Int. Ed.* **2011**, *50* (33), 7502–7519.
- (208) Kolbe, H. Beobachtungen Über Die Oxydirende Wirkung Des Sauerstoffs, Wenn Derselbe Mit Hülfe Einer Elektrischen Säule Entwickelt Wird. *J. Für Prakt. Chem.* **1847**, *41* (1), 137–139.
- (209) Behr, S.; Hegemann, K.; Schimanski, H.; Fröhlich, R.; Haufe, G. Synthesis of  $\gamma$ -Lactones from Cycloocta-1,5-Diene – Starting Materials for Natural-Product Synthesis. *Eur. J. Org. Chem.* **2004**, *2004* (18), 3884–3892.
- (210) Arai, K.; Watts, K.; Wirth, T. Difluoro- and Trifluoromethylation of Electron-Deficient Alkenes in an Electrochemical Microreactor. *ChemistryOpen* **2014**, *3* (1), 23–28.
- (211) McNally, A.; Prier, C. K.; MacMillan, D. W. C. Discovery of an  $\alpha$ -Amino C–H Arylation Reaction Using the Strategy of Accelerated Serendipity. *Science* **2011**, *334* (6059), 1114–1117.
- (212) Zuo, Z.; MacMillan, D. W. C. Decarboxylative Arylation of  $\alpha$ -Amino Acids via Photoredox Catalysis: A One-Step Conversion of Biomass to Drug Pharmacophore. *J. Am. Chem. Soc.* **2014**, *136* (14), 5257–5260.

- (213) Riehl, B.; Dyballa, K. M.; Franke, R.; Waldvogel, S. R. Electro-Organic Synthesis as a Sustainable Alternative for Dehydrogenative Cross-Coupling of Phenols and Naphthols. *Synthesis* **2017**, *49* (2), 252–259.
- (214) Ding, Y.; Zhang, C.; Zhang, L.; Zhou, Y.; Yu, G. Molecular Engineering of Organic Electroactive Materials for Redox Flow Batteries. *Chem. Soc. Rev.* **2018**, *47* (1), 69–103.
- (215) Beatty, J. W.; Stephenson, C. R. J. Amine Functionalization via Oxidative Photoredox Catalysis: Methodology Development and Complex Molecule Synthesis. *Acc. Chem. Res.* **2015**, *48* (5), 1474–1484.
- (216) McNally, A.; Prier, C. K.; MacMillan, D. W. C. Discovery of an  $\alpha$ -Amino C–H Arylation Reaction Using the Strategy of Accelerated Serendipity. *Science* **2011**, *334* (6059), 1114–1117.
- (217) Tellis, J. C.; Primer, D. N.; Molander, G. A. Single-Electron Transmetalation in Organoboron Cross-Coupling by Photoredox/Nickel Dual Catalysis. *Science* **2014**, *345* (6195), 433–436.
- (218) Collings, P. J.; Hird, M.; Hird, M. *Introduction to Liquid Crystals: Chemistry and Physics*; CRC Press, 2017.
- (219) Geem, K. M. V.; Galvita, V. V.; Marin, G. B. Making Chemicals with Electricity. *Science* **2019**, *364* (6442), 734–735.
- (220) Rahil, R.; Sengmany, S.; Gall, E. L.; Léonel, E. Nickel-Catalyzed Electrochemical Reductive Homocouplings of Aryl and Heteroaryl Halides: A Useful Route to Symmetrical Biaryls. *Synthesis* **2018**, *02* (1), 146–154.
- (221) Cole, K. P.; Groh, J. M.; Johnson, M. D.; Burcham, C. L.; Campbell, B. M.; Diserod, W. D.; Heller, M. R.; Howell, J. R.; Kallman, N. J.; Koenig, T. M.; et al. Kilogram-Scale Prexasertib Monolactate Monohydrate Synthesis under Continuous-Flow CGMP Conditions. *Science* **2017**, *356* (6343), 1144–1150.
- (222) Perera, D.; Tucker, J. W.; Brahmabhatt, S.; Helal, C. J.; Chong, A.; Farrell, W.; Richardson, P.; Sach, N. W. A Platform for Automated Nanomole-Scale Reaction Screening and Micromole-Scale Synthesis in Flow. *Science* **2018**, *359* (6374), 429–434.
- (223) Coley, C. W.; Abolhasani, M.; Lin, H.; Jensen, K. F. Material-Efficient Microfluidic Platform for Exploratory Studies of Visible-Light Photoredox Catalysis. *Angew. Chem. Int. Ed.* **2017**, *56* (33), 9847–9850.
- (224) Bédard, A.-C.; Adamo, A.; Aroh, K. C.; Russell, M. G.; Bedermann, A. A.; Torosian, J.; Yue, B.; Jensen, K. F.; Jamison, T. F. Reconfigurable System for Automated Optimization of Diverse Chemical Reactions. *Science* **2018**, *361* (6408), 1220–1225.
- (225) Moore, J. S.; Jensen, K. F. “Batch” Kinetics in Flow: Online IR Analysis and Continuous Control. *Angew. Chem. Int. Ed.* **2014**, *53* (2), 470–473.
- (226) Kumar, S.; Sobhia, M. E.; Ramachandran, U. L-Menthol as New Scaffold for Designing Chiral Phase-Transfer Catalysts. *Tetrahedron Asymmetry* **2005**, *16* (15), 2599–2605.
- (227) Fyfe, J. W. B.; Fazakerley, N. J.; Watson, A. J. B. Chemoselective Suzuki–Miyaura Cross-Coupling via Kinetic Transmetalation. *Angew. Chem. Int. Ed.* **2017**, *56* (5), 1249–1253.
- (228) Denmark, S. E.; Baird, J. D.; Regens, C. S. Palladium-Catalyzed Cross-Coupling of Five-Membered Heterocyclic Silanolates. *J. Org. Chem.* **2008**, *73* (4), 1440–1455.
- (229) Yang, J.; Liu, S.; Zheng, J.-F.; Zhou, J. (Steve). Room-Temperature Suzuki–Miyaura Coupling of Heteroaryl Chlorides and Tosylates. *Eur. J. Org. Chem.* **2012**, *2012* (31), 6248–6259.

- (230) Ge, S.; Hartwig, J. F. Highly Reactive, Single-Component Nickel Catalyst Precursor for Suzuki–Miyaura Cross-Coupling of Heteroaryl Boronic Acids with Heteroaryl Halides. *Angew. Chem. Int. Ed.* **2012**, *51* (51), 12837–12841.
- (231) Chen, H.; Huang, Z.; Hu, X.; Tang, G.; Xu, P.; Zhao, Y.; Cheng, C.-H. Nickel-Catalyzed Cross-Coupling of Aryl Phosphates with Arylboronic Acids. *J. Org. Chem.* **2011**, *76* (7), 2338–2344.
- (232) CFD Module User’s Guide, version 5.3a [www.comsol.com](http://www.comsol.com).
- (233) Chemical Reaction Engineering Module User’s Guide, version 5.3a [www.comsol.com](http://www.comsol.com).
- (234) Batey, R. A.; Quach, T. D. Synthesis and Cross-Coupling Reactions of Tetraalkylammonium Organotrifluoroborate Salts. *Tetrahedron Lett.* **2001**, *42* (52), 9099–9103.

# Appendix A Chapter 3 Supporting Information

## A.1 Reactor design details and driving motor design

The CSTR unit is composed of aluminum cover, borosilicate glass cover, PTFE impeller, ZrO<sub>2</sub> ceramic bearing, polyethylene magnets holder, high-pull magnets, PTFE inner wall, and aluminum jacket. The detailed design dimensions are shown as following (Figure A.1 – Figure A.5):

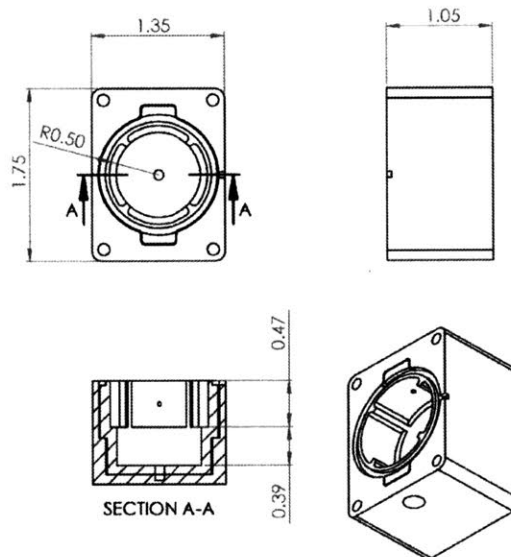


**Figure A.1. The design dimensions for aluminum jacket and inner PTFE wall. (unit: inch)**

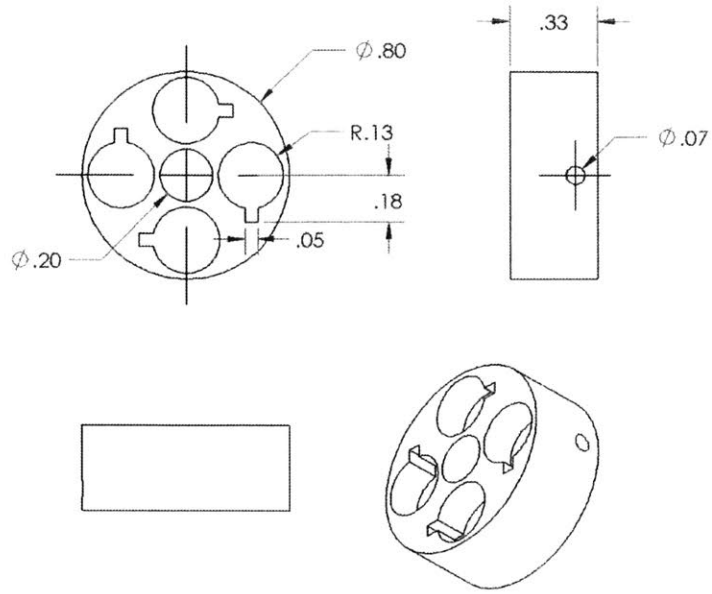


**Figure A.2. The design dimensions for the magnet holder. (unit: inch)**

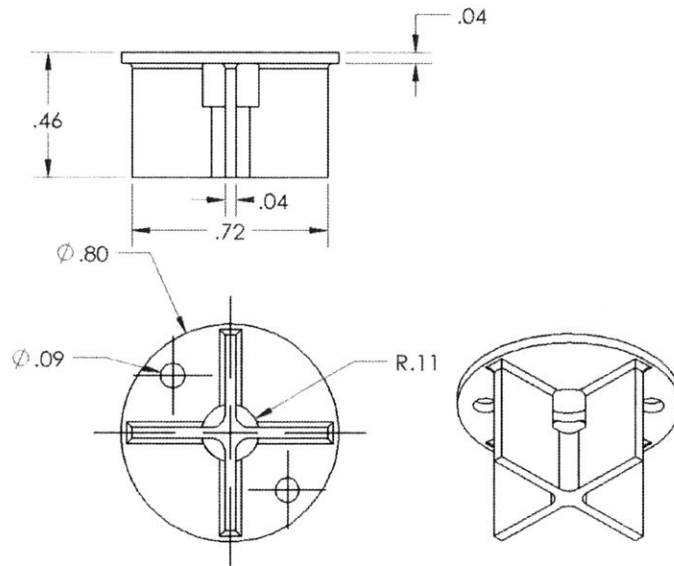


**Figure A.3. The design dimensions for the impeller. (unit: inch)**

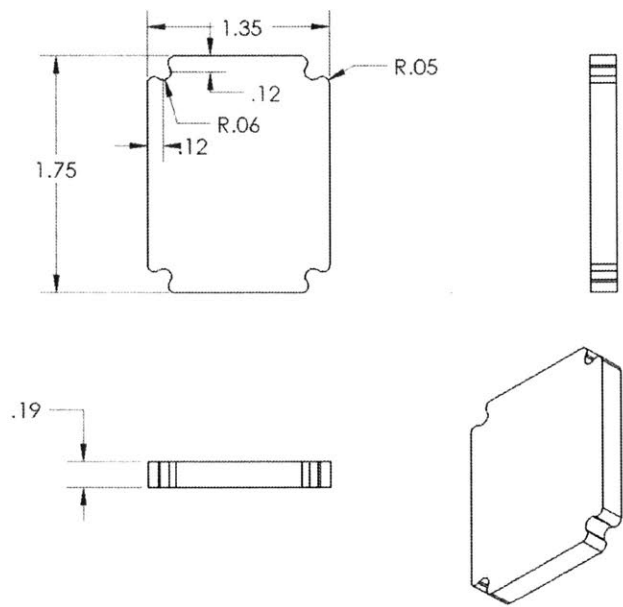


**Figure A.4. The design dimensions for the glass cover. (unit: inch)**

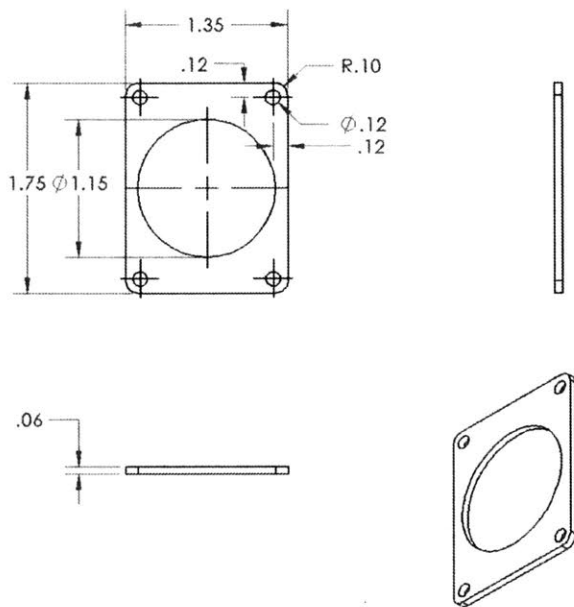


**Figure A.5. The design dimensions for the aluminum cover. (unit: inch)**

Outside the reactor, four driving magnets on the motor provide the driving force to spin the impeller inside the reactor chamber. (Figure A.1Figure A.6) The EC motor (Maxon Motors Company) provides an accurate control of the rotation speed. The position of the four driving

magnets needs to be perfectly aligned with the follower magnets inside the reactor in order to form the maximal magnetic coupling force.



**Figure A.6. The driving motor with four magnets on its shaft.**

## **A.2 Single-phase residence time distribution (RTD) measurement**

The residence time distribution (RTD) measurement was carried out using the pulse injection method. The schematics of the experimental setup is shown in Figure A.7.



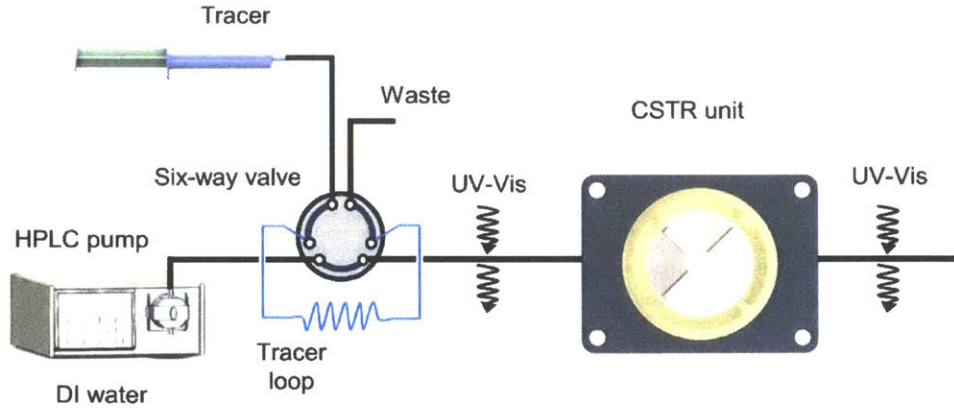


**Figure A.7. Scheme of the RTD measurement using in-line UV-Vis to record concentration profiles for inlet and outlet.**

### A.3 Droplet Size Distribution Captured Using High-Speed Imagination

The droplet size distributions for different hexane/water ratios under various different RPMs are shown in Figure A.8 – Figure A.10. The distribution under the same condition was obtained using multiple images since a single image would not provide enough number of droplets to plot the size distribution. The droplet size distribution was used to calculate the Sauter diameter ( $d_{32}$ ) for estimating the mass transfer coefficient under different conditions.

$$d_{32} = \frac{\sum_i n_i d_{pi}^3}{\sum_i n_i d_{pi}^2} \quad \text{Equation A.1}$$

Thus, the Sauter diameter is an average value across multiple steady-state images collected at different time points. Thus, the mass transfer coefficient ( $k_{1a}$ ) estimated based on the Sauter diameter does not have a corresponding error bar.

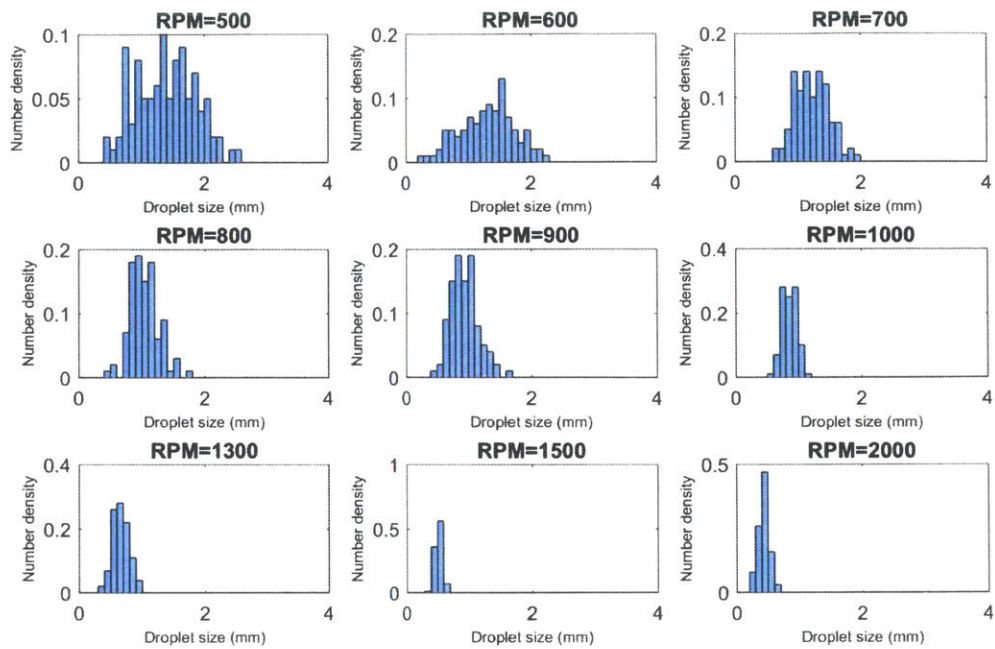


**Figure A.8. The droplet size distribution for hexane : water = 1:1 under various RPMs.**

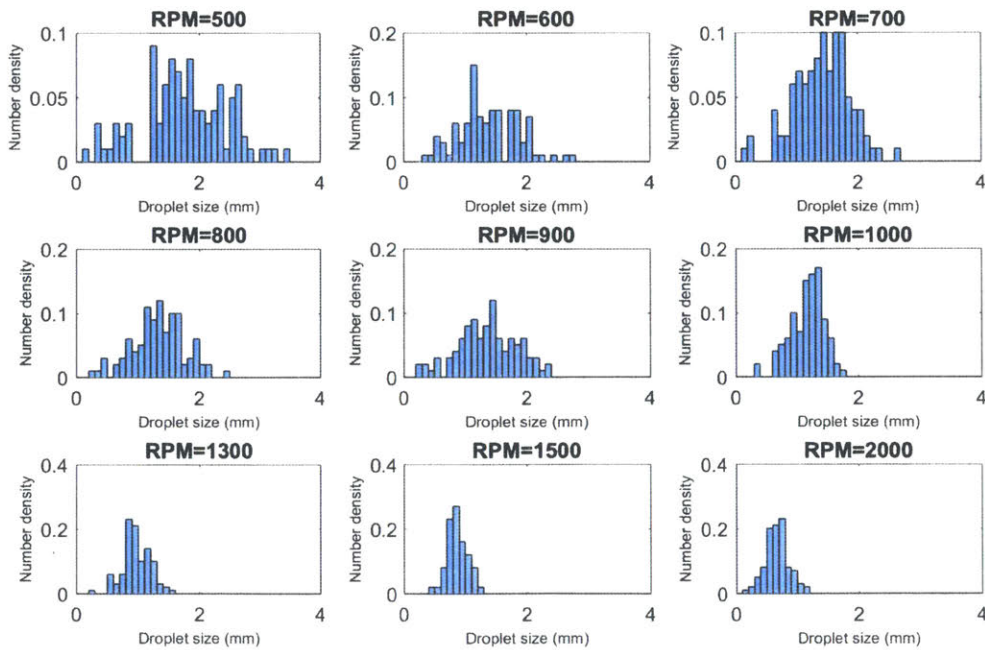


**Figure A.9. The droplet size distribution for hexane : water = 1:2 under various RPMs.**

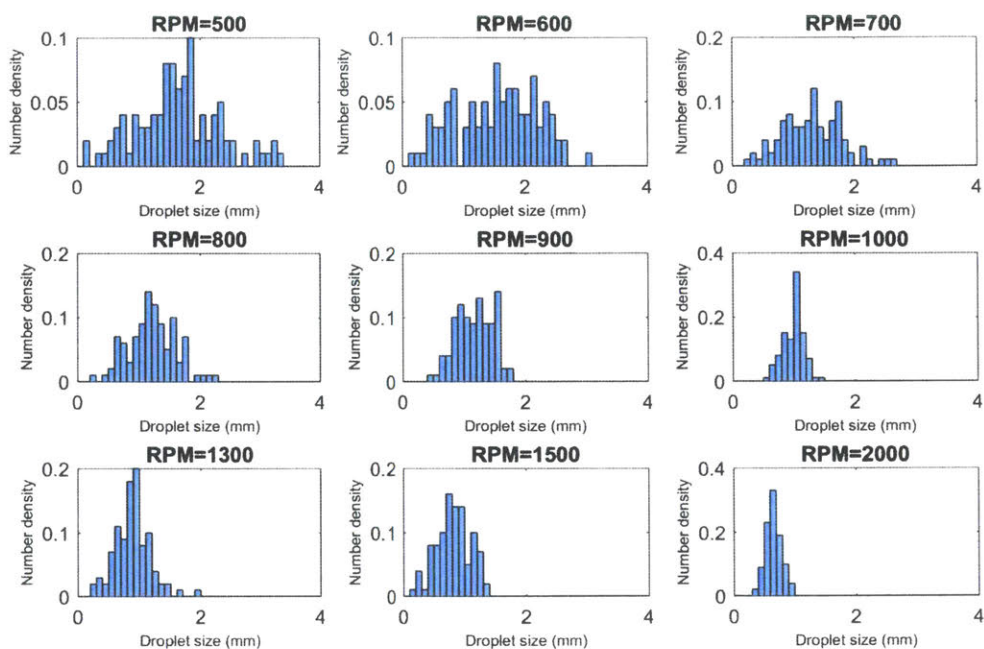


**Figure A.10. The droplet size distribution for hexane : water = 2:1 under various RPMs.**

#### **A.4 Asymmetric phase-transfer catalyzed reaction**

Further increasing the RPM from 1200 to 2000 did not improve the yield of the reaction as shown in Figure A.11, which indicates that the reaction is limited by intrinsic kinetics and the mass transfer limitation has been eliminated by the intensive agitation.

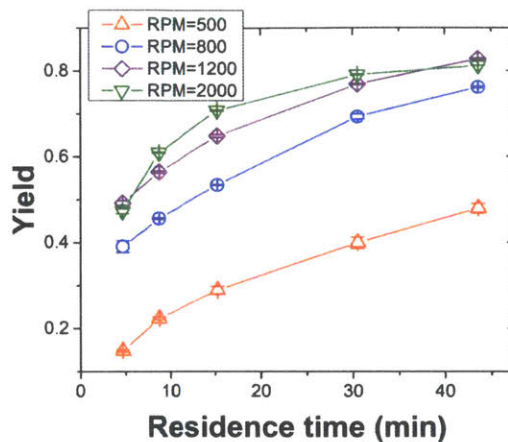


**Figure A.11.** The yield (HPLC yield) of asymmetric catalyzed reaction at different residence and rotation speed.

In order to rationalize the effect of mass transfer coefficient on the outcome of the reaction, an explicit relationship between reaction yield and mass transfer coefficient obtained from the kinetic model (Figure A.12) can clearly show the mass transfer limitation is nearly eliminated when RPM is above 1200.

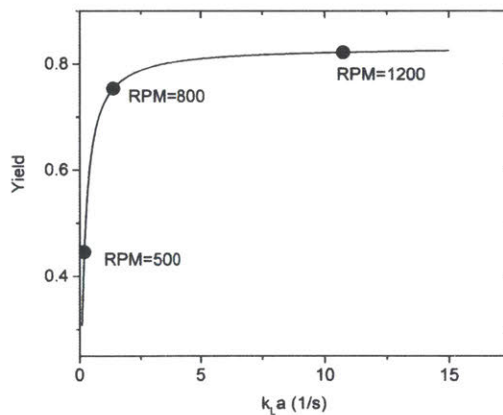


**Figure A.12.** The relationship between yield and mass transfer coefficient calculated from the kinetic model. (Identical reaction conditions and the residence time is 43 min)

## A.5 Kinetic model for makosza interfacial mechanism

As shown in Figure A.13, the reaction system contains very high-concentration KOH aqueous phase, which is 6 times more viscous than pure water. This leads to difficulty to obtain a well dispersed biphasic system. When RPM=500, the organic phase tends to stay around the wall because wall material is hydrophobic. The dispersion of organic phase gets much better when increasing the rotation speed of impeller to 1200, and it results in a more uniformly dispersed system. (Figure A.13)

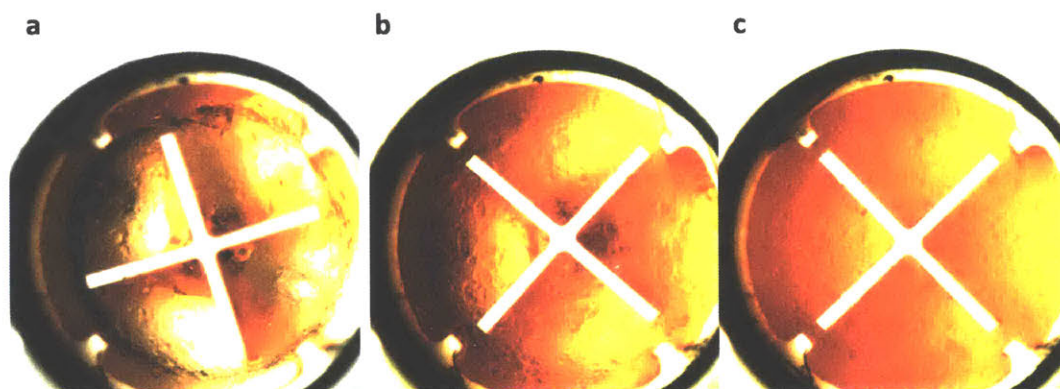


**Figure A.13. High-speed imaging of asymmetric phase transfer reaction system: (a) RPM=500, (b) RPM=800, and (c) RPM=1200.**

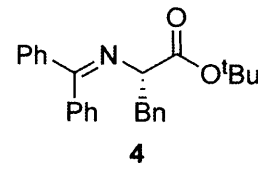
## **A.6 General Purification and Characterization Methods**

The phrase "X was concentrated" refers to removal of solvents by means of a rotary evaporator attached to a Büchi V-700 vacuum pump (bled to 40-1000 mbar as needed). SiliaFlash<sup>®</sup> F60 (230-400 mesh) from SiliCycle<sup>®</sup> was used for flash column chromatography. Analytical thin layer chromatography (TLC) was performed using EMD Millipore glass backed plates (Cat# 105715). Preparative TLC was performed using Analtech glass backed plates (Cat# 02012). TLC plates were analyzed by short wave UV illumination.

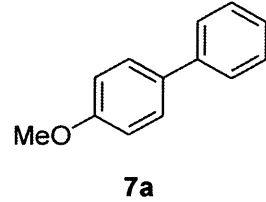
<sup>1</sup>H, <sup>13</sup>C and <sup>19</sup>F NMR spectra were recorded on a Bruker Avance 400 MHz and Varian Inova-500 spectrometer in CDCl<sub>3</sub> at ambient temperature unless otherwise indicated. Chemical

shifts are reported in  $\delta$  (ppm downfield from tetramethylsilane) and referenced to residual undeuterated solvents (7.26 for  $^1\text{H}$  NMR and 77.0 for  $^{13}\text{C}$  NMR). Coupling constants are reported in Hz with multiplicities denoted as s (singlet), d (doublet), dd (doublet of doublets), ddd (doublet of doublet of doublets), t (triplet), q (quartet), m (multiplet) and br (broad). High resolution mass spectra (HRMS) were performed by the Department of Chemistry Instrumentation Facility at Massachusetts Institute of Technology on a Bruker Daltonics APEXIV 4.7 Tesla Fourier Transform Ion Cyclotron Resonance Mass Spectrometer (FT-ICR-MS), using direct analysis in real time (DART).

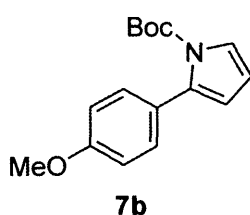
### A.7 Characterization of synthesized compounds



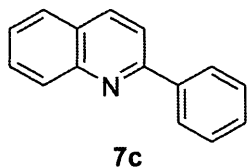
The crude product was purified by preparative TLC with hexanes/EtOAc = 20:1. NMR spectra are identical to those of literature.<sup>226</sup>  $^1\text{H}$  NMR (500 MHz,  $\text{CDCl}_3$ )  $\delta$  7.59-7.55 (m, 2H), 7.39-7.24 (m, 6H+ $\text{CHCl}_3$ ), 7.21-7.13 (m, 3H), 7.08-7.03 (m, 2H), 6.66-6.54 (m, 2H), 4.10 (dd, 1H,  $J = 9.3, 4.2$ ), 3.27-3.12 (m, 2H), 1.44 (s, 9H).  $^{13}\text{C}$  NMR (126 MHz,  $\text{CDCl}_3$ )  $\delta$  170.8, 170.3, 139.5, 138.3, 136.3, 130.0, 129.8, 128.7, 128.2, 128.05, 128.01, 127.9, 127.6, 126.1, 81.1, 67.9, 39.6, 28.0. HRMS (DART) calcd for  $\text{C}_{26}\text{H}_{28}\text{NO}_2$  ( $\text{M}+\text{H}$ )<sup>+</sup> 386.2115, found 386.2099.



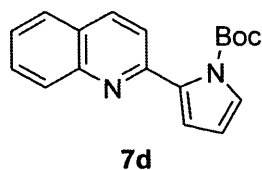
The crude product was purified by preparative TLC with hexanes/EtOAc = 20:1. NMR spectra are identical to those of literature.<sup>227</sup>  $^1\text{H}$  NMR (500 MHz,  $\text{CDCl}_3$ )  $\delta$  7.62-7.51 (m, 4H), 7.47-7.40 (m, 2H), 7.35-7.29 (m, 1H), 7.03-6.97 (m, 2H), 3.86 (s, 3H).  $^{13}\text{C}$  NMR (126 MHz,  $\text{CDCl}_3$ )  $\delta$  159.1, 140.7, 133.6, 128.6, 128.0, 126.60, 126.55, 114.1, 55.1. HRMS (DART) calcd for  $\text{C}_{13}\text{H}_{12}\text{O}$  ( $\text{M}$ )<sup>+</sup> 184.0883, found 184.0877.



The crude product was purified by preparative TLC with hexanes/toluene/EtOAc/Et<sub>3</sub>N = 20:6:0.5:0.5. NMR spectra are identical to those of literature.<sup>228</sup> <sup>1</sup>H NMR (500 MHz, CDCl<sub>3</sub>) δ 7.32 (dd, 1H, *J* = 3.3, 1.8), 7.30-7.24 (m, 2H), 6.91-6.87 (m, 2H), 6.20 (t, 1H, *J* = 3.3), 6.13 (dd, 1H, *J* = 3.2, 1.8), 3.83 (s, 3H), 1.39 (s, 9H). <sup>13</sup>C NMR (126 MHz, CDCl<sub>3</sub>) δ 158.7, 149.2, 134.7, 130.2, 126.7, 122.0, 113.8, 112.8, 110.3, 83.2, 55.0, 27.5. HRMS (DART) calcd for C<sub>16</sub>H<sub>19</sub>NO<sub>3</sub> (M+H)<sup>+</sup> 274.1438, found 274.1438.

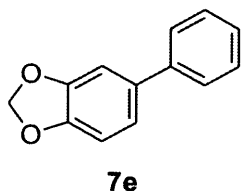


The crude product was purified by preparative TLC with hexanes/EtOAc/Et<sub>3</sub>N = 20:1:0.5. NMR spectra are identical to those of literature.<sup>229</sup> <sup>1</sup>H NMR (500 MHz, CDCl<sub>3</sub>) δ 8.22 (d, 1H, *J* = 8.7), 8.20-8.14 (m, 3H), 7.88 (d, 1H, *J* = 8.7), 7.83 (br d, 1H, *J* = 8.2), 7.76-7.70 (m, 1H), 7.56-7.50 (m, 3H), 7.50-7.44 (m, 1H). <sup>13</sup>C NMR (126 MHz, CDCl<sub>3</sub>) δ 157.2, 148.1, 139.5, 136.6, 129.59, 129.52, 129.2, 128.7, 127.4, 127.3, 127.0, 126.1, 118.8. HRMS (DART) calcd for C<sub>15</sub>H<sub>12</sub>N (M+H)<sup>+</sup> 206.0964, found 206.0973.



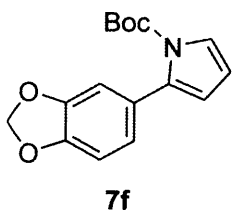
The crude product was purified by preparative TLC with hexanes/EtOAc/Et<sub>3</sub>N = 20:2:0.8. NMR spectra are identical to those of literature.<sup>230</sup> <sup>1</sup>H NMR (500 MHz, CDCl<sub>3</sub>) δ 8.13 (br d, 1H, *J* = 8.5), 8.09 (br d, 1H, *J* = 8.5), 7.82 (br d, 1H, *J* = 8.1), 7.74-7.68 (m, 1H), 7.56-7.49 (m, 2H), 7.42 (dd, 1H, *J* = 3.2, 1.7), 6.57 (dd, 1H, *J* = 3.3, 1.7), 6.30 (t, 1H, *J* = 3.3), 1.28 (s, 9H). <sup>13</sup>C NMR (126 MHz, CDCl<sub>3</sub>)

$\delta$  152.7, 149.2, 147.4, 135.2, 134.2, 129.4, 129.2, 127.4, 126.7, 126.1, 123.8, 122.0, 116.3, 110.7, 83.7, 27.4. HRMS (DART) calcd for  $C_{18}H_{19}N_2O_2$  (M+H)<sup>+</sup> 295.1441, found 295.1430.



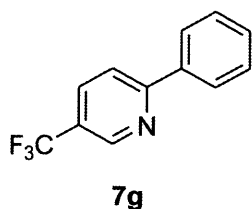
The crude product was purified by preparative TLC with hexanes/toluene = 20:3.5. NMR spectra are identical to those of literature.<sup>231</sup> <sup>1</sup>H NMR (500 MHz, CDCl<sub>3</sub>)  $\delta$  7.56-7.49 (m, 2H), 7.45-7.38 (m, 2H), 7.35-7.29 (m, 1H), 7.12-7.04

(m, 2H), 6.92-6.87 (m, 1H), 6.01 (s, 2H). <sup>13</sup>C NMR (126 MHz, CDCl<sub>3</sub>)  $\delta$  148.1, 147.0, 140.9, 135.5, 128.7, 126.85, 126.81, 120.5, 108.5, 107.6, 101.0. HRMS (DART) calcd for  $C_{13}H_{10}O_2$  (M)<sup>+</sup> 198.0675, found 198.0670.



The crude product was purified by preparative TLC with hexanes/toluene/EtOAc/Et<sub>3</sub>N = 20:5:0.3:0.4. <sup>1</sup>H NMR (500 MHz, CDCl<sub>3</sub>)  $\delta$  7.31 (dd, 1H, *J* = 3.3, 1.8), 6.84-6.78 (m, 3H), 6.19 (t, 1H, *J* = 3.3), 6.14 (dd, 1H, *J* = 3.2, 1.8), 5.97 (s, 2H), 1.41 (s, 9H). <sup>13</sup>C NMR (126 MHz, CDCl<sub>3</sub>)  $\delta$

149.1, 146.70, 146.69, 134.5, 128.0, 122.5, 122.1, 114.1, 110.3, 109.9, 107.4, 100.8, 83.3, 27.5. HRMS (DART) calcd for  $C_{16}H_{17}NO_4$  (M+H)<sup>+</sup> 288.1230, found 288.1225.

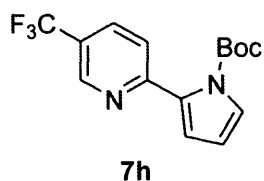


The crude product was purified by preparative TLC with hexanes/EtOAc = 100:1. NMR spectra are identical to those of literature.<sup>229</sup> <sup>1</sup>H NMR (500 MHz, CDCl<sub>3</sub>)  $\delta$  8.95 (br s, 1H), 8.07-8.01 (m, 2H), 8.01-7.96 (m, 1H), 7.87-7.82 (m, 1H), 7.55-7.45 (m, 3H). <sup>13</sup>C NMR (126 MHz, CDCl<sub>3</sub>)  $\delta$  160.5 (q, *J* = 1.5),

146.5 (q, *J* = 4.1), 137.8, 133.8 (q, *J* = 3.5), 130.0, 128.8, 127.2, 124.7 (q, *J* = 33.0), 123.7 (q, *J* =



272.2), 119.8.  $^{19}\text{F}$  NMR (470 MHz,  $\text{D}_2\text{O}$ )  $\delta$  - 62.6. HRMS (DART) calcd for  $\text{C}_{12}\text{H}_8\text{F}_3\text{N}$  ( $\text{M}+\text{H}$ ) $^+$  224.0682, found 224.0684.



The crude product was purified by preparative TLC with hexanes/acetone/ $\text{Et}_3\text{N}$  = 20:0.5:0.8. NMR spectra are identical to those of literature.<sup>230</sup>  $^1\text{H}$  NMR (500 MHz,  $\text{CDCl}_3$ )  $\delta$  8.86 (br s, 1H), 7.91 (dd, 1H,  $J$  = 8.3, 2.2), 7.53 (d, 1H,  $J$  = 8.3), 7.40 (dd, 1H,  $J$  = 3.2, 1.7), 6.53 (dd, 1H,  $J$  = 3.3, 1.6), 6.28 (t, 1H,  $J$  = 3.3), 1.41 (s, 9H).  $^{13}\text{C}$  NMR (126 MHz,  $\text{CDCl}_3$ )  $\delta$  155.8 (q,  $J$  = 1.2), 149.0, 145.7 (q,  $J$  = 4.1), 132.86, 132.84 (q,  $J$  = 3.4), 124.7, 124.3 (q,  $J$  = 33.0), 123.7 (q,  $J$  = 272.3), 122.8, 117.2, 110.9, 84.2, 27.6.  $^{19}\text{F}$  NMR (470 MHz,  $\text{D}_2\text{O}$ )  $\delta$  - 62.6. HRMS (DART) calcd for  $\text{C}_{15}\text{H}_{16}\text{F}_3\text{N}_2\text{O}_2$  ( $\text{M}+\text{H}$ ) $^+$  313.1158, found 313.1168.

## A.8 Nomenclature

$E(t)$	Residence time distribution function	$k_d$	Mass transfer coefficient in the dispersed phase
$\lambda, \mu, \sigma$	Model parameters for exponentially modified Gaussian (EMG) distribution	$u_{slip}$	Slip velocity
$t$	Time	$\mu_d$	Viscosity of the dispersed phase
$\tau$	Mean residence time	$\mu_c$	Viscosity of the continuous phase
$r$	Distance from center in the polar coordinate	$m$	Partition coefficient of phenol in hexane and water

$\theta$	Angle in the polar coordinate	$\varepsilon_d$	Hexane volume ratio
$u_\theta$	Angular velocity	F	Flowrate of organic phase
$u_r$	Radical velocity	$[A]_{inlet}$	Inlet concentration of A in the organic phase
$\rho_h$	Hexane density	$[A]_{org}$	Concentration of A in the organic phase in the reactor
$\rho_w$	Water density	$V_t$	The reactor volume
$\omega$	Angular velocity of the rotating impeller	$V_{org}$	The volume of organic phase in the reactor
$F_{drag}$	Drag forced implemented by the surrounding fluid	a	Interfacial area per reactor volume
RPM	Rotations per minute	$[A]_{in}$	Concentration of A at the interface
$u_{relative}$	Relative velocity between fluid and droplet	$[QX]_{org}$	Concentration of QX in the organic phase in the reactor
$C_D$	Drag force coefficient	$[QX]_{in}$	Concentration of QX at the interface
Re	Reynolds number	$M_1, M_2, M_3$	Partition coefficients for A, QX, and QA between organic phase and interface, respectively,
Sh	Sherwood number	$[QA]_{in}$	Concentration of QA at the interface
Pe	Péclet number	$[QA]_{org}$	Concentration of QA in the organic phase in the reactor
D	Diffusion coefficient	$[RX]_{org}$	Concentration of RX in the organic phase in the reactor
d	Diameter of the droplet	$[Q]_t$	Total concentration of Q
$k_c$	Mass transfer coefficient in the continuous phase	x	The conversion of the reaction

# Appendix B Chapter 4 Supporting Information

## B.1 Membrane reactor design and dimensions

The single-layer membrane reactor structure is illustrated in Figure 4.1b. The detailed dimensions of individual components are as follows:

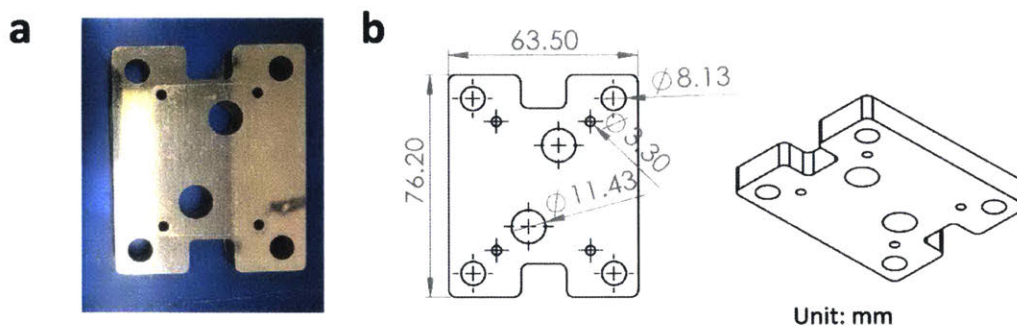


Figure B.1. (a) Photo of aluminum cover for single-layer membrane reactor. (b) Detailed dimensions of the aluminum cover for single-layer membrane reactor.

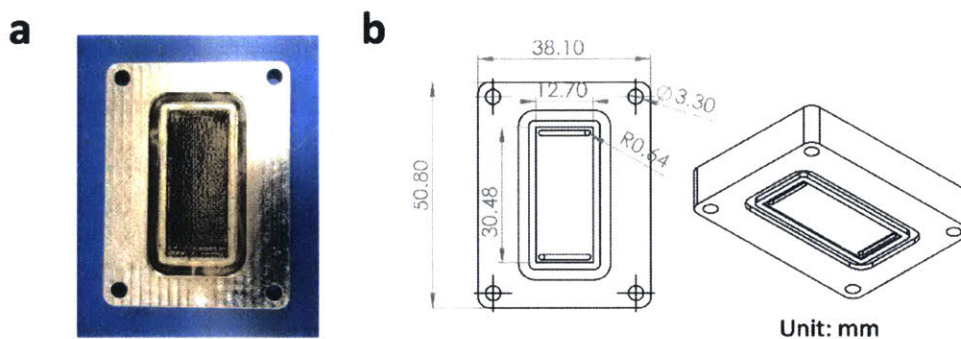
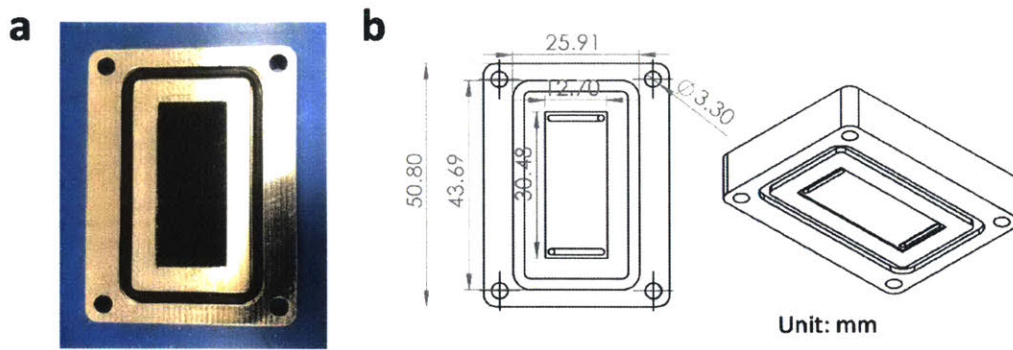
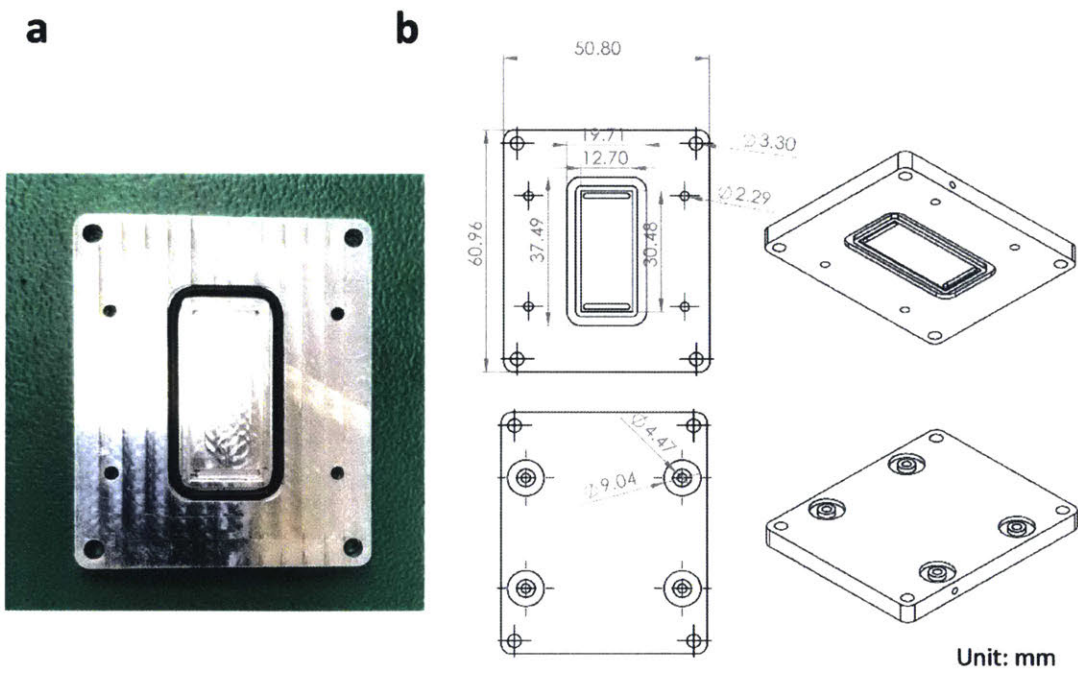


Figure B.2. (a) Photo of liquid distribution plate assembled with O-ring, Teflon AF membrane and carbon cloth for single-layer membrane reactor. (b) Detailed dimensions of the liquid distribution plate for single-layer membrane reactor.



**Figure B.3. (a) Photo of gas distribution plate assembled with O-ring and carbon cloth for single-layer membrane reactor. (b) Detailed dimensions of the gas distribution plate for single-layer membrane reactor.**

The multi-layer membrane reactor structure is illustrated in Figure 4.10b. The components of multi-layer membrane reactor structure are as follows:



**Figure B.4. (a) Photo of liquid distribution plate assembled with O-ring for multi-layer membrane reactor. (b) Detailed dimensions of the liquid distribution plate for multi-layer membrane reactor.**

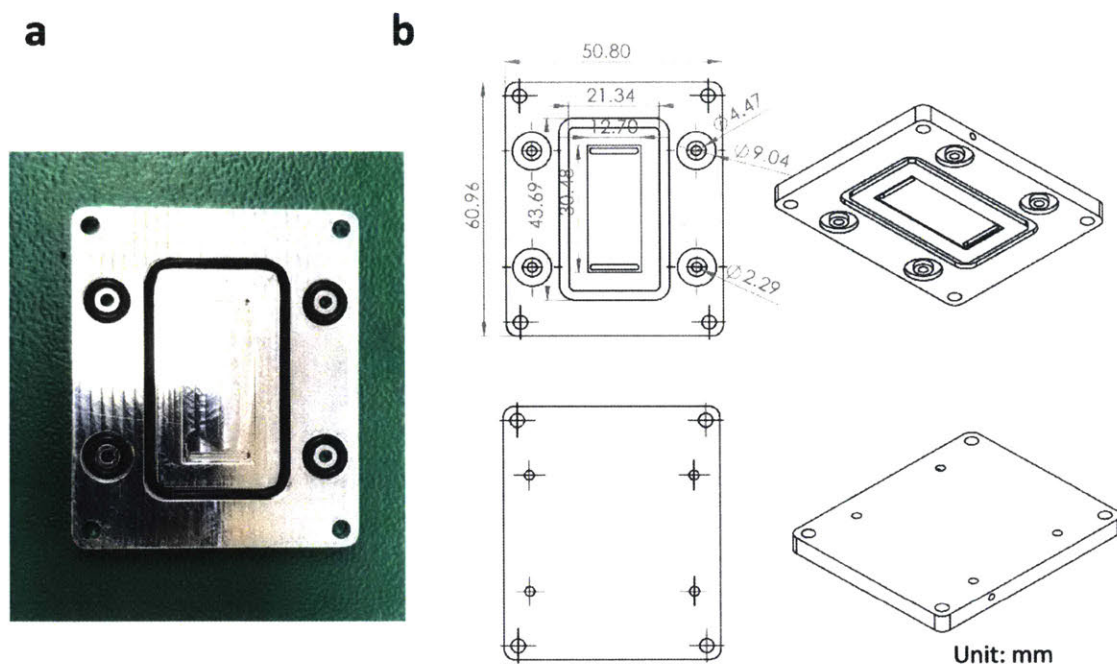


**Figure B.5. (a) Photo of gas distribution plate assembled with O-ring for multi-layer membrane reactor. (b) Detailed dimensions of the gas distribution plate for multi-layer membrane reactor.**

## **B.2 3-Dimensional COMSOL simulation of membrane reactor**

The 3-D COMSOL simulation was conducted with and without reaction. In order to evaluate the mass transfer coefficient ( $k_{L,a}$ ) for various thickness of carbon cloth, mass transfer of hydrogen into ethanol was simulated in the membrane reactor. A typical hydrogen concentration profile in the membrane reactor is shown in Figure B.6, where hydrogen gradually saturates the liquid stream along the flow direction. Figure 4.5 illustrates the dependence of  $k_{L,a}$  on the carbon cloth thickness.

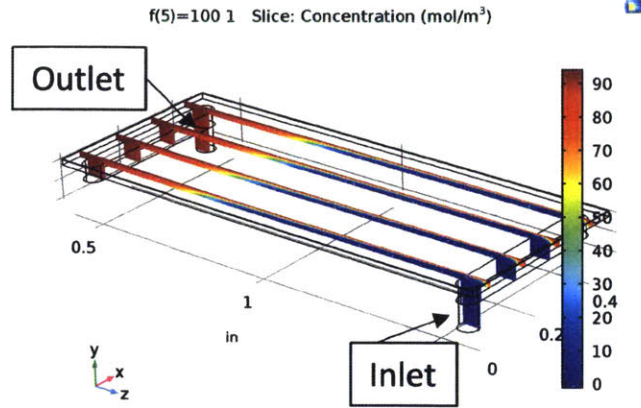


**Figure B.6. The hydrogen concentration profile in membrane reactor. Carbon cloth thickness: 0.3mm.**

To demonstrate the validity of the 1-D model proposed in the previous section, varying the values of  $Da_I$  and  $Da_{II}$  in the 3-D model can give the reaction conversion under various conditions (i.e. residence time, carbon cloth thickness, and reaction rate). As shown in Figure 4.9, the results from 3-D simulation give similar patterns as the 1-D model, thereby validating the 1-D model.

The conditions used in the COMSOL simulation are indicated in Table B.1, and the corresponding domains and boundaries described in Figure B.7. Refer to COMSOL user's guide for detailed information about the equation parameters.<sup>232,233</sup>

**Table B.1. Domain controlling equations and boundaries conditions used in the COMSOL simulation.**

Domain	Fluid Flow	Mass Transfer
A (Liquid)	$\frac{1}{\epsilon_p} \rho (\mathbf{u} \cdot \nabla) \mathbf{u} \frac{1}{\epsilon_p} = \nabla \cdot \left[ -p \mathbf{I} + \mu \frac{1}{\epsilon_p} (\nabla \mathbf{u} + (\nabla \mathbf{u})^T) \right]$ $- \left( \mu \kappa^{-1} + \beta_F  \mathbf{u}  + \frac{Q_{br}}{\epsilon_p^2} \right) \mathbf{u} + \mathbf{F}$ <p>Brinkman Equation (Fluid flow in porous media)</p>	$\nabla \cdot (-D_{e,j} \nabla c_i) + \mathbf{u} \cdot \nabla c_i = R_i + S_i$ <p>Mass transfer in porous media</p>

	$\rho \nabla \cdot (\mathbf{u}) = Q_{br}$ Continuity equation in porous media	
B (Membrane)	N.A.	$\nabla \cdot (-D_i \nabla c_i) = 0$ Diffusive mass transfer in membrane

Boundary	Fluid Flow	Mass Transfer
1 (Inlet)	$\mathbf{u} = \mathbf{U}_0$	$c_i = c_{0,i}$
2 (Outlet)	$p = p_0$	$\nabla c_i = 0$
3 (Wall)	$\mathbf{u} = 0$	$-D_i \nabla c_i + \mathbf{u} c_i = 0$
4 (Liquid – Membrane Interface)		$\frac{c_{H_2, membrane}}{c_{H_2, liquid}} = H_e$ Henry's Law boundary condition
5 (Gas – Membrane Interface)	N.A.	$c_{H_2} = c_{H_2, gas}$

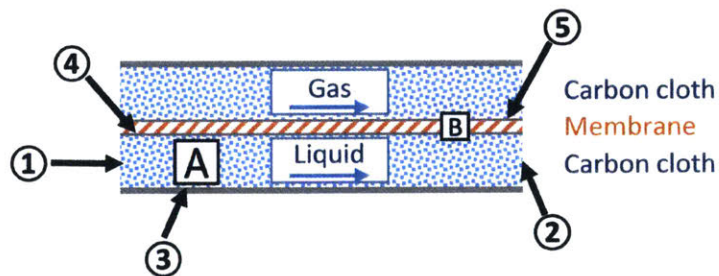
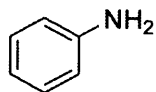
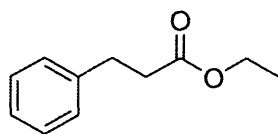


**Figure B.7. The schematics of the membrane reactor showing the positions indicated in Table B.1.**

### B.3 Experimental reaction details

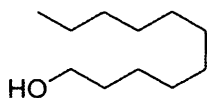


**Aniline (1b).** Prepared according to the general procedure using 0.8 mL of nitrobenzene (8.0 mmol, 1.0 equiv), carbon cloth with 4 mg/cm<sup>2</sup> Pd catalyst, and 39.2 mL of ethanol. Hydrogen gas was delivered to the system at 2.76 MPa (400 psig) and metered using a hydrogen mass flow controller. The liquid flow rate ranged from 0.05 to 0.10 mL/min (0.5 min – 1 min residence time) under a backpressure of 2.80 MPa (406 psig) and reaction temperature at 70 °C. The system was operated for a minimum of 3 residence times before collecting samples. The reaction mixture was subjected to analysis using GC-MS and compared with pure aniline purchased from Sigma Aldrich.

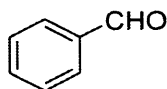


**Ethyl 3-phenylpropanoate (2b).** Prepared according to the general procedure using 3.0 mL of ethyl cinnamate (18.0 mmol, 1.0 equiv), carbon cloth with 4 mg/cm<sup>2</sup> Pd catalyst, and 27.0 mL ethyl acetate. Hydrogen gas was delivered to the system at 2.67 MPa (387 psig) and metered using a hydrogen mass flow controller. The liquid flow rate was set at 0.10 mL/min (0.5 min residence time) under a backpressure of 2.80 MPa (405 psig) and reaction temperature at 50 °C. The system was operated for a minimum of 3 residence times before collecting samples. The reaction mixture was subjected to analysis using GC-MS and compared with pure ethyl 3-phenylpropanoate purchased from Sigma Aldrich.



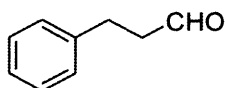


**Undecan-1-ol (3b).** Prepared according to the general procedure using 1.7 mL of 10-undecyn-1-ol (9.0 mmol, 1.0 equiv), carbon cloth with 4 mg/cm<sup>2</sup> Pd catalyst, and 28.3 mL ethyl acetate. Hydrogen gas was delivered to the system at 2.76 MPa (400 psig) and metered using a hydrogen mass flow controller. The liquid flow rate was set at 0.10 mL/min (0.5 min residence time) under a backpressure of 2.86 MPa (415 psig) and reaction temperature at 50 °C. The system was operated for a minimum of 3 residence times before collecting samples. The reaction mixture was subjected to analysis using GC-MS and compared with pure undecan-1-ol purchased from Sigma Aldrich.

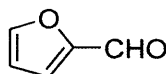


**Benzaldehyde (4b).** Prepared according to the general procedure using 0.6 mL benzyl alcohol (6.0 mmol, 1.0 equiv), 0.1 mg of tetrakisacetonitrile copper(I) triflate Cu(MeCN)<sub>4</sub>(OTf) (0.3 mmol, 0.05 equiv), 0.05 g of 2,2'-bipyridine (0.3 mmol, 0.05 equiv), 0.05 mL of 1-methylimidazole (NMI) (0.6 mmol, 0.10 equiv), 0.05 g of (2,2,6,6-tetramethylpiperidin-1-yl)oxyl (TEMPO) (0.3 mmol, 0.05 equiv), and 30.0 mL acetonitrile. Acetonitrile was sparged with argon for 1 h to remove oxygen prior to experiment. The TEMPO and alcohol substrate were mixed together and added to 25.0 mL of acetonitrile. The remaining reagents were mixed and added to 5.0 mL acetonitrile. The solution was degassed before loading the solution into the system. Oxygen gas was delivered to the system at 0.74 MPa (108 psig) and metered using an oxygen mass flow controller. The liquid flow rate for the TEMPO/alcohol solution was 0.08 mL/min and the remaining solution was 0.02 mL/min (0.5 min residence time) under a backpressure of 0.79 MPa

(115 psig) and reaction temperature at 30 °C. The system was operated for a minimum of 3 residence times before collecting samples. The reaction mixture was subjected to analysis using GC-MS and compared with pure benzaldehyde purchased from Sigma Aldrich.



**3-phenyl-1-propanal (5b).** Prepared according to the general procedure using 0.8 mL of 3-phenyl-1-propanol (6.0 mmol, 1.0 equiv), 0.1 mg of tetrakisacetonitrile copper(I) triflate  $\text{Cu}(\text{MeCN})_4(\text{OTf})$  (0.3 mmol, 0.05 equiv), 0.05 g of 2,2'-bipyridine (0.3 mmol, 0.05 equiv), 0.05 mL of 1-methylimidazole (NMI) (0.6 mmol, 0.10 equiv), 0.05 g of (2,2,6,6-tetramethylpiperidin-1-yl)oxyl (TEMPO) (0.3 mmol, 0.05 equiv), and 30.0 mL acetonitrile. Acetonitrile was sparged with argon for 1 h to remove oxygen prior to experiment. The TEMPO and alcohol substrate were mixed together and added to 25.0 mL of acetonitrile. The remaining reagents were mixed and added to 5.0 mL acetonitrile. The solutions were degassed before loading the solution into the system. Oxygen gas was delivered to the system at 2.54 MPa (368 psig) and metered using an oxygen mass flow controller. The liquid flow rate for the TEMPO/alcohol solution was 0.04 mL/min and the remaining solution was 0.01 mL/min (1 min residence time) under a backpressure of 2.69 MPa (390 psig) and reaction temperature at 50 °C. The system was operated for a minimum of 3 residence times before collecting samples. The reaction mixture was subjected to analysis using GC-MS and compared with pure 3-phenyl-1-propanal purchased from Sigma Aldrich.



**Furan-2-carbaldehyde (6b).** Prepared according to the general procedure using 0.5 mL of furfuryl alcohol (6.0 mmol, 1.0 equiv), 0.1 mg of tetrakisacetonitrile copper(I) triflate

Cu(MeCN)<sub>4</sub>(OTf) (0.3 mmol, 0.05 equiv), 0.05 g of 2,2'-bipyridine (0.3 mmol, 0.05 equiv), 0.05 mL of 1-methylimidazole (NMI) (0.6 mmol, 0.10 equiv), 0.05 g of (2,2,6,6-tetramethylpiperidin-1-yl)oxyl (TEMPO) (0.3 mmol, 0.05 equiv), and 30.0 mL acetonitrile. Acetonitrile was sparged with argon for 1 h to remove oxygen prior to experiment. The TEMPO and alcohol substrate were mixed together and added to 25.0 mL of acetonitrile. The remaining reagents were mixed and added to 5.0 mL acetonitrile. The solutions were degassed before loading the solution into the system. Oxygen gas was delivered to the system at 2.54 MPa (368 psig) and metered using an oxygen mass flow controller. The liquid flow rate for the TEMPO/alcohol solution was 0.08 mL/min and the remaining solution was 0.02 mL/min (0.5 min residence time) under a backpressure of 2.65 MPa (385 psig) and reaction temperature at 30 °C. The system was operated for a minimum of 3 residence times before collecting samples. The reaction mixture was subjected to analysis using GC-MS and compared with pure Furan-2-carbaldehyde purchased from Sigma Aldrich.

# Appendix C Chapter 5 Supporting Information

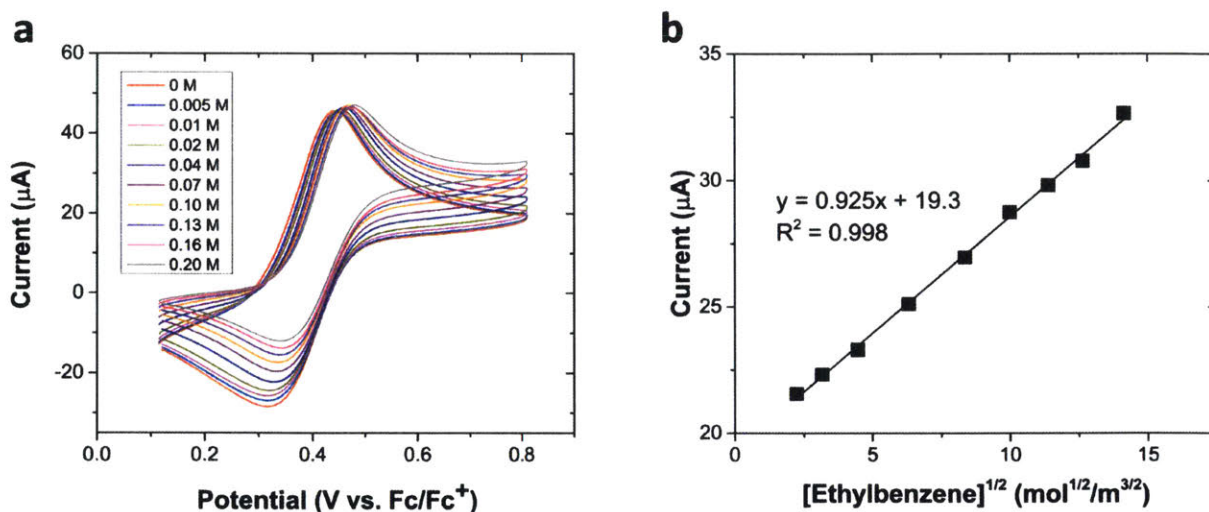
## C.1 Cyclic voltammetry kinetic study

The cyclic voltammetry kinetic study followed the reported procedures<sup>194,195</sup>. With the NHPI reaction system studied in work, the reaction happened at the anode can be simplified as below.

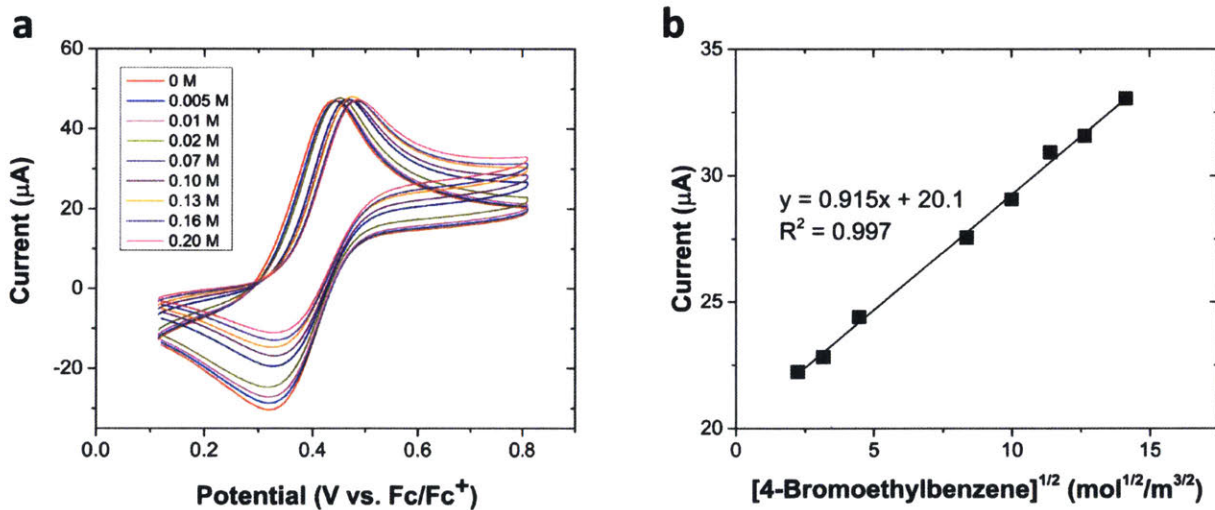


**Figure C.1. The reaction scheme for anodic side.**

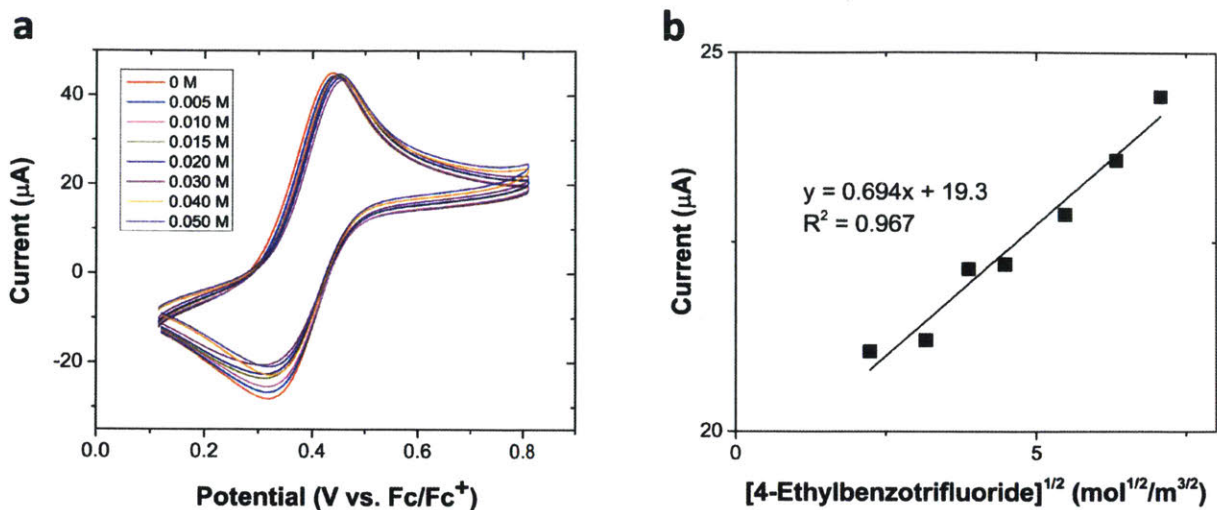
The kinetic constants were measured for various para-substituted ethylbenzenes, and their cyclic voltammograms, besides 4-ethylanisole reported in the main article (Figure 5.6a&b), are shown as following.



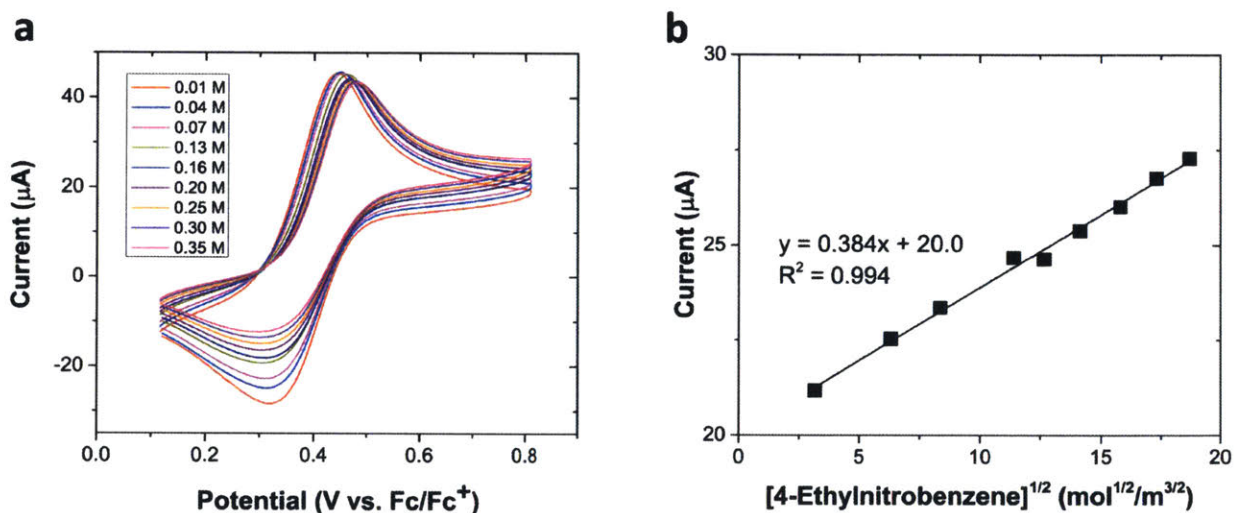
**Figure C.2.** (a) Cyclic voltammograms recorded for various reagent concentrations of ethylbenzene, corresponding to 2 mM NHPI, 0.15 M pyridine, and 0.1 M TBAP in MeCN. Scan rate: 150 mV/s. (b) Linear regression of catalytic current  $i_{cat}$  versus  $C_R^{0.5}$ .



**Figure C.3.** (a) Cyclic voltammograms recorded for various reagent concentrations of 4-bromoethylbenzene, corresponding to 2 mM NHPI, 0.15 M pyridine, and 0.1 M TBAP in MeCN. Scan rate: 150 mV/s. (b) Linear regression of catalytic current  $i_{cat}$  versus  $C_R^{0.5}$ .



**Figure C.4. (a)** Cyclic voltammograms recorded for various reagent concentrations of 4-ethylbenzotrifluoride, corresponding to 2 mM NHPI, 0.15 M pyridine, and 0.1 M TBAP in MeCN. Scan rate: 150 mV/s. **(b)** Linear regression of catalytic current  $i_{\text{cat}}$  versus  $C_R^{0.5}$ .

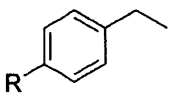
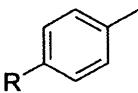


**Figure C.5. (a)** Cyclic voltammograms recorded for various reagent concentrations of 4-ethylnitrobenzene, corresponding to 2 mM NHPI, 0.15 M pyridine, and 0.1 M TBAP in MeCN. Scan rate: 150 mV/s. **(b)** Linear regression of catalytic current  $i_{\text{cat}}$  versus  $C_R^{0.5}$ .

With the kinetics obtained from the cyclic voltammetry study, the kinetic constants were compared with literature reported value using chemically generated PINO radical for the corresponding para-substituted methylbenzenes<sup>193</sup>. (Table C.1 Table C.1) The results show very

good consistency, which validates the kinetic information obtained from the cyclic voltammetry study.

**Table C.1. The comparison of kinetic constants between this study and literature values.**

Substituted group	This study ( $\text{L mol}^{-1} \text{s}^{-1}$ )	Literature ( $\text{L mol}^{-1} \text{s}^{-1}$ )
		
-OMe	$9.21 \pm 1.70$	10.3
-H	$0.720 \pm 0.0561$	0.62
-Br	$0.690 \pm 0.0705$	0.595
-CF <sub>3</sub>	$0.406 \pm 0.172$	N.A.
-NO <sub>2</sub>	$0.119 \pm 0.0159$	0.119

## C.2 Design and detailed dimensions of the electrochemical flow cell

The aluminum holder, PEEK insulator, and copper current collector were fabricated using water jet machining (OMAX MicroMAX Jet Machining Center, MIT Machine Shop). The anodic and cathodic chambers were machined using Proto Labs' CNC service. The detailed dimensions of the components are shown as below.

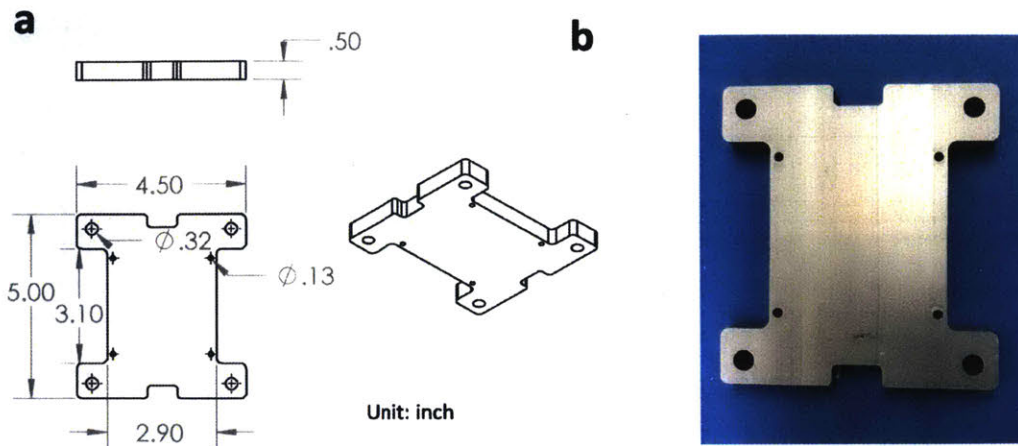


**Figure C.6. (a) Detailed dimensions for the aluminum holder; (b) Photo of the aluminum holder.**

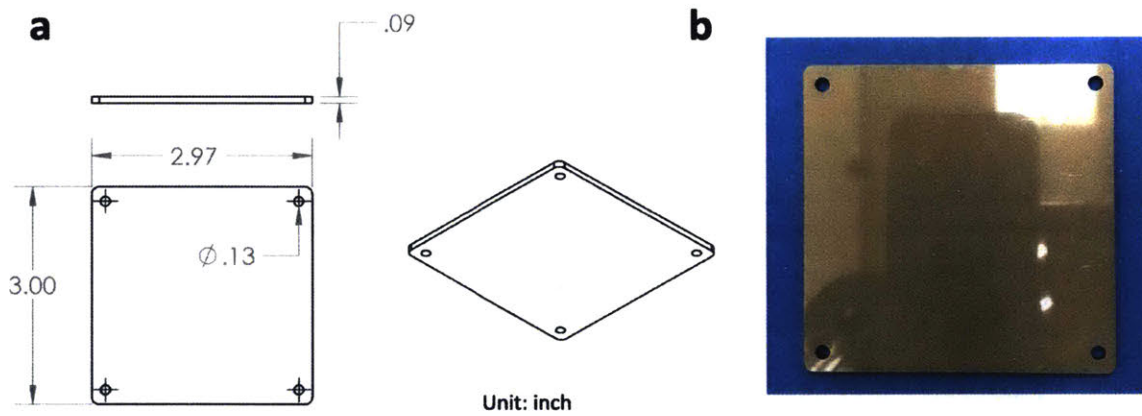


**Figure C.7. (a) Detailed dimensions for the PEEK electrical insulator; (b) Photo of the PEEK electrical insulator.**



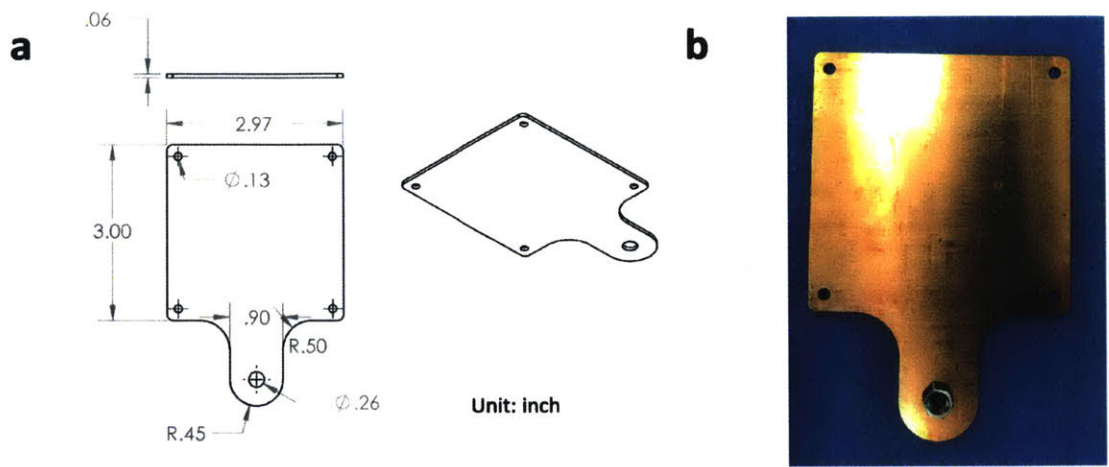


**Figure C.8. (a) Detailed dimensions for the copper current collector; (b) Photo of the copper current collector.**

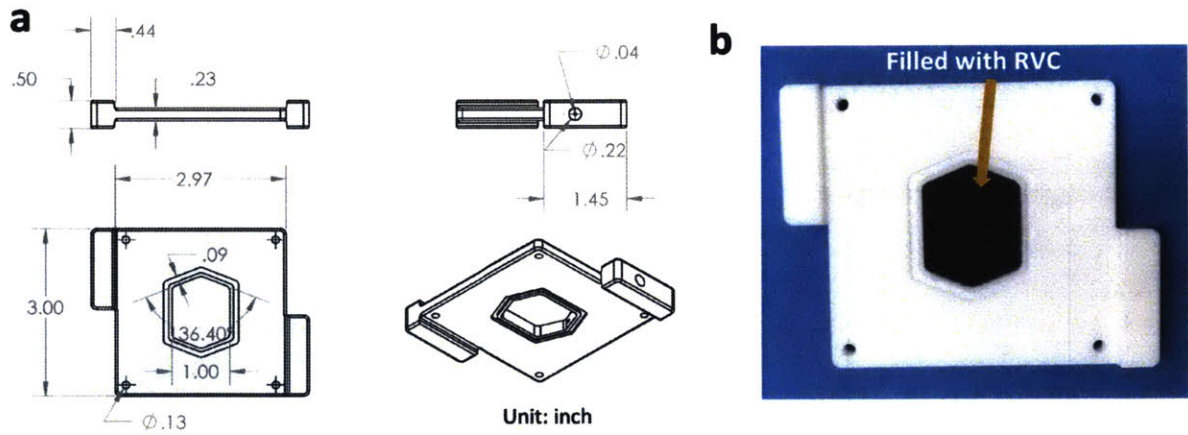


**Figure C.9. (a) Detailed dimensions for the anodic and cathodic chamber; (b) Photo of the chamber with RVC installed.**

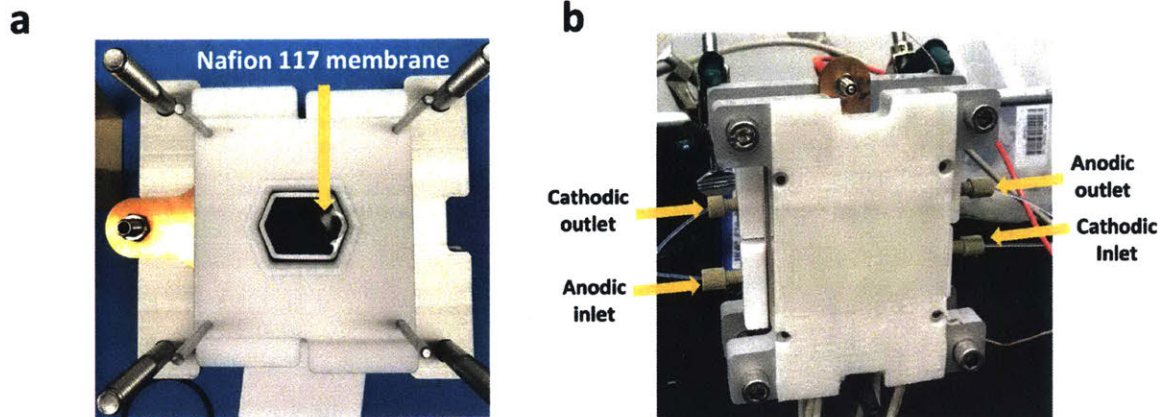


**Figure C.10. (a) Photo of the electrochemical flow cell during assembling. The Nafion membrane is sandwiched between two chambers. (b) Photo of the electrochemical cell during operation.**

# Appendix D Chapter 6 Supporting Information

## D.1 Electrode cleaning procedure

Most of the chemistries demonstrated in this manuscript show no sign of electrode fouling over a long period of running (24 h). The electrode cleaning is generally carried out to prevent cross-contamination when switching to a different substrate. A small number of substrates (noted) tend to foul the electrode gradually, and thus, intermittent cleanings of electrodes are required to ensure full conversion of the starting material.

1) Disassemble the electrochemical flow cell after the reaction; 2) Add one drop (0.1 ml) of 0.05  $\mu\text{m}$  alumina polishing fluid (Allied High Tech Products Inc., P.N. 90-187505) on the glassy carbon electrode surface; 3) Use a piece of Nylon microcloth (Buehler, P.N. 40-7212) to gently polish the surface with circular motion and even pressure for 1 min; 4) After the polishing, rinse the electrode surface with DI water to flush away any encrusted material on the surface. Sonicate electrodes to remove residual alumina polishing particles; 5) Rinse the electrode briefly with acetone and wipe it dry. The electrode is now ready to use.

## D.2 General procedure A for decarboxylative cross-coupling with aromatic nitriles

4.56 ml of 1 M  $\text{Bu}_4\text{NOH}$  methanol solution (4.56 mmol, 5.7 equiv.) is added dropwise to the corresponding carboxylic acid (4.8 mmol, 6 equiv.). After carboxylic acid gets fully dissolved in the methanol, evaporate the majority of methanol and water with rotary evaporator, and then remove the residue methanol and water under vacuum (1 mbar) and heat (50  $^\circ\text{C}$ ) for 24 h. The

prepared carboxylic acid tetrabutylammonium salt and aromatic nitrile (0.8 mmol, 1 equiv.) are dissolved in nitrogen degassed acetonitrile, and then transferred to a 10 ml volumetric flask for accurate reagent concentrations. (Additional acetonitrile is needed for less soluble substrates.) Transfer the prepared reagent solution to an 8 ml Harvard stainless steel syringe, and the syringe is placed on a Harvard syringe for accurate flowrate control.

Use 3 ml of reagent solution for reaction condition optimization. After the optimal condition is identified (the detailed reaction condition is described in each substrate), continuously collect 5 ml of reaction mixture.

### **D.3 Procedure B for cross-coupling of $\alpha$ -aminoalkyl radical and aryl nitrile**

To a 20 mL septum vial, add corresponding aromatic nitrile (1 mmol, 1 equiv.), corresponding amine (3 mmol, 3 equiv.), lithium acetate (2 mmol, 2equiv.), tetrabutylammonium tetrafluoroborate (1 mmol, 1 equiv.), and ~8 ml DMSO. The reaction mixture is stirred for ~2 h to completely dissolve lithium acetate. (Heat can be applied to accelerate dissolution.) Then, sparge the reaction mixture with nitrogen to remove dissolved oxygen. Transfer the degassed the reaction mixture to a 10 ml volumetric flask, and add remaining degassed DMSO for accurate reagent concentrations. Transfer the prepared reagent solution to an 8 ml Harvard stainless steel syringe, and the syringe is placed on a Harvard syringe for accurate flowrate control.

### **D.4 Procedure C for cross-coupling of organoboron and aryl nitrile**

Organotrifluoroborate tetrabutylammonium salt is prepared according to reported procedure.<sup>234</sup> The prepared organotrifluoroborate tetrabutylammonium salt (4.8 mmol, 6 equiv.) and aromatic nitrile (0.8 mmol, 1 equiv.) are dissolved in nitrogen degassed acetonitrile, and then transferred to a 10 ml volumetric flask for accurate reagent concentrations. Transfer the prepared

reagent solution to an 8 ml Harvard stainless steel syringe, and the syringe is placed on a Harvard syringe for accurate flowrate control.

#### **D.5 Procedure D for cross-coupling $\alpha$ -aminoalkyl radical and aryl ketone**

To a 20 mL septum vial, add corresponding benzophenone (1 mmol, 1 equiv.), corresponding amine (3 mmol, 3 equiv.), lithium acetate (2 mmol, 2equiv.), tetrabutylammonium tetrafluoroborate (1 mmol, 1 equiv.), and ~8 ml DMSO. The reaction mixture is stirred for ~2 h to completely dissolve lithium acetate. (Heat can be applied to accelerate dissolution.) Then, sparge the reaction mixture with nitrogen to remove dissolved oxygen. Transfer the degassed the reaction mixture to a 10 ml volumetric flask, and add remaining degassed DMSO for accurate reagent concentrations. Transfer the prepared reagent solution to an 8 ml Harvard stainless steel syringe, and the syringe is placed on a Harvard syringe for accurate flowrate control.

#### **D.6 Procedure E for organocatalyzed allylic C-H arylation**

Reagent mixture A:

To a 20 mL septum vial, sequentially add aromatic nitrile (1.2 mmol, 1.0 equiv.), alkene (6 mmol, 5.0 equiv.), DBU (0.48 mmol, 0.4 equiv.), tetrabutylammonium tetrafluoroborate (1 mmol, 0.83 equiv.), and ~8 ml acetone. The reagent mixture A is then cooled to  $-78\text{ }^{\circ}\text{C}$  and degassed via vacuum evacuation (5 min) and subsequent backfill with nitrogen then warming to room temperature ( $\times 3$ ). After removing the dissolved oxygen, transfer the reagent mixture to a 10 ml volumetric flask, and then add remaining acetone (oxygen-free via three freeze-pump-thaw cycles). Transfer the prepared reagent solution to an 8 ml Harvard stainless steel syringe, and the syringe is placed on a Harvard syringe for accurate flowrate control.

Reagent mixture B:

To a 20 mL septum vial, add triisopropylsilanethiol (0.48 mmol), and 4 ml acetone. The reagent mixture B is then cooled to  $-78\text{ }^{\circ}\text{C}$  and degassed via vacuum evacuation (5 min) and subsequent backfill with nitrogen then warming to room temperature ( $\times 3$ ). Transfer the prepared reagent solution to an 8 ml Harvard stainless steel syringe, and the syringe is placed on a Harvard syringe for accurate flowrate control.

Use  $\sim 2$  ml of reagent mixture A for reaction condition optimization (equivalence of triisopropylsilanethiol, potential, electrode polarity switching frequency, temperature, and flowrate). After the optimal condition is identified (the detailed reaction condition is described in each substrate), continuously collect 6 ml of reagent A.